

CHALMERS



A 1296 MHz EARTH–MOON–EARTH COMMUNICATION SYSTEM

THEORY AND PRACTICE

Master of Science Thesis

MAGNUS LINDGREN

Department of Earth and Space Sciences
CHALMERS UNIVERSITY OF TECHNOLOGY
Gothenburg, Sweden 2015

A 1296 MHz
EARTH–MOON–EARTH
COMMUNICATION SYSTEM
THEORY AND PRACTICE

MAGNUS LINDGREN

Department of Earth and Space Sciences
CHALMERS UNIVERSITY OF TECHNOLOGY
Gothenburg, Sweden 2015

A 1296 MHz
EARTH–MOON–EARTH
COMMUNICATION SYSTEM
MAGNUS LINDGREN

Version: 28th May 2015
Typeset using L^AT_EX 2 ϵ

© Magnus Lindgren, 2015,
unless otherwise noted.

Trademarks appear throughout this document
without any trademark symbol; they are the
property of their respective trademark owner.
There is no intention of infringement; the us-
age is to the benefit of the trademark owner.

Contact information:
Magnus Lindgren
[@ sm6xma@gmail.com](mailto:sm6xma@gmail.com)

Department of Earth and Space Sciences
CHALMERS UNIVERSITY OF TECHNOLOGY
412 96 GOTHENBURG
Sweden

To Ida

Abstract

The task of designing, building and characterizing an [Earth–Moon–Earth \(EME\)](#) communication system in the 1296 MHz amateur radio band has been successfully accomplished. Using the [radar](#) equation and thermal noise theory, in conjunction with measured and estimated system parameters, the lunar echo [signal to noise ratio \(SNR\)](#) has been estimated at $5.4_{-1.6}^{+1.2}$ dB (2σ) in a 100 Hz bandwidth. The results of empirical long-term averaged [SNR](#) measurements are within the boundaries of this estimate, thus adding to its validity. Additionally, measurements of the libration-induced Doppler spread of the lunar echoes show good agreement with theoretical predictions. Further experiments should be conducted however, in order to assess the repeatability of the results. Improvements to the system and measurement methods should also be considered. The report focuses on both theory and practice and apart from the above, additional attention is given to the topic of low [noise figure \(NF\)](#) measurements due to the systemic importance of the [LNA NF](#) parameter.

Acknowledgements

First and foremost I would like to thank my supervisor, professor Gunnar Elgered, for allowing me to choose this rather unusual project. I am especially grateful to him for giving me a considerable amount of freedom in its execution.

My appreciation also goes to a number of radio amateurs, who have contributed in one way or another to this project: Viggo Magnus Nilsen (LA9NEA), for donating me the parabolic dish; Sven Nordin (SM5LE), for saving me a lot of time by selling me much of the needed equipment; Ulf Kylanfall (SM6GXV), for letting me use his noise figure meter; Ingolf Larsson (SM6FHZ) and Leif Åsbrink (SM5BSZ) for their patience in answering my questions.

I am also eternally grateful to both of my parents, Björn (SM6CSO) and Gunilla, who have always supported me to the best of their ability. My father's practical experience has been of great help during the course of this project; not least during the sometimes vivid discussions ensuing when I felt the need to have my thoughts and ideas bandied about. My mother's moral support has been equally important throughout this project and beyond.

Last but not least I want to extend my gratitude and appreciation to Ida, a person very dear to me. Without her continued love and support, the result of this thesis would not have been what it is and what I wanted it to be.

Contents

Abstract	vii
Acknowledgements	ix
List of figures	xvii
List of tables	xx
List of symbols	xxi
List of constants	xxxvii
List of acronyms	xxxix
<i>I The beginning</i>	
1 Introduction	3
1.1 Task definition and criteria for success	4
1.2 Purpose and scope of the thesis	5
1.3 Method	5
1.4 Existing solutions	5
1.5 Report organization	6
1.6 Final introductory remarks	7
2 Earth–Moon–Earth communication history	9
2.1 Project Diana	10
2.2 Project PAMOR	12
2.3 The Communication Moon Relay Project	14
2.4 Project Moonbeam	15
2.5 Current state	18
<i>II In theory</i>	
3 Link budget theory	23
3.1 Effective aperture area and antenna gain	23

3.2	Equivalent isotropic radiated power (EIRP)	26
3.3	Friis transmission formula	26
3.4	Radar equation	28
3.5	Losses	31
3.5.1	Dissipative loss	31
3.5.2	Mismatch loss	32
3.5.3	Depointing loss	32
3.5.4	Antenna losses	33
3.5.5	Polarization mismatch loss	33
3.5.6	Atmospheric loss	34
4	Thermal noise theory	35
4.1	Thermal noise power from and equivalent noise temperature of a one-port	35
4.2	Noise factor, available gain and equivalent input noise temper- ature of a linear two-port	38
4.2.1	Friis and IEEE noise factor definitions	38
4.2.2	Minimum noise factor versus maximum gain	45
4.3	Equivalent input noise temperature of an attenuator	47
4.4	Equivalent input noise temperature and gain of a cascaded system	49
4.5	Noise temperature of an antenna	50
4.5.1	Brightness distribution	50
4.5.2	Flux density	50
4.5.3	Flux density observed by an antenna	51
4.5.4	Spectral power at the terminals of a lossless antenna	52
4.5.5	Power at the terminals of a lossless antenna and the equivalent antenna temperature for a constant Φ	52
4.5.6	Power at the terminals of a lossless antenna and the equivalent antenna temperature for a non-constant Φ	54
4.6	Total system noise temperature at the terminals of an antenna	56
4.7	Determining noise temperatures using the Y-factor method	59
4.7.1	Assuming a noiseless instrument	60
4.7.2	Accounting for instrument noise	65
5	Signal to noise theory	67
5.1	Signal to noise ratio and the Friis transmission formula	68
5.2	Signal to noise ratio and the radar equation	69
5.3	Signal plus noise to noise ratio	71
5.4	Maximum antenna gain versus maximum G/T_{sys}	71
5.5	Minimum detectable signal, receiver noise floor and sensitivity	73
5.6	Total-power radiometer equation	75
6	Radio astronomical measurement theory	79

6.1	G/T_{sys} figure of merit equation	79
6.2	Antenna gain determination and more	82
6.3	Source size correction	85

III In practice

7	Parts selection and system description	93
7.1	Antenna subsystem	95
7.1.1	Parabolic dish	95
7.1.2	Azimuth and elevation control	98
7.1.3	Feed horn	98
7.2	Transmitter subsystem	102
7.2.1	Drive PA 1	103
7.2.2	Drive PA 2	104
7.2.3	Main PA	104
7.3	Receiver subsystem	106
7.3.1	Two-stage very low noise amplifier	106
7.3.2	Coaxial protection relay	108
7.3.3	Interdigital band-pass filter	110
7.4	Other system parts	112
7.4.1	Transceiver	112
7.4.2	Transverter: 144 MHz \Leftrightarrow 1296 MHz	112
7.4.3	Audio and data interface	113
7.4.4	Transmit and receive sequencer	113
7.5	Software applications	115
7.5.1	Spectrum Lab	117
7.5.2	MoonSked	117
7.5.3	EME Calc	118
7.5.4	Eagle PCB design software	118
8	Receiving system measurements and estimations	119
8.1	Sources of uncertainty in LNA measurements	120
8.1.1	Warm-up stabilization of the instrument and LNA	122
8.1.2	Extraneous interference	122
8.1.3	Measurement bandwidth	123
8.1.4	Display jitter	123
8.1.5	Noise source ENR selection	124
8.1.6	ENR calibration uncertainty	125
8.1.7	Physical temperature of the noise source	126
8.1.8	Physical temperature of the LNA	127
8.1.9	Non-linearity of the LNA	127
8.1.10	Non-linearity of the noise figure meter	128
8.1.11	Noise figure of the noise figure meter	128

8.1.12	Losses from adapters etc.	129
8.1.13	Mismatch between the noise source, DUT and NFM	130
8.1.14	Varying noise source impedance and gain error	133
8.2	Assessment of the combined uncertainty in LNA measurements	138
8.3	Reducing NF uncertainty through alternative measurement methods	142
8.4	LNA noise temperature and gain measurements	148
8.4.1	Noise figure meter method	149
8.4.2	Liquid nitrogen method	150
8.4.3	Comments on the LNA measurement results	154
8.5	Receiver subsystem noise temperature estimation	154
8.6	G/T_{sys} figure of merit measurement	157
8.6.1	Obtaining the solar radio flux	157
8.6.2	Measuring the Y-factor and calculating G/T_{sys}	158
8.7	Antenna gain measurements	161
8.7.1	Half-power beam width method	163
8.7.2	Main lobe integration method	167
8.7.3	Comments on the antenna gain measurement results	167
8.8	Total system noise temperature estimation	169
8.9	Minimum detectable signal requirement	169
8.10	Antenna temperature estimation	169
8.11	Antenna temperature increase due to lunar noise	174
9	Transmitting system measurements and estimations	176
9.1	Power amplifier measurements	176
9.2	Transmitted power at the LNA input	179
10	EME signal path link budget estimation	180
10.1	Transmission	180
10.2	Transmission loss	180
10.3	Reception	181
10.4	Link budget summary	181
11	Lunar echo SNR estimation	182
11.1	SNR calculations	182
11.2	SNR uncertainty assessment	183
12	Lunar echo SNR measurements	184
12.1	Echo-data acquisition process	184
12.2	SNR measurement method and results	187
13	Lunar echo Doppler spread measurements	193
13.1	Historical results	193
13.2	Doppler spread measurement method and results	194

IV The end

14 Conclusion	209
15 Recommendations and future studies	211
References	219
A SNR degradation due to resistive loss	233
B RAS rotator specifications	238
C Audio and data interface circuit description	240
D Spectrum Lab scripts	243
D.1 Y-factor measurement	243
D.1.1 Conditional actions	244
D.1.2 Macro buttons	244
D.1.3 Frequency markers	245
D.2 EME echo-data acquisition	245
D.2.1 Conditional actions	246
D.2.2 Macro buttons	247
D.3 EME echo-data analysis	248
D.3.1 Conditional actions	248
D.3.2 Macro buttons	251
D.3.3 Frequency markers	252

List of figures

1.1	Earth–Moon distances	3
2.1	Project Diana site, Camp Evans Signal Laboratory (photo) . .	10
2.2	Stump Neck site with elliptical parabola (photo)	13
2.3	USS Hancock Moon relay facsimile (photo)	15
2.4	Amateur EME echo recording from 27 January 1953	16
2.5	300 metre dish at the Arecibo Observatory (photo)	17
2.6	144 MHz EME antenna array belonging to R7AB (photo) . .	19
3.1	Friis radio communication link	26
3.2	Radar communication link	28
4.1	Definition of the one-port equivalent noise temperature	37
4.2	A 10 dB degradation in SNR	39
4.3	Two-port noise factor, available gain and noise temperature. .	40
4.4	Definition of the two-port equivalent input noise temperature	44
4.5	Change in added output noise of a two-port due to T_s	46
4.6	An attenuator in thermal equilibrium	47
4.7	Cascaded two-port system	49
4.8	Antenna in blackbody enclosure	53
4.9	Typical receiving system with various parameters	56
4.10	Y-factor measurement set-up	60
4.11	Graphical representation of the Y-factor	61
5.1	Minimum detectable signal	74
5.2	Total-power radiometer	76
6.1	True HPBW from measured HPBW	87
6.2	Source size correction factor	87
6.3	True HPBW from measured HPBW using the Sun	89
7.1	Block diagram of the complete EME system	94
7.2	Extended parabolic dish (photo)	96
7.3	Dish extension closeups (photos)	97
7.4	RAS rotators (photo)	99

7.5	Polarization at Tx and Rx	100
7.6	OK1DFC septum-polarized feed horn (photo)	101
7.7	Drive PA 1 (photo)	103
7.8	Drive PA 2 (photo)	105
7.9	Main PA and PA 2 (photos)	107
7.10	G4DDK VLNA (photo)	109
7.11	Coaxial protection relay interior (photo)	111
7.12	Interdigital BPF (photo)	111
7.13	Audio and data interface (photo)	114
7.14	Transmit and receive sequencer (photos)	116
8.1	Sources of uncertainty during NF measurements	121
8.2	Gain error as a function of phase	136
8.3	NF measurement uncertainty of a specific LNA	139
8.4	NF measurement uncert. as a function of LNA input match	140
8.5	NF measurement uncertainty as a function of LNA gain	141
8.6	$u(T_{LNA.e})$ as a function of $T_{LNA.e}$	146
8.7	$u(T_{LNA.e})$ measurement uncertainty as a function of $B\tau$	146
8.8	LN ₂ Y-factor measurement set-up	151
8.9	LN ₂ Y-factor measurement (photos)	153
8.10	Receiver subsystem noise temperature distribution	155
8.11	Dish during solar Y-factor and drift-scan meas. (photo)	162
8.12	SL running the Y-factor measurement script	162
8.13	Normalized antenna power pattern from solar measurement	164
8.14	Normalized antenna power pattern (dB) from solar meas.	166
8.15	Average sky temp. as a function of frequency and elevation	172
12.1	SL running the EME echo-data acquisition script	186
12.2	SL running the EME echo-data analysis script	189
12.3	SL FFT settings	190
12.4	Measured SNR of the EME echoes	191
13.1	Delay of a lunar radar pulse as a function of range	195
13.2	Relative EME echo power as a function of delay and λ	196
13.3	Cumulative EME echo power as a function of lunar radius	197
13.4	Relative EME echo power as a function of delay and pol.	198
13.5	Three causes of lunar libration	200
13.6	Basic mechanism of EME echo Doppler spread	201
13.7	Measured EME echo Doppler spread	203
13.8	Predicted EME echo width	204
A.1	SNR degradation circuit	233
A.2	SNR degradation due to loss, $T_a = 30$ K	234
A.3	SNR degradation due to loss, $T_a = 40$ K	235
A.4	SNR degradation due to loss, $T_a = 50$ K	236

A.5 SNR degradation due to loss, $T_a = 60$ K	237
C.1 Circuit diagram of the audio and data interface	241

List of tables

6.1	Angular diameter of the quiet Sun at 1296 MHz	88
8.1	Noise source ENR standard uncertainties	126
8.2	Measurement uncertainty simulation input parameters	145
8.3	LNA gain and NF measurement results	150
8.4	Parameters used to calculate $T_{rx.e}$	156
8.5	G/T_{sys} measurement results	161
8.6	Measured antenna HPBW, gain and aperture efficiency	167
8.7	T_{sys} , T_{ant} and T_a measurement results	173
12.1	SNR measurement results	188
B.1	RAS rotator specifications	239
B.2	RAS rotator control box specifications	239

List of symbols

Symbol	Description	Unit	Page list
a	Largest linear dimension of either the transmitting or receiving antenna	m	28
A_e	Effective aperture area of the antenna	m^2	23–25, 30, 81
A_{em}	Maximum effective aperture area of the antenna	m^2	24, 25, 52–54, 81
A_{moon}	Physical cross section (projected area) of the Moon	m^2	181
A_{ph}	Physical aperture area of the antenna	m^2	24, 25, 84, 165, 167
$A_{r.e}$	Effective aperture area of the receiving antenna	m^2	26, 27, 29
$A_{t.e}$	Effective aperture area of the transmitting antenna	m^2	26, 27
B	Effective bandwidth. See also f_1 and f_2 !	Hz	36, 39, 43, 45, 47, 49, 53, 55, 60, 61, 63, 64, 66, 68–70, 74–77, 123, 142–147, 182
D	Diameter of the parabolic dish. See also f/D !	m	72, 95, 170
D	Directivity of the antenna		25

Symbol	Description	Unit	Page list
D_{max}	Maximum directivity of the antenna		24, 25
$EIRP$	EIRP from the transmitting antenna	W	26, 27, 30, 68–70, 180, 182, 183
ENR_{cal}	The ENR used for noise source calibration. See also ENR_{new} !		62–64
ENR_{new}	The ENR according to the new definition. See also ENR_{cal} !		63–65
F	Noise factor of the linear two-port. See also NF !		38–40, 43–45, 56, 62–66, 75
f	Focal length of the parabolic dish. See also f/D !	m	72, 170
f/D	Antenna focal length to antenna diameter. See also f and D !		71–73, 95, 96, 100, 168
f	Frequency	Hz	35, 36, 52
f_0	Maximum libration-induced Doppler spread of the EME echo	Hz	201–204
f_1	First boundary frequency of the effective bandwidth B	Hz	36
$F_{10.7}$	10.7 cm solar radio flux (SFI)	$W\ m^{-2}$ Hz^{-1}	157, 158
f_2	Second boundary frequency of the effective bandwidth B	Hz	36
df	Infinitesimal frequency width	Hz	36
F_{att}	Noise factor of the attenuator		48
F_j	Noise factor of two-port stage j		49
F_{LNA}	Noise factor of the LNA . See also NF_{LNA} !		57
F_{pmr}	Noise factor of the PMR		65, 66
F_{tot}	Total noise factor of N cascaded two-port stages		49, 65
F_{trv}	Noise factor of the transverter. See also NF_{trv} !		57

Symbol	Description	Unit	Page list
G	Gain of the antenna		25, 30, 70, 81, 84, 86, 165, 167– 169, 171, 173, 175, 180, 181, 183, 192, 216
G/T_{sys}	Radar antenna gain to system noise temperature figure of merit. See also G and T_{sys} !	K^{-1}	6, 32, 70, 79, 81, 82, 85, 86, 88, 95, 117, 157, 158, 160–162, 165, 168, 169, 171, 173–175, 182, 183, 188, 192, 209, 212, 243
ΔG	Gain error factor due to varying impedance in the DNS		134–136
G_j	Gain of stage j of the two-port		49
G_{LNA}	Available gain of the LNA		57, 149–151, 156
$G_{LNA.off}$	Available gain of the LNA when the DNS is turned off		133, 134
$G_{LNA.on}$	Available gain of the LNA when the DNS is turned on		133, 134
G_{max}	Maximum gain of the antenna		24, 25
G_{obj}	Gain of the radar object		30, 31, 69, 70, 180–183
G_r	Gain of the receiving antenna		26, 27, 29, 30, 68, 69, 71–73
G_r/T_{sys}	Receiving antenna gain to system noise temperature figure of merit. See also G_r and T_{sys} !	K^{-1}	33, 68–73

Symbol	Description	Unit	Page list
G_t	Gain of the transmitting antenna		26, 27, 29, 30, 68, 69, 71
$G_{t,max}$	Maximum gain of the transmitting antenna		26, 27
G_{tot}	Total gain of N cascaded two-port stages		49
$G_{tp.a}$	Available gain of the two-port		40–45, 60, 61, 63–66, 74, 133
G_{trv}	Available gain of the transverter		57, 156
$HPBW$	$HPBW$ of the antenna	rad	83–89, 158, 165
$HPBW_{meas}$	Measured $HPBW$ of the antenna	rad	86, 87, 89, 163–165, 167
I_{rl}	Port-to-port isolation of the coaxial relay		57, 156, 179
I_{tx}	Port-to-port Tx/Rx isolation of the feed horn when installed in the dish		58, 59, 169, 170, 179, 213
j	Number between 1 and N		49
K	Source size correction factor		85–88
k_p	Pattern factor of the antenna aperture distribution		83, 84, 165, 168
L_{ant}	Resistive loss of the antenna. See also η_{rad} !		58, 59, 169, 170, 173
L_{att}	Resistive loss of the attenuator		47, 48
L_{bp}	Resistive loss of the band-pass filter		57, 156
L_{cx}	Resistive loss of the semi-rigid coaxial cable		57, 151–153, 156
L_{fsl}	Free-space loss between the transmitting and receiving antennas. See also $L_{t,fsl}$ and $L_{r,fsl}$!		27, 30, 31, 68, 70, 180–183

Symbol	Description	Unit	Page list
$L_{r.fsl}$	Free-space loss between the radar object and the receiving antenna. See also L_{fsl} and $L_{t.fsl}$!		30, 69, 70
$L_{t.fsl}$	Free-space loss between the transmitting antenna and the radar object. See also L_{fsl} and $L_{r.fsl}$!		30, 69, 70
L_{rl}	Resistive loss of the coaxial relay		57, 156
L_{SMA}	Resistive loss of the SMA connector(s)		57, 156
$L_{tl.b}$	Transmission loss between the transmitting and receiving antennas in the bistatic radar system		30
$L_{tl.m}$	Transmission loss of the monostatic radar system		31, 181, 182
M	Quantity determining the effect of multiple reflections on power measurements		132
MDS	MDS of the receiver system	W	74, 75, 169
N	Total number of cascaded two-port elements. See also j !		49, 65
n	Number of samples. See also B and τ !		77
NF	Noise figure of the linear two-port. See also F !		44
NF_{LNA}	Noise figure of the LNA. See also F_{LNA} !		149, 150, 153, 156, 211
NF_{rest}	Noise figure of the rest of the system	K	156
NF_{rx}	Noise figure of the entire receiver system referenced to the terminals of the antenna	K	155, 156
NF_{trv}	Noise figure of the transverter. See also F_{trv} !		156

Symbol	Description	Unit	Page list
$P(\xi, \psi)$	Normalized antenna power pattern as a function of ξ and ψ . See also $P_{meas}(\xi, \psi)$!		25, 51–55, 163
$p(f)$	Planck's factor as a function of frequency f		36
$P_{cold.out}$	Measured lower output noise power during a Y-factor measurement. See also $P_{hot.out}$ and Y !	W	60, 61
$P_{hot.out}$	Measured upper output noise power during a Y-factor measurement. See also $P_{cold.out}$ and Y !	W	60, 61
$P_{meas}(\xi, \psi)$	Measured antenna power pattern as a function of ξ and ψ . See also $P(\xi, \psi)$!		163
P_n	Generic noise power	W	36, 53, 55, 71
$P_{n.dlv}$	Noise power delivered to the two-port	W	40, 42
$P_{n.in}$	Available noise power from the signal source	W	38–40, 42, 45, 74
$P_{n.out}$	Available noise power from the two-port	W	39, 42, 46, 74
ΔP_{out}	Difference in output noise power from the two-port, as a result of a difference in input noise power/temperature. See also $P_{hot.out}$ and $P_{cold.out}$!	W	61, 63–65
P_r	Received power at the receiving antenna terminals	W	23, 26, 27, 29, 30, 68– 70, 181, 182
P_s	Generic signal power	W	71
$P_{s.dlv}$	Signal power delivered to the two-port	W	40, 42, 45
$P_{s.in}$	Available signal power from the signal source	W	39–42, 45, 74
$P_{s.out}$	Available signal power from the two-port	W	39, 41, 42, 45, 46, 74

Symbol	Description	Unit	Page list
P_t	Output power at the transmitting antenna terminals	W	26, 27, 29, 30, 68–70, 178–180, 183, 214
$P_{tp.add}$	Noise power added by the two-port referenced to its output terminals. See also $P_{tp.e}$!	W	42–46, 74
$P_{tp.e}$	Equivalent input noise power of the two-port. See also $P_{tp.add}$!	W	43, 74
R	Resistance	Ω	36
r	Distance between the transmitting antenna and the receiving antenna or the radar object	m	26–28, 30, 68, 70, 181
r_r	Distance between the receiving antenna and the radar object	m	28–30, 69
r_t	Distance between the transmitting antenna and the radar object	m	28–30, 69
S	Flux density over a solid angle Ω	W m^{-2} Hz^{-1}	50, 51, 81–83, 157, 158, 161, 162, 167, 183
$SNNR$	Generic $SNNR$		38, 71
SNR	Generic SNR		38, 68–71, 78
SNR_{dlv}	Delivered SNR at the input terminals of the two-port		42
SNR_{in}	Available SNR at the output terminals of the signal source		38, 39, 42
$SNR_{moon.c}$	Calculated SNR estimate of the lunar echoes		183, 188, 191, 192
$SNR_{moon.m}$	Measured SNR of the lunar echoes		188, 191, 192
SNR_{out}	Available SNR at the output terminals of the two-port		38, 39, 42, 68, 69, 74

Symbol	Description	Unit	Page list
$SNR_{out.}^{min}$	Minimally required available SNR at the output terminals of the two-port		74, 75, 169
S_{obj}	Power density incident at the radar object	W m^{-2}	29
S_{obs}	Observed flux density over a solid angle Ω	W m^{-2} Hz^{-1}	51, 52, 81
S_r	Power density incident at the receiving antenna	W m^{-2}	23, 27, 29
$S_{r.iso}$	Power density incident at the receiving antenna for an isotropically radiating transmitter antenna	W m^{-2}	27
ΔT	Change in radiometer system noise temperature. See also ΔT_{min} and T_{sys} !	K	76–78
Δt	Time interval during the drift-scan measurement	min	163
T_a	Noise temperature of the lossless antenna	K	54, 55, 58, 59, 81, 83, 169–171, 173–175, 212
T_a^*	Noise temperature of the lossless antenna referenced to the terminals of the antenna	K	58, 59
ΔT_a	Change in noise temperature of the lossless antenna. See also ΔT_{ant} !	K	81–83, 174
T_{ant}	Noise temperature of the antenna. See also $T_{ant.hot}$ and $T_{ant.cold}$!	K	56, 58, 59, 62, 72, 74–76, 80, 169, 171, 173
ΔT_{ant}	Change in noise temperature of the antenna, from $T_{ant.cold}$ to $T_{ant.hot}$. See also ΔT_a !	K	80, 81

Symbol	Description	Unit	Page list
$T_{ant.cold}$	Noise temperature of the antenna when pointing at a cold source in the sky. See also T_{ant} , ΔT_{ant} and $T_{ant.hot}$!	K	79, 80
$T_{ant.e}$	Equivalent input noise temperature of the resistive losses of the antenna	K	58, 59
$T_{ant.e}^*$	Equivalent input noise temperature of the resistive losses of the antenna referenced to its terminals	K	58, 59, 173
$T_{ant.hot}$	Noise temperature of the antenna when pointing at a hot source in the sky. See also T_{ant} , ΔT_{ant} and $T_{ant.cold}$!	K	79, 80, 171
$T_{ant.ph}$	Physical temperature of the resistive losses of the antenna	K	58, 59, 169, 170
$T_{att.e}$	Equivalent input noise temperature of the attenuator	K	47, 48
$T_{att.ph}$	Physical temperature of the attenuator	K	48
$T_b(\theta, \phi)$	Blackbody radiation temperature (brightness temperature) as a function of θ and ϕ	K	52, 54, 55
$T_{b.avg}$	Average value of the $T_b(\theta, \phi)$ brightness temperature over its angular extension	K	55, 82, 83, 174
$T_{bp.e}$	Equivalent input noise temperature of the band-pass filter	K	57
$T_{bp.e}^*$	Equivalent input noise temperature of the band-pass filter referenced to the terminals of the antenna	K	57
$T_{bp.ph}$	Physical temperature of the band-pass filter	K	57, 156
T_c	Constant blackbody radiation temperature	K	52–55
$T_{cold.in}$	Lower noise temperature of the reference device during a Y-factor measurement. See also $T_{hot.in}$!	K	60–65, 127, 133–135, 137, 142–145

Symbol	Description	Unit	Page list
$\Delta T_{cold.in}$	Specified uncertainty of $T_{cold.in}$. See also $T_{cold.in}$!	K	143–145
$T_{cold.ph}$	Lower physical temperature of the terminating resistor reference device during a liquid nitrogen Y-factor measurement. See also $T_{hot.ph}$!	K	151, 152
$T_{cx.e}$	Equivalent input noise temperature of the coax cable	K	57, 151
$T_{cx.e}^*$	Equivalent input noise temperature of the coax cable referenced to the terminals of the antenna	K	57
$T_{cx.ph}$	Physical temperature of the coax cable	K	57, 151, 156
$T_{hot.in}$	Upper noise temperature of the reference device during a Y-factor measurement. See also $T_{cold.in}$!	K	60–65, 127, 133, 134, 137, 142–145
$\Delta T_{hot.in}$	Specified uncertainty of $T_{hot.in}$. See also $T_{hot.in}$!	K	143–145
$T_{hot.ph}$	Upper physical temperature of the terminating resistor reference device during a liquid nitrogen Y-factor measurement. See also $T_{cold.ph}$!	K	151, 152
ΔT_{in}	Difference in input noise temperature to the two-port. See also $T_{hot.in}$ and $T_{cold.in}$!	K	61, 63–66
$T_{j.e}$	Equivalent input noise temperature of stage j	K	49, 65
$T_{LNA.e}$	Equivalent input noise temperature of the LNA	K	57, 133–135, 137, 142–147, 150, 151, 153, 211
$T_{LNA.e}^*$	Equivalent input noise temperature of the LNA referenced to the terminals of the antenna	K	57

Symbol	Description	Unit	Page list
$T_{LNA.e.}^{off}$	Equivalent input noise temperature of the LNA when the DNS is turned off	K	133
$T_{LNA.e.}^{on}$	Equivalent input noise temperature of the LNA when the DNS is turned on	K	133
ΔT_{min}	Standard deviation / AC RMS value / uncertainty of the T_{sys} measurement. Also known as radiometric sensitivity or temperature resolution of the radiometer. See also T_{sys} , $T_{sys.RMS}$ and $\Delta T!$	K	76–78
T_{moon}	Average disc noise temperature of the Moon	K	174, 175
$T_{op.e}$	Equivalent noise temperature of the one-port	K	37
$T_{op.ph}$	Physical temperature of the one-port	K	36–38
T_{ph}	Physical temperature of the radiator	K	54
$T_{pmr.e}$	Equivalent input noise temperature of the PMR	K	65, 66
$T_{R.ph}$	Physical temperature of the resistor with resistance R	K	47, 48
$T_{rest.e}$	Equivalent input noise temperature of the rest of the system	K	57
$T_{rest.e}^*$	Equivalent input noise temperature of the rest of the system referenced to the terminals of the antenna	K	57
$T_{rl.e}$	Equivalent input noise temperature of the coaxial relay	K	57
$T_{rl.e}^*$	Equivalent input noise temperature of the coaxial relay referenced to the terminals of the antenna	K	57
$T_{rl.ph}$	Physical temperature of the coaxial relay	K	57, 156

Symbol	Description	Unit	Page list
$T_{rx.e}$	Equivalent input noise temperature of the entire receiver system (excluding the antenna) referenced to the terminals of the antenna	K	56, 57, 72, 79, 80, 154–156, 169, 171, 173
T_s	Noise temperature of the signal source (the physical temperature of the output impedance of the signal source)	K	40
$T_{sa.e}$	Equivalent input noise temperature of the spectrum analyser	K	151, 152
$T_{SMA.e}$	Equivalent input noise temperature of the SMA connector(s)	K	57
$T_{SMA.ph}$	Physical temperature of the SMA connector(s)	K	57, 156
T_{sys}	Total system noise temperature. See also $T_{sys.RMS}$, ΔT_{min} and $\Delta T!$	K	56, 57, 68–73, 75–78, 80, 81, 151, 152, 169, 171, 173–175, 182, 216
$T_{sys.RMS}$	Total system noise temperature RMS value. See also T_{sys} and $\Delta T_{min}!$	K	78
$T_{tot.e}$	Total equivalent input noise temperature of N cascaded two-port stages	K	49, 65
$T_{tp.e}$	Equivalent input noise temperature of the two-port	K	40, 43–45, 60–66, 74, 75, 133
T_{tr}	Noise temperature of the terminating resistor connected to the LNA coaxial relay	K	57, 156
T_{tr}^*	Noise temperature of the terminating resistor, connected to the LNA coaxial relay, referenced to the terminals of the antenna.	K	57, 58
$T_{trv.e}$	Equivalent input noise temperature of the transverter	K	57

Symbol	Description	Unit	Page list
$T_{trv.e}^*$	Equivalent input noise temperature of the transverter referenced to the terminals of the antenna	K	57
T_{tx}	Noise temperature at the Tx-port during quiescent PA operation	K	58, 59, 169, 170, 212
T_{tx}^*	Noise temperature at the Tx-port during quiescent PA operation, referenced to the Rx-terminals of the antenna.	K	58, 59, 173, 213
$u(\diamond)$	Standard uncertainty of \diamond . See also $U!$		126, 132, 143–145
$U(\diamond)$	Expanded uncertainty of \diamond . See also $u!$		126, 183, 188
v_n	Noise voltage	V	36
w	Spectral power present at the terminals of the lossless antenna	W Hz ⁻¹	52–55
Y	Y-factor power ratio. See also $P_{hot.out}$ and $P_{cold.out}!$		61–64, 79–82, 124, 126, 133, 134, 142–145, 152, 157, 161, 171, 183
Z_s	Source impedance. See also Γ_s and $\Gamma_{s.opt}!$	Ω	40
$Z_{tp.in}$	Input impedance of the two-port	Ω	40
δ_s	Declination of the astronomical radio source	rad	161, 163
η_{ap}	Aperture efficiency of the antenna		24, 25, 84, 165, 167

Symbol	Description	Unit	Page list
η_{beam}	Main beam efficiency of the antenna. See also Ω_M !		83, 84, 165, 167, 168, 171, 173, 216
η_{rad}	Radiation efficiency of the antenna. See also L_{ant} !		24, 25, 58, 59, 81, 84, 165, 167, 168, 170
$\Gamma_{dns.off}$	Reflection coefficient of the DNS, relative to Z_0 , when turned off. See also $\Gamma_{dns.on}$!		121, 134–137
$\Gamma_{dns.on}$	Reflection coefficient of the DNS, relative to Z_0 , when turned on. See also $\Gamma_{dns.off}$!		121, 134–137
Γ_g	Generic generator reflection coefficient relative to Z_0		132
Γ_l	Generic load reflection coefficient relative to Z_0		132
$\Gamma_{LNA.in}$	Reflection coefficient of the input of the LNA relative to Z_0 (S11)		121, 134–136, 139, 140
$\Gamma_{LNA.out}$	Reflection coefficient of the output of the LNA relative to Z_0 (S22)		121
Γ_{NFM}	Reflection coefficient of the NFM relative to Z_0		121
Γ_s	Source reflection coefficient of Z_s relative to $Z_{tp.in}$. $\Gamma_s = 0$ constitutes a reflection-less source impedance match. See also $\Gamma_{s.opt}$ and Z_s !		40–42, 45–47
$\Gamma_{s.opt}$	Optimum source reflection coefficient (source impedance mismatch) for minimum NF. See also Γ_s and Z_s !		45, 46, 48

Symbol	Description	Unit	Page list
λ	Wavelength	m	24, 25, 27–30, 52–54, 68–70, 81–84, 162, 165, 167, 168, 181
Ω	Arbitrary solid angle	sr	25, 50–55
Ω_A	Beam solid angle (total beam area) of the antenna	sr	25, 51, 53, 55, 82–84, 167, 174
Ω_M	Main beam solid angle (main beam area) of the antenna. See also η_{beam} !	sr	83, 84, 167, 168
$d\Omega$	Infinitesimal solid angle	sr	25, 50–55
Ω_s	Source solid angle (angular extension) of $\Phi(\theta, \phi)$. See also θ_s !	sr	51, 55, 81, 83, 86, 88, 174
$\Phi(\theta, \phi)$	Brightness distribution as a function of θ and ϕ . See also Ω_s !	W m^{-2} $\text{Hz}^{-1} \text{sr}^{-1}$	50–53
Φ_c	Constant brightness	W m^{-2} $\text{Hz}^{-1} \text{sr}^{-1}$	53
ϕ	Spherical angle coordinate in the sky coordinate frame. See also θ !	rad	50–55
ϕ_a	Spherical displacement angle between the antenna and sky coordinate systems. See also θ_a !	rad	51–56, 81
$d\phi$	Infinitesimal spherical angle in the sky coordinate frame	rad	50
ψ	Spherical angle coordinate in the antenna coordinate frame. See also ξ !	rad	25, 51, 54
$d\psi$	Infinitesimal spherical angle in the antenna coordinate frame	rad	25
σ	RCS of an object	m^2	28–30, 69, 70, 181, 183
τ	Integration time. See also B and n !	s	76, 77, 123, 142–147

Symbol	Description	Unit	Page list
θ	Spherical angle coordinate in the sky coordinate frame. See also ϕ !	rad	50–55
θ_a	Spherical displacement angle between the antenna and sky coordinate systems. See also ϕ_a !	rad	51–56, 81
θ_s	Angular diameter of the source. See also Ω_s !	rad	83, 85–89, 174
$d\theta$	Infinitesimal spherical angle in the sky coordinate frame	rad	50
ξ	Spherical angle coordinate in the antenna coordinate frame. See also ψ !	rad	25, 51, 54, 163
$d\xi$	Infinitesimal spherical angle in the antenna coordinate frame	rad	25

List of constants

Const.	Description	Value	Unit	Page list
c	Speed of light	$2.998 \cdot 10^8$	m s^{-1}	52
e	Euler's number (the base of the natural logarithm)	2.718		36, 52
h	Planck's constant	$6.626 \cdot 10^{-34}$	J s	36, 52
k	Boltzmann constant	$1.381 \cdot 10^{-23}$	J K^{-1}	36, 37, 39, 43, 47, 52–55, 60, 61, 63, 64, 66, 68–70, 74, 75, 81–83
kT_0	Power spectral density	$4.004 \cdot 10^{-21}$	W Hz^{-1}	37
kT_0	Power spectral density	–174.0	dBm Hz^{-1}	37
π	Ratio of the circumference to the diameter of a circle	3.142		24, 25, 27, 29, 30, 50, 51, 53–55, 68–70, 81–84, 167
T_0	Standard reference noise temperature	290	K	36, 37, 39, 42–44, 48, 57, 62–64, 75, 126, 127, 130, 135

Const.	Description	Value	Unit	Page list
Z_0	Characteristic or nominal impedance	50	Ω	32, 39, 41, 105, 120, 121, 132, 133

List of acronyms

Acronym	Description	Page list
AC	Alternating Current. See also DC!	76, 78, 239
ACW	AntiClockWise. See also CW!	98, 239
AF	Audio Frequency	5, 113, 158, 159
AGC	Automatic Gain Control	159
ALC	Automatic Level Control	104
AM	Amplitude Modulation	14, 112
ARRL	American Radio Relay League	16, 75, 115, 169–171
Az	Azimuth	99, 117, 161, 188, 213, 239
BASIC	Beginner’s All-purpose Symbolic Instruction Code	117
BPF	Band-Pass Filter	106, 110–113, 156, 160
CAD	Computer-Aided Design	118
CI-V	Communications Interface V (five)	113, 240–242
CIA	Central Intelligence Agency	14
CW	Continuous Wave	112, 113, 115, 148, 177, 185, 186, 240–242, 245
CW	ClockWise. See also ACW!	98, 239

Acronym	Description	Page list
DC	Direct Current. See also AC!	75, 76, 78, 104, 106, 107, 110, 177, 188, 239
DNS	Diode Noise Source	62, 64, 120, 126, 127, 134, 139–141, 144– 150, 216
DTR	Data Terminal Ready	185, 245
DUT	Device Under Test	59, 60, 66, 121, 123, 124, 128–131, 133, 147
DWG	Double Worm Gears	239
EIRP	Equivalent (or Effective) Isotropic Radiated Power	26, 30, 68–70, 180, 183, 209
El	Elevation	99, 117, 161, 188, 213, 239
ELINT	ELEctrical INTelligence	12, 14
EME	Earth–Moon–Earth	3–10, 12, 14, 16–19, 23, 30– 34, 45, 71–73, 75, 78, 79, 82, 85, 86, 88, 93– 95, 98, 100, 102, 106, 108, 109, 112, 117– 119, 122, 124, 125, 127, 129, 133, 137, 141, 142, 148, 154, 157, 159, 171, 174–178, 180, 182, 184–189, 191–193, 196, 198, 199, 201– 204, 209, 214, 215, 248
EMW	ElectroMagnetic Wave	33

Acronym	Description	Page list
ENR	Excess Noise Ratio	62–64, 124–126, 128–131, 134–139, 141–146, 149, 150
FET	Field-Effect Transistor	108, 127
FFT	Fast Fourier Transform	117, 187, 188, 190, 191, 243, 248
FM	Frequency Modulation	112
FR	Flame Retardant	115
FTP	File Transfer Protocol	157, 160
FU	Flux Unit. See also SFU!	50, 51
GaAs	Gallium Arsenide	108, 127
GPS	Global Positioning System	214, 215
HEMT	High Electron Mobility Transistor	108, 109, 127
HPBW	Half-Power Beam Width	32, 51, 81, 82, 84–86, 88, 95, 98, 161, 163–168, 171, 174, 213
I/O	Input/Output	112, 115, 240, 242
IC	Integrated Circuit	240, 242
ICBM	InterContinental Ballistic Missile	9
IEEE	Institute of Electrical and Electronics Engineers	23, 24, 29, 36, 38, 42, 43, 59, 98
IET	Institution of Engineering and Technology	200
IF	Intermediate Frequency	110, 112, 113
IRE	Institute of Radio Engineers	42
ITU	International Telecommunication Union	82
LDMOS	Laterally Diffused Metal Oxide Semiconductor	104, 105, 177, 188
LED	Light-Emitting Diode	240–242

Acronym	Description	Page list
LHCP	Left Hand Circular Polarization. See also RHCP!	98
LN ₂	Liquid (boiling) Nitrogen	144–146, 148, 150–153, 156
LNA	Low Noise Amplifier. See also VLNA!	4, 31, 32, 45, 46, 56, 58, 66, 80, 94, 103, 106, 108, 110, 112, 115, 120–122, 124–129, 132–142, 148–156, 160, 173–176, 179, 209, 211, 212, 215, 216, 233–237
MDS	Minimum Detectable Signal	6, 73–75, 169
MFSK	Multiple Frequency-Shift Keying	215
NAIC	National Astronomy and Ionosphere Center	17
NASA	National Aeronautics and Space Administration	10
NF	Noise Figure	4, 7, 11, 32, 38, 44, 56, 57, 60, 103, 108, 113, 120, 122–132, 134–142, 145, 147–150, 153–156, 173, 175, 209, 211, 216, 233–237
NFM	Noise Figure Meter (or analyser)	62, 65, 120, 122–125, 127–134, 139, 147–150, 153, 156, 216
NOAA	National Oceanic and Atmospheric Administration	157, 158, 160, 163
NRL	Naval Research Laboratory	9, 12–15
NSF	National Science Foundation	17

Acronym	Description	Page list
OCXO	Oven-Controlled X-tal (crystal) Oscillator	214
ODU	Out Door Unit	103
PA	Power Amplifier	4, 58, 72, 102–107, 110, 112, 115, 170, 176–178, 188, 190, 209, 213–215
PAMOR	PASSive MOon Relay	12, 14
PCB	Printed Circuit Board	104, 105, 109, 115, 118, 240, 242
PMR	Power Measuring Receiver	60, 65, 66, 128, 129
PSK	Phase-Shift Keying	215
PTFE	PolyTetraFluoroEthylene	104, 106, 177, 178
PTT	Push-To-Talk	112, 113, 115, 185, 186, 240–242, 245
RADAR	RAdio Detection And Ranging	4–7, 9–12, 14, 28–31, 34, 69, 70, 73, 180, 182–184, 192–195, 199, 209, 215
RCS	Radar Cross Section. See also σ !	28, 29, 181, 183
RF	Radio Frequency	75, 98, 104–106, 108, 109, 112, 122, 177
RHCP	Right Hand Circular Polarization. See also LHCP !	98
RMS	Root Mean Square	76, 78
RSS	Root Sum Square	129, 138, 143, 183
RTS	Request To Send	185, 245

Acronym	Description	Page list
Rx	Receive or receiver. See also Tx!	32, 58, 80, 94, 100, 101, 104, 106, 108, 110, 112, 113, 115, 170, 174, 176, 179, 184, 185, 188, 212–215, 245
SDR	Software Defined Radio	18, 117, 148, 214, 243
SFI	Solar Flux Index. See also $F_{10.7}$!	157
SFU	Solar Flux Unit. See also FU!	51, 158, 167, 183
SL	Spectrum Lab	113, 117, 148, 159, 161–163, 184–190, 202, 203, 214, 215, 243, 245, 248
SMA	SubMiniature version A	109, 110, 152, 155, 156, 173
SNNR	Signal plus Noise to Noise Ratio	71, 75, 187
SNR	Signal to Noise Ratio	4–7, 11, 32, 38, 39, 41–43, 46, 48, 67–75, 78, 82, 106, 117, 119, 137, 147, 148, 154, 174–177, 180– 192, 209–215, 233–237, 248
SSB	Single SideBand	112, 158, 185, 242
TTL	Transistor–Transistor Logic	240, 242

Acronym	Description	Page list
Tx	Transmit or transmitter. See also Rx!	32, 58, 59, 94, 100, 101, 104, 106, 110, 112, 113, 115, 170, 171, 173, 176– 179, 184–186, 188, 212, 215, 245
UART	Universal Asynchronous Receiver/Transmitter	242
UHF	Ultra High Frequency	14, 16
USB	Universal Serial Bus	242
UTC	Universal Time Coordinated	161, 188, 203
UV	UltraViolet	97
VHF	Very High Frequency	16
VLNA	Very Low Noise Amplifier. See also LNA!	106, 108, 109, 127
XOR	eXclusive OR	115

Part I

THE BEGINNING

Chapter 1

Introduction

Among amateur radio enthusiasts the practice of communicating via the Moon, using it as a passive reflector, is often considered *the* ultimate technical challenge. Studying fig. 1.1 this is understandable; The average distance to the Moon is in excess of 380 000 km and it takes about 2.5 seconds for the radio signal to travel from the Earth to the Moon and back. Due to these great distances and the poor reflection properties of the lunar surface, the average two-way path loss is a staggering 271 dB at 1296 MHz. Furthermore, most of the transmitted energy is shot past the moon since its angular diameter in the sky is only 0.5° . As a consequence, there is a fine line between success and failure and not much room is left for error or chance.

Referred to as *moonbounce*, *Earth–Moon–Earth (EME) communication* or simply just *EME*, this method of communication spans numerous technical disciplines, all wound up into one communication system. Getting such a system to send and receive its first *EME* echo, though no small feat in itself, is however only one part of the challenge. Another and perhaps greater part, which the author strenuously discovered while writing this thesis, is to

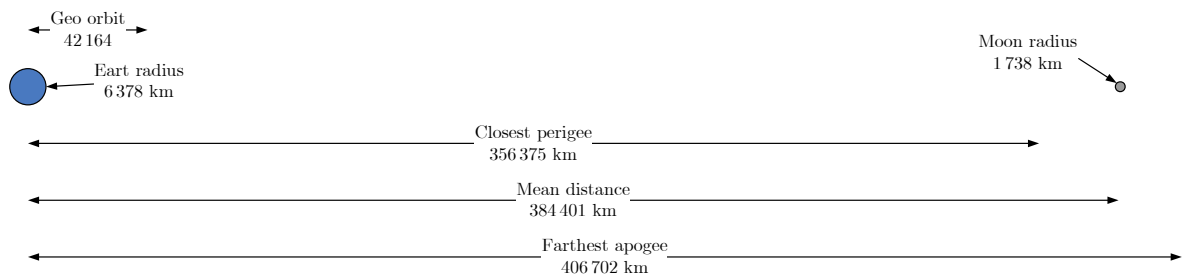


Figure 1.1 The Earth–Moon distances involved in *EME* communication (to scale). It takes approximately 2.5 seconds for the signal to travel from the Earth to the Moon and back, with a two-way path loss in the order of 271 dB. The distance of the geostationary orbit has been added for comparison.

try and understand the ‘whats’, ‘whys’ and ‘hows’ of **EME** communication. What system parameters are the most important? Why are they important? How can they be measured? What can be done to improve them? These are no easy questions to answer when dealing with a subject encompassing such vast areas as radio communication, radio astronomy, **radar** theory, antenna theory, noise theory, **low noise amplifiers (LNAs)**, low noise measurements, **power amplifiers (PAs)**, high power measurements, electronics, mechanics, computers, automation etc.

Nevertheless, this Master of Science thesis is the author’s attempt at answering some of these questions. It will do so by dealing with the design, realization and characterization of an **EME** communication system in the 1296 MHz amateur radio band. Furthermore, as part of the **LNA** characterization, the critical topic of low **noise figure (NF)** measurements, which proved more complicated than what first meets the eye, is given additional attention.

Without losing the overall system perspective, the above analysis will be established in both theory and practice, in a complementing manner. The explicit details of this are presented below.

1.1 Task definition and criteria for success

The following tasks are to be accomplished in this project:

1. Design, build and characterize an **EME** communication system in the 1296 MHz amateur radio band, with the goal of hearing ones own lunar echoes in the radio loudspeaker, chosen to correspond to at least a 3 dB average **signal to noise ratio (SNR)** in a 100 Hz bandwidth.
2. Theoretically estimate the expected **SNR** of lunar echoes, using estimated and measured quantities, and compare this to empirically measured results.

The project will be considered successful if task 1 is accomplished and if the results of task 2 show an agreement between theory and practice which is within estimated uncertainties.

A few comments are appropriate in regard to task 1 above. The ‘design phase’, which includes parts selection, will be heavily limited due to economical reasons, calling for technical compromise. As such, the system solution will likely be ‘functional’ rather than ‘optimal’. It is therefore vital that ‘rule of thumb estimates’ of the system performance be performed at regular intervals during the design process, so as to ensure that success is nonetheless attainable in the end.

1.2 Purpose and scope of the thesis

This thesis presents a project carried out at the *Department of Earth and Space Sciences at Chalmers University of Technology* in Gothenburg, Sweden. The project was supervised by professor Gunnar Elgered, who also was the examiner. The thesis is part of the broader requirements needed for obtaining a Master of Science degree in Electrical Engineering.

Since the author is a licensed radio amateur,¹ the topic of designing, building and characterizing an EME communication system was based on the author's suggestions. The purpose of this thesis is to document the relevant issues related to this project, while adhering to the task definition and the criteria for success, given above.

Apart from numerous chapters on theory, measurements and experiments, this thesis also presents *one* possible solution to an EME system. The scope of the thesis is limited to presenting this system from a system perspective. As such, its purpose is *not* to present an in-depth and detailed analysis on what parts to choose for such a system; it is not a step-by-step 'beginner's guide'. It does however provide much of the knowledge and the references needed, to understand what is important when designing an EME system.

1.3 Method

The theoretical framework, used for the theoretical aspects of task 2 in section 1.1, consists mainly of the radar equation and thermal noise theory. The former deals with the signal link budget, while the latter deals with the system noise temperature. Combining these, the SNR of the received signal can be estimated.

The parameters needed for calculating the SNR are determined through various measurements and estimations. The resulting SNR can finally be compared to a long-term SNR average of actual EME echoes, measured at audio frequency (AF) using a computer with appropriate software.

1.4 Existing solutions

There exists historical scientific research regarding the practice of EME communication. The work done today however, using modern and sometimes even cutting edge technology, is accomplished by radio amateurs around the world. Naturally, the author has studied some of their work to get inspiration, to see what can be accomplished by what means and what

¹ The author's call sign is SM6XMA. Please refer to page iv for contact information.

results to expect. This ‘benchmark knowledge’ has been valuable during the parts selection process of the system design phase. It has also prevented the author from falling into some, though unfortunately not all, pitfalls associated with realizing an EME system. Some lessons simply have to be learned by trial and error!

1.5 Report organization

This report is organized into four parts with numerous chapters in each part. A brief summary of this content is given below.

Part I – The beginning

Chapter 1, [introduction](#), is this chapter.

Chapter 2, [Earth–Moon–Earth communication history](#), presents a brief history of EME communication, from its origin at around the time of the Second World War and onwards.

Part II – In theory

Chapter 3, [link budget theory](#), provides the necessary theory leading up to the Friis transmission formula and the [radar](#) equation. Various signal path losses are also presented.

Chapter 4, [thermal noise theory](#), provides the theory needed to understand concepts such as ‘equivalent input noise temperature’, ‘noise factor’, ‘antenna noise temperature’ and ‘total system noise temperature’. It also presents the fundamental equations for Y-factor measurements.

Chapter 5, [signal to noise theory](#), combines the theory from the previous two chapters in order to introduce the concept of the ‘SNR’, as it applies to the Friis transmission formula and the [radar](#) equation. Related subjects such as ‘antenna G over T’, ‘[minimum detectable signal \(MDS\)](#)’ and the ‘[radiometer equation](#)’ are also presented.

Chapter 6, [radio astronomical measurement theory](#), presents the necessary theory to calculate the antenna G over T and the antenna gain, using results from celestial radio source measurements. The theory needed in order to compensate for source extension is also provided.

Part III – In practice

Chapter 7, [parts selection and system description](#), introduces all the major parts of the EME system, including various software applications used during the course of the project.

Chapter 8, [receiving system measurements and estimations](#), presents the measurements and estimations needed to characterize the receiver part of the

system. The various results are discussed in conjunction with their respective presentation. An extensive discussion on problems and uncertainties related to low **NF** measurements is also given.

Chapter 9, **transmitting system measurements and estimations**, presents the measurements and estimations needed to characterize the transmitter part of the system. A discussion about transmitted power ‘leaking’ into the receiver subsystem is also given. The various results are discussed in conjunction with their respective presentation.

Chapter 10, **EME signal path link budget estimation**, presents an **EME** link budget estimate, based on the monostatic **radar** equation.

Chapter 11, **lunar echo SNR estimation**, provides a calculated estimate of the lunar echo **SNR**, accompanied by an uncertainty assessment.

Chapter 12, **lunar echo SNR measurements**, presents **SNR** measurements of actual **EME** echoes. The calculated estimate from chapter 11 is compared to these time-averaged measurements. The results are then discussed.

Chapter 13, **lunar echo Doppler spread measurements**, provides a brief investigation into libration-induced ‘Doppler spread’ and ‘multipath fading’. Measurements of the former are compared to theoretical results provided by others. The results are then discussed briefly.

Part IV – The end

Chapter 14, **conclusion**, provides a summary of the essential results as well as an evaluation of the project, in regard to the **task definition and criteria for success** presented in section 1.1.

Chapter 15, **recommendations and future studies**, lists a number of recommendations in regard to system and measurement improvements. It also provides a number of proposals for future investigations.

In addition to the above, the **references** on page 219 are intended to serve as a basis for further study.

1.6 Final introductory remarks

As was explained in section 1.4 the field of **EME** communication is today driven by amateur radio enthusiasts, that is mostly outside the realm of scientific institutions. As such, most of what has been written in recent years on this and related topics is not published in the peer reviewed literature. At certain times this has posed somewhat of a dilemma to the author, when deciding which sources to cite in the **references**.

After having contemplated upon this problem, the author opted for citing amateur radio literature which can be considered ‘semi-professional’. This

includes primarily ‘DUBUS Magazine’ [47] but also, to some degree, the ‘EME conference papers’ which are published in book form in conjunction with the biennial ‘EME conference’ which attracts attendees from around the world. However, citations referring to webpages of certain well-reputed personalities within the amateur radio community, have also been selected.

Additionally, a few comments are necessary in regard to the use of names in this thesis. When referring to somebody in the amateur radio community, it is customary to be on a first-name basis in combination with the unique ‘call sign’ of that person. As such, surnames are maybe known but not frequently used. This is in contrast to scientific literature where initials and surnames are exclusively used. To accommodate for this, a compromise has been chosen in this thesis when referring to persons with an amateur radio background. For these cases, the author has chosen to state the full name followed by the call sign surrounded by parentheses. The exception to this rule is in the [references](#) where initials have been used instead of the first name.

Finally, it should be noted that numerals in this thesis are sometimes presented with more digits than there are significant figures motivated by precision. The purpose of this is to make the calculations easier to follow, so as to facilitate understanding. However, since uncertainties are often presented as well, there should be no problem in leaving the matter of significant numbers to the judgement of the reader. Also, all calculations in this thesis have been carried out without rounding the numbers, until at the very end.

Chapter 2

Earth–Moon–Earth communication history

Bouncing radio signals off the Moon is not a recent endeavour. According to Trexler [110] the US [Naval Research Laboratory \(NRL\)](#) [115] searched for lunar echoes ‘as early as 1924 and continuing through the 1930s’, making regular attempts as [radar](#) technology progressed. These technological improvements originated in the ionospheric research of the 1920s and 30s, but the decisive progress came in the shape of military technology during the second world war. After the war, there was an abundance of surplus [radar](#) equipment, as well as a large pool of engineers and scientists in pursuit of peacetime careers. Consequently, it was not until the end of the war that circumstances permitted [EME](#) experiments which were ultimately successful.

At war’s end ionospheric research resumed its roll as a driving force in [radar](#) technology, eventually enabling the field of [radar](#) astronomy. Lunar studies became a part of this research, in its turn opening up further areas of interest; both civilian and military, not seldom with the latter under the guise of the former. As a consequence of the ensuing cold war, two of the goals of these and following projects were to develop long-range [radars](#) for detecting [intercontinental ballistic missile \(ICBM\)](#) and locating Soviet [radars](#) by intercepting those of their signals which bounced off the Moon. Another goal was to use the Moon as a passive relay in long-range communication circuits, both for commercial and military purposes. Some of the people involved in these projects were also keen radio amateurs. Hence it should come as no surprise that amateur radio enthusiasts were not far behind in trying to bounce radio signals off the Moon.

This chapter will present some of the most prominent projects related to the above. Among these are [Project Diana](#), [Project PAMOR](#), the [Communication Moon Relay Project](#) and [Project Moonbeam](#) which was an amateur radio



Figure 2.1 Aerial view of the Project Diana site, Camp Evans Signal Laboratory, where the first planned [radar](#) signals were received from the Moon on January 10, 1946. (Photo courtesy of Camp Evans InfoAge WWII museum and national historic landmark [39].)

project. Last but not least, a few words on the [current state](#) of amateur radio [EME](#) communication will be presented. The information in this chapter was compiled from mainly two [NASA](#) history office sources, which should be of interest to those seeking more knowledge [35, ch. 1][36, ch. 2]. Additional sources are also given in each section below.

2.1 Project Diana

Project Diana, named after the Moon goddess of the Roman mythology, was the first deliberate and successful attempt at bouncing [radar](#) signals off the Moon. The first echoes were successfully detected at 11:58 AM on January 10, 1946. In charge of the project was Lt. Col. John H. DeWitt Jr. of the US Army Signal Corps at Evans Signal Laboratory at Fort Monmouth near Belmar, New Jersey. See [fig. 2.1](#)!

The equipment consisted of a modified ‘SCR-271 early-warning [radar](#)’, providing 3 kW of output power at 111.5 MHz using 0.25 second pulses. The antenna was a reflector array consisting of 64 horizontally polarized half-wave dipoles, providing a gain of approximately 24 dBi. The antenna, clearly visible in [fig. 2.1](#), was mounted on a 30 metre tower and was only controllable in azimuth. On the receiver side, the front-end amplifier had a gain of 30 dB

with an NF amounting to 4 dB which was considered low at the time. The receiver bandwidth was only 57 Hz, centred at 180 Hz, making accurate Doppler calculations for every test a necessity. Visual echo indication was furthermore provided on a radar scope.

Formally, the objectives of Project Diana were to determine whether radio signals could be transmitted through the ionosphere and to develop radars capable of detecting Soviet missiles. The Moon was chosen as a target since no missiles were available for the experiments. Informally however, being a radio amateur, DeWitt also had personal motives for the project. While working as chief engineer of radio station WSM in Nashville, Tennessee, DeWitt had already tried, in May 1940, to bounce radio signals off the Moon, alas unsuccessfully due to insufficient receiver sensitivity. He also had an interest in astronomy, sparked by Karl Jansky's discovery of cosmic noise in the early 1930s [71]. Hence, when the war ended it is not surprising that DeWitt seized the opportunity to initiate a project like Diana, before being discharged from the Army. Furthermore, one cannot help but wonder if it was a coincidence or not, that three out of five chief members of the project were radio amateurs. The five lead members were John H. DeWitt Jr. (W4ERI, formerly W4FU and later N4CBC), Herbert P. Kauffman¹ (W2OQU), Edwin King Stodola (W3IYF later W2AXO), Harold D. Webb and Jack Mofenson. Naturally, more people were involved in the project, some of which were also radio amateurs.

DeWitt's team was however not alone in fulfilling their ambition to bounce radio signals off the Moon. Just a few weeks after the success of Project Diana, a team from Hungary, led by Zoltán Bay, succeeded in their attempts as well [25]. However, having a less powerful system than the Americans, Bay had to somehow increase the received SNR. This led him to inventing the important technique of *time integration*, using a so called *hydrogen coulometer*. Unfortunately, Bay had to operate during war-time conditions, forcing him to entirely rebuild his system three times over. Had this not been the case, it is quite possible that Bay would have succeeded before DeWitt in deliberately receiving echoes from the Moon.

The word 'deliberately' is important in this context. For according to several sources [32, ch. 10.2.1], operators of a German experimental radar succeeded in hearing their own lunar echoes in January 1944, by pure chance. This so called 'Würzmann radar' was built by the Telefunken company and was situated on the island of Rügen in the Baltic Sea. It operated at 560 MHz with a peak power of 120 kW, having a very narrow beam antenna consisting of an array with no less than 640 dipoles.

Regardless of the above, Project Diana was the the first calculated and successful attempt at receiving radar echoes from the Moon, determining

¹ Kauffman happened to be the first to hear the received lunar echoes.

with certainty that radio waves could penetrate the Earth's ionosphere. This discovery was a prerequisite for all space related communication projects to come, thus marking the beginning of the space age.

For more information on Project Diana, please refer to the literature [39, 45, 74, 86].

2.2 Project PAMOR

Project PAMOR (passive Moon relay) was a highly classified project to intercept radar signals reflected from the Moon, originating from transmitters deep within the Soviet Union. It became an official US Navy intelligence program in 1950, though its origin can be traced back to 1947 after the success of Project Diana. The prime mover of the project was an engineer and radio amateur by the name of James H. Trexler,² assigned to the electronic countermeasures group of the US NRL.

It was in 1948, after having read a paper entitled 'Considerations of Moon-Relay Communication' [60], that Trexler determined that it should be possible to use the Moon for the above mentioned eavesdropping purpose. During the next two years the project evolved at the NRL's Blue Plains field facility in Washington DC, showing promise. As a result, the effort was formalized by mid 1950 and funds were directed towards building a new antenna at Stump Neck, Maryland. The antenna, a 67 by 80 metres fixed elliptical parabola, was built and commissioned in 1951. It had a limited tracking capability, but in return it was built for optimum performance towards the 'Sino-Soviet Block'. See fig. 2.2!

In order to learn more about the reflection properties of the lunar surface, the first EME echoes, using the new antenna, were received in October 1951. The transmitter operated at 198 MHz, delivering about 750 W using 10 μ s pulses. To Trexler's surprise, most of the received energy originated from the centre region of the lunar disc, meaning that the signals were much more coherent than expected [110]. The potential of the project was thus greater than previously believed. As a result, PAMOR was given more priority and a higher security status.

However, by 1954 it had become obvious that the project had outgrown the Stump Neck site. In order to satisfy all of the proposed electrical intelligence (ELINT) needs, a significantly larger antenna was required. Plans were thus made to build a 183 metre dish in Sugar Grove, West Virginia, though these plans never came into existence. Fortunately, there were other antennas at hand, alas these were only 46 metres in diameter which was the required

² The author has unfortunately not been able to find out Mr. Trexler's radio amateur call sign.



Figure 2.2 The [NRL's](#) Stump Neck site with the 67 by 80 metres elliptical parabola. The focal point is approximately 27 metres above the dish, where a horn-type feed is used. The gain and beam width were measured using the Sun as well as a 'horn gain standard', which can be seen on the ground to the right of the parabola. (Photo courtesy of the [NRL](#) [115].)

minimum. One of these was ‘The Dish’, located in Palo Alto, California, while another was located at the [NRL’s](#) Chesapeake Bay facility. Using these dishes, detailed information was acquired about the Soviet Union’s anti-ballistic missile [radar](#) systems.

In a declassified [Central Intelligence Agency \(CIA\)](#) document entitled ‘Moon Bounce [ELINT](#) – The monitoring of Soviet [radars](#) by way of the lunar surface’ [49], the author Frank Eliot tellingly concludes: ‘The Moon Bounce effort is one of those intelligence collection techniques which seemed at first “far out” but has in the event more than paid for itself.’

2.3 The Communication Moon Relay Project

The initial 1951 tests at Project [PAMOR’s](#) Stump Neck site revealed that [EME](#) echoes had a greater degree of coherence than first anticipated, as was mentioned in section 2.2. In practice, this meant that the Moon could be used as part of a modern communication system. This was a matter of great interest to the US Navy, who considered reliable communication to its fleet vital to national security. By 1954, further experiments had shown promise and a spin-off of Project [PAMOR](#) was therefore initiated within the [NRL](#). It was named the ‘Communication Moon Relay Project’ or ‘Moon Relay’ for short, though it was also known as ‘Operation Moon Bounce’.

By now, Project [PAMOR](#) had left the Stump Neck facility, leaving it solely for the purpose of lunar communication experiments. Having installed a 10 kW [UHF](#) klystron amplifier, experiments using teletype, facsimile and voice communication ensued. The latter was accomplished on 24 July 1954, when Trexler was the first person to hear his own voice from [AM](#) signals reflected off the Moon. Morse code communication had already been demonstrated on 21 October 1951.

While the transmitter used the Stump Neck dish, shown in fig. 2.2, the receiving end relied on standard military [radar](#) antennas. Operating at 301 MHz, the first successful transcontinental tests were made between Stump Neck, Maryland, and the Navy Electronics Laboratory in San Diego, California, in November 1955. Only a few weeks later, using similar equipment, communication was established between Stump Neck and Wahiawa, Oahu, Hawaii.

Within a few months the Navy had signed development contracts for further experimental systems. Furthermore, by the end of 1956 it was recommended that US submarine communication should be based on the Moon Relay system. By 1960 a fully operational system for communication between Washington DC and Hawaii had been developed. At its launch a picture

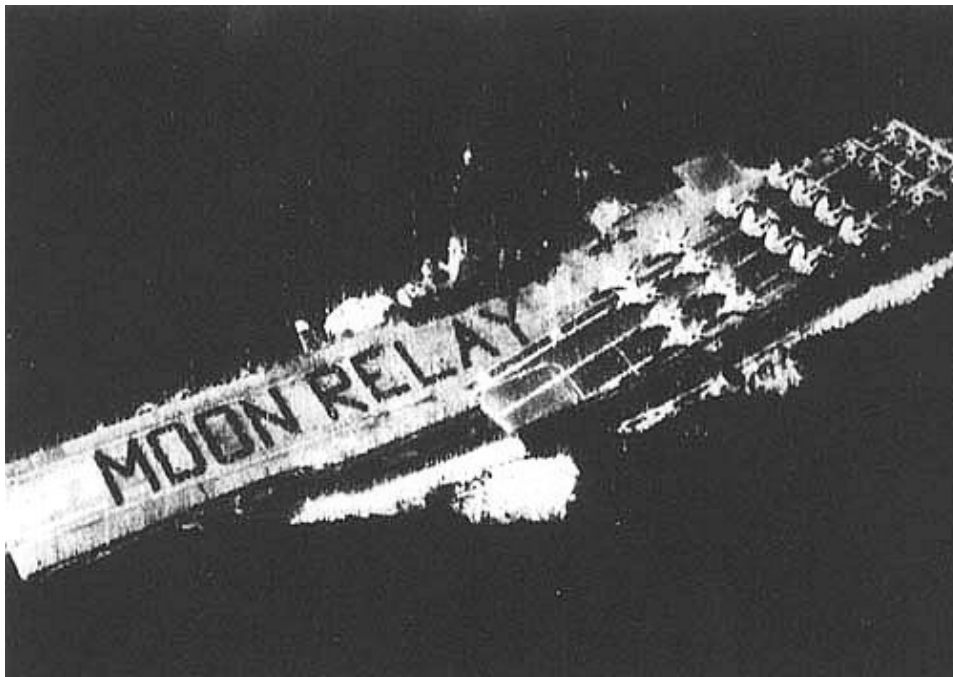


Figure 2.3 A facsimile picture transmitted from Honolulu, Hawaii, to Washington DC via the Moon on 28 January 1960. The picture features ship officers and crew aboard the USS Hancock spelling out ‘MOON RELAY’. (Photo courtesy of the NRL [115].)

of the crew aboard the aircraft carrier USS Hancock, forming the words ‘MOON RELAY’, was transmitted as a facsimile via the Moon. See fig. 2.3!

The final Moon Relay system was based on 28 metres steerable dishes fed by 100 kW transmitters operating at 400 MHz. Its capacity was limited to 16 simultaneous teletypewriter channels operating at 60 words per minute, capable of handling teletype and photographic facsimiles. In 1961, tests aboard the USS Oxford resulted in the first shore-to-ship Moon Relay communication in history, using a ship-mounted 5 metre dish. In 1962 a 1 kW transmitter was added to the Oxford, allowing for two-way communication. The experience gained during these tests paved the way for the Navy’s man-made satellite communication system, which were to arrive within a few years.

For more historic information on lunar communication, please refer to the literature [60, 110][36, ch. 3].

2.4 Project Moonbeam

The US Military projects presented in the previous sections were very ambitious and involved hundreds if not thousands of scientists and engineers.

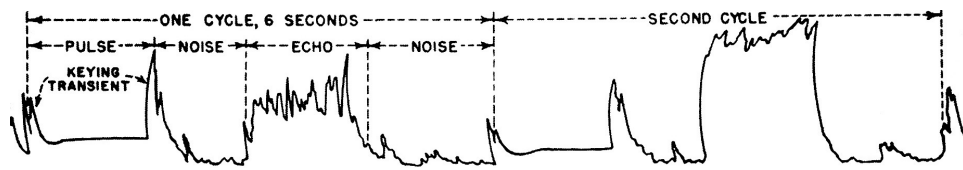


Figure 2.4 The first strong amateur radio [EME](#) echoes, recorded on 27 January 1953 as part of Project Moonbeam. The pioneers behind this feat were Ross Bateman (W4AO), Bill Smith (W3GKB) and Ted Tuckerman (W3LZD). (From [109]. Reprinted with the permission of the [ARRL](#). Copyright © [ARRL](#).)

However, in parallel with these large scale [EME](#) efforts a small number of radio amateurs, mainly from the US, were planning their own attempts at ‘reaching the Moon’, using more modest equipment. Naturally, these radio amateurs were faced with the same technical challenges as the military. Their solutions on the other hand, were seriously restricted due to economical reasons; the output powers were lower and the dishes were smaller, calling for narrow-band communication. With technology nowhere near today’s standards, especially in regard to [UHF](#) and microwave receiver front-ends, the author reckons that the challenge must have been quite a bit bigger than today.

Nevertheless, eventually came the success of Project Moonbeam, a joint effort between two American radio amateurs by the name of Ross Bateman (W4AO) and Bill Smith (W3GKB). After numerous unsuccessful attempts they finally succeeded in hearing their own 144 MHz echoes at 5:03 AM, 15 July 1950. The output power of their system amounted to 1 kW, which was fed into a 20 wavelength stacked rhombic array antenna. However, although their echoes were recorded they were also very weak. Thus instead of making their success public, they decided to continue their work on improving the equipment. Joined by Ted Tuckerman (W3LZD) in their quest for stronger echoes, it would take the trio another two and a half years of hard work and testing, before breakthrough came on 27 January 1953. The results of this work is shown in fig. 2.4, presenting a series of two strong echoes recorded on that day.

The amateur radio community had to wait another seven years though, until it could finally witness the first two-way [EME](#) contact between amateur radio stations, on 21 July 1960. It was established on 1296 MHz between the ‘Rhododendron Swamp [VHF](#) Society’ (W1BU) in Massachusetts and the ‘Eimac Radio Club’ (W6HB) in California. This milestone sparked an increased interest in [EME](#) communication among radio amateurs worldwide. New records followed and on 11 April 1964 the first two-way contact between the US and Europe was established on 144 MHz, between Bill Conkel (W6DNG) in California and Lenna Suominen (OH1NL) in Finland.



Figure 2.5 The 300 metre dish at the Arecibo Observatory in Puerto Rico. It was used by radio amateurs for [EME](#) communication in 1964, 1965 and 2010. (Photo courtesy of the [NAIC](#) – Arecibo Observatory [114], a facility of the [NSF](#).)

Two fantastic opportunities were given in June 1964 and July 1965, when the largest telescope in the world, the Arecibo Observatory in Puerto Rico [114], engaged in amateur radio [EME](#) communication on 144 and 432 MHz, operating under the KP4BPZ call sign. The Arecibo dish is 300 metres in diameter, which enabled radio amateurs from around the world to establish two-way contacts using Morse code and very modest equipment. More capable stations were even successful in using voice communication. It would take another 45 years, in April 2010, until radio amateurs were once again given the opportunity to operate from the Arecibo observatory, this time using the KP4AO call sign, on 432 MHz. This time around, JT65B digital communication was also used. See [fig. 2.5](#) for a photo of the Arecibo antenna!

For more information on amateur radio lunar communication history, please refer to the literature [30, 58, 89, 90, 109].

2.5 Current state

Even though the professional use of lunar communication declined with the advent of man-made satellites, the practice increased and is still very popular among amateur radio enthusiasts around the world. The barrier-to-entry has furthermore been lowered during the years, not least with the introduction of advanced digital communication modes such as JT65 by Joe Taylor (K1JT) [107]. However, this does by no means imply that the level of ambition has declined among EME amateurs. On the contrary, limits are constantly being pushed as new technology emerges: Software defined radio (SDR) technology is in regular use and evolving, opening up a multitude of possibilities previously unseen; modern microwave technology is continuously being explored, gradually increasing transmitter as well as receiver performance; computer simulation software is employed, resulting in better antennas and circuit design; advanced digital communication modes keep appearing; mechanical construction capabilities are improving and so on. These advances have enabled radio amateurs to make EME contacts at frequencies ranging from 50 MHz up to no less than 47 GHz and echoes have been received as high up as 77 GHz. In March 2009 radio amateurs in Germany were even able to detect 2.4 GHz echoes from signals they bounced off Venus [20]!

Due to the technical challenges involved in EME communication, it should come as no surprise that some radio amateurs take their hobby very seriously, spending an incredible amount of time and money on building and improving their systems. An example of this, though certainly not an isolated one, is given in fig. 2.6 which shows a 144 MHz antenna array belonging to Alexander ‘Sam’ Dubovtsev (R7AB) in Krasnodar, Russia [46].

Regardless of where ones level of ambition lies, EME communication offers a great opportunity to develop a good understanding of complex communication systems, involving skills from fields such as electrical, mechanical and computer engineering.



Figure 2.6 A 144 MHz EME antenna array belonging to Sam Dubovtsev (R7AB). The array consists of 64 crossed long-yagi antennas with 2×15 elements each, yielding a total gain of about 34 dBi. Vertical or horizontal polarization can be chosen at the flick of a switch. Resting on several wheels the antenna has full azimuth as well as elevation control capability. (Courtesy of Sam Dubovtsev [46].)

Part II

IN THEORY

Chapter 3

Link budget theory

This chapter will present some theory regarding link budget calculations for an EME communication system. The concepts of *effective aperture area and antenna gain* as well as *equivalent isotropic radiated power (EIRP)* will be presented first. This will be followed by the *Friis transmission formula* which is then evolved into the *radar equation*. Last but not least, *losses* associated with the signal path are mentioned.

For precise definitions of terms, please refer to the IEEE standard definitions of terms documents [65, 66, 67].

3.1 Effective aperture area and antenna gain

Let P_r (W) be defined as the available power at the output terminals of a receiving antenna and S_r be the *power density*, that is the power per unit area (W m^{-2}), of an incident field at the antenna. The *effective aperture area* (m^2) of the antenna is then defined as [54, 66]

$$A_e = \frac{P_r}{S_r} \quad (3.1)$$

Rearranging this we get

$$P_r = S_r A_e \quad (3.2)$$

Equation (3.2) states that *the available power at the antenna terminals equals the power flowing through an area equal to the effective aperture area of the antenna*. Note that this definition does *not* impose a condition of no ohmic (dissipative) losses in the antenna!

Another measure of interest is the dimensionless *aperture efficiency*¹ of the antenna, given as the ratio of its effective and physical aperture areas (m²):

$$\eta_{ap} = \frac{A_e}{A_{ph}} \quad (3.3)$$

From a physical perspective, *the aperture efficiency gives an indication of how efficiently an antenna utilizes the space it occupies.* The aperture efficiency may assume values greater than unity,² though it cannot exceed this value for large aperture antennas such as those employing paraboloid reflectors [79, ch. 2-17]. For these antennas an aperture efficiency between 50 and 70 percent is more common [79, ch. 2-18, 12-9].

Related to the effective aperture area is the dimensionless *maximum antenna gain* which is given by [66][79, ch. 3-15]

$$G_{max} = \frac{4\pi A_e}{\lambda^2} \quad (3.4a)$$

A closely related term is the *maximum antenna directivity* given by [66][79, ch. 2-8, 3-13]

$$D_{max} = \frac{4\pi A_{em}}{\lambda^2} \quad (3.4b)$$

where λ (m) is the wavelength and A_{em} (m²) is the *maximum effective aperture area* [66], which is obtained for a theoretical antenna without ohmic losses. A_e is related to A_{em} as

$$\eta_{rad} = \frac{A_e}{A_{em}} \quad (3.5a)$$

where $0 \leq \eta_{rad} \leq 1$ is the dimensionless *radiation efficiency* [66] of the antenna, that is a factor relating to the ohmic losses of the antenna. Using eqs. (3.4a), (3.4b) and (3.5a) it can also be expressed in terms of the antenna gain and directivity as

$$\eta_{rad} = \frac{G_{max}}{D_{max}} \quad (3.5b)$$

The gain of a *lossless* antenna thus equals its directivity since $\eta_{rad} = 1$ in this case. This approximation can often be made when determining the gain of real world antennas.³

¹ The IEEE definition calls this the *antenna efficiency* [41, 66].

² The quarter wave dipole antenna is an example of this [79, ch. 2-21].

³ Dissipative antenna losses should however not be neglected when assessing the antenna noise temperature in a low noise system. See section 4.6!

The maximum antenna directivity is also given by the ratio of the maximum to the average power density of the antenna. It can be shown [79, ch. 2-8, 3-13] that this can be expressed as

$$D_{max} = \frac{4\pi}{\Omega_A} \quad (3.6)$$

where Ω_A (sr) is the *total beam area* or *beam solid angle* [66][79, ch. 2-5, 3-13] of the antenna, given by

$$\Omega_A = \iint_{\substack{\text{Sphere} \\ \Omega=4\pi}} P(\xi, \psi) d\Omega = \int_0^{2\pi} \int_0^\pi P(\xi, \psi) \sin \xi d\xi d\psi \quad (3.7a)$$

where $P(\xi, \psi)$ is the *normalized antenna power pattern* (dimensionless) [66], which is a measure of the antenna response to radiation as a function of direction from the antenna. ξ and ψ are spherical angle coordinates (rad) in the antenna coordinate frame and $d\Omega = \sin \xi d\xi d\psi$ an infinitesimal solid angle (sr) on the sphere of integration.

Assuming rotational symmetry of the antenna pattern, there is no variation with ψ . The expression for Ω_A can then be reduced to

$$\Omega_A = 2\pi \int_0^\pi P(\xi) \sin \xi d\xi \quad (3.7b)$$

From a physical perspective, *the beam solid angle can be seen as the solid angle through which all power from a transmitting antenna would flow, if the power per unit solid angle were constant and equal to its maximum value.*

Equating eq. (3.4b) with eq. (3.6) and rearranging we get

$$\Omega_A = \frac{\lambda^2}{A_{em}} \quad (3.8)$$

Rearranging eq. (3.5a) to get A_e and inserting this into eq. (3.3), the aperture efficiency can also be expressed as

$$\eta_{ap} = \eta_{rad} \frac{A_{em}}{A_{ph}} \quad (3.9)$$

The gain is most often given in decibels, either as referenced to a lossless and spherically radiating (isotropic) antenna (dBi) or to a half-wave dipole antenna (dBd). The directivity on the other hand is always given in dBi. When talking about antenna gain and directivity their maximum (boresight) values are usually implied, that is $G = G_{max}$ and $D = D_{max}$.

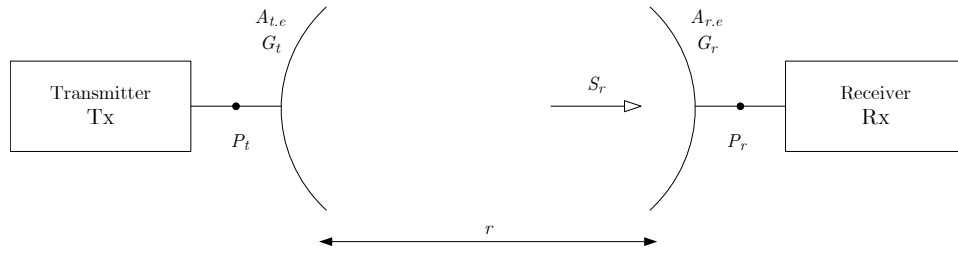


Figure 3.1 A radio communication link with the transmitter to the left and the receiver to the right. Their antennas, being a distance r apart, have a gain G_t and G_r as well as effective aperture areas $A_{t,e}$ and $A_{r,e}$ respectively. The power supplied at the terminals of the transmitting antenna is P_t , while the available power at the terminals of the receiving antenna is P_r .

3.2 Equivalent isotropic radiated power (EIRP)

The *equivalent (or effective) isotropic radiated power (EIRP)* is defined as [66][81, ch. 5.1]

$$EIRP = P_t G_t \quad (3.10)$$

where P_t (W) is the power delivered to the terminals of a transmitting antenna and G_t its gain in the direction of the receiver. Hence the unit for *EIRP* is Watts, though it is often given in dB relative to one Watt (dBW) or, if lower output powers are used, to one milliwatt (dBm).

Equation (3.10) states that the *EIRP* is the amount of power a theoretical, isotropically radiating antenna would have to emit, in order to produce the same power density at a receiving antenna, as a transmitting antenna having a gain G_t (in the direction of the receiving antenna). It is usually implied that $G_t = G_{t,max}$ where $G_{t,max}$ is the maximum gain (at boresight) of the transmitting antenna. If the antenna is pointing off target a so called *depointing loss* is introduced, rather than altering the *EIRP*. See section 3.5.3!

3.3 Friis transmission formula

The Friis transmission formula [54, 67, 79] illustrates the usefulness of the effective aperture area concept, introduced in section 3.1. It gives the relation between the transmitted (P_t) and received (P_r) powers in a radio communication link, as shown in fig. 3.1.

The receiving antenna, having an effective aperture area $A_{r,e}$ (m^2), intercepts some of the power radiated by the transmitting antenna, having an effective aperture area $A_{t,e}$ (m^2). Assuming an isotropically radiating transmitting antenna, that is $G_t = 1$, the power density (W m^{-2}) at the receiving antenna

is given by

$$S_{r.iso} = \frac{P_t}{4\pi r^2} \quad (3.11)$$

Assuming instead an antenna gain $G_t = G_{t.max}$ at the transmitter, in the direction of the receiver, the power density (W m^{-2}) at the receiving antenna is now given by

$$S_r = \frac{P_t G_t}{4\pi r^2} \quad (3.12)$$

Using eq. (3.2) the power collected by the receiving antenna, as measured at its terminals, is

$$P_r = S_r A_{r.e} \quad (3.13)$$

Inserting eq. (3.12) into eq. (3.13) we get

$$P_r = \frac{P_t G_t A_{r.e}}{4\pi r^2} \quad (3.14)$$

Using eq. (3.4a) to get either the antenna gain or the effective aperture area, and inserting this into eq. (3.14), one finally gets the *Friis transmission formula* [54] as either of the following:

$$P_r = \frac{P_t A_{t.e} A_{r.e}}{r^2 \lambda^2} \quad (3.15a)$$

$$P_r = \frac{P_t G_t G_r \lambda^2}{(4\pi r)^2} \quad (3.15b)$$

where G_r is the gain of the receiving antenna in the direction of the transmitter.

Inserting eq. (3.10) into eq. (3.15b) we get

$$P_r = \frac{EIRP \cdot G_r}{L_{fsl}} \quad (3.15c)$$

Equation (3.15c) is the Friis transmission formula formulated using *EIRP* and L_{fsl} . The latter is the so called *free-space loss* or *spreading loss* [66, 67, 93] [81, pg. 201], which is *the ratio of the transmitted and received powers*, given as

$$L_{fsl} = \left(\frac{4\pi r}{\lambda} \right)^2 \quad (3.16)$$

This definition is in adherence to the nomenclature in this report, where a loss is always given as a number greater than unity, in linear terms. It is important to note that the free-space loss is *not* a dissipative loss but

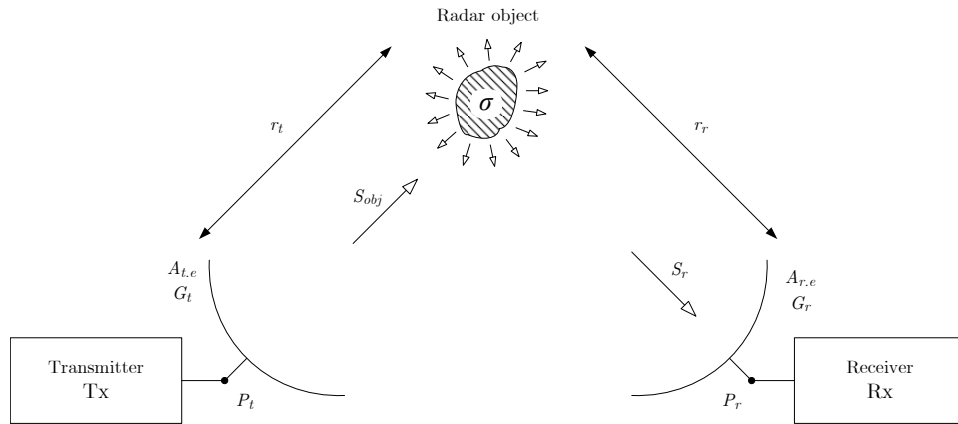


Figure 3.2 A radio communication link with the transmitter to the left, receiver to the right and a *radar object* or *target* with **radar cross section** σ in-between. The distances between the antennas and the **radar** object is r_t and r_r for the transmitter and receiver respectively. The aperture areas, gains and powers are analogous to fig. 3.1.

rather a geometric loss, stemming from the fact that the power flux density decreases with the square of the separation distance r .

In using eq. (3.15) one must be aware of their limiting assumptions, one of these being that the antennas need to be in each others *far-fields*, a distance r apart. A plane wave front is assumed at this distance and eq. (3.15) is, by rule of thumb, said to be correct if [54][79, ch. 2-31]

$$r \geq \frac{2a^2}{\lambda} \quad (3.17)$$

where a (m) is the largest linear dimension of either the transmitting or receiving antenna.

The other assumption is that eq. (3.15) only applies for free space propagation, which often is a valid approximation. In case this approximation is *not* valid, for example in the case of propagation above ground or through a lossy medium, corrections may be introduced.

3.4 Radar equation

In section 3.3 the Friis transmission formula was presented. Now, suppose instead of having a direct communication link as in fig. 3.1, the signal is reflected off a passive reflector before it reaches the receiving antenna, as in fig. 3.2. This scenario will be used to present the *radar equation* [79, ch. 17-5].

In analogy with eq. (3.12) the power density (W m^{-2}) incident at the passive reflector, also called the *radar object*, *radar target* or *scatterer*, is

$$S_{obj} = \frac{P_t G_t}{4\pi r_t^2} \quad (3.18)$$

where r_t (m) is the distance from the transmitting antenna to the radar object.

Depending on the physical properties of the radar object as well as on the frequency, polarization and angle of incidence of the radar signal, different amounts of power will be reflected in the direction of the receiving antenna. Introducing the so called *radar cross section (RCS)* σ (m^2), which is a function of these parameters, the power density incident at the receiving antenna is given by

$$S_r = \frac{S_{obj}\sigma}{4\pi r_r^2} \quad (3.19)$$

where r_r (m) is the distance from the radar object to the receiving antenna.

Thus, slightly rewording the definition given by Skolnik [99, ch. 2.7], *the RCS of a radar object is the hypothetical area intercepting that amount of power which, when scattered isotropically, produces a power density at the receiver equal to that from the actual object.* The word ‘hypothetical’ is crucial since no radar object actually scatters the reflected power isotropically. It is simply a theoretical construct, used to *define* the RCS in a way which makes calculations easier. Hence instead of having to know the exact manner in which a radar object scatters an incoming wave, one can instead use the concept of its RCS and assume spherical scattering. For more on the RCS please also refer to Milligan [85, ch. 1-5] and also the IEEE definitions of terms documents [65, 66, 67].

Using eq. (3.2) the power collected by the effective aperture area $A_{r.e}$ (m^2) of the receiving antenna is now given by

$$P_r = S_r A_{r.e} \quad (3.20)$$

Inserting eqs. (3.18) and (3.19) into eq. (3.20) we get

$$P_r = \frac{P_t G_t}{4\pi r_t^2} \cdot \frac{\sigma}{4\pi r_r^2} \cdot A_{r.e} = \frac{P_t G_t \sigma A_{r.e}}{(4\pi)^2 r_t^2 r_r^2} \quad (3.21)$$

Rearranging eq. (3.4a) to get the aperture area and inserting this into eq. (3.21), one finally arrives at the *bistatic radar equation* as

$$P_r = \overbrace{\frac{P_t G_t}{4\pi r_t^2}}^{\text{Transmission and propagation}} \cdot \overbrace{\frac{\sigma}{4\pi r_r^2}}^{\text{Reflection and isotropic reradiation}} \cdot \overbrace{\frac{G_r \lambda^2}{4\pi}}^{\text{Reception } (A_{r.e})} = \frac{P_t G_t G_r \lambda^2 \sigma}{(4\pi)^3 r_t^2 r_r^2} \quad (3.22a)$$

Using eqs. (3.10) and (3.16) and adding notations for transmitter and receiver in the subscript, we get the bistatic radar equation expressed in terms of the EIRP and the free-space loss as

$$P_r = \frac{EIRP}{L_{t,fsl}} \cdot \frac{\sigma}{4\pi r_r^2} \cdot G_r = \frac{EIRP}{L_{t,fsl}} \cdot \frac{4\pi\sigma}{\lambda^2} \cdot \frac{G_r}{L_{r,fsl}} \quad (3.22b)$$

Studying the middle term on the right hand side of eq. (3.22b) and comparing it to eq. (3.4a), we see that it can be interpreted as the gain of the radar object. Calling this gain G_{obj} we get

$$P_r = \overbrace{EIRP}^{\text{Transmission}} \cdot \overbrace{\frac{G_{obj}}{L_{t,fsl} \cdot L_{r,fsl}}}^{\text{Transmission loss (inverse)}} \cdot \overbrace{G_r}^{\text{Reception}} \quad (3.22c)$$

where G_{obj} is thus given by

$$G_{obj} = \frac{4\pi\sigma}{\lambda^2} \quad (3.23)$$

and the *bistatic radar transmission loss* is given by

$$L_{tl,b} = \frac{L_{t,fsl} \cdot L_{r,fsl}}{G_{obj}} \quad (3.24)$$

Now, assuming the transmitter and receiver are colocated and are using the same antenna, as is the case during an EME echo experiment, one has $G = G_t = G_r$ and $r = r_t = r_r$. Inserting this into eq. (3.22a) we get the *monostatic radar equation* as [79, ch. 17-5]

$$P_r = \overbrace{\frac{P_t G}{4\pi r^2}}^{\text{Transmission and propagation}} \cdot \overbrace{\frac{\sigma}{4\pi r^2}}^{\text{Reflection and isotropic reradiation}} \cdot \overbrace{\frac{G \lambda^2}{4\pi}}^{\text{Reception } (A_e)} = \frac{P_t G^2 \lambda^2 \sigma}{(4\pi)^3 r^4} \quad (3.25a)$$

In analogy with eq. (3.22b) and setting $L_{fsl} = L_{t,fsl} = L_{r,fsl}$, we get the monostatic radar equation expressed in terms of the EIRP and the free-space loss as

$$P_r = \frac{EIRP}{L_{fsl}} \cdot \frac{\sigma}{4\pi r^2} \cdot G = \frac{EIRP}{L_{fsl}} \cdot \frac{4\pi\sigma}{\lambda^2} \cdot \frac{G}{L_{fsl}} \quad (3.25b)$$

In analogy with eq. (3.22c), using the gain G_{obj} of the radar object, P_r can also be written as

$$P_r = \overbrace{EIRP}^{\text{Transmission}} \cdot \overbrace{\frac{G_{obj}}{L_{fsl}^2}}^{\text{Transmission loss (inverse)}} \cdot \overbrace{G}^{\text{Reception}} \quad (3.25c)$$

where the *monostatic radar transmission loss* is thus given by

$$L_{tl,m} = \frac{L_{fsl}^2}{G_{obj}} \quad (3.26)$$

In eqs. (3.22a) and (3.25a) respectively, the first term represents *the power density incident at the radar object*, the second term represents *the power density incident at the receiving antenna* and the third term represents *the effective aperture area of the receiving antenna, collecting the received power*. Alternatively this can also be expressed in terms of eqs. (3.22c) and (3.25c) in which the first term represents *the effective power from the transmitter*, the second term represents *the transmission loss from the transmitter to the receiver* and the third term is *the gain of the receiving antenna*. For EME communication at 1296 MHz, the transmission loss (sometimes called the path loss) is in the order of 271 dB.

Of course, the limiting far-field assumption given by eq. (3.17) on page 28 also applies to the radar equations above. In the case of an EME communication system however, this limiting assumption will never come into play because of the huge distances involved.

Calculations involving the radar equation in regard to the Moon will be presented chapter 10, dealing with the EME link budget.

3.5 Losses

Associated with the signal path are also losses, which will have to be subtracted from the received signal power in eqs. (3.22) and (3.25). Some of these will be presented in this section. A considerable amount of time has been spent on improving system parameters associated with these losses regarding the EME system in fig. 7.1 on page 94, which will be presented in chapter 7.

3.5.1 Dissipative loss

On the transmitting side of the system, losses are mainly given by heat dissipation due to ohmic and dielectric losses in the coaxial cable, connecting the power amplifier to the antenna. To maximize the power transfer to the antenna, short low loss cables are thus preferable.

Dissipative losses are also present in the connectors and coaxial protection relay connecting the antenna to the LNA. In case of an EME system, where low noise temperatures of the antenna and amplifier are prominent, these losses have a more adverse effect on the receiver *noise* level than on the received *signal* level. Losses in this part of the communication link are

therefore *highly detrimental* to receiver performance and consequently must not be underestimated. This will be explained further in section 4.4. Much care must therefore be taken to minimize dissipative losses in front of the LNA. This can be done by mounting the LNA directly to the coaxial protection relay, which in turn is directly mounted to the receiving port of the feed horn. Naturally, a low loss and high isolation coaxial relay is desirable. Please refer also to appendix A for general graphs relating to the above.

3.5.2 Mismatch loss

The nominal system impedance usually used in a communication system is $Z_0 = 50 \Omega$. Sometimes though it can be hard matching every part of the system to this value, resulting in non-dissipative *mismatch loss*. The coax to waveguide transition in the feed horn of the antenna is one example where this might be hard to achieve, thus reducing the transmitted power. For maximum power transfer to occur, the mismatch loss must be kept to a minimum in the Tx part of the system.

Since mismatch loss is non-dissipative, it does not add any noise. For the low noise Rx front-end of an EME system, it is thus not as detrimental as its dissipative counterpart. In fact, mismatch can even be desirable. One such example is at the input of the LNA where mismatch loss, even though it reduces the received signal at the input, reduces the noise at the output of the LNA proportionately more, so as to achieve a minimum NF. For more on this please refer to section 4.2.2.

3.5.3 Depointing loss

It can be difficult pointing the antenna in the exact right direction, such as at the Moon in the case of an EME communication system. This might for example be due to a lack of accuracy or resolution of the antenna rotor system, in relation to the antenna *half-power beam width (HPBW)*. It could also be due to a lack of knowledge regarding the shape of the antenna power pattern.

Regardless, these problems result in a loss of antenna gain in the intended direction, since the antenna boresight is beaming slightly off target. This so called *depointing loss* can be especially problematic when the HPBW of an antenna is in the same order of magnitude as the angular extension of the target one is aiming at. Examples affected by this problem are G over T, antenna gain and lunar echo SNR measurements, such as those which will be presented in sections 8.6 and 8.7 and chapter 12. In the case of the latter, the depointing loss will come into play twice since the same antenna is used during both transmission and reception.

The depointing loss can be alleviated through the use of a high resolution antenna rotor system and careful calibration, as well as by measuring the antenna power pattern using celestial sources.

3.5.4 Antenna losses

Losses in the antenna are accounted for in the value of the *effective aperture area* and thus in the all-embracing *aperture efficiency*, presented in section 3.1. Improving upon this figure of merit is of course of interest!

Though it can be hard improving the dissipative (ohmic) losses, as represented by the *radiation efficiency*, other efficiency measures are easier to handle. They are often such that they indicate a lack of potential improvement in antenna performance. One factor which can be improved upon is the *phase efficiency*, in part determined by the correct axial placement of the feed horn in a reflector dish antenna. Another improvement may be done to the *aperture blockage efficiency*, relating to the size of the feed horn structure and support struts. *Reflector transparency efficiency*, depending on the mesh size of meshed reflector surfaces, can also be improved upon. Another area of improvement is the *spillover efficiency*, revealing to which degree the feed horn is illuminating past the edge of the dish.

Since the spillover efficiency is a trade-off between increased antenna gain and decreased antenna noise temperature, an under-illuminated dish can be beneficial in an EME system. For even though this dispenses with an opportunity for higher antenna gain, and thus reduces the aperture efficiency, it also reduces the amount of ambient noise being picked up by the antenna. In this case, maximizing the G over T figure of merit is more important than maximizing the antenna gain. For more on this please refer to section 5.4.

For an informative clarification of the various efficiencies for reflector antennas, please refer to Van Capellen [41]. A more thorough discussion is presented elsewhere in the literature [66, 79, 85].

3.5.5 Polarization mismatch loss

The *polarization mismatch loss* is the magnitude, expressed in decibels, of the polarization efficiency of an antenna [66]. It is thus a measure of the relative power loss occurring, due to the polarization of an *electromagnetic wave (EMW)* differing from that of the receiving antenna. In EME communications at 1296 MHz, where an agreed upon circular polarization is used (see fig. 7.5 on page 100), polarization mismatch loss occurs due to *depolarization*.

The depolarization of an EMW is an occurrence in which parts of the signal power in the wanted sense of polarization, that is the co-polarized component,

is being converted into the opposite sense of polarization, that is the cross-polarized component. In an EME system this is caused by the wave being distorted on its path from the transmitting to the receiving station, for example due to influences from the ionosphere and the reflection on the lunar surface.

However, a significant portion of the polarization mismatch loss is also caused by the imperfect polarization properties of the antennas themselves. That is, the transmitting antenna does not generate a perfect co-polar wave, and the receiving antenna is not capable of perfectly accepting such a wave. Polarization mismatch loss will thus always exist to some degree.

The polarization efficiency is, strictly speaking, part of the aperture efficiency mentioned in section 3.5.4. However, the antenna measurements in this thesis have been made using the Sun, a highly uncorrelated and randomly polarized source for antenna beam widths which are wide in relation to its angular extension. The polarization efficiency of the measured antenna is thus unknown and has to be estimated and then accounted for. However, assuming near perfect antenna reciprocity the antenna should be fairly matched to its own polarization during monostatic radar echo tests, such as those presented in chapter 12. The author therefore assumes that the need to account for the effects of polarization efficiency is negligible during these tests.

3.5.6 Atmospheric loss

Although *atmospheric loss* can be considerable at higher frequencies, it is negligible at 1296 MHz where so called *libration fading* is of more importance. The latter, which is a type of multipath fading, will be covered briefly in chapter 13. A more detailed survey of atmospheric losses at various frequencies is presented elsewhere in the literature [81, ch. 5.7][98, ch. 6][93].

Chapter 4

Thermal noise theory

Noise consists of all *unwanted* contributions of power, which add to the *wanted* carrier power in the bandwidth in question. It reduces the ability to correctly extract the information contained in the carrier being received.

Noise can either be generated by sources of radiation located within the antenna reception area or by the components used in the receiving equipment. Various types of noise exist such as *flicker noise* (*1/f-noise*), *thermal noise* and *shot noise*. Flicker noise is dominant at relatively low frequencies, depending on the type of semiconductor material used in active circuits, while thermal noise as well as shot noise are broadband and Gaussian in nature [13, pg. 6, 21, 26][43, ch. 8.2].

Since thermal noise is readily modelled, it is often used as a representation for the combined effect of other causes of noise in a system. This chapter will therefore deal with theory regarding thermal noise and how it is modelled in a receiving system. Man-made interference, though also important, will not be considered since it may be resolved for example by filtering and shielding or by the elimination of the noise sources.

Thermal noise was investigated experimentally by Johnson [73] and theoretically by Nyquist [88] in the late 1920s and is therefore sometimes also referred to as *Johnson noise* or *Nyquist noise*.

4.1 Thermal noise power from and equivalent noise temperature of a one-port

Thermal noise is generated by thermal agitation of charge carriers, usually electrons, for example inside a resistor (conductor) at thermal equilibrium. This random motion of electrons occurs regardless of the applied voltage, even in the case of an open circuit. This produces Gaussian distributed

voltage fluctuations across the resistor terminals, in accordance with the central limit theorem. The mean-square value of this one-port noise voltage (V) is given by [13, pg. 25]

$$\overline{v_n^2} = 4kT_{op.ph} \int_{f_1}^{f_2} R(f)p(f) df \quad (4.1)$$

where $p(f)$, that is Planck's factor which accounts for quantum mechanical effects, is given by

$$p(f) = \frac{hf/kT_{op.ph}}{e^{hf/kT_{op.ph}} - 1} \quad (4.2)$$

In these equations, k ($1.381 \cdot 10^{-23}$ J K⁻¹) is *Boltzmann's constant*, $T_{op.ph}$ (K) is the *physical temperature* of the conductor, R (Ω) is the *resistance*, f (Hz) is the *frequency*, f_1 (Hz) and f_2 (Hz) specify the *bandwidth* over which the voltage is observed and h ($6.626 \cdot 10^{-34}$ J s) is *Planck's constant*.

For temperatures in the vicinity of the IEEE-adopted reference temperature $T_0 = 290$ K, and at frequencies below say 100 GHz, $hf \ll kT_{op.ph}$ so that Planck's factor in eq. (4.2) is approximately equal to one. This so called *Rayleigh-Jeans approximation* results in eq. (4.1) turning into eq. (4.3), which was derived experimentally by Johnson [73]:

$$\overline{v_n^2} = 4kT_{op.ph}R \cdot (f_2 - f_1) = 4kT_{op.ph}RB \quad (4.3)$$

In this equation $B = f_2 - f_1$ (Hz) is the previously mentioned bandwidth over which R furthermore has been assumed constant.

Now, suppose that the noise power from the one-port resistor is to be transferred to an ideal noiseless matched load,¹ that is a condition of maximum power transfer. In this case half the noise voltage is divided across the matched load, so that the noise power (W) in the load is given by [44, ch. 4.2]

$$P_n = \frac{\overline{(v_n/2)^2}}{R} = \frac{\overline{v_n^2}}{4R} \quad (4.4)$$

Inserting eq. (4.3) into eq. (4.4) we get the following equation which has been theoretically verified by Nyquist [88], based on thermodynamical reasoning [44, app. D]:

$$P_n = kT_{op.ph}B \quad (4.5)$$

It is worth mentioning that neither resistance nor frequency are part of eq. (4.5). The latter implies that *thermal noise has a uniform response*

¹ 'Noiseless' can in this context be thought of as if we disregard the noise being generated in a noisy load, that is we only consider the noise being delivered to the load since this is what we are interested in.

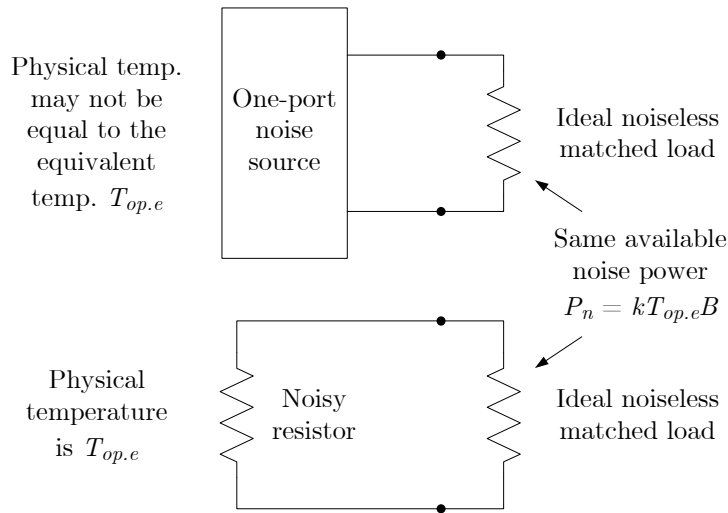


Figure 4.1 Definition of the equivalent noise temperature of a one-port noise source.

over a broad band of frequencies and that its magnitude depends only on the physical temperature of the one-port and the observed bandwidth. For this reason, thermal noise is sometimes also called *white noise* [44, ch. 4.1]. Even though this might not be the case for real noise sources, the model is convenient for real noise observed over a limited bandwidth.

The product $kT_{op,ph}$ is called the *power spectral density* and at $T_{op,ph} = T_0 = 290$ K it has a value of $kT_0 = 4.004 \cdot 10^{-21}$ W Hz⁻¹ = -174.0 dBm Hz⁻¹. The Boltzmann constant k is thus a conversion constant used for expressing energy in terms of a temperature in kelvin, as opposed to joule (W Hz⁻¹). However, the temperature notation is primarily used for energies (or powers) associated with noise.

In case of a noisy one-port element which is *not* a resistor, we introduce $T_{op,e}$ (K). This is the *equivalent thermodynamic temperature of a resistor, which delivers the same amount of noise power as the source under consideration*. This so called *equivalent (or effective) noise temperature* is therefore not necessarily (nor likely) equal to the physical temperature of the one-port element in question. See fig. 4.1!

Since noise power is directly proportional to noise temperature according to eq. (4.5), noise temperatures can be added in the same manner as noise power. However, this requires that each temperature is associated with the same bandwidth.

4.2 Noise factor, available gain and equivalent input noise temperature of a linear two-port

In the previous section, the noise power from a one-port resistor with a thermodynamic temperature $T_{op.ph}$ was presented. Furthermore, the concept of an equivalent noise temperature of an arbitrary one-port element was also presented.

This section will define the so called *noise factor*, and its dB equivalent called the *noise figure (NF)*, of a linear two-port element such as an amplifier.² The Friis noise factor definition will be presented first, followed by a derivation arriving at the IEEE definition as well as at equations used for noise factor calculations. Along the way, the *available gain* and the *equivalent input noise temperature* of a two-port will also be derived. From this, a discussion about *minimum noise factor* and *maximum available gain*, in regard to *source impedance*, will also be presented. Apart from the literature referenced to in this section, please also refer to Mohr [87] for an informative summary.

While reading this section, please have in mind that it deals with the theoretical *definition* of the noise factor of a linear two-port. It does not deal with the practical aspects of noise factor measurements, which instead will be discussed in sections 8.1 to 8.4.

4.2.1 Friis and IEEE noise factor definitions

The *noise factor* of a linear two-port is a *unit-less quantity which characterizes the degradation of the SNR* caused by the two-port as a signal passes through it. This degradation is a result of the unavoidable amount of inherent noise being added by the two-port. The SNR at the output of a two-port will thus always be worse, than at its input. Figure 4.2 shows an example of a 10 dB degradation of the SNR, due to the noise added by an amplifier.³

Another and more precise way of explaining it, is the way it was initially defined by Friis [53]. His definition is based on a circuit requiring the presence of a noisy signal source, as shown in fig. 4.3, and can be formulated as follows: *The noise factor F of a linear two-port, connected to a noisy signal source, is the ratio of the SNR at the output terminals of the signal source (SNR_{in}), to the SNR at the output terminals of the two-port (SNR_{out}), when the available noise power from the signal source ($P_{n.in}$) has a corresponding noise*

² In this context, the amplifier is noisy but assumed to be ideal in every other aspect.

³ Figure 4.2 assumes that $SNNR \approx SNR$ since the signal is much stronger than the noise. See also section 5.3!

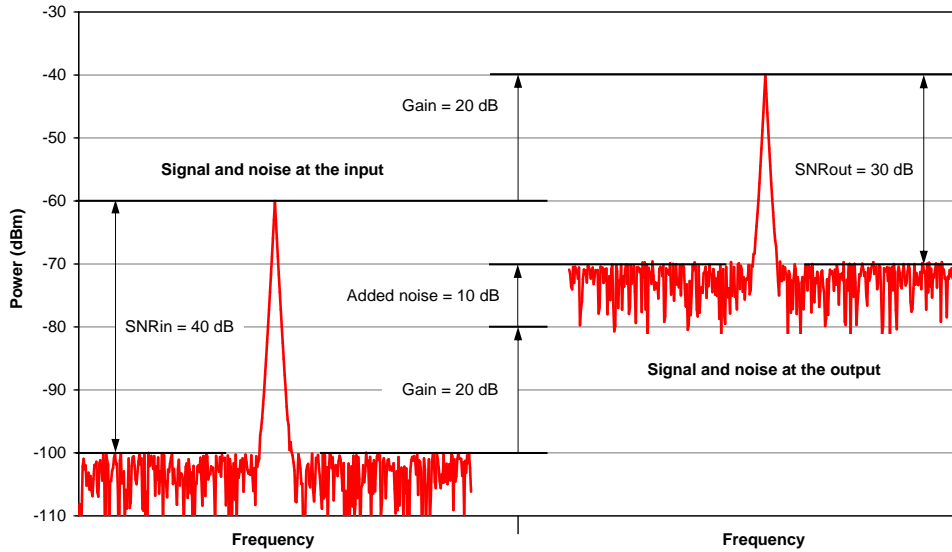


Figure 4.2 An example of a 10 dB degradation in SNR for a signal passing through a noisy amplifier. The input signal and noise is shown to the left while the corresponding output is shown to the right. The amplifier gain is 20 dB and an extra 10 dB of internal noise is added to the output, thus increasing the noise level more than the signal level. (This figure was inspired by [13, fig. 1-2].)

temperature $T_0 = 290$ K. Mathematically this definition is given by

$$F = \begin{cases} \frac{SNR_{in}}{SNR_{out}} = \frac{P_{s.in}/P_{n.in}}{P_{s.out}/P_{n.out}} & (4.6a) \\ P_{n.in} = kT_0B & (4.6b) \end{cases}$$

where $P_{s.in}$ (W) and $P_{n.in}$ (W) are the *available signal and noise powers respectively, at the output terminals of the signal source*. Correspondingly, $P_{s.out}$ (W) and $P_{n.out}$ (W) are the *available signal and noise powers respectively, at the output terminals of the two-port*. See fig. 4.3!

Note that the *available power* is defined [69, pg. 986] as the amount of power which would be transferred from a specified source, with a fixed source impedance, to a *complex conjugate matched*⁴ load, that is a condition of maximum power transfer. Thus $P_{s.in}$ and $P_{n.in}$ are, by this *definition*, independent of a potential impedance mismatch between the output of the signal source and the input of the two-port network. Analogous, $P_{s.out}$ and $P_{n.out}$ are, by this same *definition*, independent of a potential impedance mismatch between the output of the two-port and that which follows it. *The two latter do however depend on the degree of mismatch between the signal*

⁴ In case of a purely resistive (real) source impedance such as $Z_0 = 50 \Omega$, this equates to a reflection-less impedance match.

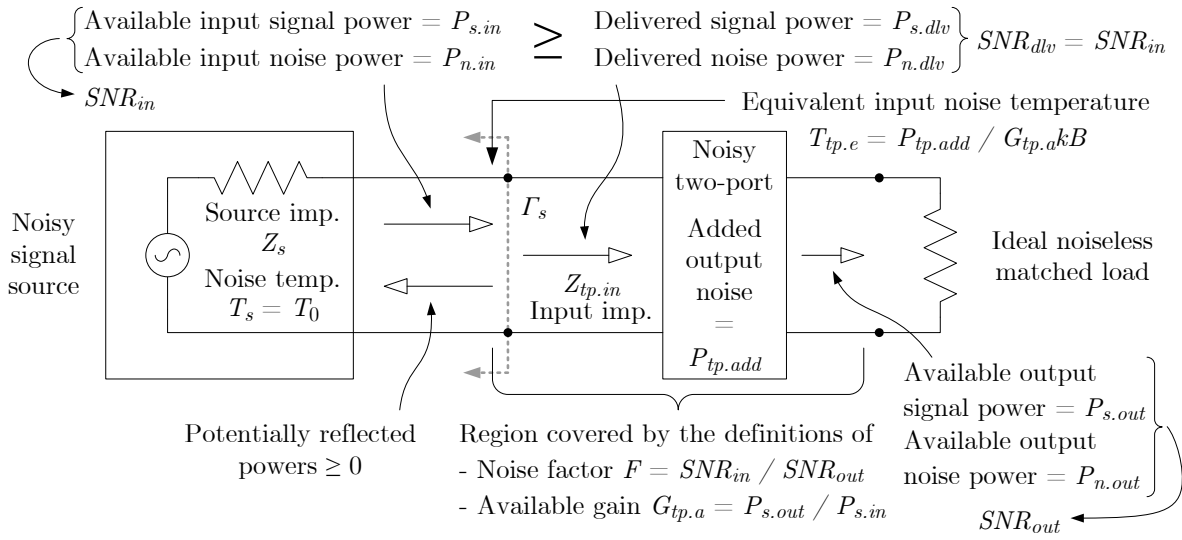


Figure 4.3 The noise factor F , the available gain $G_{tp,a}$ and the equivalent input noise temperature $T_{tp,e}$ of a two-port. The potential source impedance mismatch, symbolized by the dotted grey line marked by the reflection coefficient Γ_s , is accounted for in the noise factor definition.

source and the two-port, since their magnitudes depend on the amount of delivered signal and noise powers, that is on $P_{s.dlv}$ and $P_{n.dlv}$. From the definition of mismatch loss, these can be expressed as

$$P_{s.dlv} = (1 - |\Gamma_s|^2) P_{s.in} \tag{4.7a}$$

$$P_{n.dlv} = (1 - |\Gamma_s|^2) P_{n.in} \tag{4.7b}$$

where Γ_s is the reflection coefficient of the source impedance Z_s relative to the input impedance $Z_{tp.in}$ of the two-port. See fig. 4.3! From the above we draw the conclusion that due to the use of available powers in its definition, the noise factor of a two-port depends on the degree of source mismatch at the input terminals.

In his 1944 paper [53, pg. 419], Friis had the following comments regarding his choice of using available powers for the noise factor definition:

The input and output impedances of the [two-port] network may have reactive components and they may be matched or mismatched to the generator and the output circuit, respectively.

[...]

It is the presence of such mismatch conditions in amplifier input circuits that makes it desirable to use the term available power in this paper.

That is, Friis' choice of using available powers in the noise factor definition was an intentional one, so as to take source impedance mismatch at the input terminals of the two-port into account.

We now define the *available (power) gain* of the two-port as [69, pg. 995]

$$G_{tp.a} = \frac{P_{s.out}}{P_{s.in}} \quad (4.8)$$

Since $P_{s.out}$ depends on the source mismatch, we conclude that *the available gain of the two-port, by its definition, also depends on the degree of source mismatch at the input terminals*. Regarding this definition, Friis had the following comment [53, pg. 420]:

This is an unusual definition of gain since the gain of an amplifier is generally defined as the ratio of its output and input powers. This new definition is introduced here for the same reason that made it desirable to use the term available power. Note that while the gain is independent of the impedance which the output circuit presents to the [two-port] network, it does depend on the impedance of the [source] signal generator.

Thus in analogy with the noise factor definition, the definition of available gain also takes the source impedance mismatch at the input terminals into account, due to its use of available powers. For more on this and other gain definitions please refer to Pozar [92, ch. 6.2], Agilent Technologies AN57–1 [13, ch. 4] and the definitions of terms of the IRE Standards Committee [69].

So far we have concluded that both the noise factor and the available gain of a two-port, due to the use of available powers in their definitions, depend on the degree of source mismatch at the input terminals. Thus, *in specifying the available gain and the noise factor of a two-port, one also has to specify the accompanying source impedance to which its input must be connected, for these values to have any meaning* [69, pg. 1000].⁵ In other words, *connecting a two-port to a source impedance other than that used during its characterization will change its noise factor and available gain*, due to the use of available powers in their definitions. This is a consequence of a change in the source impedance mismatch at the input, resulting in a changed degradation of the SNR between the input and output, in accordance with eq. (4.6a).

Notice however, that the SNRs are the same at either immediate side of the Γ_s boundary in fig. 4.3, since only a mismatch loss and no dissipative (noisy) loss is introduced at this boundary. That is, both the input signal and input noise powers are equally attenuated due to the mismatch loss and

⁵ Though *not* part of the noise factor definition, the standard $Z_0 = 50 \Omega$ impedance is implied in most cases when specifying the noise factor of a device.

no new noise is added. This is given mathematically by inserting eqs. (4.7a) and (4.7b) into the expression of the delivered SNR as

$$SNR_{dlv} = \frac{P_{s.dlv}}{P_{n.dlv}} = \frac{(1 - |\Gamma_s|^2)P_{s.in}}{(1 - |\Gamma_s|^2)P_{n.in}} = \frac{P_{s.in}}{P_{n.in}} = SNR_{in} \quad (4.9)$$

In contrast to the source mismatch at the input of the two-port, the potential mismatch at the *output* has no relevance for the presented *definitions*, as was explained previously in this section.⁶ For simplicity, so as to facilitate understanding, the output of the two-port in fig. 4.3 is therefore assumed purely resistive and connected to a matched load.

Moving along in the thought process, we see that from the definition of available gain in eq. (4.8), the *output signal power* is given by

$$P_{s.out} = G_{tp.a}P_{s.in} \quad (4.10)$$

Since the two-port is a linear device the available gain of the noise is the same as that of the signal. We thus get the following expression for the *output noise power*

$$P_{n.out} = G_{tp.a}P_{n.in} + P_{tp.add} \quad (4.11)$$

where the first term on the right-hand side is the output noise, due to the amplified input noise. Furthermore $P_{tp.add}$ (W) is the *internally added two-port noise*, referenced to the *output* terminals of the two-port. See fig. 4.3!

Inserting eqs. (4.10) and (4.11) into eq. (4.6a) we get the following expression for the degradation of the SNR

$$\frac{SNR_{in}}{SNR_{out}} = \frac{G_{tp.a}P_{n.in} + P_{tp.add}}{G_{tp.a}P_{n.in}} \quad (4.12)$$

It is evident here, as was also pointed out in the Friis noise factor definition on pages 38 and 39, that the degradation of the SNR due to the two-port is a function of the available source noise power $P_{n.in}$. See also eq. (4.6a)! By this definition, *the degradation of the SNR by a two-port is only equal to its noise factor when the source noise temperature at its input is equal to $T_0 = 290$ K.*⁷ See eq. (4.6b)! This proposal by Friis was later adopted by the **Institute of Radio Engineers (IRE)**, a predecessor to the **IEEE**, as the standard reference

⁶ The output match *is* relevant for noise factor measurements however, as we shall see in section 8.1.

⁷ This is a fortunate definition, since *terrestrial antennas* used at microwave frequencies have an antenna temperature close to 290 K, due to its surroundings. The same is true for *satellite borne antennas* pointed towards Earth. In these cases a change in receiver noise factor by some amount, will result in about the same amount of change in the SNR at the receiver output terminals. (A lower antenna temperature would result in an increased change in the SNR, for the same change in receiver noise factor. See appendix A!)

noise temperature for the noise factor definition [69, pg. 1000], which is thus implied. By utilizing this in eq. (4.12), the degradation of the SNR is now called the *noise factor*, given by

$$F = \frac{\overbrace{G_{tp.a}kT_0B + P_{tp.add}}^{\text{Total output noise due to input noise and added noise}}}{\underbrace{G_{tp.a}kT_0B}_{\text{Output noise due to input noise}}} \quad (4.13)$$

Studying eq. (4.13), we notice that the noise factor of a two-port can also be expressed as *the ratio of the total available noise power at the output of a two-port, to that portion of this power which is due to the available input noise power at the standard noise temperature $T_0 = 290$ K*. This is essentially the IEEE definition of the noise factor [69, pg. 1000].

Rewriting eq. (4.13) we can get

$$F = 1 + \frac{P_{tp.add}/G_{tp.a}}{kT_0B} \quad (4.14)$$

where $P_{tp.add}/G_{tp.a}$ can be interpreted as the added noise power of the two-port, referenced to its input terminals.⁸ This so-called *equivalent input noise power* (W) of the two-port is thus given by

$$P_{tp.e} = \frac{P_{tp.add}}{G_{tp.a}} \quad (4.15)$$

Expressing this noise power in terms of a noise temperature we get

$$P_{tp.e} = kT_{tp.e}B \quad (4.16)$$

where $T_{tp.e}$ (K) is the *equivalent (or effective) input noise temperature* of the two-port. It is defined as *the thermodynamic temperature of a noisy resistor, connected to the input of a noiseless two-port element which gives the same output noise power as the noisy but otherwise equivalent two-port element, with an ideal noiseless source at its input*. See figs. 4.3 and 4.4 as well as the literature [70, pg. 435]! The equivalent input noise temperature is thus a measure of the noise generated by the internal components of the two-port, referenced to its input terminals.⁸ This means that *the true nature of the two-port noise is no longer relevant, since it is now given as the equivalent thermodynamic temperature of a noisy input resistor*.

Since $G_{tp.a}$ by definition depends on the degree of source mismatch, so does $P_{tp.e}$. Consequently, *the equivalent input noise temperature $T_{tp.e}$ of the two-port also depends on the degree of source mismatch at its input terminals*.

⁸ Including the source mismatch loss, since $G_{tp.a}$ is defined using available powers.

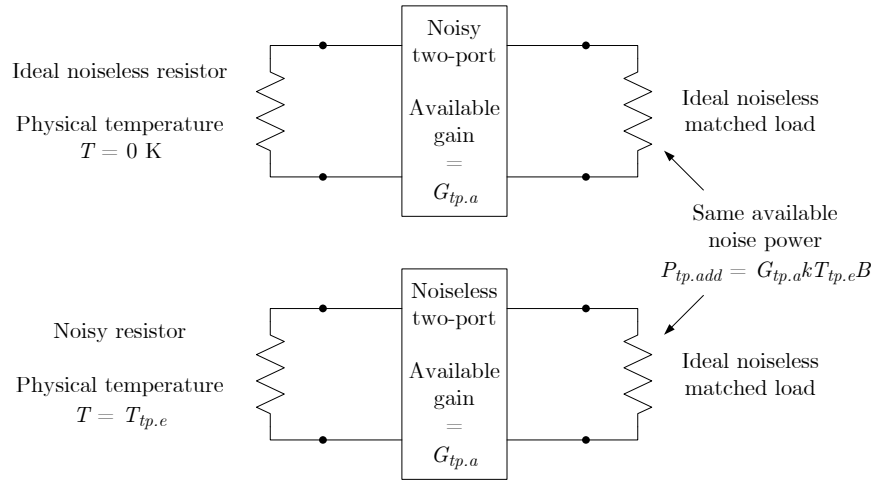


Figure 4.4 The definition of the equivalent input noise temperature $T_{tp,e}$ of a two-port. The available gain $G_{tp,a}$ accounts for a potential source impedance mismatch at the input.

Combining eqs. (4.15) and (4.16), rearranging to get $P_{tp,add}$, inserting this into eq. (4.13) and cancelling, the noise factor is also given by

$$F = \frac{T_0 + T_{tp,e}}{T_0} = 1 + \frac{T_{tp,e}}{T_0} \tag{4.17}$$

Solving for the equivalent input noise temperature we instead get

$$T_{tp,e} = (F - 1)T_0 \tag{4.18}$$

Notice that neither bandwidth nor signal power are part of eqs. (4.17) and (4.18)! Thus only the equivalent input noise temperature of the two-port has to be known, which implies knowing the accompanying source impedance,⁵ when calculating the noise factor. It is then referenced to the standard noise temperature $T_0 = 290 \text{ K}$. This highlights an advantage of using the concept of noise temperature, instead of noise factor, for characterizing a two-port. It eliminates the need for specifying the reference source noise temperature T_0 , since it is independent of this quantity. It is thus a more concise representation than the noise factor. Another advantage is in regards to the characterization of one-ports, where an analogous concept of noise factor does not exist.

The *noise figure* is finally given by the common (base 10) logarithm of the noise factor as

$$NF = 10 \log F \tag{dB} \tag{4.19}$$

Historically though, the *noise figure* was synonymous with what we today call the noise factor. Both are thus often used interchangeably even today.

4.2.2 Minimum noise factor versus maximum gain

As we shall see in more detail in section 4.4, it is desirable to have an LNA with a minimum noise factor at the same time as having a maximum amount of available gain. This would give the lowest overall system noise factor, which is of utmost importance in an EME system. It is therefore of interest to examine the prerequisites for these circumstances a bit closer. We will do this by pragmatically and in a simplified manner analyse the definitions and equations presented in section 4.2.1, mainly in regard to F and $G_{tp.a}$ for a varying source mismatch Γ_s . Unaffected variables such as the bandwidth B and the available input signal and noise powers, $P_{s.in}$ and $P_{n.in}$ respectively, are assumed constant. At first, to facilitate understanding, we temporarily ignore the influence of Γ_s on the internally added two-port noise $P_{tp.add}$, which is thus also assumed constant.

We can see from eq. (4.14) that the noise factor F , and thus the equivalent input noise temperature $T_{tp.e}$, is at its minimum when the available gain $G_{tp.a}$ is at its maximum. Furthermore, from eq. (4.8), we see that $G_{tp.a}$ is at its maximum when the available output signal power $P_{s.out}$ is at its maximum as well. This, in turn, occurs when the delivered signal power $P_{s.dlv}$ is at its maximum, which is the case when the two-port is conjugate matched to the signal source. In case of a purely resistive source impedance, which is usually assumed, the conjugate match equates to a reflection-less impedance match where the reflection coefficient $\Gamma_s = 0$. See eq. (4.7a) and fig. 4.3! A purely resistive source impedance will be assumed for the rest of this section, to facilitate understanding.

Thus, according to this simplified reasoning, a minimum noise factor and maximum available gain occur, and coincide, when there is a perfect impedance match between the signal source and the two-port. *In practice however, $P_{tp.add}$ varies as a function of Γ_s and consequently does not necessarily have to be at its minimum when $\Gamma_s = 0$, that is during a perfect source match. Since maximum available gain still occurs during a perfect source match however, the minimum noise factor does not have to coincide with the maximum available gain.* Some optimum amount of source impedance mismatch ($\Gamma_{s.opt}$) at the input is thus needed, in order to achieve a minimum noise factor. In these cases the available gain will be lower than its maximum possible value, which still occurs during perfect source match, that is when $\Gamma_s = 0 \neq \Gamma_{s.opt}$. Thus as so usually is the case in engineering, there is a conflict between desired goals, calling for compromise!

The reason for the above discrepancy between theory and practice lies in simplified assumptions regarding the model of the internally added noise power $P_{tp.add}$, used in the noise factor definition. This model assumes that all internal noise sources of the two-port are *uncorrelated*, that is they do not depend on each other, and can be added up linearly and modelled as

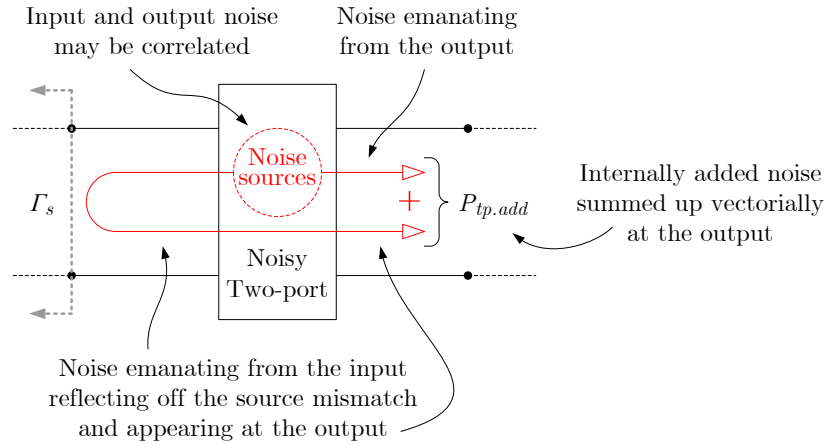


Figure 4.5 The change in added output noise $P_{tp.add}$ as a function of source mismatch Γ_s . If the noise emanating from the input and output are correlated, their vectorial sum at the output may increase or even decrease $P_{tp.add}$ and thus the noise factor. A noise factor minimum occurs when $\Gamma_s = \Gamma_{s.opt}$, while maximum gain occurs when $\Gamma_s = 0 \neq \Gamma_{s.opt}$.

one noise source. Furthermore, the model erroneously assumes that these noise sources only emanate noise at the output of the two-port and not at its input, towards the source.⁹

For active devices such as LNAs the various internal noise sources correlate to some degree and can thus not be added up linearly, but must instead be added vectorially. Therefore, noise emanating from the *input* of such a device will reflect off the source mismatch Γ_s and re-enter into the input, where it will interfere constructively or destructively to either increase or decrease the amount of noise emanating from the *output* of the device. See fig. 4.5!

In other words, *although the available output signal $P_{s.out}$ is reduced due to the impedance mismatch at the input, the available output noise $P_{n.out}$ is reduced proportionally more, thus lowering the noise factor of the device since the degradation in the SNR will now be smaller and vice versa.* Friis mentioned this in his 1944 paper [53, pg. 419], saying:

In amplifier input circuits a mismatch condition may be beneficial due to the fact that it may decrease the output noise more than the output signal.

As a consequence of the above, $P_{tp.add}$ varies with the magnitude and phase of Γ_s in such a way that it will likely not be at its minimum when there

⁹ Even though the output noise power is *referenced* to the input, by dividing with the available gain, its *origin* is still at the output of the two-port in this model.

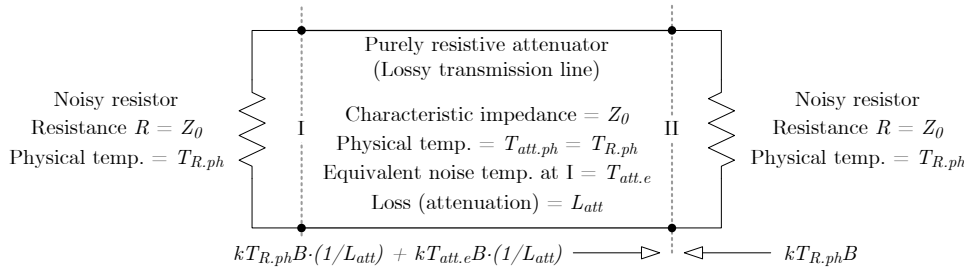


Figure 4.6 A perfectly *matched* attenuator in the form of a lossy transmission line. All parts are in *thermal equilibrium*, that is the net power flow at any point is zero. This fact is used in the derivation of the equivalent input noise temperature $T_{att.e}$ of the attenuator.

is a perfect match between the signal source and the two-port input, that is when $\Gamma_s = 0$ and the available gain is at its maximum. Naturally, this phenomenon is frequency dependent, adding to complexity.

How the noise factor of a device changes in this way, as a function of the source impedance mismatch, is described by its so called *noise parameters*. For more on this subject please refer to Collier and Skinner [43, ch. 8.7], Pozar [92, ch. 6.5] and the ‘Accuracy Limitations’ chapter in Agilent Technologies AN1408–20 [12, pg. 9–18]. Regarding gain considerations please refer to Pozar [92, ch. 6.4].

4.3 Equivalent input noise temperature of an attenuator

A two-port element containing only passive components is called an *attenuator*. To derive its equivalent input noise temperature, consider a set-up with a purely resistive attenuator as shown in fig. 4.6!

Since the attenuator is in *thermal equilibrium* with *matched* resistors at either end, the net power flow at any point is zero, in accordance with the second law of thermodynamics. Thus, if we consider all contributions of power flowing into for example point II in fig. 4.6, the following equation can be set up:

$$\begin{aligned}
 \overbrace{kT_{R.ph}B \cdot (1/L_{att})}^{\text{Left resistor contribution}} + \overbrace{kT_{att.e}B \cdot (1/L_{att})}^{\text{Attenuator contribution}} &= \overbrace{kT_{R.ph}B}^{\text{Right resistor contribution}} \Rightarrow & (4.20) \\
 T_{R.ph} \cdot (1/L_{att}) + T_{att.e} \cdot (1/L_{att}) &= T_{R.ph}
 \end{aligned}$$

where k ($1.381 \cdot 10^{-23} \text{ J K}^{-1}$) is *Boltzmann’s constant*, $T_{R.ph}$ (K) is the *physical temperature* of the resistors, B (Hz) is the *bandwidth*, L_{att} is the *loss*

or attenuation (greater than unity) of the attenuator and $T_{att.e}$ (K) is the *equivalent input noise temperature* of the attenuator.

Solving eq. (4.20) for $T_{att.e}$ we get the following expression for the *equivalent input noise temperature* of the attenuator:

$$T_{att.e} = (L_{att} - 1)T_{R.ph} \quad (4.21a)$$

Taking into account the fact that the physical temperature $T_{att.ph}$ (K) of the attenuator is the same as those of the resistors, that is all components are in thermal equilibrium, results in $T_{att.ph} = T_{R.ph}$. Using this in eq. (4.21a) we get the following expression for the equivalent input noise temperature of the attenuator:

$$T_{att.e} = (L_{att} - 1)T_{att.ph} \quad (4.21b)$$

Inserting eq. (4.21b) into eq. (4.17) we get the *noise factor* of the attenuator as

$$F_{att} = 1 + (L_{att} - 1) \frac{T_{att.ph}}{T_0} \quad (4.22)$$

As a matter of curiosity, if $T_{att.ph} = T_0$ we have $F_{att} = L_{att}$, that is the noise factor equals the attenuation of the attenuator if the physical temperature of the attenuator is T_0 . Hence, if such an attenuator is connected to a noisy signal source (such as a terrestrial antenna) having a noise temperature T_0 , the degradation of the SNR due to the attenuator will equal its loss. Furthermore, if $L_{att} = 2$ (3 dB) we have $T_{att.e} = T_{att.ph}$, that is the equivalent input noise temperature of the attenuator equals its physical temperature if its loss is 3 dB.

In case the attenuator is *not* perfectly matched to its source at point I, the equivalent input noise temperature will be greater than given by eq. (4.21b) [92, ch. 3.6]. The reason for this being that noise emanating at point I is reflected off the source mismatch, re-enters the attenuator at point I and appears at point II, where it will add to the noise already destined there. Since this is a passive device, the internal noise contributions are *not* correlated and can thus be added linearly. Consequently, a minimum noise factor occurs when the attenuator is matched to its source impedance. Compare this to the reasoning in section 4.2.2 and also to fig. 4.5 with $T_{s.opt} = 0$!

4.4 Equivalent input noise temperature and gain of a cascaded system

Consider N cascaded, *matched* two-port elements, each having a gain G_j and an equivalent input noise temperature $T_{j,e}$ (K), where $j = 1, 2, \dots, N$, as in fig. 4.7!

Since the noise contributions from the various stages are uncorrelated, they can be added linearly. The total equivalent input noise temperature (K) of this system is thus given by

$$T_{tot,e} = T_{1,e} + \frac{T_{2,e}}{G_1} + \frac{T_{3,e}}{G_1 G_2} + \dots + \frac{T_{N,e}}{G_1 G_2 \dots G_{N-1}} \quad (4.23)$$

Naturally, this equation assumes that each noise temperature is associated with the same noise bandwidth B .

The corresponding total system noise factor is given by inserting eq. (4.23) into eq. (4.17) on page 44, resulting in the *cascade noise equation* given by

$$F_{tot} = F_1 + \frac{F_2 - 1}{G_1} + \frac{F_3 - 1}{G_1 G_2} + \dots + \frac{F_N - 1}{G_1 G_2 \dots G_{N-1}} \quad (4.24)$$

The total system gain is given by the products of the individual gains of each stage, that is

$$G_{tot} = G_1 G_2 \dots G_N \quad (4.25)$$

Equations (4.23) and (4.24) show the importance of the first stage having a low noise temperature as well as high gain, for the benefit of the noise performance of the entire system. Vice versa, they also show the detrimental effect on noise performance, when having resistive loss in front of the first active stage in a receiving system. Please refer also to appendix A for general graphs relating to this.

In case the prerequisite of impedance match between the stages is not fulfilled, a more rigorous analysis beyond the scope of this thesis is required. Suffice

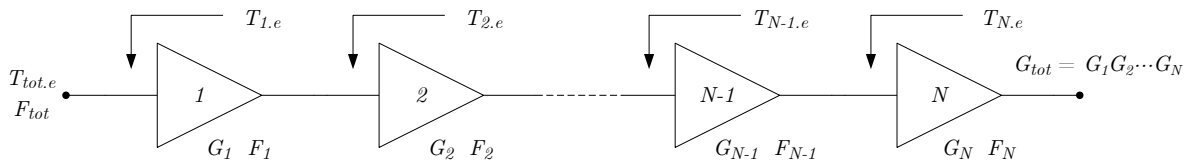


Figure 4.7 A cascaded two-port system with the gains, equivalent input noise temperatures and noise factors of the individual stages given. The total equivalent input noise temperature $T_{tot,e}$ and noise factor F_{tot} of the system, are given furthest to the left. The total gain G_{tot} is given to the right.

it to say that both the noise factor and the available gain of each individual stage may vary, depending on the source impedance being presented to it by the output of the preceding stage. See also section 4.2!

4.5 Noise temperature of an antenna

Noise in a receiving system also enters through the antenna, in which case it is often given as the so called *antenna (noise) temperature*. When dissipative (ohmic) losses in the antenna are negligible, the antenna noise temperature has nothing to do with the physical temperature of the antenna. Instead, it is wholly dependent on the noise received from its surroundings, such as that from the sky, atmosphere, ground, vegetation and so forth. We shall therefore introduce the concepts of *brightness distribution*, *flux density*, *spectral power*, *power* and *brightness temperature* of an object and see how these, combined with the properties of the antenna, influence the *antenna temperature*.

For those wishing to enter more deeply into this subject, Kraus [78, ch. 3] is highly recommended reading.

4.5.1 Brightness distribution

The *brightness* Φ is a fundamental quantity of radio astronomy, which measures the received power per unit area per unit bandwidth per unit solid angle, that is $\text{W m}^{-2} \text{Hz}^{-1} \text{sr}^{-1}$. Since different objects have different amounts of brightness, it is a function of direction in regard to a fixed location. We call this variation in brightness as a function of direction the *brightness distribution*, that is $\Phi = \Phi(\theta, \phi)$ where θ and ϕ are spherical angle coordinates (rad) in the sky coordinate frame.

4.5.2 Flux density

Integrating the above given brightness distribution $\Phi(\theta, \phi)$ over a solid angle $0 \leq \Omega \leq 4\pi$ (sr), gives the energy flow per unit area ($\text{W m}^{-2} \text{Hz}^{-1}$) or the *flux density* over this solid angle as

$$S = \iint_{\Omega} \Phi(\theta, \phi) \, d\Omega \quad (4.26)$$

where $d\Omega = \sin\theta \, d\theta \, d\phi$ is an infinitesimal solid angle on the sphere of integration.

The flux density S is often given in a quantity referred to as a *flux unit (FU)* or *Jansky (Jy)*, after the American physicist and radio engineer Karl Guthe

Jansky. In SI units $1 \text{ FU} = 1 \text{ Jy} = 10^{-26} \text{ W m}^{-2} \text{ Hz}^{-1}$. For strong radio sources, such as the Sun, the flux density is also given in *solar flux units (SFUs)* where $1 \text{ SFU} = 10\,000 \text{ FU} = 10^{-22} \text{ W m}^{-2} \text{ Hz}^{-1}$.

4.5.3 Flux density observed by an antenna

If an antenna is being used to observe the surroundings, we have to take into account the fact that antennas are not equally sensitive to every point in the sky. The brightness distribution in eq. (4.26) thus has to be ‘weighted’¹⁰ by the *normalized* antenna power pattern $P(\xi, \psi) = P(\theta - \theta_a, \phi - \phi_a)$. The resulting *observed flux density* over a solid angle Ω , as seen by an antenna, is thus given by

$$S_{obs}(\theta_a, \phi_a) = \iint_{\Omega} \Phi(\theta, \phi) P(\theta - \theta_a, \phi - \phi_a) d\Omega \quad (4.27)$$

where S_{obs} has the same dimension as the flux density S above, that is $\text{W m}^{-2} \text{ Hz}^{-1}$. In this equation the antenna and sky coordinate systems are furthermore displaced by the spherical displacement angles θ_a and ϕ_a (rad), that is the antenna boresight is pointing with an arbitrary (θ_a, ϕ_a) offset in the sky coordinate frame.

Assume now that $\theta_a = \phi_a = 0$ and that the antenna boresight is pointing straight at a source with brightness $\Phi(\theta, \phi)$. Assume also that the angular extension of this source is small compared to the antenna HPBW, that is the source solid angle $\Omega_s \ll \Omega_A$ of the antenna. The source can then be regarded as a *point source* and $P(\theta, \phi) \approx 1$ over its angular extension Ω_s . Equation (4.27) can then be simplified as

$$\begin{aligned} S_{obs} &= \iint_{\substack{\text{Sphere} \\ \Omega=4\pi}} \Phi(\theta, \phi) P(\theta, \phi) d\Omega \\ &= \iint_{0 \leq \Omega \leq \Omega_s} \Phi(\theta, \phi) \overbrace{P(\theta, \phi)}^{\approx 1} d\Omega + \iint_{\Omega_s < \Omega \leq 4\pi} \overbrace{\Phi(\theta, \phi)}^{=0} P(\theta, \phi) d\Omega \\ &\approx \iint_{0 \leq \Omega \leq \Omega_s} \Phi(\theta, \phi) d\Omega = S \end{aligned} \quad (4.28)$$

where eq. (4.26) has been used in the last step. *The observed flux density S_{obs} is thus equal to the true source flux density S , in the case of a point source.* In the general case above, where $\Phi(\theta, \phi)$ is non-uniform, S and hence S_{obs} will be equal to the *average* flux density of the source, averaged over its angular extension Ω_s .

¹⁰Equation (4.27) is essentially a convolution integral. The antenna is thus a filter, smoothing the spatial components of the brightness distribution. See Kraus [78, ch. 3-4, 6-9] and Campbell [40, ch. 8]!

4.5.4 Spectral power at the terminals of a lossless antenna

Assume that the antenna in section 4.5.3 has no dissipative (ohmic) losses, has an effective aperture area A_{em} (m^2) and is connected to a matched load. The power per unit bandwidth or *spectral power* (W Hz^{-1}) entering the load at the antenna terminals, due to a solid angle Ω , is then given by

$$w(\theta_a, \phi_a) = \frac{A_{em}}{2} \iint_{\Omega} \Phi(\theta, \phi) P(\theta - \theta_a, \phi - \phi_a) d\Omega \quad (4.29a)$$

Inserting eq. (4.27) into eq. (4.29a) yields

$$w(\theta_a, \phi_a) = \frac{A_{em} S_{obs}(\theta_a, \phi_a)}{2} \quad (4.29b)$$

where $\frac{1}{2}$ is due to the fact that a polarized antenna only receives half the power of an unpolarized signal, as is the case with noise.

4.5.5 Power at the terminals of a lossless antenna and the equivalent antenna temperature for a constant Φ

Suppose the antenna in section 4.5.4 is totally surrounded by an enclosure having a temperature distribution $T_b(\theta, \phi)$ (K). Furthermore, suppose this enclosure radiates as a *blackbody* on the inside, for the antenna to pick up. According to *Planck's radiation law* for blackbody radiation, the *brightness distribution* of this blackbody is given by

$$\Phi(\theta, \phi) = \frac{2hf^3}{c^2} \frac{1}{e^{hf/kT_b(\theta, \phi)} - 1} \quad (4.30)$$

In analogy with eq. (4.2) on page 36, the Rayleigh–Jeans approximation can be applied if $hf \ll kT_b$. Equation (4.30) then turns in to the *Rayleigh–Jeans radiation law* given by

$$\Phi(\theta, \phi) = \frac{2kT_b(\theta, \phi)}{\lambda^2} \quad (4.31)$$

where in the above two equations $\Phi(\theta, \phi)$ ($\text{W m}^{-2} \text{Hz}^{-1} \text{sr}^{-1}$) is the *brightness distribution*, h ($6.626 \cdot 10^{-34}$ J s) is *Planck's constant*, f (Hz) is the *frequency*, c ($2.998 \cdot 10^8$ m s $^{-1}$) is the *speed of light*, k ($1.381 \cdot 10^{-23}$ J K $^{-1}$) is *Boltzmann's constant*, λ (m) is the *wavelength*, T_b (K) is the *blackbody radiation temperature* or *brightness temperature* as a function of θ and ϕ which are *spherical coordinates* (rad).

Assume now that the brightness temperature $T_b(\theta, \phi)$ is equal to a constant temperature T_c (K) for every θ and ϕ . See fig. 4.8! From this follows

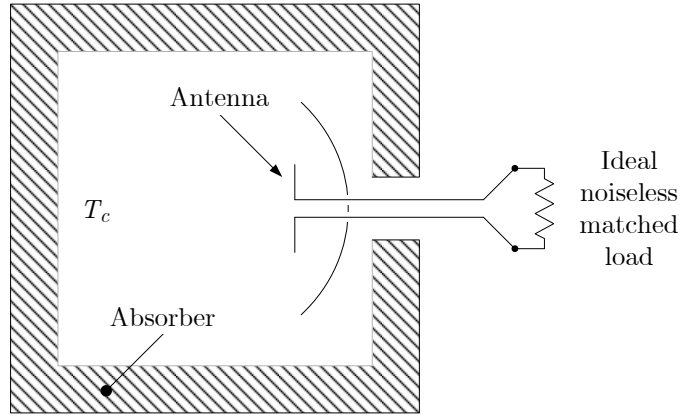


Figure 4.8 A matched, lossless antenna placed inside a blackbody enclosure of constant temperature T_c .

that the brightness distribution $\Phi(\theta, \phi)$ is also constant for every θ and ϕ . Equation (4.31) can then be rewritten as

$$\Phi(\theta, \phi) = \Phi_c = \frac{2kT_c}{\lambda^2} \quad (4.32)$$

Inserting eq. (4.32) into eq. (4.29a) gives the spectral power in a matched load at the antenna terminals as

$$w = \frac{kT_c A_{em}}{\lambda^2} \iint_{\substack{\text{Sphere} \\ \Omega=4\pi}} P(\theta - \theta_a, \phi - \phi_a) d\Omega \quad (4.33a)$$

where integration is done over a whole sphere due to the antenna being fully enclosed.

Substituting integration variables and inserting eq. (3.7a) on page 25 into eq. (4.33a) gives

$$w = \frac{kT_c A_{em}}{\lambda^2} \Omega_A \quad (4.33b)$$

Furthermore, inserting eq. (3.8) on page 25 into eq. (4.33b) yields

$$w = kT_c \quad (4.33c)$$

Multiplying the spectral power in eq. (4.33c) with the bandwidth B , one gets the noise power delivered to the matched load at the terminals of the lossless antenna as

$$P_n = kT_c B \quad (4.34)$$

Now, comparing eq. (4.34) to eq. (4.5) on page 36, one realizes that they are indeed the same if the temperature of the resistor equals the temperature T_c of the blackbody radiator, surrounding the antenna!

Thus, we come to the conclusion that *the noise power delivered to a matched load at the terminals of a lossless antenna, due to noise power picked up by the antenna from a surrounding blackbody radiator, can be modelled as the power delivered from a resistor at a temperature equal to that of the blackbody radiator*. This temperature is called the *antenna (noise) temperature* T_a (K) and has *nothing* to do with the physical temperature of a lossless antenna.

In the case above $T_a = T_c$, that is the temperature of the blackbody surrounding the antenna. Thus, we also come to another conclusion, namely that *the antenna can be seen as a remote temperature sensing device, measuring the equivalent blackbody temperature of its surroundings as observed by the antenna due to its normalized power pattern* $P(\xi, \psi) = P(\theta - \theta_a, \phi - \phi_a)$. The word ‘equivalent’ in the previous sentence means that, even if a radiating source is *not* a true blackbody radiator, it can always be modelled as one emitting the same amount of radiation as the true radiator. Thus while the true radiator has a physical temperature T_{ph} (K), its blackbody equivalent has a temperature T_b , called its *brightness temperature* as mentioned earlier.

4.5.6 Power at the terminals of a lossless antenna and the equivalent antenna temperature for a non-constant Φ

In case the antenna is *not* surrounded by a constant brightness distribution, that is it is not observing a constant brightness temperature as is the case in section 4.5.5, the brightness temperature distribution has to be ‘weighted’¹¹ by the normalized antenna power pattern. This more general situation results in a number of equivalent *observed brightness temperatures* for every direction about the antenna, the sum (or integral) of which gives the total antenna temperature.

Inserting eq. (4.31) into eq. (4.29a), we get the spectral power in a matched load at the antenna terminals as

$$w(\theta_a, \phi_a) = \frac{kA_{em}}{\lambda^2} \iint_{\substack{\text{Sphere} \\ \Omega=4\pi}} T_b(\theta, \phi) P(\theta - \theta_a, \phi - \phi_a) d\Omega \quad (4.35a)$$

¹¹Equation (4.36) is essentially a convolution integral. The antenna is thus a filter, smoothing the spatial components of the brightness temperature. See Kraus [78, ch. 3-4, 6-9] and Campbell [40, ch. 8]! (This is analogous to footnote 10 on page 51.)

Notice how setting $T_b(\theta, \phi) = T_c$ in eq. (4.35a) yields eq. (4.33a).

Analogous to eq. (4.33c), inserting eq. (3.8) on page 25 into eq. (4.35a) gives

$$w(\theta_a, \phi_a) = \frac{k}{\Omega_A} \iint_{\substack{\text{Sphere} \\ \Omega=4\pi}} T_b(\theta, \phi) P(\theta - \theta_a, \phi - \phi_a) d\Omega = kT_a(\theta_a, \phi_a) \quad (4.35b)$$

where the total antenna temperature $T_a(\theta_a, \phi_a)$ is thus given by

$$T_a(\theta_a, \phi_a) = \frac{1}{\Omega_A} \iint_{\substack{\text{Sphere} \\ \Omega=4\pi}} T_b(\theta, \phi) P(\theta - \theta_a, \phi - \phi_a) d\Omega \quad (4.36)$$

Analogous to eq. (4.34), multiplying the spectral power in eq. (4.35b) with the bandwidth B , one gets the total noise power delivered to the matched load at the antenna terminals as

$$P_n(\theta_a, \phi_a) = kT_a(\theta_a, \phi_a)B \quad (4.37)$$

As can be seen from the equations above, *the antenna temperature changes, and hence also the noise power at the antenna connector, as the antenna moves in regard to its surroundings.*

Analogous to the reasoning in section 4.5.3 regarding eq. (4.28), eq. (4.36) can also be simplified in the case of a point source. Using the same assumptions as in section 4.5.3, we then get

$$\begin{aligned} T_a &= \frac{1}{\Omega_A} \iint_{\substack{\text{Sphere} \\ \Omega=4\pi}} T_b(\theta, \phi) P(\theta, \phi) d\Omega \\ &= \frac{1}{\Omega_A} \left[\iint_{0 \leq \Omega \leq \Omega_s} T_b(\theta, \phi) \overbrace{P(\theta, \phi)}^{\approx 1} d\Omega + \iint_{\Omega_s < \Omega \leq 4\pi} \overbrace{T_b(\theta, \phi) P(\theta, \phi)}^{=0} d\Omega \right] \\ &\approx \frac{1}{\Omega_A} \iint_{0 \leq \Omega \leq \Omega_s} T_b(\theta, \phi) d\Omega = \frac{\Omega_s}{\Omega_A} \cdot T_{b.avg} \end{aligned} \quad (4.38)$$

where $T_{b.avg}$ (K) is the average value of $T_b(\theta, \phi)$, averaged over its angular extension Ω_s . *In the case of a point source, the antenna temperature T_a is thus equal to the fraction of the angular extension of the source to the beam solid angle of the antenna, times the average source brightness temperature $T_{b.avg}$.*

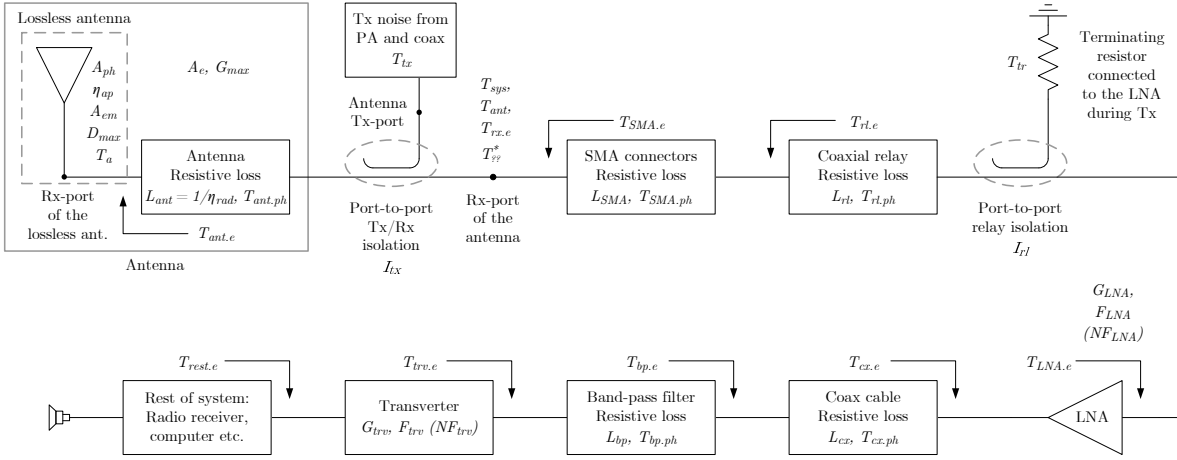


Figure 4.9 A typical receiving system with various system parameters given. A loss is denoted by L , a gain by G and a temperature by T (K). A temperature ending with ‘.ph’ denotes a physical temperature (K) while ‘.e’ denotes an equivalent input noise temperature (K). Noise factors are given by F and noise figures by NF .

4.6 Total system noise temperature at the terminals of an antenna

A receiving system consists of the various building blocks described in the sections above. An example of such a system is shown in fig. 4.9 where various system parameters and associated units are also given, some of which have already been introduced in previous sections.

The so called *system noise temperature* is a measure of the total sum of the noise being generated internally in the receiving system and the noise added by the antenna, from its surroundings and internal losses. In determining this parameter, one must begin with choosing a suitable reference point in the receiving system. Usual choices of reference points are at the input of the receiver (LNA) or at the terminals of the antenna, that is after the ohmic losses of the antenna. For determining the system noise temperature of the system in fig. 4.9, the latter of these reference points is chosen. Hence, the total system noise temperature T_{sys} (K) can now, dropping the ‘ (θ_a, ϕ_a) ’ notation for antenna direction, be expressed as

$$T_{sys} = T_{rx,e} + T_{ant} \tag{4.39}$$

where T_{ant} (K) is the *antenna temperature* and $T_{rx,e}$ (K) is the *equivalent input noise temperature of the entire receiver system, referenced to the terminals of the antenna*. Thus, $T_{rx,e}$ includes all the noise being generated between the antenna connector to and including the transceiver, a part of ‘rest of system’ as shown in fig. 4.9. Making this antenna versus receiver distinction within

T_{sys} provides useful information on system performance, should improvements be of interest.

To determine $T_{rx.e}$, the equivalent input noise temperatures of each individual component must first be calculated, using eqs. (4.18) and (4.21b) on pages 44 and 48. This requires having knowledge about some of the following for each component: loss, gain, isolation, physical temperature, noise temperature and NF. Second, the equivalent input noise temperatures of these components must be referenced to the output of the antenna. Last and third, these temperatures must be added according to eq. (4.23) on page 49 so as to yield $T_{rx.e}$, which is thus given by

$$T_{rx.e} = T_{SMA.e} + T_{rl.e}^* + T_{tr}^* + T_{LNA.e}^* + T_{cx.e}^* + T_{bp.e}^* + T_{trv.e}^* + T_{rest.e}^* \quad (4.40)$$

The terms on the right side of eq. (4.40) are the equivalent temperatures (K) of the individual components, as referenced to the output of the antenna. These are in turn given by

$$T_{SMA.e} = (L_{SMA} - 1)T_{SMA.ph} \quad (4.41a)$$

$$T_{rl.e}^* = \overbrace{(L_{rl} - 1)T_{rl.ph}}^{T_{rl.e}} \cdot L_{SMA} \quad (4.41b)$$

$$T_{tr}^* = T_{tr} \cdot \frac{L_{SMA}L_{rl}}{I_{rl}} \quad (4.41c)$$

$$T_{LNA.e}^* = \overbrace{(F_{LNA} - 1)T_0}^{T_{LNA.e}} \cdot L_{SMA}L_{rl} \quad (4.41d)$$

$$T_{cx.e}^* = \overbrace{(L_{cx} - 1)T_{cx.ph}}^{T_{cx.e}} \cdot \frac{L_{SMA}L_{rl}}{G_{LNA}} \quad (4.41e)$$

$$T_{bp.e}^* = \overbrace{(L_{bp} - 1)T_{bp.ph}}^{T_{bp.e}} \cdot \frac{L_{SMA}L_{rl}L_{cx}}{G_{LNA}} \quad (4.41f)$$

$$T_{trv.e}^* = \overbrace{(F_{trv} - 1)T_0}^{T_{trv.e}} \cdot \frac{L_{SMA}L_{rl}L_{cx}L_{bp}}{G_{LNA}} \quad (4.41g)$$

$$T_{rest.e}^* = T_{rest.e} \cdot \frac{L_{SMA}L_{rl}L_{cx}L_{bp}}{G_{LNA}G_{trv}} \quad (4.41h)$$

Thus an asterisk (*) in the exponent of an equivalent temperature, as given to the left in eq. (4.41), denotes a shift in its reference point: From the input of the component in question, to the output of the antenna. Please refer to fig. 4.9 for parameter definitions and associated units!

It should be noted that if the port-to-port isolation of the coaxial protection relay is poor, extra noise from the terminating resistor, less the isolation,

is added to the LNA input during reception. This is given by T_{tr}^* (K) in eqs. (4.40) and (4.41c).

T_{ant} in eq. (4.39) is the *antenna temperature* given by

$$T_{ant} = T_a^* + T_{ant.e}^* + T_{tx}^* \quad (4.42)$$

Referenced to the terminals of the antenna, T_a^* (K) is the antenna temperature of the lossless antenna (determined by its surroundings), $T_{ant.e}^*$ (K) is the equivalent temperature of the ohmic losses of the antenna (determined by its physical temperature) and T_{tx}^* (K) is the noise at the Tx-port of the dual polarization feed horn during reception. Please refer to fig. 4.9.

T_{tx}^* has its origin in the coax and PA connected to the Tx-port. This noise will radiate from the Tx-probe in the feed horn and reverse polarization when reflected in the parabolic dish. Some of this noise will therefore end up at the Rx-port, inevitably reducing the inherent port-to-port isolation of the feed horn itself. This effect might seem insignificant, but considering that the output noise from a quiescent (biased) PA can reach hundreds or even thousands of kelvins, it is enough to increase the antenna noise temperature at the Rx-port by several kelvins! One should therefore turn the PA bias off during Rx or eliminate the PA noise through other means. Unfortunately, noise from the coax, as well as from terminating resistors in possible PA-hybrid combiners, will still be present at the Tx-port. This will also increase the noise temperature at the Rx-port by a few kelvins, as we shall see in section 8.10. Please refer to the literature for a more detailed discussion regarding the effects of dish reflection on the port-to-port isolation of dual polarization feed horns [91].

The starred temperatures in eq. (4.42) are given by the following three equations, whose parameter definitions and associated units are given in fig. 4.9:

$$T_a^* = \frac{T_a}{L_{ant}} = \eta_{rad} T_a \quad (4.43)$$

$$T_{ant.e}^* = \frac{T_{ant.e}}{L_{ant}} = \frac{(L_{ant} - 1)T_{ant.ph}}{L_{ant}} = (1 - \eta_{rad})T_{ant.ph} \quad (4.44)$$

$$T_{tx}^* = \frac{T_{tx}}{I_{tx}} \quad (4.45)$$

where $T_{ant.e}$ (K) in eq. (4.44) has been substituted using eq. (4.21b) on page 48. In eqs. (4.41), (4.43) and (4.44) the fact that gain and loss are each others inverses has also been used, since denoting an attenuator by its loss makes more sense than giving it a gain of less than unity. Furthermore, in

eqs. (4.43) and (4.44) the radiation efficiency η_{rad} has been used, the inverse of which equals the resistive loss L_{ant} of the antenna.¹² That is

$$L_{ant} = \frac{1}{\eta_{rad}} \quad (4.46)$$

Inserting eqs. (4.43) to (4.45) into eq. (4.42) we get the following expression for the antenna temperature:

$$T_{ant} = \eta_{rad}T_a + (1 - \eta_{rad})T_{ant.ph} + \frac{T_{tx}}{I_{tx}} \quad (4.47a)$$

In case T_{tx}^* (K) can be neglected or does not even exist, as in the case of a single port feed horn without a dedicated Tx-port, the last term is omitted leaving only:

$$T_{ant} = \eta_{rad}T_a + (1 - \eta_{rad})T_{ant.ph} \quad (4.47b)$$

Last but not least, it should be stressed once again that $T_{ant.ph}$ (K) and $T_{ant.e}$ is the physical and equivalent temperature respectively, of the combined *resistive losses* of the antenna. They must *not* be mistaken for the lossless antenna temperature T_a , which is *wholly and solely determined by the surroundings of the antenna*, as explained in section 4.5. Together with T_{tx} (K) they form the antenna temperature, as given by eq. (4.47a).

Notice how $T_{ant.e}^* \approx 0$ K and thus how $T_{ant} \approx T_a^* \approx T_a$ when $\eta_{rad} \approx 1$, in case T_{tx}^* can be omitted. See eqs. (4.43), (4.44) and (4.47b)!

4.7 Determining noise temperatures using the Y-factor method

Determining the noise temperature of a device can be done using various methods, such as for example the *Y-factor method*, *cold source (direct noise) method* or some form of *signal generator method* [12, 13]. For measuring low noise devices, the Y-factor method is the most common in use and will thus be presented here.

The basic principle of this method is to compare the unknown noise power, generated by a *device under test (DUT)*, to the known noise powers generated by two reference devices. From this comparison and the so called *Y-factor*, the unknown noise power of the DUT can then be determined [44, ch. 5.6]. A measurement set-up, such as the one presented in fig. 4.10, is employed by the Y-factor method.

¹²According to the IEEE standard definitions of terms for antennas [66, ch. 2.308], the radiation efficiency is defined as ‘*The ratio of the total power radiated by an antenna to the net power accepted by the antenna from the connected transmitter*’. Analysing this definition, one realizes that η_{rad} equals the inverse of L_{ant} .

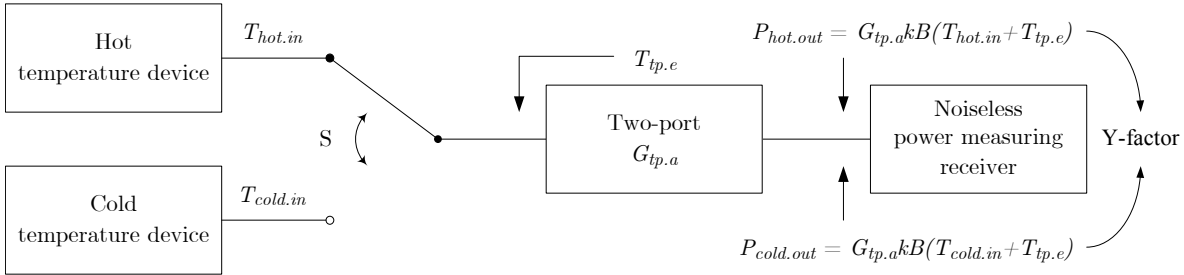


Figure 4.10 A principle set-up of a Y-factor method measurement. The switch S is used for switching between the *hot* and *cold* devices to the left, giving different readouts at the *PMR* to the right. The *two-port* can consist of various system parts, such as those given in fig. 4.9. The *DUT* usually consists of the two-port, but it can also be either of the one-port devices to the left.

To facilitate understanding, a perfect impedance match is assumed between the output of the two-port and the *power measuring receiver (PMR)*. Moreover, the two-port is assumed to be presented with an identical source impedance, regardless of which temperature device is connected through the switch S . This ensures that the *NF* and available gain of the two-port remain constant throughout the measurement. See section 4.2!

A theoretical framework where the *PMR* is assumed noiseless will now be presented.¹³ This will be followed by a section describing the more realistic case, where instrument noise needs to be accounted for.

4.7.1 Assuming a noiseless instrument

Assume that the noise power, measured by the *PMR* to the right in fig. 4.10, equals $P_{hot.out}$ (W) and $P_{cold.out}$ (W) when the switch S is positioned at the hot and cold temperature device respectively. This is given mathematically by

$$P_{hot.out} = G_{tp.a} k B (T_{hot.in} + T_{tp.e}) \quad (4.48a)$$

$$P_{cold.out} = G_{tp.a} k B (T_{cold.in} + T_{tp.e}) \quad (4.48b)$$

where k is *Boltzmann's constant* ($1.381 \cdot 10^{-23} \text{ J K}^{-1}$), B is the measurement *bandwidth* (Hz) (which must be equal to or smaller than the bandwidth of the *DUT*) and $T_{hot.in}$ (K) and $T_{cold.in}$ (K) are the equivalent noise temperatures of the hot and cold temperature devices in fig. 4.10. Furthermore, $G_{tp.a}$ is the *available gain* of the two-port, which is given by subtracting eq. (4.48b)

¹³'Noiseless' can in this context be thought of as if we disregard the noise being generated in the *PMR*, that is we only consider the noise being delivered *to* the *PMR* since this is what we are interested in.

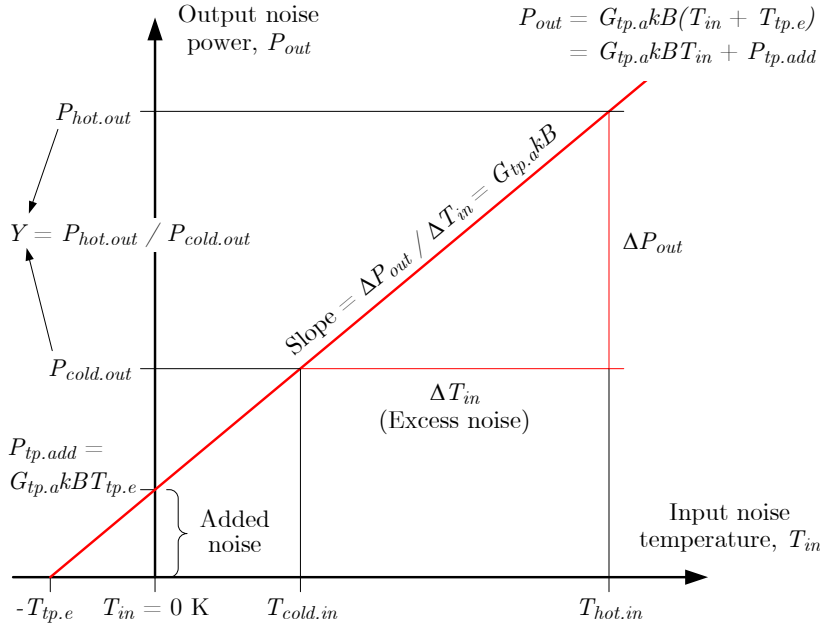


Figure 4.11 A Graphical representation of the mathematics behind the Y-factor method, showing the output noise power from the two-port as a function of the input noise temperature. Both axes are in linear quantities.

from eq. (4.48a) and solving for $G_{tp.a}$. This yields the following

$$G_{tp.a} = \frac{P_{hot.out} - P_{cold.out}}{kB(T_{hot.in} - T_{cold.in})} = \frac{\Delta P_{out}}{kB\Delta T_{in}} \quad (4.49)$$

The Y-factor is given by the ratio of $P_{hot.out}$ and $P_{cold.out}$ in eq. (4.48) as

$$Y = \frac{P_{hot.out}}{P_{cold.out}} = \frac{T_{hot.in} + T_{tp.e}}{T_{cold.in} + T_{tp.e}} \quad (4.50)$$

The above can be represented graphically according to fig. 4.11.

Depending on the unknown parameter we wish to determine, we can rewrite eq. (4.50) to get either of the following.

$$T_{tp.e} = \frac{T_{hot.in} - YT_{cold.in}}{Y - 1} \quad (4.51a)$$

$$T_{cold.in} = \frac{T_{hot.in} - (Y - 1)T_{tp.e}}{Y} \quad (4.51b)$$

$$T_{hot.in} = Y(T_{cold.in} + T_{tp.e}) - T_{tp.e} \quad (4.51c)$$

Equation (4.51a) is used when determining the equivalent noise temperature of a two-port, such as an amplifier, using the two temperature devices to the

left in fig. 4.10 as known references. If instead $T_{tp.e}$ and $T_{hot.in}$ are the known references, $T_{cold.in}$ can be determined by the use of eq. (4.51b). The one-port device having an equivalent temperature $T_{cold.in}$ could for example be an antenna, in which case $T_{ant} = T_{cold.in}$. The same reasoning is applicable to eq. (4.51c) and devices having an analogous unknown temperature $T_{hot.in}$.

Usually though, one is interested in determining the noise factor of a two-port. This is done by inserting eq. (4.51a) into eq. (4.17) on page 44 and simplifying, resulting in

$$F = \frac{\left(\frac{T_{hot.in}}{T_0} - 1\right) - Y \left(\frac{T_{cold.in}}{T_0} - 1\right)}{Y - 1} \quad (4.52)$$

The temperature reference devices to the left i fig. 4.10 can in fact consist of only *one* device, capable of outputting two different and known noise levels. One example of such a device would be a *terminating resistor* at two different but known physical temperatures. Another example would be an *antenna*, used as both the hot and cold reference. This is done by pointing the antenna at celestial objects with different but known brightness temperatures, achieving the Y-factor. Yet another example would be a so called *diode noise source (DNS)*, consisting of an attenuator and a noise diode. The latter is a special type of avalanche diode which, when switched on or rather reversed-biased in avalanche breakdown mode, generates an equivalent noise temperature of several thousand kelvins for $T_{hot.in}$. When switched off the attenuator, having a physical temperature at about the ambient room temperature, generates $T_{cold.in}$. A commonly used Y-factor measurement instrument, used in conjunction with calibrated DNSs, is the so called *noise figure meter (or analyser) (NFM)*. Other variants of Y-factor noise sources also exist, such as using a coupled line coupler to introduce an additional amount of known noise into the system.

A term used when characterizing noise sources is the so called *excess noise ratio (ENR)*. According to an application note by Agilent Technologies [14, pg. 9] there is both an old and a new definition of ENR. The old definition is still relevant since it is the one used when characterizing for example DNSs. It is given as *the difference between $T_{hot.in}$ and T_0 , referenced to T_0* . The new definition is more general and is given as *the difference between $T_{hot.in}$ and $T_{cold.in}$, referenced to T_0* . Thus, unlike the old definition where T_0 is used as a reference for noise source calibration, the new definition does not assume that $T_{cold.in}$ is a constant equal to T_0 . Both definitions are given mathematically as follows

$$ENR_{cal} = \frac{T_{hot.in} - T_0}{T_0} = \frac{T_{hot.in}}{T_0} - 1 \quad (4.53a)$$

$$ENR_{new} = \frac{T_{hot.in} - T_{cold.in}}{T_0} = \frac{\Delta T_{in}}{T_0} \quad (4.53b)$$

Notice how $ENR_{new} = ENR_{cal}$ when $T_{cold.in} = T_0$! When referring to ‘the ENR’, ENR_{cal} is usually implied.

The difference in each of the numerators in eqs. (4.53a) and (4.53b) is called the *excess noise* of the noise source. In the case of eq. (4.53b) and fig. 4.10, this is the difference in noise temperature between the hot and cold noise sources to the left in this figure. For eq. (4.53a) this is only true when the temperature of the cold noise source is equal to T_0 .

$G_{tp.a}$, $T_{tp.e}$ and F can be expressed in terms of ENR_{cal} or ENR_{new} . Thus, rewriting eq. (4.53a) to get $T_{hot.in}$ and inserting this into eq. (4.49), $G_{tp.a}$ can be expressed in terms of ENR_{cal} as

$$G_{tp.a} = \frac{\Delta P_{out}}{kBT_0 \left[ENR_{cal} - \left(\frac{T_{cold.in}}{T_0} - 1 \right) \right]} \quad (4.54a)$$

In case $T_{cold.in} = T_0$ we get

$$G_{tp.a} = \frac{\Delta P_{out}}{kBT_0 ENR_{cal}} \quad (4.54b)$$

Rewriting eq. (4.53a) to get $T_{hot.in}$ and inserting this into eq. (4.51a) we can express $T_{tp.e}$ in terms of ENR_{cal} as

$$T_{tp.e} = \frac{T_0 ENR_{cal} - YT_{cold.in} + T_0}{Y - 1} \quad (4.55a)$$

In case $T_{cold.in} = T_0$ we get

$$T_{tp.e} = \frac{T_0 ENR_{cal} - (Y - 1)T_0}{Y - 1} \quad (4.55b)$$

Inserting eq. (4.53a) into eq. (4.52) we can express F in terms of ENR_{cal} as

$$F = \frac{ENR_{cal} - Y \left(\frac{T_{cold.in}}{T_0} - 1 \right)}{Y - 1} \quad (4.56a)$$

In case $T_{cold.in} = T_0$ in eq. (4.56a) we get

$$F = \frac{ENR_{cal}}{Y - 1} \quad (4.56b)$$

Analogous to the above, we can express $G_{tp.a}$, $T_{tp.e}$ and F in terms of ENR_{new} instead. Thus, Rewriting eq. (4.53b) to get ΔT_{in} (K) and inserting this into eq. (4.49), $G_{tp.a}$ can be expressed in terms of ENR_{new} as

$$G_{tp.a} = \frac{\Delta P_{out}}{kBT_0 ENR_{new}} \quad (4.57)$$

In case $T_{cold.in} = T_0$ in eq. (4.57) we arrive at eq. (4.54b) given above.

Rewriting eq. (4.53b) to get $T_{hot.in}$ and inserting this into eq. (4.51a) we get

$$T_{tp.e} = \frac{T_0 ENR_{new} - (Y - 1)T_{cold.in}}{Y - 1} \quad (4.58)$$

In case $T_{cold.in} = T_0$ in eq. (4.58) we arrive at eq. (4.55b) given above.

Inserting eq. (4.53b) into eq. (4.52) we can express F in terms of ENR_{new} as

$$F = \frac{ENR_{new} - (Y - 1) \left(\frac{T_{cold.in}}{T_0} - 1 \right)}{Y - 1} \quad (4.59)$$

In case $T_{cold.in} = T_0$ in eq. (4.59) we arrive at eq. (4.56b) given above.

ENR_{cal} can also be converted to ENR_{new} and vice versa. This is achieved by combining eqs. (4.53a) and (4.53b) and solving for ENR_{new} or ENR_{cal} , resulting in

$$ENR_{new} = ENR_{cal} - \left(\frac{T_{cold.in}}{T_0} - 1 \right) \quad (4.60a)$$

$$ENR_{cal} = ENR_{new} + \left(\frac{T_{cold.in}}{T_0} - 1 \right) \quad (4.60b)$$

However, in relation to the above it is worth noting that one cannot simply convert ENR_{cal} to ENR_{new} and use this value instead of ENR_{cal} in eqs. (4.54a), (4.55a) and (4.56a). This will yield faulty results, especially if $T_{cold.in}$ differs from T_0 by several degrees. Naturally, the reverse is true for eqs. (4.57) to (4.59).

For low ENR DNSs, matters are slightly different than above. In these the noise temperature generated by the avalanche diode passes through an attenuator, before emerging at the output. This attenuator has an output noise temperature of its own, equal to $T_{cold.in}$, which represents the noise temperature when the noise source is turned off. However, $T_{cold.in}$ is still present when the noise source is turned on. This means that the noise temperature $T_{hot.in}$, emerging at the output when the noise source is turned on, is the sum of the attenuated noise from the avalanche diode and $T_{cold.in}$.

$T_{hot.in}$ is thus directly proportional to $T_{cold.in}$, resulting in ΔT_{in} and thus also ENR_{new} in eq. (4.53b) remaining constant regardless of how $T_{cold.in}$ changes.

As long as a correct value for $T_{cold.in}$ is supplied to the instrument when using a modern NFM, the corrective calculations needed are handled automatically. It is therefore beyond the scope of this thesis to present a derivation of the equations needed for these corrections.

4.7.2 Accounting for instrument noise

If the PMR in fig. 4.10 is *not* noiseless, the results obtained from the equations above will not only include the two-port noise as before, but also the noise contribution from the PMR itself. This so called *second stage contribution* must therefore be subtracted from these results, to arrive at the correct values for $T_{tp.e}$ and F . This is done using eqs. (4.23) and (4.24) respectively, for a two-stage system ($N = 2$) where the two-port is the first stage and the PMR is the second stage.¹⁴

In eq. (4.23) $T_{tot.e}$ is the total equivalent input noise temperature of the two stages, referenced to the input of the two-port. It is obtained instead of $T_{tp.e}$ when using eq. (4.51a), (4.55) or (4.58) when a noisy PMR is used. Furthermore $T_{1.e}$ equals the two-port noise temperature of interest, that is $T_{tp.e}$, while $T_{2.e}$ equals the noise temperature of the PMR, that is $T_{pmr.e}$ (K). To remove the second stage contribution from $T_{tot.e}$, the following equation is thus used:

$$T_{tp.e} = T_{tot.e} - \overbrace{\frac{T_{pmr.e}}{G_{tp.a}}}^{\text{Second stage contribution}} \quad (4.61)$$

Using eq. (4.24) an analogous expression for the noise factor is given by

$$F = F_{tot} - \overbrace{\frac{F_{pmr} - 1}{G_{tp.a}}}^{\text{Second stage contribution}} \quad (4.62)$$

where the noise factor F_{tot} of the two stages is obtained instead of F when using eq. (4.52), (4.56) or (4.59).

The available gain of the two-port is still given by the gain equations in section 4.7.1, since neither ΔT_{in} nor ΔP_{out} are influenced by the amount of noise added by the PMR.

Practically determining $T_{pmr.e}$ and F_{pmr} is done by letting the PMR measure its own noise, that is a process of *calibration*. This is accomplished by

¹⁴Hence the expression ‘second stage contribution’.

removing the two-port in fig. 4.10 and connecting the switch S directly to the PMR, after which a Y-factor measurement is performed. One then gets $T_{pmr.e}$ and F_{pmr} instead of $T_{tp.e}$ and F when using eqs. (4.51a), (4.52), (4.55), (4.56), (4.58) and (4.59). In connection with this, $kB\Delta T_{in}$ can be determined by calculating the difference between the measured hot and cold states. This can be used later on in eq. (4.49) to calculate the available two-port gain, $G_{tp.a}$. As before, the measurement bandwidth B must be equal to or smaller than the bandwidth of the DUT.

The LNA noise factor measurements, as well as the associated difficulties and uncertainties, will be presented in sections 8.1, 8.2 and 8.4.

Chapter 5

Signal to noise theory

In chapter 3 a means for calculating the received signal power of a radio communication link, that is a link budget, was established. Furthermore, in chapter 4, the concept of thermal noise in a receiving system was examined. Intuitively it is clear that the strength of a received signal, in relation to the noise level present in a receiving system, is of utmost importance for how successful one will be in extracting the information contained in the signal. For this reason the so called *signal to noise ratio*, *S/N ratio* or just simply the *SNR* will be examined in this chapter. This subject was briefly introduced in section 4.2 when defining the noise factor of a two-port, but will be covered here in the context of communication links. Non-thermal phenomena degrading the *SNR*, such as for example intermodulation distortion or oscillator phase noise, will not be covered. These can be mitigated through proper shielding, filtering and careful equipment selection.

The *SNR* is a vital figure of merit for any communication system, since it determines technical as well as economic prerequisites for the design of such a system. Its level is set by the needed channel capacity and the demand on quality of service.

The *signal to noise ratio* and the *Friis transmission formula* will be covered first, followed by the *signal to noise ratio and the radar equation*. After having covered the *SNR* as well as the *signal plus noise to noise ratio*, a brief discussion on *maximum antenna gain versus maximum G/T_{sys}* will be presented. This is followed by an introduction to the concepts of *minimum detectable signal*, *receiver noise floor* and *sensitivity* since these are closely related to the *SNR* and the total system noise temperature. Last but not least the *total-power radiometer equation* will be presented, since it is also related to the above.

5.1 Signal to noise ratio and the Friis transmission formula

The received signal power P_r , present at the terminals of the receiving antenna in a point to point communication system in free space, was given by eq. (3.15) on page 27 in section 3.3, dealing with the Friis transmission formula.

The total system noise temperature at the antenna terminals of the receiving system was given by eq. (4.39) on page 56. The *total system noise power* in a bandwidth B is thus given by $kT_{sys}B$.

Thus by dividing P_r from eq. (3.15b) on page 27 by the total system noise power, the output SNR¹ of the receiving system is given by

$$SNR = \frac{\overbrace{P_t G_t G_r \lambda^2}^{\text{Signal } (P_r)}}{(4\pi r)^2} \cdot \overbrace{\frac{1}{kT_{sys}B}}^{\text{1/Noise}} = \frac{P_t G_t \lambda^2}{(4\pi r)^2} \cdot \left(\frac{G_r}{T_{sys}} \right) \cdot \frac{1}{kB} \quad (5.1a)$$

Expressed in decibels this can also be written as

$$SNR = P_t + G_t + 2\lambda - 20 \log(4\pi) - 2r + \left(\frac{G_r}{T_{sys}} \right)_{\text{dB}} - k - B \quad (\text{dB}) \quad (5.1b)$$

Using eq. (3.15c) page 27 for P_r instead, the SNR is alternatively given in terms of the EIRP and the free-space loss as

$$SNR = \frac{\overbrace{EIRP \cdot G_r}^{\text{Signal } (P_r)}}{L_{fsl}} \cdot \overbrace{\frac{1}{kT_{sys}B}}^{\text{1/Noise}} = \frac{EIRP}{L_{fsl}} \cdot \left(\frac{G_r}{T_{sys}} \right) \cdot \frac{1}{kB} \quad (5.2a)$$

Expressed in decibels this can also be written as

$$SNR = EIRP - L_{fsl} + \left(\frac{G_r}{T_{sys}} \right)_{\text{dB}} - k - B \quad (\text{dB}) \quad (5.2b)$$

G_r/T_{sys} (K^{-1}) in eqs. (5.1) and (5.2) is the so called *G over T figure of merit* of the receiving system. It is given as a ratio since it is far easier to determine the ratio itself, than determining either G_r or T_{sys} individually. Fortunately though, as long as the EIRP of the transmitter is known, only the ratio is needed as can be seen in eqs. (5.1) and (5.2). The G over T is an important characteristic and will therefore be covered in more detail in section 5.4.

¹ SNR in eqs. (5.1) and (5.2) is equivalent to SNR_{out} from sections 4.2.1 and 5.5.

Since the SNR is usually given in decibels, eqs. (5.1b) and (5.2b) are also given. In these equations G_r/T_{sys} is meant to be seen as the decibel value of a fractional number.

Section 3.5 lists a number of losses associated with the signal path, which have not been accounted for above. However, eqs. (5.1) and (5.2) can easily be modified to reflect these losses, should so be needed.

5.2 Signal to noise ratio and the radar equation

Having just covered the SNR expression associated with the Friis transmission formula, we proceed with obtaining the equivalent expressions for the bistatic and monostatic radar equations, given in section 3.4.

In analogy with section 5.1 the received signal power P_r , present at the terminals of the receiving antenna in a radar system in free space, was given by eqs. (3.22) and (3.25) for the bistatic and monostatic radar equations respectively. See pages 29 and 30!

The total system noise power at the antenna terminals in the receiving system is the same as that given in section 5.1, that is $kT_{sys}B$.

Thus by dividing P_r from eq. (3.22a) on page 29 by the total system noise power, the output SNR² of the *bistatic* radar system is given by

$$SNR = \overbrace{\frac{P_t G_t}{4\pi r_t^2} \cdot \frac{\sigma}{4\pi r_r^2} \cdot \frac{G_r \lambda^2}{4\pi}}^{\text{Signal } (P_r)} \cdot \overbrace{\frac{1}{kT_{sys}B}}^{1/\text{Noise}} = \frac{P_t G_t \lambda^2 \sigma}{(4\pi)^3 r_t^2 r_r^2} \cdot \left(\frac{G_r}{T_{sys}} \right) \cdot \frac{1}{kB} \quad (5.3a)$$

Expressed in decibels this can be written as

$$SNR = P_t + G_t + 2\lambda + \sigma - 30 \log(4\pi) - 2r_t - 2r_r + \left(\frac{G_r}{T_{sys}} \right)_{\text{dB}} - k - B \quad (\text{dB}) \quad (5.3b)$$

Using eq. (3.22c) on page 30 for P_r instead, the SNR can alternatively be expressed in terms of the EIRP, the gain of the radar object and the free-space loss as

$$SNR = \overbrace{\frac{EIRP \cdot G_{obj} \cdot G_r}{L_{t.fsl} \cdot L_{r.fsl}}}^{\text{Signal } (P_r)} \cdot \overbrace{\frac{1}{kT_{sys}B}}^{1/\text{Noise}} = \frac{EIRP \cdot G_{obj}}{L_{t.fsl} \cdot L_{r.fsl}} \cdot \left(\frac{G_r}{T_{sys}} \right) \cdot \frac{1}{kB} \quad (5.4a)$$

² SNR in eqs. (5.3) to (5.6) is equivalent to SNR_{out} from sections 4.2.1 and 5.5.

Given in decibels this can be written as

$$SNR = EIRP - L_{t.fsl} + G_{obj} - L_{r.fsl} + \left(\frac{G_r}{T_{sys}} \right)_{dB} - k - B \quad (\text{dB}) \quad (5.4b)$$

For a *monostatic* radar system, the output SNR^2 is given by dividing P_r from eq. (3.25a) on page 30 with the total system noise power from above. This yields

$$SNR = \overbrace{\frac{P_t G}{4\pi r^2} \cdot \frac{\sigma}{4\pi r^2} \cdot \frac{G \lambda^2}{4\pi}}^{\text{Signal } (P_r)} \cdot \overbrace{\frac{1}{k T_{sys} B}}^{1/\text{Noise}} = \frac{P_t G \lambda^2 \sigma}{(4\pi)^3 r^4} \cdot \left(\frac{G}{T_{sys}} \right) \cdot \frac{1}{kB} \quad (5.5a)$$

Expressed in decibels this can be written as

$$SNR = P_t + G + 2\lambda + \sigma - 30 \log(4\pi) - 4r + \left(\frac{G}{T_{sys}} \right)_{dB} - k - B \quad (\text{dB}) \quad (5.5b)$$

Using eq. (3.25c) on page 30 for P_r instead, the SNR can alternatively be expressed in terms of the $EIRP$, the gain of the radar object and the free-space loss as

$$SNR = \overbrace{\frac{EIRP \cdot G_{obj} \cdot G}{L_{fsl}^2}}^{\text{Signal } (P_r)} \cdot \overbrace{\frac{1}{k T_{sys} B}}^{1/\text{Noise}} = \frac{EIRP \cdot G_{obj}}{L_{fsl}^2} \cdot \left(\frac{G}{T_{sys}} \right) \cdot \frac{1}{kB} \quad (5.6a)$$

Given in decibels this can be written as

$$SNR = EIRP + G_{obj} - 2L_{fsl} + \left(\frac{G}{T_{sys}} \right)_{dB} - k - B \quad (\text{dB}) \quad (5.6b)$$

Since only one antenna is used in a monostatic radar system, G is present to a power of two and T_{sys} to a power one in eqs. (5.5) and (5.6). Thus apart from only having to determine G/T_{sys} (K^{-1}) to calculate the SNR , as was the case in section 5.1, either G or T_{sys} has to be determined as well to get G .

Analogous to section 5.1, there are a number of losses associated with the signal path which have not been accounted for above. However, eqs. (5.3) to (5.6) can easily be modified to reflect these losses, should so be needed. Please refer also to section 3.5.

On a final note of curiosity, solving eq. (5.5) for r determines the maximum usable range of a radar system. The resulting equation is called the *radar range equation* in which a minimally required SNR of the radar echo needs to be specified.

5.3 Signal plus noise to noise ratio

In reality, when attempting to *measure* the SNR, one cannot separate the signal P_s (W) from the noise P_n (W), since the noise is always present. However, if $P_s \gg P_n$ in the bandwidth occupied by P_s , this can be neglected. Otherwise, one has to measure the *signal plus noise to noise ratio (SNNR)* from which the SNR can be obtained. Mathematically this is given by

$$SNNR = \frac{P_s + P_n}{P_n} = \frac{P_s}{P_n} + 1 = SNR + 1 \quad (5.7a)$$

from which the SNR is obtained as

$$SNR = SNNR - 1 \quad (5.7b)$$

5.4 Maximum antenna gain versus maximum G/T_{sys}

The *G over T* is a system specific measure of how sensitive a system is to receiving a signal. It can therefore be used to easily compare different receiving systems or to set a technical lower limit for the design of such a system. Furthermore, as was shown in sections 5.1 and 5.2, it is also an integral part of the resulting SNR performance of a system. Consequently, maximizing the *G over T* is a desirable goal in EME and other weak signal communication methods. Unfortunately however, even though the antenna gain is in the numerator of the G_r/T_{sys} ratio, maximizing the gain does not mean maximizing the *G over T* since doing this simultaneously influences T_{sys} . Maximizing the antenna gain while at the same time minimizing the system temperature are thus somewhat contradictory criteria. As will be explained below, this is especially true for low noise systems such as those used for EME communication.

From the point of view of a *transmitting* system the higher the antenna gain G_t the better, since this increases the resulting SNR at the receiving station. This can be seen from the equations in sections 5.1 and 5.2. As a rule of thumb, designing an antenna for maximum possible gain implies that the feed horn illuminates the dish with about a 10 dB edge taper. Achieving this means choosing a dish with a certain f/D ratio, suited to the particular type of feed horn being used or vice versa.

In contrast, from the perspective of a *receiving* system the higher the *G over T* the better, since this increases the obtainable SNR. This can also be seen from the equations in sections 5.1 and 5.2. However, designing an antenna for maximum G_r/T_{sys} is more tricky than designing it for maximum gain since not only G_r but now also T_{sys} is part of the optimization process. Complicating matters is the fact that both of these change as a function of

the f/D ratio of the dish. Furthermore, T_{sys} depends not only on the antenna temperature T_{ant} , which should be noted is antenna direction specific, but also on the noise temperature $T_{rx.e}$ of the receiver system. *Designing an antenna for maximum G over T thus requires knowledge about a) $T_{rx.e}$ b) how G_r and T_{ant} change as a function of the dish f/D ratio and c) how T_{ant} changes with the antenna direction.* This implies having detailed knowledge about the feed horn radiation pattern and how the resulting antenna pattern changes as a function of f/D .

To illustrate the above: If one were to gradually increase the f/D ratio of the dish (by increasing f but keeping D constant) until the antenna is optimized for maximum gain, one would also increase the illumination spillover around the edge of the dish. Conversely this means that the feed horn will pick up more ground noise, increasing the antenna temperature T_{ant} and thus also the system temperature T_{sys} . Ultimately, at some point, more will be lost to T_{sys} than what is won in G_r . This will reduce G_r/T_{sys} as well as the resulting SNR. *An antenna optimized for maximum gain is thus less suited for the reception of weak signals, than an antenna optimized for maximum G over T .*

It is obvious that finding the optimum f/D ratio for maximum G over T , for a specific feed horn, is a non-trivial matter. It can be achieved however through computer simulation. The results of such work, involving the ‘W2IMU dual mode horn’ [111], has been presented in an article by Rastislav Galuščák (OM6AA) et al. [57]. An interesting observation presented in this article is that *the optimum f/D ratio, for maximum G over T , increases with the system temperature and vice versa.* The article is well worth reading, especially for those using a W2IMU-type horn.³

From the above we can draw the conclusion that for a receiving system with a very *high* system noise temperature, maximizing the G over T essentially means maximizing the antenna gain. In regard to EME communication however, where the system noise temperature is very *low*, this is not the case. For such a system the optimum f/D , which maximizes the G over T , will be somewhere between the f/D which minimizes the antenna temperature and the f/D which maximizes the antenna gain. Finding this optimum f/D ratio is desirable since receiving weak EME signals with an amateur sized dish makes the resulting SNR very dependent on the system G over T . At the same time, the loss in potential antenna gain when transmitting is marginal in comparison. Besides, this loss can be compensated for by increasing the output power of the PA or reducing feed line losses.

³ Another article, in part by the same authors, examines the port-to-port isolation of a circularly polarized feed horn as a function of the f/D ratio of the dish [91]. Since this influences the system noise temperature as well, it is also worth reading. For more on this, in regard to the author’s system, please refer to section 8.10.

Nevertheless, most radio amateurs do not have the means to perform complex computer simulations, in order to find the optimum f/D , nor the luxury of choosing their own antenna system from scratch. Most of us simply come by an antenna on the surplus market with some arbitrary f/D ratio. We then build or buy a feed horn which seems suitable and try to make the best of it. In the case of the author's antenna, this involved extending the diameter of the dish to get a decent illumination with the horn at hand. Since the diameter had to be extended in any case, the author opted for 'overdoing' this extension so as to be sure to really lower the antenna temperature. The result is likely a dish which is optimized more so for minimum T_{sys} , than for maximum G_r/T_{sys} . Please refer to section 7.1 for more on the author's antenna, as well as to the photos in figs. 7.2, 7.3 and 8.11 on pages 96, 97 and 162.

Regardless of the above, it is always of great interest to compare ones G_r/T_{sys} to that of others using similar equipment and dish diameters. Fortunately, determining the G_r/T_{sys} ratio can be done through a simple Y-factor measurement. Thus neither G_r nor T_{sys} need to be individually determined in order to get G_r/T_{sys} . Details on how to theoretically and practically determine all three of these parameters, concerning the author's EME system, will be covered in sections 6.1, 6.2 and 8.6 to 8.8.

On a final note, it can be shown that the G over T ratio is constant at every point in a receiver system [85, ch. 1.15]. This is intuitive, since both the gain and the system temperature are both multiplied and divided by the same gains and losses when moving through the possible reference points of the system.

5.5 Minimum detectable signal, receiver noise floor and sensitivity

The MDS specifies the lower limit of the signal power needed (detectable) at the input of a receiver, in order to obtain a certain SNR at its output. Its level is determined by a) the total system noise temperature (power), referenced to the input of the receiver and b) the minimally required SNR at the output of the receiver, prior to the demodulator. The mathematical expression for the MDS thus provides the interface between the Friis or radar communication link equation, and the equation for the required SNR of the chosen demodulation scheme. Please refer also to sections 3.3, 3.4 and 4.6 as well as to the literature [92, ch. 10.2][65].

Revisiting the two-port circuit in fig. 4.3 on page 40 and using some of the accompanying equations in section 4.2.1, the mathematical expression for the MDS will now be derived. We will assume that the two-port in fig. 4.3

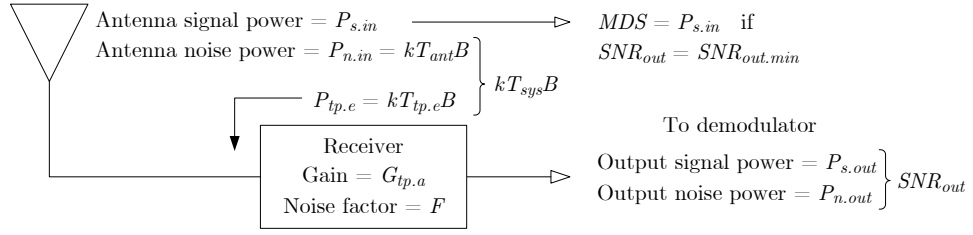


Figure 5.1 The circuit and notation used in the derivation of the **MDS**.

is the receiver and the signal source is the connected antenna. A simplified circuit using this notation is shown in fig. 5.1.

Since the **MDS** is a function of the **SNR** at the output of the receiver, we will start the derivation with this expression, given by

$$SNR_{out} = \frac{P_{s.out}}{P_{n.out}} \tag{5.8}$$

The output signal power $P_{s.out}$ can be expressed in terms of the available receiver gain $G_{tp.a}$ and the input signal power $P_{s.in}$ using eq. (4.10) on page 42. Inserting this into eq. (5.8) and solving for $P_{s.in}$, we get

$$P_{s.in} = \frac{P_{n.out}}{G_{tp.a}} \cdot SNR_{out} \tag{5.9}$$

Solving eq. (4.15) on page 43 for $P_{tp.add}$ and inserting this into eq. (4.11) on page 42, we get the total noise power at the output of the receiver as

$$P_{n.out} = G_{tp.a}(P_{n.in} + P_{tp.e}) \tag{5.10}$$

Inserting this into eq. (5.9) we get the antenna signal power at the receiver input as

$$P_{s.in} = (P_{n.in} + P_{tp.e}) \cdot SNR_{out} \tag{5.11}$$

Evaluating eq. (5.11) for the minimally required **SNR** at the receiver output, we finally get **MDS (W)** at the input of the receiver as

$$MDS = \overbrace{(P_{n.in} + P_{tp.e})}^{\text{Total output noise power referenced to the receiver input}} \cdot SNR_{out.min} \tag{5.12}$$

The antenna noise power $P_{n.in}$ can be expressed in terms of the antenna noise temperature as

$$P_{n.in} = kT_{ant}B \tag{5.13}$$

Analogous, $P_{tp.e}$ can be expressed in terms of $T_{tp.e}$, the equivalent input noise temperature of the receiver, using eq. (4.16) on page 43. Thus, inserting

eqs. (4.16) and (5.13) into eq. (5.12), we get the MDS expressed in terms of the total system noise temperature as

$$MDS = kB \overbrace{(T_{ant} + T_{tp.e})}^{\text{Total system noise temperature referenced to the receiver input } (T_{sys})} \cdot SNR_{out.min} \quad (5.14a)$$

Expressing $T_{tp.e}$ in terms of the receiver noise factor F using eq. (4.18) on page 44, the MDS can also be written as

$$MDS = kB [T_{ant} + (F - 1)T_0] \cdot SNR_{out.min} \quad (5.14b)$$

In the special case when the antenna temperature $T_{ant} = T_0$ we get the more familiar expression

$$MDS = kT_0BF \cdot SNR_{out.min} \quad (5.15)$$

Remember though that eq. (5.15) is only valid when the antenna temperature is equal to T_0 , which is an approximation often used for terrestrial antennas.⁴ In an EME system however, the antenna temperature is *significantly* lower, thus requiring the use of eq. (5.12) or (5.14) instead.

In case the minimum output SNR is equal to unity (0 dB), that is the signal and noise powers at the receiver output are equal in magnitude, the MDS is called the *receiver noise floor*. Analogous, if the SNNR is equal to 10, that is if the SNR is equal to 9 (9.5 dB) according to eq. (5.7b) on page 71, the MDS is instead called the *receiver sensitivity*. Both are common receiver figures of merit, usually also given in microvolts across 50 Ω . It is advised to specify the minimum output SNRs when using these figures of merit, since their definitions unfortunately vary.

For more on these and other receiver figures of merit such as the *dynamic range*, *1 dB compression point* and *third order intercept point*, please refer to the literature [92, ch. 3.7, 10.2][18, ch. 25.6]. For information on their measurement, please refer to the [American Radio Relay League's \(ARRL's\) test procedures manual](#) [19].

5.6 Total-power radiometer equation

In radio astronomy one measures the radiated noise power from astronomical radio sources, that is the ‘signal’, using a so called *radiometer*. This is a purpose-built receiver used in radio telescopes, which outputs a DC voltage proportional to the mean RF input power using a square-law detector and an averaging time integrator.⁵ A change in the antenna noise temperature, for

⁴ See also footnote 7 on page 42!

⁵ This can also be seen as a low-pass filter, since an integration in the time domain corresponds to a low-pass filtering in the frequency domain.

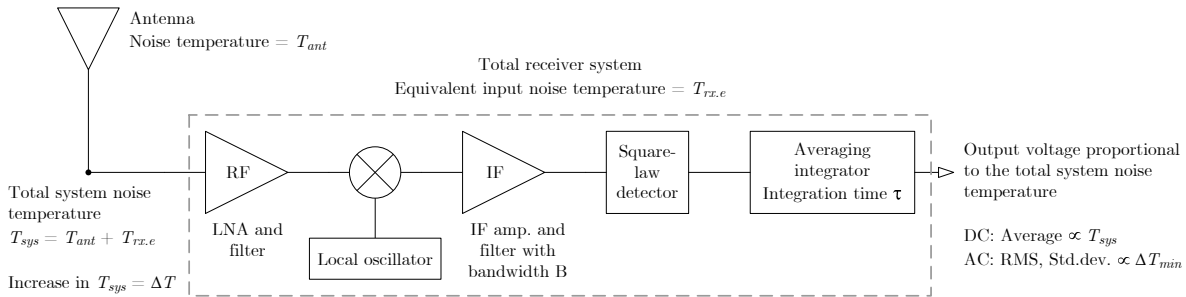


Figure 5.2 A super-heterodyne total-power radiometer. This type of receiver measures the total system noise temperature T_{sys} , and thus also changes in the antenna noise temperature T_{ant} . Such changes are reflected linearly in the DC component of the output voltage to the right. Random noise fluctuations are observed as a superimposed AC component with a standard deviation, that is an RMS value, proportional to ΔT_{min} . The pre-detector bandwidth is B and the post-detector integration time is τ .

example due to an astronomical radio source, will thus result in a proportional change in the DC voltage at the radiometer output. If this change in antenna temperature is determined by measuring the total system noise temperature, that is the sum of the antenna and receiver noise temperatures, the device is called a *total-power radiometer*. Thus, *the output voltage of a total-power radiometer is a measure proportional to the total system noise temperature*. The concepts of voltage and noise temperature will therefore be used interchangeably in the following. A block diagram of a total-power radiometer is given in fig. 5.2.

Since noise is random in nature, the system noise temperature will show random fluctuations about its mean value T_{sys} . These fluctuations might well be in the same order of magnitude as the change in antenna temperature one wishes to measure. Thus, how can one determine if an increase ΔT (K) in T_{sys} , as measured at the output of the radiometer, is indeed related to an increase in the antenna temperature due to a radio source, and not simply a result of random noise fluctuations? To try and answer this question one has to know or estimate the standard deviation, that is the RMS value, of these fluctuations, as measured at the radiometer output, and compare it to the measured increase ΔT . From this it is then possible to calculate the probability that this increase is due to an astronomical radio source, rather than due to random fluctuations. This probability increases the larger ΔT is in comparison to the standard deviation, which we will call ΔT_{min} (K).

While T_{sys} and ΔT_{min} have their reference points at the antenna terminals to the left in fig. 5.2, they are *measured* as voltages at the radiometer output to the right. T_{sys} is measured as a DC voltage, while the noise fluctuations are seen as a superimposed AC voltage. The standard deviation of this AC voltage, that is its RMS value, is a measure of ΔT_{min} . Fortunately ΔT_{min} is

reduced by means of sample averaging or time integration, thus increasing the probability to correctly determine the cause of the increase ΔT . This is the reason why there is an integrator at the output of the square-law detector in fig. 5.2.

Since the output voltage from the *square-law detector* is exponentially distributed, its standard deviation equals its mean which is directly proportional to T_{sys} . It can be shown from the basic properties of the variance, that averaging n measurements of this voltage decreases the standard deviation as $1/\sqrt{n}$. The resulting standard deviation ΔT_{min} , also called the *minimum detectable (measurable) change* in T_{sys} , is thus given by

$$\Delta T_{min} = \frac{T_{sys}}{\sqrt{n}} \quad (5.16a)$$

We now need to relate n to the pre-detector bandwidth B and the post-detector integration time τ (s). Loosely speaking, the time frame needed for the output power in the bandwidth B to be statistically independent from a previous value, is approximately B^{-1} seconds. Thus, integrating over a time of τ seconds yields $\tau/B^{-1} = B\tau$ independent samples, equalling n . Using this, eq. (5.16a) can now be written as

$$\Delta T_{min} = \frac{T_{sys}}{\sqrt{B\tau}} \quad (5.16b)$$

Equation (5.16) is called the *ideal total-power radiometer equation*. The *minimum detectable change* ΔT_{min} is also referred to as the *radiometric sensitivity* or the *temperature resolution* of the radiometer. It can also be interpreted as the *uncertainty in the measurement* of T_{sys} . Solving eq. (5.16b) for τ , one can determine what integration time is needed for a certain ΔT_{min} .

According to the central limit theorem, the fluctuations about T_{sys} will tend toward a Gaussian distribution as n increases. Knowing this, one can use the cumulative distribution function to calculate the probability that an increase ΔT is due to random noise fluctuations, as opposed to an astronomical radio source. Assuming that the measured increase ΔT is three times the standard deviation ΔT_{min} , the probability of this occurring due to random noise fluctuations is only $1.35 \cdot 10^{-3}$. This corresponds to once every $7.41 \cdot 10^2 \cdot \tau$ seconds, equalling about once every hour when $\tau = 5$ seconds. If ΔT is four times the standard deviation, the corresponding numbers are once every $3.16 \cdot 10^4 \cdot \tau$ seconds, equalling almost once every other day when $\tau = 5$ seconds [78, pg. 247]. The above assumes that $\Delta T \ll T_{sys}$, since its contribution to T_{sys} is neglected.

As can be seen in eq. (5.16b), the measurement uncertainty decreases as the bandwidth B or integration time τ increases, and vice versa. One can therefore be led to believe that the uncertainty can be made arbitrarily small,

just by increasing these variables. Unfortunately this is not the case since system instabilities, such as those related to radiometer gain, limit these attempts. The reason for this being that variations in the total system noise temperature, as measured at the output of the radiometer, are indistinguishable from variations in the total system gain. A difficulty associated with total power radiometers hence lies in their ability to detect relatively small changes in the usually much larger total system noise temperature. A high degree of system stability is therefore crucial!

For more on this and a more stringent and in depth derivation of the above, please refer to the literature [78, ch. 3-19, 7-1c, d, e][40, ch. 5, 6].

Since the total system noise temperature has a mean DC value equal to T_{sys} and an AC RMS value equal to ΔT_{min} , its total RMS value, as measured at the output of the radiometer, is given by

$$T_{sys.RMS} = \sqrt{\underbrace{T_{sys}^2}_{\substack{\text{Mean DC} \\ \text{component} \\ \text{(squared)}}} + \underbrace{\Delta T_{min}^2}_{\substack{\text{AC RMS} \\ \text{component} \\ \text{(squared)}}}} \quad (5.17)$$

$T_{sys.RMS}$ (K) can be used instead of T_{sys} in the SNR calculations of sections 5.1 and 5.2 when the integration time is limited and ΔT_{min} cannot be neglected. In the radio astronomy field however, the SNR is instead given by the measured increase ΔT relative to the radiometric sensitivity ΔT_{min} , that is

$$SNR = \frac{\Delta T}{\Delta T_{min}} \quad (5.18)$$

The receiving system presented in section 4.6 can be used as an elementary total-power radiometer. Provided a sufficiently strong radio source, the same is true for the EME receiver subsystem shown in fig. 7.1 on page 94, which will be presented in chapter 7. The square-law detector and the integrator are then realized in computer software. Employing the system for this purpose, using the Sun as the astronomical radio source of choice, will be presented in sections 8.6 and 8.7.

Chapter 6

Radio astronomical measurement theory

There are several known celestial radio sources in the sky, such as radio galaxies, nebulas, quasars, supernova remnants, stars and planets. Some of these sources can be used to measure quantities related to the antenna performance of an EME system. Examples of such measurements will be presented in sections 8.6 and 8.7, where the G/T_{sys} figure of merit and the antenna gain will be determined by means of the Sun. This chapter will derive the equations needed to calculate these and a few other parameters of interest, starting with the *G/T_{sys} figure of merit equation*. This will be followed by a section on *antenna gain determination and more*. Finally, a procedure for *source size correction* will be presented.

6.1 G/T_{sys} figure of merit equation

By pointing the antenna boresight at two respective sources in the sky with different noise temperatures, a Y-factor measurement can be made using the receiving equipment. In analogy with eq. (4.50) on page 61, this Y-factor can be written mathematically as

$$Y = \frac{T_{ant.hot} + T_{rx.e}}{T_{ant.cold} + T_{rx.e}} \quad (6.1a)$$

where $T_{ant.hot}$ (K) and $T_{ant.cold}$ (K) are the hot and cold antenna noise temperatures respectively. As before, $T_{rx.e}$ is the noise temperature of the entire receiver system as presented in section 4.6.

Letting the increase in antenna temperature, from $T_{ant.cold}$ to $T_{ant.hot}$, be equal to ΔT_{ant} (K) and furthermore letting T_{ant} be equal to $T_{ant.cold}$, the Y-factor can be written as

$$Y = \frac{T_{ant} + \Delta T_{ant} + T_{rx.e}}{T_{ant} + T_{rx.e}} \quad (6.1b)$$

Inserting eq. (4.39) on page 56 the Y-factor can be expressed in terms of the system noise temperature T_{sys} as

$$Y = \frac{T_{sys} + \Delta T_{ant}}{T_{sys}} \quad (6.1c)$$

Solving eq. (6.1c) for T_{sys} yields

$$T_{sys} = \frac{\Delta T_{ant}}{Y - 1} \quad (6.2)$$

while solving for ΔT_{ant} yields

$$\Delta T_{ant} = T_{sys}(Y - 1) \quad (6.3)$$

If the noise picked up by the antenna back and side lobes were to remain constant during the Y-factor measurement, ΔT_{ant} would be entirely attributed to the change in noise temperature between the hot and cold sources in the sky. Such a condition can essentially be achieved in practice by pointing the antenna in a fixed direction, where the celestial radio source is predicted to pass through as the Earth rotates. When the source is at boresight the ‘hot measurement’ is performed, while the ‘cold measurement’ is made as soon as the source has swept by and ceased adding any measurable noise. Since the antenna remains stationary throughout the measurement, ground-based noise picked up by its back and side lobes will remain constant. The change in sky-based side lobe noise can be assumed negligible, especially if the change in the sky brightness temperature surrounding the source is small between the two measurements. Note that the Y-factor measurement should be performed at a time when the radio source is at a high elevation, so that the main lobe does not pick up ground-based noise, increasing the antenna temperature.

Another advantage of not moving the antenna during the measurement, is that the impedance presented at the Rx-port to the LNA is kept constant. This mitigates possible gain error and noise parameter effects, as presented in sections 8.1.14 and 4.2.2 respectively.

Having established the procedure for the Y-factor measurement, the equations needed to arrive at G/T_{sys} will be derived next. First off, by equating eqs. (4.29b) and (4.35b) on pages 52 and 55, the expression for the maximum effective aperture area of the antenna, introduced in section 3.1, is obtained as

$$A_{em} = \frac{2kT_a}{S_{obs}} \quad (6.4a)$$

where the (θ_a, ϕ_a) notation for antenna direction has been dropped.

However, if we only consider an *increase* in antenna temperature *due to a specific source*, that is if S_{obs} is the observed flux density of a source over its angular extension Ω_s , we get

$$A_{em} = \frac{2k\Delta T_a}{\underbrace{S_{obs}}_{\substack{\text{Evaluated} \\ \text{over } \Omega_s}}} \quad (6.4b)$$

where ΔT_a (K) is the antenna temperature increase.

If the source is a point source, that is if its angular extension is small compared to the antenna HPBW, eq. (4.28) on page 51 is applicable. Equation (6.4b) can then be written as

$$A_{em} = \frac{2k\Delta T_a}{S} \quad (6.4c)$$

It can be shown from eq. (4.47a) on page 59 that the increase $\Delta T_a = \Delta T_{ant}/\eta_{rad}$, that is that ΔT_a is the lossless analogue to ΔT_{ant} . From eq. (3.5a) on page 24 we furthermore know that $A_{em} = A_e/\eta_{rad}$. Inserting this into eq. (6.4c), the effective aperture of the antenna is given by

$$A_e = \frac{2k\Delta T_{ant}}{S} \quad (6.5)$$

Inserting eq. (6.5) into eq. (3.4a) on page 24 and dropping the ‘max’ notation, the antenna gain can be written as

$$G = \frac{8\pi k\Delta T_{ant}}{S\lambda^2} \quad (6.6a)$$

Inserting eq. (6.3) the antenna gain can also be expressed in terms of the Y-factor and the system noise temperature as

$$G = \frac{8\pi kT_{sys}(Y-1)}{S\lambda^2} \quad (6.6b)$$

from which G/T_{sys} is finally given by

$$\frac{G}{T_{sys}} = \frac{8\pi k(Y - 1)}{S\lambda^2} \quad (6.7)$$

The **G over T** figure of merit can thus be obtained through a simple Y-factor measurement, involving a celestial point source with a known flux density S . Section 8.6 shows an example of such a measurement performed in practice, using the Sun as the source of choice.

It is worth reminding that G/T_{sys} is a function of antenna temperature, that is it is dependent on the antenna direction due to the variations in the sky and ground brightness temperatures. This is of importance if one wishes to calculate the expected SNR of EME echoes, as presented in chapter 11. One should in this case determine G/T_{sys} for an antenna direction as close as possible to where the EME communication is to occur. Naturally, the most favourable directions are towards regions in the sky where the brightness temperatures are at their lowest, that is close to Leo or Pictor when in the northern or southern hemisphere respectively.

Apart from radio astronomers, EME operators are not the only ones using the above given method to determine the **G over T** of their antennas. The International Telecommunication Union (ITU) recommends this as one of the methods by which to measure earth station antennas, used in fixed-satellite services [94, Anx. 1].

6.2 Antenna gain determination and more

This section will present a few equations which are of interest in radio astronomical calculations. An equation by which to calculate the average brightness temperature of a source, from its flux density, will be presented first. The means by which to calculate the antenna beam solid angle from its HPBW, to ultimately determine the antenna gain, will be discussed thereafter. As in the previous section, the source is assumed to be a point source. For the event that this is not the case, a thorough investigation into source size correction factors is provided in section 6.3.

Inserting eq. (6.4c) into eq. (3.8) on page 25, the antenna beam solid angle can be written as

$$\Omega_A = \frac{S\lambda^2}{2k\Delta T_a} \quad (6.8)$$

The antenna temperature, caused by a source with an average brightness temperature $T_{b.avg}$, is given by eq. (4.38) on page 55. If an *increase* in

antenna temperature due to this source is of interest, T_a in eq. (4.38) can instead be written as

$$\Delta T_a = \frac{\Omega_s}{\Omega_A} \cdot T_{b.avg} \quad (6.9)$$

Combining eqs. (6.8) and (6.9) and solving for the average source brightness temperature finally yields

$$T_{b.avg} = \frac{S\lambda^2}{2k\Omega_s} \quad (6.10)$$

In the above equation Ω_s can be approximated through the *angular diameter* θ_s (rad) of the source, which assumes a disc-shaped source geometry. Ω_s is then approximately given by

$$\Omega_s \approx \frac{\pi\theta_s^2}{4} \quad (6.11)$$

Furthermore, according to Kraus [79, ch. 2-5] and assuming rotational symmetry, the antenna beam solid angle can be approximated by its half-power beam width (rad) as

$$\Omega_A \approx HPBW^2 \quad (6.12a)$$

An enhanced version of this formula, which can be derived from Kraus [79, ch. 3-13], is given by

$$\Omega_A \approx \frac{k_p}{\eta_{beam}} \cdot HPBW^2 \quad (6.12b)$$

where k_p is the *pattern factor* of the antenna aperture distribution, which ranges from about 1.0 for a uniform distribution to 1.13 for a Gaussian one [79, ch. 12-9]. η_{beam} is the *main beam efficiency*, equal to '0.75 ± 0.15 for most large antennas'¹ [79, ch. 3-13] and defined as [79, ch. 2-7]

$$\eta_{beam} = \frac{\Omega_M}{\Omega_A} \quad (6.13)$$

where Ω_M (sr) is the *main beam area* or *main beam solid angle* of the antenna. η_{beam} is thus a measure of how 'clean' the antenna pattern is in regard to side and back lobes. More formally it can also be defined as *the ratio of the power radiated in the main beam to the total radiated power* [66]. The ideal situation where $\eta_{beam} = 1.0$ thus means there are no side or back lobes at all, since the total beam area is entirely in the main beam.

Combining eqs. (6.12b) and (6.13) the main beam area can also be expressed as

$$\Omega_M \approx k_p \cdot HPBW^2 \quad (6.14)$$

¹ η_{beam} is equal to 1.0 for a purely Gaussian (theoretical) aperture distribution.

The **HPBW** of the antenna can be determined by a *drift-scan measurement* of the antenna power pattern. Such a measurement is accomplished by letting a celestial point source sweep past the antenna lobes in the plane of their peak values, as the Earth rotates, while simultaneously recording the received noise power on a relative scale.² The result is a ‘power versus time’ graph corresponding to the antenna power pattern, which is then normalized. Correcting for the source declination, the time x-axis can be converted to radians or degrees since the rotational speed of the Earth is known. The **HPBW** can then readily be determined from the resulting graph. Ω_A can in its turn be estimated from the **HPBW** by means of eq. (6.12b). When combining this with eqs. (3.5b) and (3.6) on pages 24 and 25, the antenna gain can be estimated from the **HPBW** as

$$G \approx \frac{4\pi \cdot \eta_{beam} \cdot \eta_{rad}}{k_p \cdot HPBW^2} \quad (6.15)$$

By furthermore combining eqs. (3.3) and (3.4a) on page 24 and inserting eq. (6.15), the aperture efficiency is estimated by

$$\eta_{ap} \approx \frac{\eta_{beam} \cdot \eta_{rad} \cdot \lambda^2}{k_p \cdot HPBW^2 \cdot A_{ph}} \quad (6.16)$$

An example of a measurement using this approach, along with more details, is presented in section 8.7.1.

Ω_A can also be determined by numerically integrating the normalized antenna power pattern, according to eq. (3.7b) on page 25. In case the source flux density is not high enough to resolve anything but the main lobe, integrating over this segment alone will yield Ω_M . Ω_A can then be determined through eq. (6.13) by estimating the beam efficiency. In analogy with the above, combining this with eqs. (3.5b) and (3.6) on pages 24 and 25, the antenna gain can be calculated as

$$G = \frac{4\pi \cdot \eta_{beam} \cdot \eta_{rad}}{\Omega_M} \quad (6.17)$$

By furthermore combining eqs. (3.3) and (3.4a) on page 24 and inserting eq. (6.17), the aperture efficiency is given by

$$\eta_{ap} = \frac{\eta_{beam} \cdot \eta_{rad} \cdot \lambda^2}{\Omega_M \cdot A_{ph}} \quad (6.18)$$

An example of a ‘drift-scan integration’ to determine Ω_M , and ultimately the antenna gain G , is presented in section 8.7.2.

² If voltage or current values are recorded, these need to be squared in order to get the power.

6.3 Source size correction

The prerequisite in sections 6.1 and 6.2 of using a point source is necessary, in order to achieve a correct G/T_{sys} and antenna power pattern measurement. A very wide source, where $\theta_s \gg \text{HPBW}$, would result in a broadening of the measured antenna power pattern. In essence, the antenna is then measuring the source instead of the other way around. A point source on the other hand, where $\theta_s \ll \text{HPBW}$, would in theory produce an exact (mirrored) representation of the antenna power pattern.³ In case $\theta_s \simeq \text{HPBW}$, a *source size correction factor* may be introduced to compensate for the broadening of the beam measurement. Depending on the type, the correction factor is either applied to the measured antenna gain or to the measured HPBW. In both cases is the correction factor applied by means of multiplication.⁴

A number of gain correction factors have been proposed for various combinations of antenna power patterns and extended source brightness distributions [23, 61, 100]. Fortunately, the combinations needed are not that many. The power pattern of pencil beam antennas, such as those used in EME communication, can usually be approximated by a rotationally symmetric Gaussian function [24, ch. 5.3.2]. Furthermore, most extended radio sources can be described by either a Gaussian or a uniform disc brightness distribution [23, Table I]. Among the latter is the (quiet) Sun [61, pg. 232] which is a popular radio source used among EME operators.⁵ For this type of antenna-source combination, that is a Gaussian antenna power pattern and a uniform disc brightness distribution, Solovey and Mittra [100] have proposed a gain correction factor given by

$$K = \frac{\left(1.616 \cdot \frac{\theta_s}{\text{HPBW}}\right)^2}{4 \cdot \left[1 - J_1^2\left(1.616 \cdot \frac{\theta_s}{\text{HPBW}}\right) - J_0^2\left(1.616 \cdot \frac{\theta_s}{\text{HPBW}}\right)\right]} \quad (6.19)$$

where J_0 and J_1 are zeroth and first order Bessel functions of the first kind. K is said to be correct to within 0.03 dB for θ_s/HPBW up to 1.5. The three papers mentioned above [23, 61, 100] also provide simpler formulas for K . Guidice and Castelli [61, pg. 232] proposes an alternative expression, which likewise applies to sources having a uniform disc brightness distribution,

³ Mathematically a point source can be seen as a Dirac delta function which is convolved with the antenna power pattern. See also footnote 10 on page 51!

⁴ In the case of the gain correction, this can also be seen as dividing the flux density by the correction factor.

⁵ At the higher microwave bands, the Moon is a popular source as well. Please refer to Guidice and Castelli [61, pg. 229].

given by

$$K \approx \left(1 + 0.18 \cdot \left(\frac{\theta_s}{HPBW} \right)^2 \right)^2 \quad (6.20)$$

This equation is said to be valid for several antenna power patterns, among them the Gaussian pattern, for $\theta_s/HPBW \leq 1$.

However, as can be seen in eqs. (6.19) and (6.20), K can only be calculated if the *true* HPBW of the antenna is already known. Stutzman and Ko [104] has presented a solution to this problem by introducing yet another correction factor, available in tabular and graphical form, which can be used to correct a broadened HPBW measurement. Multiplying the *measured* HPBW by this correction factor thus yields the *true* HPBW, which can then be used in eq. (6.19) or (6.20) to determine K . Once K is known, it can be used to correct the measured antenna gain or G/T_{sys} .

However, using eqs. (3.5b), (3.6) and (6.12a) we can assume that $G \propto 1/HPBW^2$. From this we can draw the pragmatic conclusion that the measured HPBW (rad) can be written as

$$HPBW_{meas} = HPBW \cdot \sqrt{K} \quad (6.21)$$

Solving this equation the true HPBW can be determined from the measured one. Despite the pragmatical approach of eq. (6.21), combining it with eq. (6.19) yields results which are surprisingly similar to those presented by Stutzman and Ko [104]; at least for $\theta_s/HPBW_{meas} \leq 0.8$. Figure 6.1 shows a graphical representation of this solution for $\theta_s/HPBW_{meas} \leq 0.5$. Figure 6.2 furthermore shows the gain correction factor for $\theta_s/HPBW \leq 0.5$, according to eq. (6.19).

Since the Sun is a popular radio source used among EME operators, it is of interest to know its angular diameter to determine the amount of measurement correction needed when using it. Even though the angular diameter averages at about 0.53° at optical wavelengths, it is on average larger at 1296 MHz. Furthermore, the solar disc is less circular at this frequency, being wider at its equator than at its poles. Using data provided by Benz [26, fig. 5], an estimation of the angular diameter of the *quiet* Sun at 1296 MHz is presented in table 6.1.

Since drift-scan *pattern* measurements at noon are essentially performed along the equator of the Sun, the author suggests that corrective calculations should rely on the angular diameter along this direction, that is $\theta_s = 0.62^\circ$. However, when correcting G/T_{sys} or gain measurements relying on the *source area* or *source solid angle* Ω_s , which is calculated according to eq. (6.11), the author suggests that the average value $\theta_s = 0.56^\circ$ should be used instead.

A variant of fig. 6.1 is shown in fig. 6.3 for the specific case where $\theta_s = 0.62^\circ$, that is for a source the same size as the quiet Sun along its equator. Using

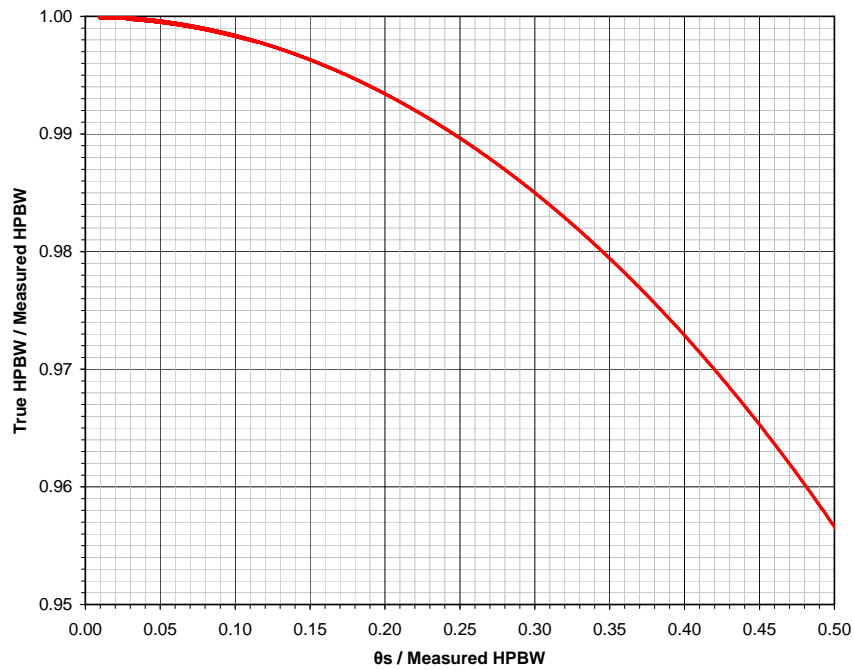


Figure 6.1 The true half-power beam width $HPBW$ as a function of the source angular diameter θ_s , both normalized to the measured half-power beam width $HPBW_{meas}$.

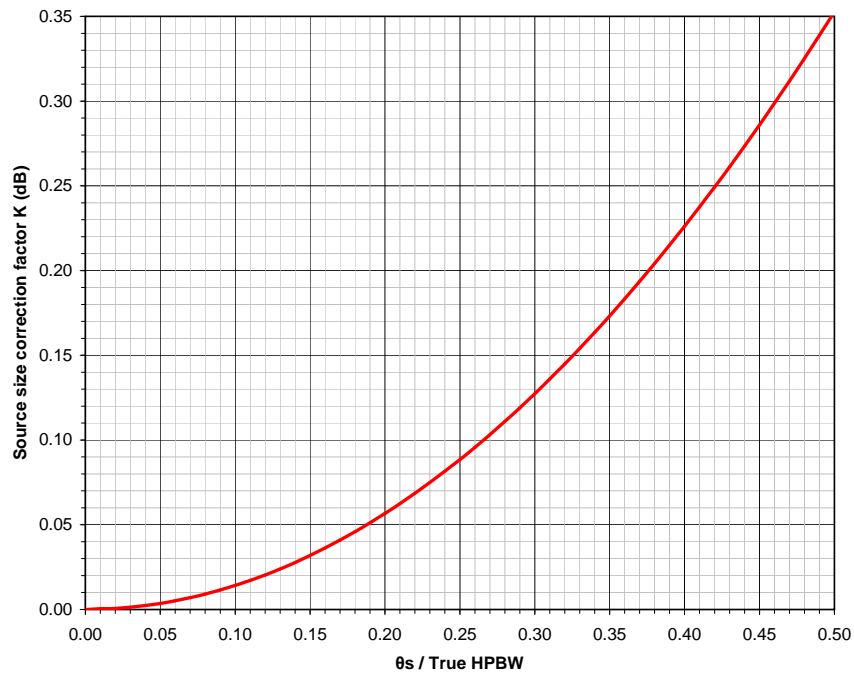


Figure 6.2 The gain correction factor K as a function of the source angular diameter θ_s , normalized to the true half-power beam width $HPBW$. Note that K is given in dB as opposed to in eq. (6.19).

Table 6.1 The angular diameter of the quiet Sun at 1296 MHz. At this frequency, the angular diameter at the equator of the Sun is about 25% larger than at the poles and about 10% larger than the average value of both. For the active Sun, the values will be larger.

Quiet Sun angular diameter		Comment
Type	θ_s at 1296 MHz	
Polar	0.50°	
Equatorial	0.62°	Used for correcting drift-scan pattern measurements, such as the HPBW .
Average	0.56°	Used for correcting measurements relying on Ω_s , such as the gain or G/T_{sys} .

this figure, the true [HPBW](#) can be directly determined from the measured [HPBW](#) when using the Sun.

As can be seen in figs. 6.1 to 6.3, the corrections needed are quite small when performing measurements using the Sun. For most amateur [EME](#) stations, these are likely negligible in comparison to the overall measurement uncertainty. As an example, doing a ‘backwards calculation’: If a gain correction factor $K = 0.1$ dB is needed, this would according to fig. 6.2 entail that $\theta_s/HPBW \approx 0.266$. For $\theta_s = 0.62^\circ$ this means that the true [HPBW](#) would be $HPBW \approx 2.33^\circ$. According to fig. 6.3, a true [HPBW](#) equal to 2.33° would imply a measured [HPBW](#) only slightly larger at 2.36° . Resolving this small difference to determine K , using amateur equipment, is non-trivial. Furthermore, such a narrow [HPBW](#) would imply a dish diameter of more than 7 metres at 1296 MHz! *Thus for most amateur [EME](#) operators in the 23 cm band, the Sun can be considered a point source and no source size correction needs to be applied.*

The above should be put in contrast to professional radio telescopes. For these, the literature recommends applying a correction factor if $\theta_s \gtrsim 0.2 \cdot HPBW$ [61, pg. 232][23, pg. 470], that is if $HPBW \lesssim 3.1^\circ$ for $\theta_s = 0.62^\circ$. This implies a dish diameter of about 5.2 metres or more at 1296 MHz. Since radio telescopes are usually much larger than this, source size correction needs to be applied even for sources much smaller than the Sun.

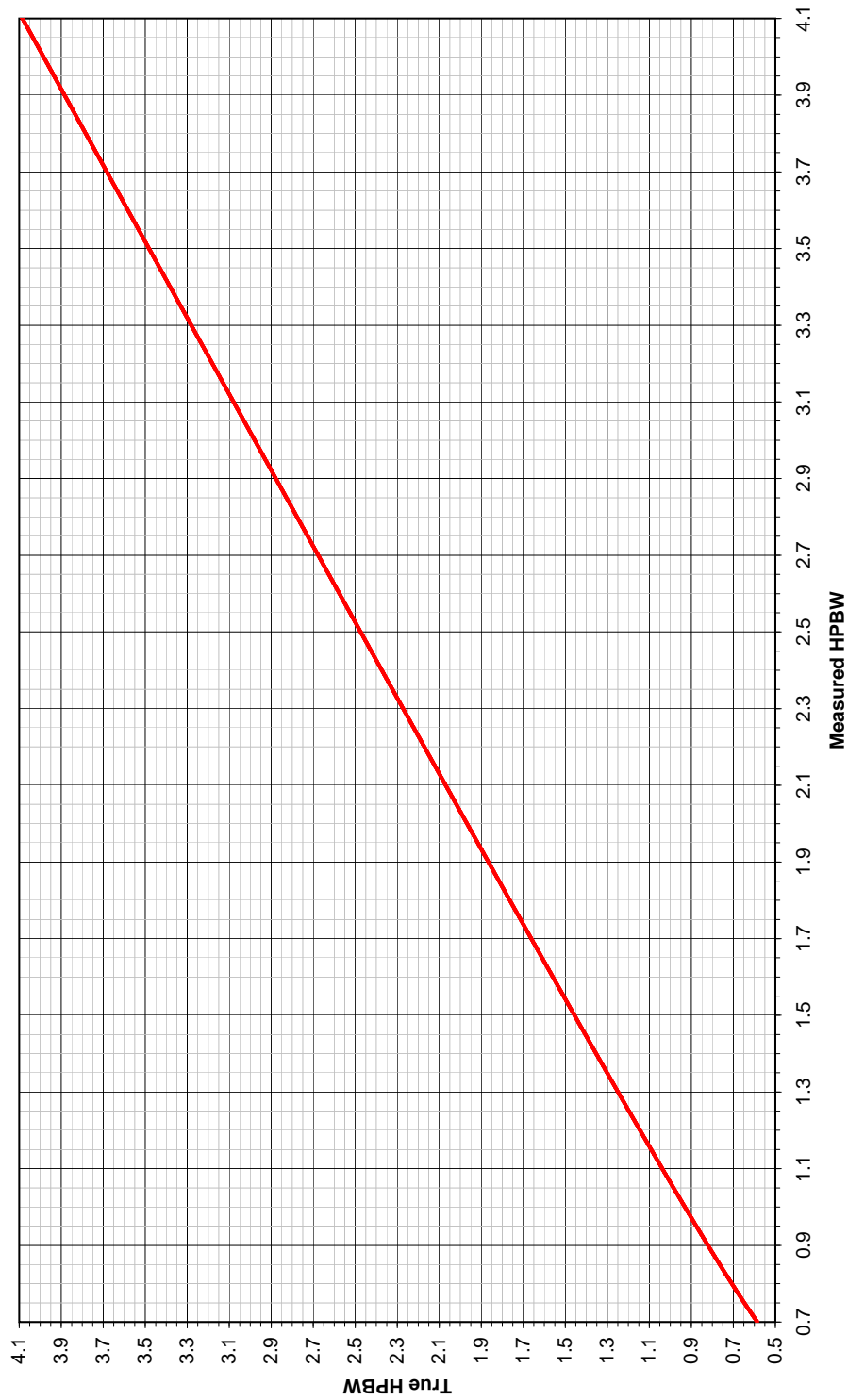


Figure 6.3 The true half-power beam width $HPBW$ as a function of the measured half-power beam width $HPBW_{meas}$, assuming a source angular diameter equal to that of the solar equator for the quiet Sun ($\theta_s = 0.62^\circ$).

Part III

IN PRACTICE

Chapter 7

Parts selection and system description

An [EME](#) communication system consists of many different parts which need to operate correctly, in order for the system as a whole to function as intended. This chapter will therefore give an overall description of the various parts composing the system and why they were selected. However, the goal is not to make an in depth analysis of every aspect and component of the system, since this is beyond the scope of this thesis. Instead, the goal is to focus on the system as a whole and broadly present each part with this backdrop in mind. [Figure 7.1](#), which shows a block diagram of the entire [EME](#) system, will therefore serve as a basis for this chapter.

In regard to the above, it is worth repeating what was said in the [introduction](#), namely that the parts selection process has been heavily limited due to economical reasons. Since such restraints call for technical compromise, the probability of success is unfortunately reduced. To ensure that project success is nevertheless attainable, the author has throughout the part selection process used ‘rule of thumb calculations’ to estimate the final system performance. The [task definition and criteria for success](#), as stipulated in [section 1.1](#), have thus been a continuous part of the design phase.

The presentation of the various system parts will begin with the *antenna subsystem*, followed by the *transmitter subsystem* as well as the *receiver subsystem*. *Other system parts*, used during both transmission and reception, will be covered thereafter. Finally, and unrelated to [fig. 7.1](#), various *software applications* will be covered which have been used throughout this project.

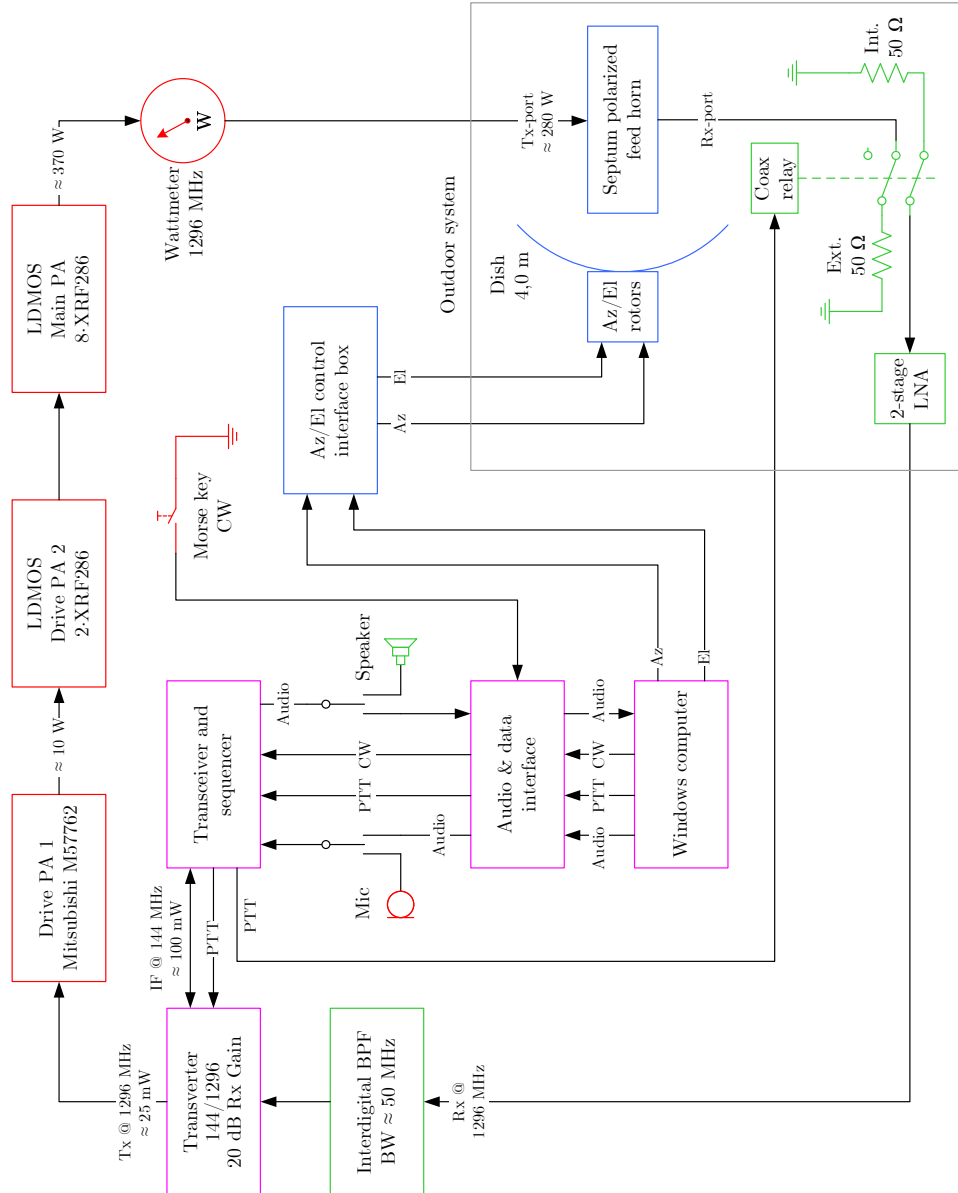


Figure 7.1 A block diagram of the complete EME system. Red (■) represents the Tx subsystem, green (■) represents the Rx subsystem, blue (■) represents the antenna subsystem and magenta (■) represents the subsystem used during both Tx and Rx. Components contained within the grey (■) square are located outdoors. The coaxial protection relay is shown in Tx-mode with both the LNA and feed horn Rx-port connected to 50 Ω terminations. Also shown are frequencies and approximate power levels at certain points in the system.

7.1 Antenna subsystem

The antenna subsystem, shown in blue in fig. 7.1, basically consists of the parabolic dish, the azimuth and elevation control rotators and the square septum-polarized feed horn with associated support struts. These parts will be covered in the following.

7.1.1 Parabolic dish

When operating at 1296 MHz there are a couple of advantages in choosing a parabolic dish reflector antenna, instead of for example an array of stacked Yagi antennas. The most prominent reason being the relative ease in obtaining a high antenna gain and a low antenna temperature, as compared to when opting for an array. Furthermore, some drawbacks of using an array are mechanical construction difficulties, the problem of feeding multiple antennas and not least the accompanying losses in the phasing networks. Yet another problem is the realization of the polarization switching between transmission and reception. For the above reasons the author chose to use a *prime focus dish*, which furthermore is easier to come by and to illuminate than offset dishes.

The author was graciously donated a 2.7 metres solid surface dish by fellow radio amateur Viggo Magnus Nilsen (LA9NEA). This dish was extended by the author to a diameter of $D = 4.0$ m, by means of 24 aluminium ribs and fine-meshed wire netting. See figs. 7.2 and 7.3! The motives for this extension were to achieve a higher antenna gain and a lower antenna temperature by reaching an f/D ratio suited to match the feed horn described in section 7.1.3. This resulted in an antenna gain and an HPBW of about 31 dBi and 4.4° respectively. Instead of modifying the dish, the feed horn could have been modified by adding a flare. Though naturally, this would not have resulted in the desired increase in antenna gain. It would furthermore have had an unknown impact on the polarization properties of the antenna as a whole.

In fact, the 4.0 metres diameter is actually greater than what is needed to match the dish to the type of horn being used. As a result, the f/D ratio of the antenna is approximately 0.30 whereas the optimum f/D for the horn is said to be approximately 0.36. Apart from a slight increase in antenna gain this also leads to an *under-illumination* of the dish by the horn. This results in less ground noise being picked up by the horn, thus lowering the antenna noise temperature. This is very important in an EME communication system in which front-end noise needs to be lowered in order to try and maximize the so called G over T figure of merit. For more on this, please refer to section 5.4.



Figure 7.2 The extended prime focus parabolic dish. The dish diameter is solid out to 2.7 metres and extended to 4.0 metres using 24 aluminium ribs and meshed wire netting, resulting in $f/D = 0.30$. Also shown is the septum polarized feed horn and the four accompanying support struts.



(a) Above



(b) Below

Figure 7.3 Closeups of the dish extension (a) from above and (b) from below. 24 U-shaped aluminium ribs were taken to a machine shop where they were rolled to match a template of the extended parabolic curve. The ribs were then bolted to the dish, using two bolts each. Sections of flat aluminium bars were used along the circumference to join the ribs together, resulting in only a slight deviation from the parabolic shape. The wire netting is folded around the flat aluminium bars along the circumference and attached to the ribs and the dish using durable and UV-resistant cable ties.

7.1.2 Azimuth and elevation control

The *azimuth and elevation control system* was acquired on the surplus market but was originally manufactured by SPID Elektronik [102]. The model used is the ‘RAS rotator’ with technical specifications according to appendix B. Apart from the rotators there is also a ‘rotator control box’ which permits manual as well as computer control via RS232. Figure 7.4 shows a photo of the rotators mounted behind the dish.

The *resolution* of each rotator is said to be 1° , though unfortunately no information is given about the expected *accuracy* of the system. This makes it difficult to estimate the uncertainty and the *depoining loss* of the system. This lack of knowledge could have proven problematic since the *HPBW* of the antenna is approximately 4.4° , whereas the angular diameter of the Moon is only about 0.5° . A slight error in the antenna direction could thus decrease the received signal power by several dBs. However, knowing that others have used this rotator with success, and having obtained the unit for a reasonable price, the author chose to accept this risk. Fortunately, the accuracy of the system turned out to be adequate even though an increased accuracy would have been desirable. Please refer to section 3.5.3 for more information on depointing loss.

As was mentioned above, the rotators can be controlled by means of a computer. This enables automatic tracking of the Moon, provided that suitable software is installed. A popular application used among radio amateurs for doing this is MoonSked [22], developed by David Anderson (GM4JJJ) [21]. Since the author chose to use this software as well, it will be presented briefly in section 7.5.2.

7.1.3 Feed horn

The amateur radio community has agreed upon using *circular polarization* for EME communication in the 23 cm band. This means that the polarization vector rotates 360° in the plane perpendicular to the direction of wave propagation, for every RF cycle, creating a ‘cork screw’ pattern along its way. According to the IEEE definition [67], this is called *right hand circular polarization (RHCP)* if the wave rotates *clockwise (CW)* in the direction of propagation and *left hand circular polarization (LHCP)* if it rotates *anticlockwise (ACW)*. *The agreement is to use RHCP for transmission and LHCP for reception.* The reason for the difference between the two lies in the fact that the sense of polarization is reversed when the wave is reflected off the Moon. However, since reflection in the dish reverses the polarization as well, the *feed horn* must transmit in LHCP and receive in RHCP. See fig. 7.5!

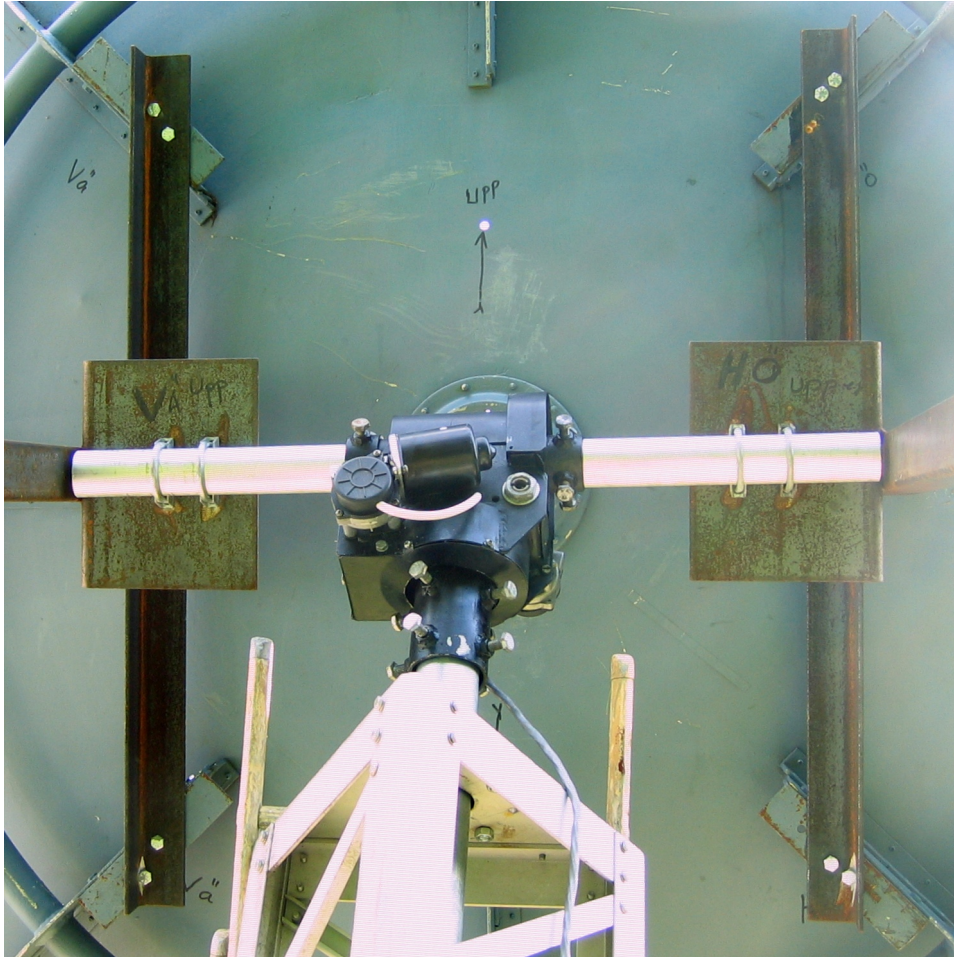


Figure 7.4 The RAS Az/EI rotators mounted as a single unit behind the dish. Also shown is the metal support frame connecting the dish to the elevation rotator. The azimuth rotator is connected to the self-supporting tower using a vertical pipe, which can also be seen. The Az/EI sensors, used for feedback to the control box, are contained within the rotator housing. The beginning of two girders, which extend perpendicularly away from the dish, can be seen to the left and right. These carry the counterweights which are needed to balance the construction.

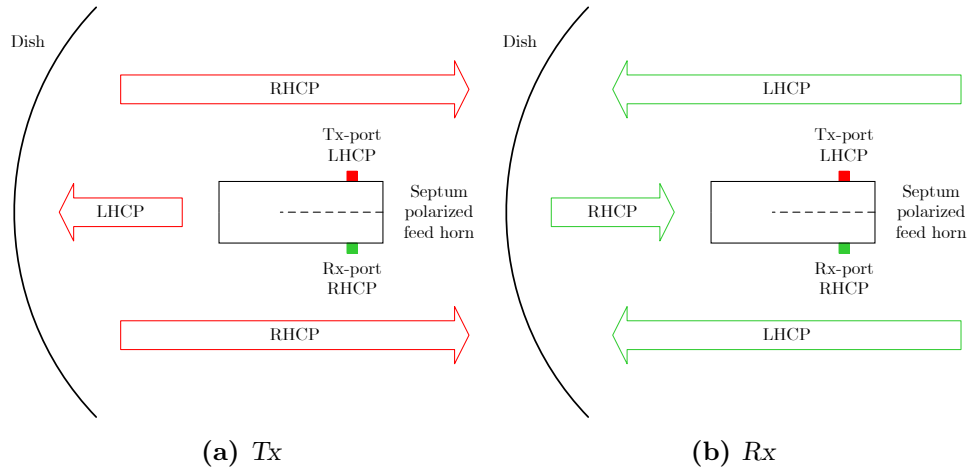


Figure 7.5 The polarization before and after reflection in the dish during (a) Tx, in red (■) and (b) Rx, in green (■).

To accommodate the above, the feed horn needs to have some sort of mechanism to handle both circular polarizations. One way is to use a waveguide with two orthogonal probes excited with the same signal but with a $\pm 90^\circ$ time phase shift, where ‘ \pm ’ designates the sense of polarization. Such an arrangement uses external coaxial relays to switch the polarization between Tx and Rx, thus introducing unwanted losses and costs. Another and perhaps more modern way of accomplishing the 90° phase shift, is to place some kind of well defined ‘obstacle’ in front of the excitation area. This obstacle could for example be a dielectric slab or a so called *stepped septum polarizer* made out of metal. A feed horn using such a device will have two dedicated ports for Tx and Rx respectively. The need for lossy phasing networks is thus totally eliminated.

A very common feed horn used among EME operators, not just in the 23 cm band, is the ‘OK1DFC septum-polarized feed horn’ [97] by Zdeněk Samek (OK1DFC) [96]. This feed horn uses a square wave guide and a four-step septum originally described by Chen and Tsandoulas [42]. Even though there today exist more modern designs with better performance [52, 56],¹ the author nevertheless chose to use this type of horn since it turned up on the surplus market at a reasonable price. The acquired horn had previously been equipped with a ‘choke ring’ which the author decided to leave intact. See fig. 7.6! With this choke, the maximum dish f/D ratio which should be used with the horn is said to be approximately 0.36.

There are mainly two reasons why it is better to use circular instead of linear polarization for 23 cm EME communication. These are

¹ Ingolf Larsson (SM6FHZ) and Hannes Illipe (SM6PGP) have presented, though not formally published, some interesting feed horn designs as well [80].

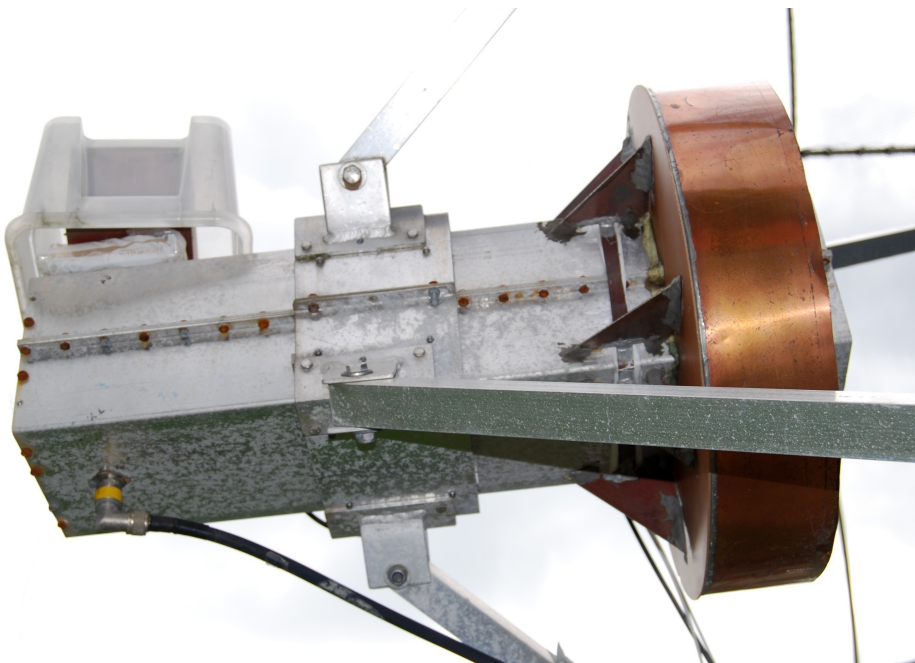


Figure 7.6 The OK1DFC septum-polarized feed horn with a choke ring added by the previous owner. Both the Rx- and Tx-port use standard female chassis mount N-connectors. Also shown are three of the four support struts and the ‘carriage’ holding the horn. The carriage makes it possible to adjust the position of the horn relative to the dish.

1. The spatial polarization offset between distant earth stations, resulting from *a)* the spherical nature of the Earth and *b)* the position of the Moon in relation to these two stations.
2. Faraday rotation in the ionosphere which rotates the polarization vector *non-reciprocally* by an unknown and varying amount.

Assuming *linear* polarization, item 1 could for example lead to a horizontally polarized wave transmitted from one location on Earth, arriving vertically polarized at another location. Complicating matters further is item 2 which in practice adds an unpredictable amount of rotation to the wave. These two effects combined result in a *polarization mismatch loss* which is hard to predict and also is non-reciprocal. The latter means that Faraday rotation does *not* operate in reverse when the direction of communication is reversed. This can lead to one station hearing the other, but not the other way around.

Consequently, one way of eliminating or at least mitigating the above mentioned problems is to use circular polarization. The obvious reason for this being that additional rotation due to items 1 and 2 is irrelevant, since the wave is already rotating. Given the relative advantage of circular polarization over linear polarization, it should come as no surprise that radio amateurs have chosen circular polarization for [EME](#) communication in the microwave bands.

For those deciding to build a feed horn on their own it is worth noting that the *tolerances* are not that critical, while *symmetry* on the other hand is [\[118\]](#). Furthermore, when mounting the horn in the dish it is important to align the horn perpendicular to the centre of the dish. In order to achieve this, the author used ordinary laser pointers which were placed in the horn and pointed towards the dish. It is also important that the so called *phase centre* of the horn aligns with the focal point of the dish, since failing to achieve this will ultimately result in suboptimal antenna gain performance. To this end, the author constructed a ‘carriage’ which enables to adjust the position of the horn relative to the dish. See [fig. 7.6!](#)

7.2 Transmitter subsystem

The transmitter subsystem consists of three *PAs*: Drive [PA 1](#), drive [PA 2](#) and the main [PA](#). These are shown in red in [fig. 7.1](#) on page [94](#) and will be discussed in more detail below. Other parts, which are used during both transmission and reception and which are shown in magenta in [fig. 7.1](#), are presented in section [7.4](#).

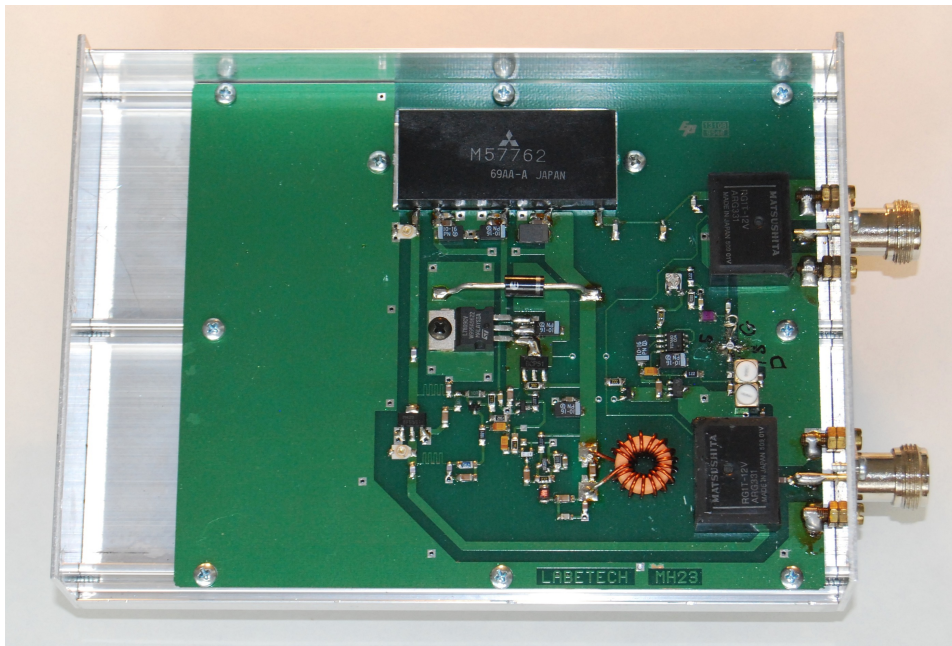


Figure 7.7 The interior of drive PA 1. Notice the M57762 amplifier module manufactured by Mitsubishi. The input and output connectors are of the N-type.

7.2.1 Drive PA 1

Drive PA 1, which drives PA 2, consists of the linear transmitter amplifier section of an ‘out door unit’ (ODU), once manufactured by a company named Parabolic AB. It was bought on the surplus market together with the transverter system, which will be presented in section 7.4.2. The ODU also contains an LNA receiver front-end, with an NF below 1 dB. As such, the ODU is intended to be mounted as close to the antenna as possible. In the author’s application however, it is only used indoors as a drive PA which needs to be activated using a 22 kHz control signal. This signal is supplied to the unit via the main coax, along with 13.5 V, from the ‘Parabolic interface’ which interconnects the ODU to the transverter. (This interface is omitted from the schematic representation in fig. 7.1 on page 94.)

The PA of the ODU is based on a Mitsubishi M57762 amplifier module capable of delivering 18 W output power. In the ODU however, this device is limited to outputting about 10 W at a maximum 25 mW input drive. The unit also has a helical filter with a half-power bandwidth of ± 25 MHz, centred at 1290 MHz. The spurious rejection of the transmitted signal is in excess of 60 dBc. See fig. 7.7!

7.2.2 Drive PA 2

The second drive PA, which drives the main PA, was built by the author and is based on a kit using two Motorola XRF286S LDMOS transistors. The XRF286S is a pilot production prototype of the more known MRF286. The ‘S’ indicates that the transistor is to be soldered to a copper heat spreader. These transistors were acquired on the surplus market while the kit containing the printed circuit boards (PCBs), using low-loss Rogers 4003c substrate, was bought from Jim Klitzing (W6PQL) [77]. A kit was chosen since buying an assembled product was deemed too costly. Solid state technology was furthermore chosen in preference to power grid tubes, in order to avoid lethal voltages and delicate mechanical work.

The input power to PA 2 is divided equally between the two transistors using a 90° hybrid coupler, which is part of the input PCB. Similarly, the output power is combined using an identical hybrid coupler which is part of the output PCB. Each transistor has its own bias control to ensure that they operate linearly at the correct quiescent current and generate the same output power. The combined output power can be monitored using a circuit at the output, consisting mainly of a small sampling coupler and a rectifying diode. Though currently not put into operation, this circuit could be used in the future to drive the automatic level control (ALC) of the transceiver. Please refer to fig. 7.8 for a closeup of the PA.

When driven by 10 W this type of PA should be able to deliver approximately 150 W, though the author only managed to reach slightly more than 90 W. Operating at this level the unit consumes about 12 A at 28 VDC. The reasons for and the possible solutions to these disappointing results are contemplated upon in section 9.1, dealing with the power amplifier measurements.

Unfortunately, due to the low DC efficiency, a lot of heat needs to be dissipated in the heat spreaders. This did not turn out to be a problem however, since each transistor is soldered to a copper slab, which in its turn is bolted to an aluminium heat spreader with thermal compound in-between. A radial blower fan is furthermore used to increase the cooling capacity, which guarantees adequate cooling even during high Tx/Rx duty cycles. However, to reduce both RF and audible interference during reception this fan is only active during transmission.

7.2.3 Main PA

The main PA is built using four of the same units which make up drive PA 2, thus totalling eight XRF286S LDMOS transistors. The input power is split equally between the four amplifier boards using three 90° hybrid couplers, etched onto a separate PCB using low loss PTFE substrate. Similarly, the

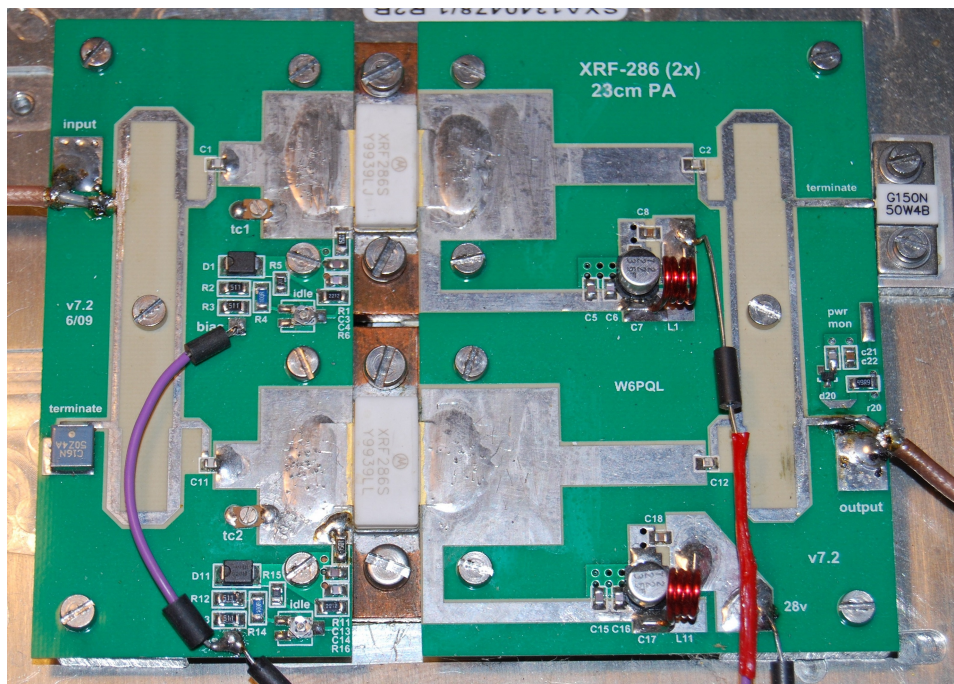


Figure 7.8 Drive PA 2 consisting of two XRF286S LDMOS transistor. These are soldered to two copper slabs which are bolted to an aluminium heat spreader. The PCBs are equipped with bias and impedance matching circuitry as well as RF chokes for the drain supply. Ferrite beads are used to reduce the influence of RF interference. The hybrid couplers are terminated with $Z_0 = 50 \Omega$ terminations, of which the one at the output hybrid is bolted to the heat spreader. A power monitoring circuit can be seen at the output to the right.

output power is combined using an identical triple hybrid coupler board. Both of these boards were bought from Jim Klitzing (W6PQL) [77]. Thin and easy to handle PTFE cables are used to connect the hybrid coupler boards to the four PA units. Please refer to fig. 7.9a which shows a closeup of the main PA and fig. 7.9b which shows the main PA and drive PA 2.

Unfortunately, since the main PA uses the same design as drive PA 2, it suffers from the same problems as these. Thus when driven by 40 W, instead of delivering the expected 600 W it only delivers about 370 W. Operating at this level the unit consumes about 50 A at 28 VDC from a power supply bought on the surplus market. For more on the PA measurements and the suspected reasons for and possible solutions to this poor performance, please refer to section 9.1.

As in the case with drive PA 2 there is a lot of excessive heat which needs to be dissipated. A sizeable aluminium heat spreader, salvaged from a surplus Ericsson cellular base station, is therefore used for all four PA units. The underside of this heat spreader consists of cooling flanges to which six powerful axial computer fans are mounted. However, to reduce RF interference these fans are only active during transmission. The same is true for the transistor bias voltage which is cut-off during reception, thus reducing the level of noise at the Tx-port and ultimately Rx-port of the feed horn. Please refer to section 4.6 for more on the latter.

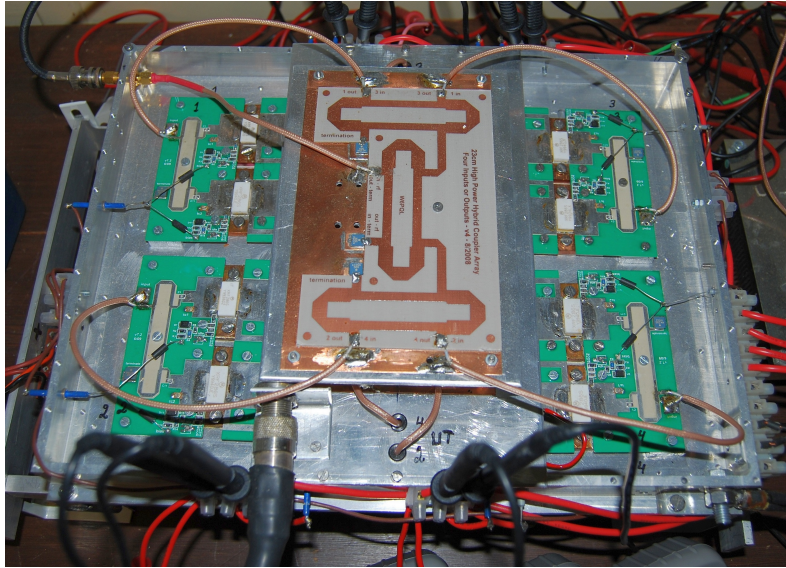
Unfortunately, the cooling capacity turned out to be inadequate during the Tx/Rx duty cycles used during the *echo-data acquisition process* presented in section 12.1. As we shall see in section 12.2, this manifested itself as a gradual decrease in the output power and the measured echo SNR. However, instead of increasing the cooling capacity, the DC efficiency should be increased by curing the presumed problems contemplated upon in section 9.1.

7.3 Receiver subsystem

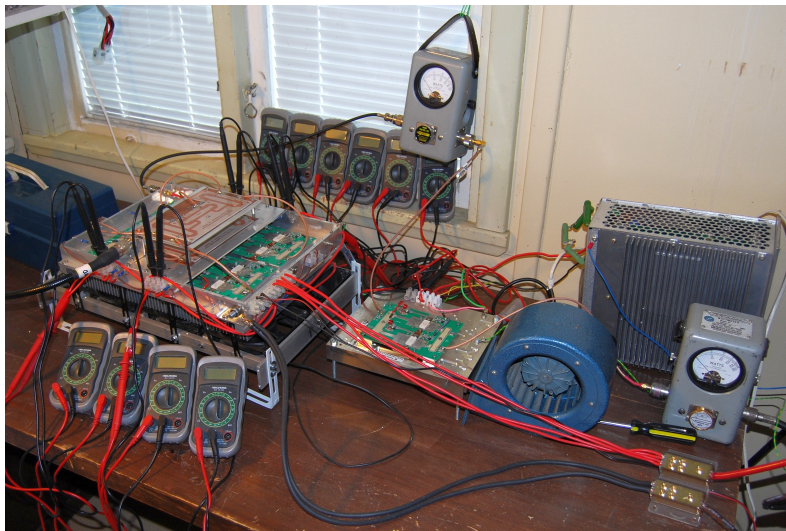
The receiver subsystem consists of a two-stage LNA, a coaxial protection relay and an interdigital band-pass filter (BPF). These are shown in green in fig. 7.1 on page 94 and will be discussed in more detail below. Other parts, which are used during both transmission and reception and which are shown in magenta in fig. 7.1, are presented in section 7.4.

7.3.1 Two-stage very low noise amplifier

In an EME communication system it is of utmost importance to have a *very low noise amplifier (VLNA)* as the first stage in the receiver front-end. Furthermore, since losses in front of the LNA are highly detrimental to



(a) Main PA closeup



(b) Main PA and drive PA 2

Figure 7.9 A closeup of the main PA is shown in (a) while (b) shows the system consisting of the main PA and drive PA 2. Eight ammeters are used to individually measure the drain currents of each transistor in the main PA. The triple hybrid coupler board, used for splitting the input power equally between the four PA boards, is clearly seen in the middle of the closeup. Hidden below this board is the equivalent output board, used for combining the output power from the four PA stages to a standard female chassis mount N-connector. Also shown are two wattmeters, a radial blower fan and the power supply for drive PA 2. Notice the thickness of the cables in the lower right corner of figure (b), supplying the main PA with 50 A at 28 VDC.

system performance, the LNA should be placed as close to the Rx-port of the feed horn as possible, with a minimum number of components in-between. This is especially important at 1296 MHz where the antenna temperature is very low. It is therefore sensible to choose an LNA with a front-end transistor having extremely low noise characteristics, and forsake other parameters such as intermodulation performance. Equally important, in order to reduce the effect of noise contributions from subsequent stages, is that the LNA has a very high gain. See section 4.4!

An LNA which satisfies these demands, and which has become somewhat of a standard among the EME community, is the ‘G4DDK VLNA’ by Sam Jewell (G4DDK) [72], which can be bought as a kit or as an assembled device. Jewell’s design is originally based on a dual-transistor design by Tommy Henderson (WD5AGO) et al. and has since also incorporated significant improvements as suggested by Sergei Zhutyaev (RW3BP) [123]. However, these improvements were not yet incorporated into the early version built by the author. The LNA has a super low noise GaAs-FET HEMT transistor (NEC, NE32584C) at its very input, followed by a second HEMT transistor (Avago, ATF54143) for increased gain. See fig. 7.10!

Typical NFs for the G4DDK VLNA range from about 0.25 to 0.45 dB, but NFs well below 0.20 dB have been reported with versions incorporating the improvements proposed by Sergei Zhutyaev (RW3BP) [123]. The LNA gain is typically in the region of 36 dB, which should guarantee that front-end noise predominates.² The NF of the author’s device was measured at 0.41 dB (28.6 K) with the accompanying gain amounting to 36.2 dB. Please refer to section 8.4 for more information on the LNA measurements.

7.3.2 Coaxial protection relay

The LNA is *very* sensitive to strong RF signals which can easily destroy the front-end transistor. Since transmitted power emerges at the Rx-port of the feed horn during transmission, the LNA thus needs to be isolated from this port during these instances. A *coaxial protection relay* is therefore connected between the Rx-port and the LNA input. The default operation of this relay is to protect the LNA in case the relay loses its power supply.

During transmission this relay ensures that both the LNA and the feed horn Rx-port are connected to 50 Ω terminations. The LNA is connected to the *internal* low-power termination of the relay, whereas the feed horn is connected to a termination which is *external* to the relay. The external termination must be able to handle several watts since some of the transmitted power emerges at the Rx-port after having been reflected in the dish. In case

² To ensure this, the noise power from the speaker of the transceiver should increase by about 17 dB when turning on the LNA.

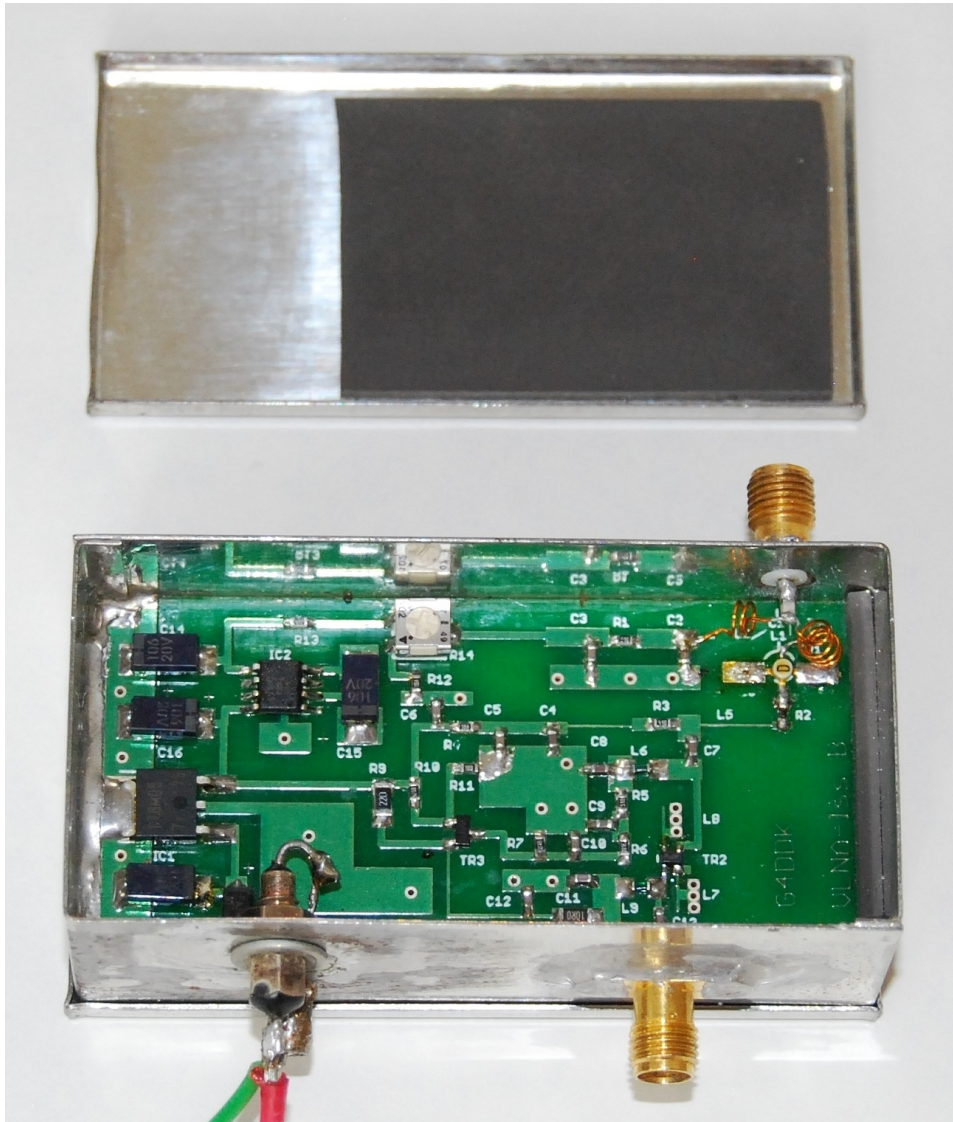


Figure 7.10 The G4DDK dual amplifier stage VLNA [72] used in the EME receiver subsystem. 12 V is supplied via the feed-through capacitor at the lower left of the tin box. This supplies the power regulator circuitry to the left on the PCB. The input SMA connector, the matching circuitry and the first HEMT transistor (NE32584C) are located at the top right of the box, while the output connector is at the lower right. In-between is the second HEMT transistor (ATF54143), used to increase the gain. The bias circuitry is seen in the middle and top of the PCB. Notice the grey RF absorbing material in the cover as well as along the right-hand side of the box, used for eliminating oscillations.

of the author's system, the power at the Rx-port was theoretically estimated at 4.4 W. Please refer to section 9.2 for more on this. It is debatable whether the feed horn actually needs to be terminated or not. However, this solution was chosen since the author assumes that the polarization property of the horn is designed with a 50Ω match at the Rx-port in mind.³

To really ensure that the LNA is adequately protected when isolated, the relay also needs to have a sufficient amount of port-to-port isolation. In case of the author's system, at least 67 dB of isolation is required. However, should the author wish to increase the main PA output power to 1 kW in the future, the relay isolation needs to be at least 72 dB. See section 9.2! At the same time the resistive loss of the relay needs to be kept at a minimum, so that the receiver noise performance is not considerably degraded. It should also be possible to mount the relay onto the Rx-port of the feed horn, using as few adapters as possible.

There are several coaxial relays on the market which satisfy these demands. One such relay, which was acquired by the author on the surplus market, is the 'HP 33311-60045 Coaxial Switch' which is of very high quality. It has more than 90 dB port-to-port isolation, less than 0.20 dB insertion loss, two internal terminations, three external ports with female SMA connectors and an operating frequency ranging from DC to 18 GHz. The unit is shown in fig. 7.11 with its cover removed.

It is obvious that the timing of the switching procedure is very important, that is transmission is not to be engaged before the LNA has been isolated. This is controlled by the sequencer which will be presented in section 7.4.4.

7.3.3 Interdigital band-pass filter

The *interdigital BPF* is connected between the LNA and the transverter. It has a -3 dB bandwidth of 33 MHz and an insertion loss of 0.2 dB at the 1296 MHz centre frequency. The filter, shown in fig. 7.12, was bought from ID-Elektronik GmbH [64].

This filter is very important since it operates as an *image rejection filter*. Without it, since the LNA is broadband, the noise from the mirror frequency⁴ of the transverter would be added to the *intermediate frequency (IF)* output. *This would increase the front-end noise of the system by about 3 dB, thus severely decreasing the receiver performance.*

Admittedly, the transverter incorporates an image rejection filter on its own. Nevertheless, the author considered it prudent to better be safe than sorry in regard to the negative consequences of inadequate image rejection.

³ The same reasoning is applied in footnote 17 on page 170, in regard to the Tx-port.

⁴ 1296 MHz minus two times the 144 MHz IF, equalling 1008 MHz.

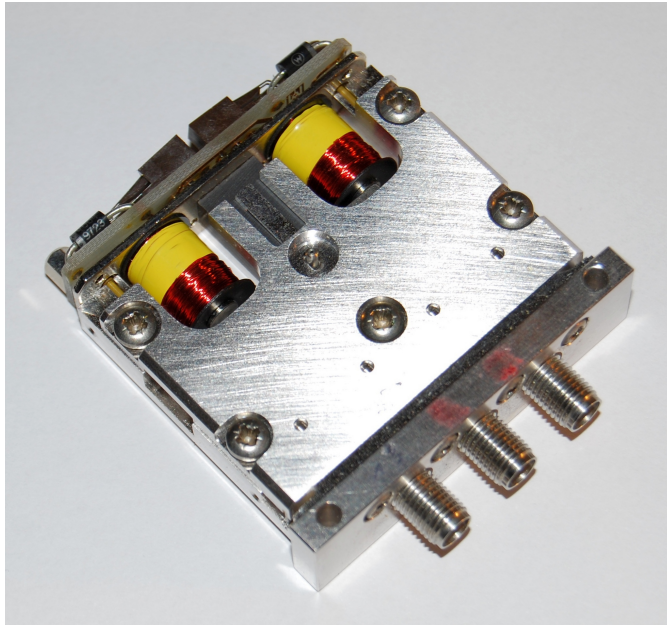


Figure 7.11 The coaxial protection relay with its cover removed. The unit makes a solid, high quality impression.



Figure 7.12 The interdigital BPF with a -3 dB bandwidth amounting to 33 MHz. The insertion loss is 0.2 dB at the 1296 MHz centre frequency.

7.4 Other system parts

There are some parts of the EME system which are used during both transmission and reception. These are shown in magenta in fig. 7.1 on page 94 and will be discussed in more detail below. They consist of the transceiver, the transverter, the audio and data interface as well as the transmit and receive sequencer.

7.4.1 Transceiver

For the generation and reception of the RF signal a so called *transceiver*⁵ is used, model 'IC-820H' manufactured by Icom Inc. [63]. This is a multimode amateur radio transceiver which has been on the market for several years. It is a two-band unit capable of operating at both 144 MHz and 432 MHz, making it popular for amateur radio satellite operation. It can operate in CW, SSB, AM or FM mode but it can also handle digital modes using external equipment. For this project however, it is set to SSB mode at 144 MHz, which is the IF of the transverter, but operates using CW. In this mode the output power can be regulated between 6 W and 35 W, so an external attenuator is required to match the output power to the input level of the transverter.

Various functions of the transceiver, such as PTT and CW, can be controlled through external connections located on the rear panel of the unit. Fixed audio level I/Os are found here as well, via an 'accessory socket'. Using these connections to control the transceiver, the audio and data interface as well as the transmit and receive sequencer enable automatic, computer controlled measurements to be performed. Such a procedure is presented in chapter 12, whereas more information on the interface and sequencer is given in sections 7.4.3 and 7.4.4.

7.4.2 Transverter: 144 MHz \rightleftharpoons 1296 MHz

During reception, the purpose of the so called *transverter* is to convert the 1296 MHz signal from the LNA (via the interdigital BPF) to 144 MHz IF and deliver it to the transceiver. During transmission, the 144 MHz signal from the transceiver is converted to 1296 MHz after which it is delivered to drive PA 1 (via the 'Parabolic interface' mentioned in section 7.2.1). As such, the transverter is a three-port device which is essentially connected to the LNA at the Rx-port, the transceiver at the IF-port and drive PA 1 at the Tx-port. Switching between the Tx-port and the Rx-port is handled

⁵ A transceiver being a combined **transmitter** and **receiver** in the same housing.

internally by the transverter after having received a signal from the transmit and receive sequencer, which will be presented in section 7.4.4.

The receive gain of the transverter can be adjusted between 0 dB and 23 dB but is set to 20 dB from the factory. Also, the NF of the device is less than 1.2 dB and the image rejection is at least 50 dB. The image rejection is however increased further by the interdigital BPF presented in section 7.3.3. On the transmitter side, the 144 MHz IF drive from the transceiver must be between 10 mW and 1 W. At the same time, the 1296 MHz output from the transverter is at least 100 mW. The spurious and harmonic suppression is in excess of 60 dBc. Finally, the switching delay is approximately 100 ms.

7.4.3 Audio and data interface

The *audio and data interface* was designed and built by the author. It is connected between the computer and the transceiver and its purpose is to

1. Route the audio between the transceiver and the computer.
2. Control the PTT and CW functionality of the system.
3. Control various transceiver functions via the so called ‘CI-V’ communication protocol.

The applications put to use in this project are the ones mentioned in items 1 and 2. Application 1 is used when recording measurements at AF, using the sound card of the computer. The audio from the transceiver is then obtained at a fixed level from the ‘accessory socket’ on its rear panel. Application 2 is realized by interfacing the computer serial port to the sequencer (for PTT) and the transceiver (for CW). Using Spectrum Lab (SL), which will be presented in section 7.5.1, this enables automatic computer control of for example measurements. This will be presented in sections 8.6 and 8.7 as well as in chapter 12.

Though not made use of here, application 3 could be of interest in future projects. Numerous software applications, among them SL, have the ability to communicate with the transceiver using the CI-V protocol. Using this, continuous Doppler correction could for instance be achieved.

A photo of the audio and data interface is shown in fig. 7.13. For a detailed circuit description, including a circuit diagram, please refer to appendix C.

7.4.4 Transmit and receive sequencer

The purpose of the *transmit and receive sequencer* or just *sequencer* is to handle the sequence in which the system is switched from Rx to Tx and vice versa. The design of such a device was presented in the 2007 edition of the



Figure 7.13 The audio and data interface, used for interfacing the computer to the rest of the system. The audio and serial port connectors are on the opposite side of the box.

ARRL Handbook under ‘TR Time Delay Generator’ [17, ch. 19]. The circuit essentially consists of a resistor–capacitor timer circuit, a voltage ladder and comparators buffered with high current transistors which connect with the outside world through four outputs. Exclusive OR (XOR) gates furthermore enable individual selection of active-high or active-low I/Os, using jumpers. Since a single-sided PCB design was supplied with the ARRL Handbook, the author decided to build this device using a home-etched PCB from FR4 laminate. The choice of output transistors was slightly modified however, in order to accommodate for devices which are easier to come by in Europe. The finished device is shown in fig. 7.14.

The switching sequence, from Rx to Tx, is initiated by an active-low PTT signal from either a ‘foot pedal’ or the computer serial port. Once PTT is applied, the four outputs of the sequencer initiate the following actions in the given order. The timing of these actions can be altered by adjusting the component values of the resistor–capacitor timer circuit or the voltage ladder.

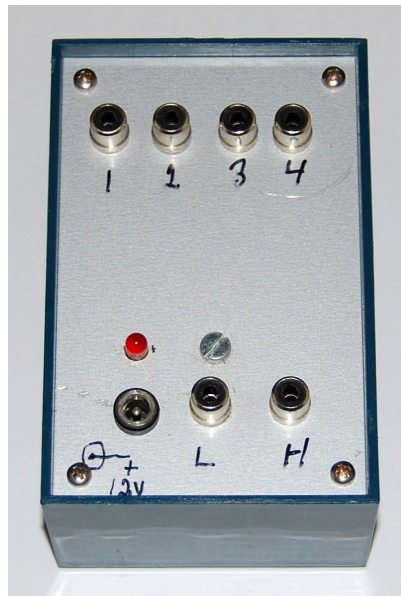
1. Switch the coaxial protection relay in order to isolate the LNA during Tx.
2. Switch the transverter from Rx mode to Tx mode.
3. Activate the gate bias of the main PA.
4. Switch the transceiver from Rx mode to Tx mode.

The reverse of this sequence occurs as soon as the PTT signal is removed. As long as PTT is active however, full output power is achieved by applying an active-low CW signal to the transceiver. This signal can either originate from the computer serial port or from a Morse key.

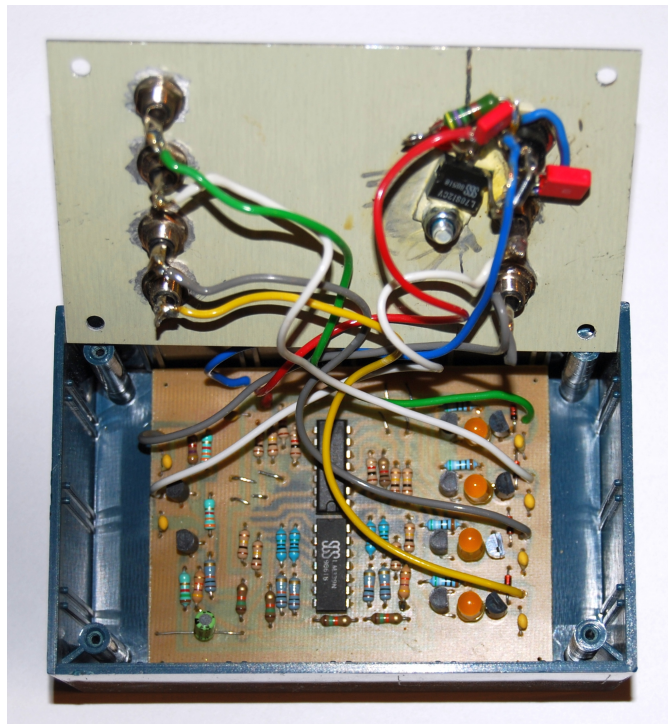
In regard to step 1, it is worth pointing out that the default operation of the coaxial protection relay is to protect the LNA in case the relay loses its power supply. Apart from this, there is yet another security measure to protect the LNA: Step 4 can only be carried out in case an additional mechanical relay (not a coaxial relay) is successfully closed in step 1. This means that the signal to the transceiver will be inhibited if step 1 was not successful. This is an extra protective measure in case the signalling lines to the protective coaxial relay get damaged or the sequencer malfunctions.

7.5 Software applications

A number of software applications have been used throughout this project. These will be briefly presented below in regard to their respective roles. For a more detailed description of each application, please refer to their respective documentation.



(a) Outside



(b) Inside

Figure 7.14 The transmit and receive sequencer (a) from the outside and (b) from the inside. The sequencer is used for handling the sequence in which the system is switched to and from transmission.

7.5.1 Spectrum Lab

An application which has been a tremendous asset throughout this project is ‘[Spectrum Lab](#)’ ([SL](#)) [34]. It is actively developed by Wolfgang Büscher ([DL4YHF](#)) [33] and runs on Windows as well as on Linux, using Wine. Even though the source code is closed, the applications is free to download and use.

[SL](#) can be seen as a ‘Swiss Army knife’ of signal processing, since it is extremely versatile. It has a steep learning curve but this is compensated for by an extensive user manual and an active user community, willing to answer questions. [SL](#) can accept signal input from sources such as [SDRs](#), packet streams, computer sound cards and audio files. It is also possible to exchange data and commands between multiple instances of [SL](#). For this project however, only the sound card and audio file options have been used. Signals are shown visually in the main screen in the form of a ‘waterfall’.

A very useful part of [SL](#) is its internal script interpreter which is programmed in a language similar to [BASIC](#). Most of [SL](#) functions can be controlled via this interpreter, which thus enables highly customizable and automated solutions for various tasks. Writing data to text and audio files, exporting images, changing [FFT](#) filter parameters, controlling an internal signal generator, controlling the serial port and performing numerous signal measurements is just a fraction of what can be done using the interpreter. There are also several programmable push buttons which enable user interaction, along with menus.

The above means that [SL](#) can be tailored to very specific needs. Many of the measurements in this project have thus been conducted using [SL](#). Section 8.6 describes how the [G over T](#) figure of merit was determined by means of a Y-factor measurement using the Sun. Continuing, section 8.7 illustrates how the antenna gain was determined in two different ways, also using solar measurements. Yet another example is presented in chapter 12, dealing with measuring the [SNR](#) of actual [EME](#) echoes. Finally, the broadening of the signal due to Doppler spread is analysed in chapter 13. Please refer to these chapters and sections for more details, including screenshots. Please refer also to appendix D which contains the source code for the associated interpreter scripts.

Needless to say, [SL](#) has been an almost indispensable tool throughout this project. Its usefulness and versatility can not be overestimated!

7.5.2 MoonSked

There are many software applications capable of controlling various antenna [Az/EI](#) rotators for the purpose of tracking for example the Moon and the

Sun. One such application, which is specifically aimed at amateur radio [EME](#) operators, is ‘MoonSked’ [22] by David Anderson (GM4JJJ) [21]. It is a commercial piece of software which is available for Windows, Macintosh and Linux. However, a limited trial version is also available.

Apart from its main purpose, that is real-time tracking of the Moon, MoonSked also offers other functions such as the calculation of Doppler shift, Doppler spread and times for mutual lunar visibility between stations. It also features a Moon footprint on a world map as well as a radio source map with noise source tracking capability.

7.5.3 EME Calc

‘[EME Calc](#)’ [83], developed by Doug McArthur (VK3UM) [82], is a Windows application used for estimating the performance of an [EME](#) system. As such, it can be used to estimate the design of a new system or to check for problems in an existing one. In this project however, it has mainly been used as a tool for estimating ‘ballpark values’ of various system parameters. Even though the source code is closed, the applications is free to download and use.

7.5.4 Eagle PCB design software

For documentation purposes the author decided to draw the circuit diagram of the audio and data interface, presented in section 7.4.3, using some sort of [computer-aided design \(CAD\)](#) software. To this end the author chose ‘[Eagle PCB Design Software](#)’ [38] by Cadsoft [37], which is popular among hobbyists and professionals alike. [Eagle PCB](#) is a commercial piece of software which is available for Windows, Macintosh and Linux. However, a free but limited edition exists for non-commercial use. The reason for choosing [Eagle PCB](#) was that the author had prior experience using this application, from earlier projects. The resulting circuit diagram, accompanied by a detailed circuit description, can be found in appendix C.

Chapter 8

Receiving system measurements and estimations

The necessary theory has been covered in previous chapters. Associated with this theory are various system parameters, the measurement and accompanying methods and results of which will now be presented. Furthermore, these measurements will be used to calculate and estimate other system parameters of interest.

Some *sources of uncertainty in LNA measurements* and associated measurement difficulties, will be presented first. Second, an *assessment of the combined uncertainty in LNA measurements* will be given, followed by a section on *reducing NF uncertainty through alternative measurement methods*. Two *LNA noise temperature and gain measurements* will then be presented, leading to a *receiver subsystem noise temperature estimation*. Next, the *G/T_{sys} figure of merit measurement* will be dealt with. This will be followed by two *antenna gain measurements*, making it possible to perform a *total system noise temperature estimation*. From this, the *minimum detectable signal requirement* and an *antenna temperature estimation* will be obtained. Finally, the *antenna temperature increase due to lunar noise* will be estimated.

Knowledge attained in this chapter will be used in chapter 10 to calculate the EME link budget, as well as in chapter 11 to estimate the SNR of the EME echoes.

8.1 Sources of uncertainty in LNA measurements

The basic theory regarding LNA gain and noise measurements, using the Y-factor method, was presented in section 4.7. Even though this theory is rather straight forward, there are quite a few pitfalls associated with real life NF measurements which one should be aware of. This is especially true when using DNSs to measure very low NF devices having a high degree of input reflection, that is a low return loss. Results obtained from such measurements might suffer from such a high degree of uncertainty, that they can be considered totally misleading.

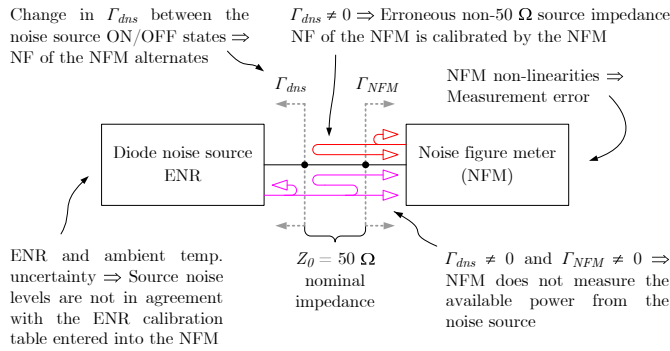
This section will therefore serve to present some of the difficulties and sources of uncertainty to have in mind, when measuring LNAs using the Y-factor method. It will also present ways in which some of these uncertainties can be mitigated. However, since the field of low noise measurements could in itself be the subject of many a thesis, its goal is not to present an in depth analysis of these matters. Rather, its goal is to present an oversight, pointing to various sources for further study. Two such sources are sections 4.2 and 4.7 of this thesis, which are advised reading before proceeding.

As was explained in section 4.7 the Y-factor measurement procedure is divided into mainly two parts: the *calibration process* and the *measurement process*. Both are associated with their respective sources of uncertainty, some of which are presented in fig. 8.1. This figure will serve as a basis for the discussions in this section.

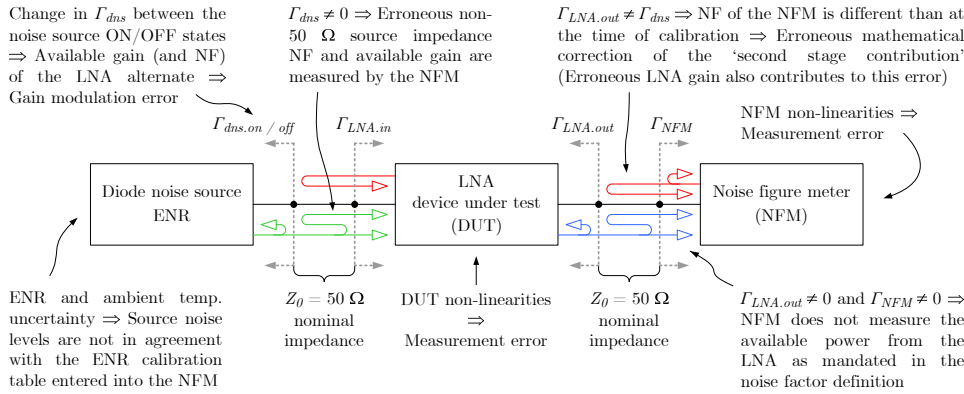
It is worth remembering that the noise factor definition, given in section 4.2, does *not* mandate which source impedance to use when specifying the noise factor of a device. In practice however, the source impedance is given by a *nominal system impedance* $Z_0 = 50 \Omega$.¹ Every part in a system is designed for, though this does not necessarily mean matched to, this system impedance. For example, the source impedance from a DNS or a signal generator should be *fixed* to Z_0 , for maximum power transfer, while the input impedance of an LNA would have some amount of mismatch so as to achieve a minimum NF. The reference impedance is shown *symbolically* in fig. 8.1 as short pieces of lossless line having an impedance equal to Z_0 .

Even though the information in this section will focus on measurements performed using NFMs, its applicability will not be entirely limited to such instruments. Other means of Y-factor measurement will be subject to the same or similar difficulties as those of NFMs. Information in this section will hence be of interest in these cases as well. For more on the subjects presented in this section, please refer to the literature [4, 10, 12, 13, 14, 15, 27, 28, 29, 43, 103, 120].

¹ 75 Ω is used in certain applications such as for example consumer television systems.



(a) Calibration process



(b) Measurement process

Figure 8.1 Sources of uncertainty during (a) the calibration process and (b) the measurement process. Not shown are additional sources of uncertainty due to insertion losses from connectors and adapters. These are dissipative (noisy) or reflective in nature and must be accounted for to the best of one's ability. Red (□) arrows represent unwanted reflected powers due to noise parameter effects. Magenta (□) arrows represent the diode noise source power and its unwanted reflections during calibration. Green (□) arrows represent the diode noise source power and its unwanted reflections during measurement. Blue (□) arrows represent the output noise power from the LNA (DUT), including its unwanted reflections. $\Gamma_{dns.on}$, $\Gamma_{dns.off}$, $\Gamma_{LNA.in}$, $\Gamma_{LNA.out}$ and Γ_{NFM} are the reflection coefficients of the respective parts, relative to $Z_0 = 50 \Omega$.

8.1.1 Warm-up stabilization of the instrument and LNA

To reduce uncertainties related to temperature drift and non-linearity, it is important that the entire measurement system must be allowed to warm-up for about an hour prior to calibration and measurement. This includes not only the measurement equipment, but also the LNA. Once the warm-up is complete, it is equally important that the ambient room temperature is kept reasonably constant throughout the calibration and measurement procedures. Instrument calibration will be in error if the physical temperatures of the NFM or noise source change between calibration and measurement. Furthermore, the uncertainties specified in the technical specification of the noise source are only valid at a certain ambient temperature interval, which must thus be adhered to. The LNA is also susceptible to changes in physical temperature, since this changes its NF. See also sections 8.1.7 and 8.1.8!

8.1.2 Extraneous interference

Since noise contributions from typical EME LNAs are small, NF measurements of these devices are sensitive to extraneous RF interference. Such interference, which might enter the measurement set-up either through radiation or conduction, will masquerade as noise and thus have an adverse effect on the accuracy of NF and associated gain measurements. Interference problems might be suspected if measurement results are unstable or show anomalies at certain frequencies during a frequency-swept measurement. In this case, a closer inspection with a spectrum analyser or a receiver is advisable, so as to ascertain the source of interference and its impact.

General sources of interference include for example mobile phones, base stations, fluorescent lights, TV or radio transmitters, amateur radio equipment, lab equipment, computers, unshielded data-bus cables, local oscillators, switched-mode power supplies, WLAN access points, microwave ovens, electric fences, pagers, etc. It is evident from this list that some interference issues can be mitigated by simply turning off the interfering equipment. In other cases, when possible, skipping over certain measurement frequencies might suffice. Usually though, care must be taken to employ adequate shielding of cables, the LNA itself and possibly even the measurement equipment. Shielding is especially important at points in the measurement set-up where signal levels are at their lowest.

Please refer to the literature for more information [14, ch. 3.1][15, hint 2].

8.1.3 Measurement bandwidth

Even though the NF of a device is independent of its bandwidth, which is evident from eq. (4.17) on page 44, the bandwidth *does* matter during NF measurements. The reason for this is that the measurement bandwidth has to be the same during both the calibration process and the measurement process. In practice, this means that the bandwidth of the NFM has to be narrower than the bandwidth of the DUT. If this is *not* the case, the NFM will measure more noise from the noise source during the calibration process than during the measurement process. This will lead to an error, understating the measured gain and NF of the device.

Frequency instability in the NFM can lead to a similar problem to the above, if the instrument pass band drifts away and ceases being overlapped by the DUT pass band. This problem could arise if the measurement bandwidth is about the same width as the device bandwidth. A margin of safety is therefore advisable. Of course, changing the measurement bandwidth also influences the averaging time needed to reduce jitter. See section 8.1.4!

A more general way of stating the above, is to say that the amplitude of the device bandwidth must be constant over the measurement bandwidth. This is assumed in the equations presented in section 4.7.

For more information, please also refer to the literature [14, ch. 3.7][15, hint 8].

8.1.4 Display jitter

Due to the random nature of noise, there is a statistical uncertainty in the mean power levels measured by the NFM. This manifests itself as *display jitter*, that is a fluctuation in the NF value presented to the operator. Fortunately, this measurement uncertainty can be reduced by means of time integration and an increased measurement bandwidth.

Since an NFM is essentially a total power radiometer, the theory presented in section 5.6 is applicable in estimating this kind of uncertainty. As can be seen from eq. (5.16b) on page 77 it decreases as $1/\sqrt{B\tau}$, where B is the measurement bandwidth and τ is the integration time. Thus, when decreasing the measurement bandwidth the integration time has to increase with the same amount, so as not to influence the measurement uncertainty. In other words, there will always be a trade-off between speed and accuracy.

Naturally, the described uncertainty is not only present during the measurement process, but during the calibration process as well. As a result, care should be taken to use as wide a measurement bandwidth as permissible (see section 8.1.3) and as long an integration time as tolerable, during the

calibration process. This will have a favourable impact on the measurement uncertainties of all subsequent measurements.

For more information, please also refer to the literature [13, pg. 15][15, hint 4].

8.1.5 Noise source ENR selection

Besides its frequency range, a noise source is also characterized by its ENR value. A so called *low ENR noise sources* has a nominal ENR value of about 6 dB, while a *high ENR noise source* has a corresponding value of about 15 dB. This is equivalent to a hot temperature of about 1400 K and 9500 K respectively.

Which type of noise source to use depends on the NF of the DUT. The reason for this is that a high NF device masks the noise from the noise source, thus reducing the Y-factor measured by the NFM and vice versa. This can be seen by solving for Y in eq. (4.56b) on page 63. Furthermore, since it is more difficult to accurately measure reduced Y-factor ratios, even with longer integration times, one must use a high ENR noise source to counteract this effect when measuring high NF devices.

However, since a low ENR noise source has several advantages over its high ENR counterpart, the former should always be used whenever possible. When measuring low NF devices, such as EME LNAs, this is always the case. A general rule of thumb is that NFs up to about 10 dB above the noise source ENR can be measured by the NFM.

Some of the advantages of using a low ENR noise source are the following:

1. A smaller measurement range reduces the measurement uncertainties related to non-linearity in the LNA and NFM. See sections 8.1.9 and 8.1.10!
2. A smaller measurement range might also reduce the NF of the NFM and thus the measurement uncertainty. See section 8.1.11!
3. Mismatch uncertainty resulting from the impedance mismatch of the noise source is reduced by an internal attenuator. See section 8.1.13!
4. Gain error, resulting from the change in the output impedance of the noise source between its hot and cold states, is also reduced by the internal attenuator. See section 8.1.14!

For more information, please also refer to the literature [13, pg. 12][14, ch. 3.2][15, hint 1].

8.1.6 ENR calibration uncertainty

A diode noise source is characterized by a calibration table, providing calibrated ENR values at various operating frequencies. The NFM uses these values when calculating² the NF and gain of the LNA being measured. Since the calibration data is traceable to national standards, there is nothing to be done about the accompanying ENR uncertainty, apart from regular noise source recalibrations.

However, it is desirable to know to what extent the calibration uncertainty influences the final measurement uncertainty of the LNA NF. This is most easily estimated by studying eq. (4.56b) on page 63, from which it is evident that *any uncertainty in the ENR is directly reflected in the uncertainty of the final NF measurement, dB for dB*. Even though this statement is a slight simplification of reality, it is a very accurate one.

Consequently, it is of interest to know the ENR uncertainties of commonly used diode noise sources. Studying the typical characteristics of the Agilent N4000A SNS series noise source (4.6 to 6.5 dB ENR), we learn that the expanded ENR uncertainty is equal to ± 0.16 dB in the 10 MHz to 1.5 GHz range [9, pg. 7]. The corresponding value for the Agilent 346A noise source (4.5 to 6.5 dB ENR) is ± 0.21 dB [11, pg. 7]. According to Agilent, these ‘characteristic values are met or bettered by 90% of instruments with 90% confidence’. Assuming Gaussian distributed measurements, a 90% confidence interval equals approximately ± 1.645 standard deviations, that is a coverage factor equal to 1.645. The characteristic standard uncertainties³ of the two noise sources can thus be calculated from their expanded uncertainties above. The results of these calculations are presented in table 8.1. Given to the rightmost in this table are also the corresponding uncertainty values obtained from the Agilent Technologies noise figure uncertainty calculator [75]. These are a bit less conservative than the characteristic values given in the mid-column.

The results given in table 8.1 are problematic in regard to absolute very low NF measurements, since they are in the same order of magnitude as the NFs being measured. Current state of the art EME LNAs at 1296 MHz are no exception to this, since their NFs are in the vicinity of a mere 0.13 dB or about 8.8 K. Even though an instrument specific standard uncertainty value for an N4000A noise source, calculated from its measurement calibration report, is lower at about ± 0.066 dB at 1296 MHz, this still poses a problem for absolute measurements. *Relative* measurements on the other hand, are not influenced by the ENR uncertainty. The reason being that the ENR

² See equations presented in section 4.7!

³ A standard uncertainty being equal to a ± 1 standard deviation uncertainty.

Table 8.1 ENR standard uncertainties of the Agilent N4000A and 346A noise sources according to their typical characteristics [9, 11] as well as to the Agilent NF uncertainty calculator [75].

Noise source	ENR	
	standard uncertainty	
	$u(\text{ENR})^a$ (dB)	$u(\text{ENR})^b$ (dB)
N4000A	± 0.097	± 0.075
346A	± 0.13	± 0.10

^a According to [9, 11]

^b According to [75]

uncertainty is constant regardless of which LNA is being measured, provided that the frequency is the same.

Ambitious investigations performed by Leif Åsbrink (SM5BSZ) and Mart Sakalov (SM0ERR) indicate that the N4000A ENR uncertainty, as specified by Agilent Technologies, is rather conservative. The results of their measurements suggest an ENR uncertainty of no more than 0.03 dB [6].

It is worth mentioning that the author has no reason to believe that noise sources from Agilent are any worse than those of other manufacturers. Agilent states that ‘a significant proportion of the expanded uncertainty ($U(Y)$) is based on the uncertainties provided by the National Standards Institutes’. Thus, the levels of uncertainty seen are more likely inherent to diode noise sources as such.

Finally, one must keep in mind that the ENR uncertainty, even though being a significant contributing factor, is only *one* component of the combined measurement uncertainty, which will be greater still. Another significantly contributing factor is the mismatch uncertainty, which will be presented in section 8.1.13, and possibly the gain error which is covered in section 8.1.14.

For more information, please also refer to the literature [103, pg. 11–13].

8.1.7 Physical temperature of the noise source

As was described when the concept of ENR was introduced on page 62, the values in the ENR calibration table assume a cold reference temperature equal to T_0 . This is given mathematically by eq. (4.53a). Since the cold temperature of the DNS is equal to its physical temperature, this implies that its physical temperature has to be equal to T_0 for the ENR values to reflect

reality. If this is *not* the case the LNA NF calculated by the NFM will be in error, unless the discrepancy from T_0 is accounted for in the calculations.

The just mentioned discrepancy can be visualized in fig. 4.11 on page 61, where the sloping red line in this figure will move upwards if the physical temperature of the noise source is greater than believed and down otherwise. This does not change the measured gain, since the slope remains constant.⁴ The intersection with the Y-axis, equalling the device NF, does change however.

Of course, the above implies that the correct physical temperature is entered into the NFM by the operator, or supplied to it automatically by the noise source. In either case there will be uncertainties involved in measuring these temperatures, thus increasing the overall uncertainties of the final NF and gain values. Please refer to the technical specification of the noise source for detailed information regarding uncertainties related to temperature.

For more information, please also refer to the literature [15, hint 10].

8.1.8 Physical temperature of the LNA

For a passive two-port, such as an attenuator, the NF changes according to eq. (4.22) on page 48. Naturally, the NF of an LNA also changes as a function of its physical temperature. High accuracy measurements [7], performed by Leif Åsbrink (SM5BSZ) [1] on a G4DDK VLNA [72] among others, reveal a dependency on its equivalent input noise temperature equal to 0.13 K/°C. The measured version of the G4DDK VLNA is similar to the one presented in section 7.3.1 as part of the EME receiver subsystem.

Comparable types of LNAs, also based on GaAs-FET HEMT transistors, will probably show similar dependencies. A 30°C change in physical temperature, for example due to season, will thus amount to more than a 0.05 dB change in NF for a typical EME LNA. The physical temperatures of the LNA should therefore be recorded at the time of the measurement, in case further corrective calculations are needed.

8.1.9 Non-linearity of the LNA

The concept of noise factor, presented in section 4.2, is only relevant to linear two-port devices. The same applies when measuring the NF of an LNA by means of the Y-factor method, introduced in section 4.7. The importance of linearity becomes especially evident when studying fig. 4.11 on page 61. If

⁴ These results are only true for a DNS, where $T_{hot.in}$ is directly proportional to $T_{cold.in}$. If on the other hand $T_{hot.in}$ is independent of $T_{cold.in}$, the gain changes as well since $T_{hot.in}$ remains constant.

the LNA is *non*-linear the sloping red line in this figure will instead be curved, thus introducing uncertainties in the linear equations used to calculate the NF and available gain.

Since noise is random in nature, it is important to have in mind that its peak values will be considerably higher than its mean value. This can lead to a non-linear behaviour of the LNA due to peak compression, reducing the measured Y-factor and thus resulting in a too high NF measurement. This can be seen from eq. (4.56b) on page 63. To avoid the LNA from entering its non-linear region, a low ENR noise source should be used. Furthermore, when tuning the LNA the bias point of the transistor must be chosen to be sufficiently far away from a point of saturation. Last but not least, extraneous interference can also lead to non-linear behaviour if left unremedied.

For more information, please also refer to the literature [14, ch. 3.6.1][15, hint 5][103, pg. 5].

8.1.10 Non-linearity of the noise figure meter

A non-linear behaviour of the PMR in an NFM will lead to measurement uncertainty. This situation is comparable to what was described in section 8.1.9 regarding a non-linear LNA. One difference though, is that the non-linearity of the NFM is present during not only the measurement process, but during the calibration process as well.

Using a low ENR noise source will utilize less of the dynamic range of the PMR, thus reducing the effect of non-linearity. A high gain DUT could still pose a problem though, if the instrument is not auto-ranging. A noise limiting filter or an attenuator can be of use in these circumstances.

Fortunately, NFMs are built to be very linear, which is especially true for modern instruments. As a result, this so called *instrument gain uncertainty*, even though being the primary instrument uncertainty component, has a minor influence on the combined measurement uncertainty.

Please refer to the technical specification of the NFM for details regarding instrument non-linearity. For more information, please also refer to the literature [14, ch. 3.6.1, 6.2][15, hint 5][103, pg. 6].

8.1.11 Noise figure of the noise figure meter

Using a high ENR noise source might require the auto ranging function of the instrument to add internal attenuation, so as to limit instrument non-linearity. Since attenuators add noise this would result in an increase in the instrument NF. This would in its turn increase the measurement uncertainty, especially if the gain of the DUT is low. This can all be seen by studying the

‘master equation for RSS uncertainty’, given in Agilent Technologies AN57–1 [13, ch. 6.1].

As a result of the above, low ENR noise sources should be used whenever possible so as to reduce measurement uncertainty. See also section 8.1.5! In addition, a high gain DUT would help to further reduce the measurement uncertainty added by the second stage contribution. Fortunately, EME LNAs tend to be very high gain devices since this reduces the overall NF of an EME system, as was described in section 4.4. The above mentioned uncertainty is thus relatively small when measuring these types of LNAs.

Apart from the instrument NF adding to the measurement uncertainty, the uncertainty of the instrument NF itself does so too. This can be seen by performing a more in depth study [13, ch. 5.3] of the above mentioned RSS uncertainty equation. However, this so called *instrument noise figure uncertainty* has a minor influence on the combined measurement uncertainty.

Typical instrument NFs range from about 5 to 15 dB depending on the frequency and type of instrument used. Regular measurement recalibrations should be performed to compensate for possible drift due to instabilities. See sections 4.7.2 and 8.1.1!

Please refer to the technical specification of the NFM for details regarding instrument NF and its accompanying instrument uncertainty. For more information, please also refer to the literature [14, ch. 6.2][15, hint 1].

8.1.12 Losses from adapters etc.

Even though it should be avoided, it is sometimes necessary to use components such as adapters between parts in the measurement circuit. These introduce insertion loss which can be broken down into two parts, each with adverse effects on NF measurements:

1. Resistive loss which
 - a. attenuates the noise passing through it.
 - b. adds thermal noise to the measurement according to section 4.3.
2. Mismatch loss which increases the measurement uncertainty due to reflections. See fig. 8.1!

This section will deal with item 1 while item 2 will be covered in section 8.1.13.

Measuring the insertion loss can be done by means of for example a network analyser or a signal generator in combination with a PMR. Separating this small measurement into resistive loss and mismatch loss can prove a bit more problematic though. This matter has been examined in more detail by Leif Åsbrink (SM5BSZ) [5].

If adapters are needed, one should strive to place these where signal levels are at their highest. In the case of an amplifier, this is *after* the DUT. They should then be included in the NFM calibration process, in which case their NFs are absorbed into the instrument NF. If not included in the calibration process, manual corrections must be applied to the measurements using eqs. (4.17), (4.21b) and (4.23) on pages 44, 48 and 49.

If it is unavoidable to use adapters *before* the amplifier DUT, these must *not* be included in the calibrations process but must instead be accounted for manually. This is done by applying the same equations as mentioned above. Naturally, this also entails measuring the resistive loss of the adapters. Since the plane of reference for the ENR values is at the output of the noise source, the adapter NFs are absorbed into the DUT NF during measurement.

Doing the math, one can see that any resistive loss prior to the DUT will add directly, dB for dB, to the measured NF. This also means that *any uncertainty in determining this loss will contribute, dB for dB, to the final uncertainty of the corrected NF measurement*. Strictly speaking, these two statements are only true if the physical temperature of the adapter is equal to T_0 . For realistic temperatures in the vicinity of T_0 though, the difference becomes negligible for small losses, such as those associated with adapters.

Of course, the above mentioned corrections do not only apply to adapters. Losses introduced by cables, attenuators, isolators and switches etc. need to be treated in the same way. It is worth noting that contact pressure, or rather the increased resistance caused by a lack of it, is an important factor in regard to losses.

For more information, please also refer to the literature [14, ch. 3.9, 4.1–4.3] [15, hint 9].

8.1.13 Mismatch between the noise source, DUT and NFM

The noise factor definition, given in section 4.2.1, builds upon the concept of *available power*. What this means for NF measurements, is that we have to be able to measure the available noise power from the noise source, as well as from the output of the DUT. In a $50\ \Omega$ environment this implies that the noise source, the output of the DUT and the NFM all have to be matched to $50\ \Omega$.⁵ The equations in section 4.7, used by the instrument to calculate the NF and available gain of the DUT, rely on this to be the case. In reality though, impedance mismatch is present during both the calibration and measurement processes. This leads to noise power reflections, resulting in gain and NF measurement uncertainties which are both frequency and phase

⁵ As in the case of the noise factor definition, a possible mismatch at the *input* of the DUT is part of its properties and hence its NF. This is another way of saying that its NF is a function of source impedance.

dependent. See fig. 8.1! Thus, *we do not actually measure the true 50 Ω NF and gain of a DUT, even though the result is presented as such.* This unknown discrepancy is estimated and added to the overall measurement uncertainty.

Naturally, one would assume that detailed knowledge of the various reflection coefficients could be used to mathematically compensate for the adverse effects of mismatch on measurement accuracy. That is, one could maybe use a network analyser with noise measuring capability, to try and figure out what the true gain and NF measurements would have been in a perfect 50 Ω environment. *While such an approach improves the gain measurement, it omits to consider the noise parameter effects associated with both the DUT and the NFM.* For, as was explained in section 4.2.2, the internally added noise of a device, and thus its NF, changes as a function of source impedance. That is, *even if we manage to mathematically correct the gain measurement, we still have no way of knowing what the true 50 Ω NF of the device would be.* Even worse, correcting the gain might make the resulting NF even *less* accurate, since the gain is used in correcting for the second stage contribution. See eqs. (4.61) and (4.62) on page 65!

The noise parameter effect arises in regard to the NF of the NFM as well. If the impedance of the noise source differs from the output impedance of the DUT, the NF of the NFM will change slightly between the calibration and measurement processes. See fig. 8.1! This will increase the uncertainty of the second stage contribution, and thus also the uncertainty of the final DUT NF. Fortunately though, this effect is reduced by the gain of the DUT. This can also be seen in eqs. (4.61) and (4.62) on page 65.

The noise parameter effect is one reason why the influence of mismatch has to be treated as an uncertainty when using an NFM. Even a network analyser is incapable of providing the complete information needed to correct for the adverse effect of mismatch on NF measurements. An additional impedance tuner, presenting a number of known complex source impedances to a device, is needed to mathematically determine how the device NF changes with source impedance, that is determining its noise parameters. Please refer to section 4.2.2 and the literature referenced to in that section.

Mismatch is, together with the ENR calibration uncertainty presented in section 8.1.6, one of the most predominant sources of uncertainty in NF measurements. Care must therefore be taken to try and minimize it. The use of unnecessary adapters and cables etc. should be avoided, while isolators and attenuators can be used to reduce remaining reflections. Furthermore, a low ENR noise source should be used whenever possible. These contain an attenuator which not only limits the ENR, but also reduces reflections. Please also refer to section 8.1.5.

When every step has been taken to minimize mismatch in the measurement set-up, it is of interest to estimate its final impact on measurement uncertainty. Since the noise parameter effects remain unknown, this estimate is limited to the effect multiple reflections have on the amount of noise source power being delivered to the NFM. This determines the Y-factor and gain measurements, which are used by the instrument to calculate the final NF by means of equations from section 4.7.

Using an example consisting of a mismatched generator and a mismatched load, the effect of multiple reflections on the power delivered to the load can be shown [43, ch. 15.2.1] to be governed by the following factor:

$$M = |1 - \Gamma_g \Gamma_l|^2 \quad (8.1)$$

where Γ_g and Γ_l are the respective complex reflection coefficients of the generator and the load, relative to Z_0 . If these are known, the effect of multiple reflections can be entirely compensated for. Typically though, only the magnitudes of Γ_g and Γ_l are known, either through datasheet information or measurements, while their phases remain unknown. This is another reason why the influence of mismatch has to be treated as an uncertainty. Using the magnitude information alone, it is possible to calculate the extremes of M . Employing certain statistical assumptions though, it is also possible to determine its standard uncertainty $u(M)$.

The most common prerequisites to adopt when determining $u(M)$ is to assume that Γ_g and Γ_l take on their maximum magnitudes as presented in datasheets, while assuming a uniform probability distribution to their phases. This results in M having a U-shaped probability distribution, with a standard uncertainty given by [43, ch. 3.2.1]

$$u(M) = \sqrt{2} |\Gamma_g| |\Gamma_l| \quad (8.2)$$

In a white paper published by Agilent Technologies [10], this standard uncertainty is shown to be *very* conservative though. Alternative calculations are presented, relying on facts showing that the magnitudes of Γ_g and Γ_l are Rayleigh distributed. These result in a more realistic value for $u(M)$, amounting to approximately only one sixth of what is given by eq. (8.2).

Even though $u(M)$ does not account for noise parameter effects, these are small in comparison to the change in gain. This is especially true when measuring LNAs tuned to the region of their minimum NF, where the change in NF is particularly shallow.

On a final note, it is worth remembering that minimizing the NF of an LNA also means having to tolerate some degree of mismatch at its input. Ironically, this also increases the uncertainty in measuring its NF! A solution to this could be to use an isolator and in some cases an attenuator between

the noise source and the LNA during measurement, also making sure to minimize reflections between the noise source and the isolator. Naturally, one would then have to compensate for the loss introduced by the isolator and attenuator. Unfortunately isolators are inherently narrow band,⁶ but this poses no problem when measuring LNAs used in narrow band EME communication. Though, as was explained in section 8.1.3, one must keep in mind that the measurement bandwidth of the NFM has to be narrower than that of the isolator and DUT.

For more information, please also refer to the literature [13, pg. 10–11, 18, 22–23][14, ch. 3.4][15, hint 3][12, pg. 11–18].

8.1.14 Varying noise source impedance and gain error

Unfortunately, the problems described in section 8.1.13 are not the only ones related to mismatch. The case is that the output impedance of the noise source not only *differs* from Z_0 , it actually *changes* vectorially between the hot and cold states of the noise source. What this implies, is that the available gain and the internally added noise of the LNA alternate between two values depending on if the noise source is either turned on or off, leading to measurement uncertainty.

Mathematically this change manifests itself in eqs. (4.48a) and (4.48b) on page 60, where $G_{tp.a}$ and $T_{tp.e}$ of the two-port now have different values in each of these two equations. Thus, the resulting measured Y-factor is no longer given by eq. (4.50) on page 61 but rather by eq. (8.3) below, where the subscript notation has been changed from ‘tp’ to ‘LNA’.

$$Y = \frac{G_{LNA.on}}{G_{LNA.off}} \cdot \frac{T_{hot.in} + T_{LNA.e.on}}{T_{cold.in} + T_{LNA.e.off}} \quad (8.3)$$

$G_{LNA.on}$ and $T_{LNA.e.on}$ as well as $G_{LNA.off}$ and $T_{LNA.e.off}$ are the gains and noise temperatures of the LNA, existing at the actual source impedances being presented to it when the noise source is either turned on or off respectively. As before, $T_{hot.in}$ and $T_{cold.in}$ are the output noise temperatures of the noise source.

The change from $T_{LNA.e}$ to either $T_{LNA.e.on}$ or $T_{LNA.e.off}$ will be neglected in eq. (8.3). The reason being that the vectorial change in the impedance of the noise source will have a more prominent impact on LNA gain, than on its

⁶ The pass-band centre frequency can be moved by suitably attaching permanent magnets to the isolator.

NF due to noise parameter effects.⁷ Equation (8.3) can thus be simplified as

$$Y = \Delta G \cdot \frac{T_{hot.in} + T_{LNA.e}}{T_{cold.in} + T_{LNA.e}} \quad (8.4)$$

where $\Delta G = G_{LNA.on}/G_{LNA.off}$ is the so called *gain error* which can be expanded as [28, pg. 30]

$$\Delta G = \frac{1 - |\Gamma_{dns.on}|^2}{|1 - \Gamma_{LNA.in}\Gamma_{dns.on}|^2} \cdot \frac{|1 - \Gamma_{LNA.in}\Gamma_{dns.off}|^2}{1 - |\Gamma_{dns.off}|^2} \quad (8.5a)$$

This equation assumes that the input of the NFM is perfectly matched to 50Ω . If $|\Gamma_{LNA.in}| < 2.0$, $|\Gamma_{dns.on}| < 0.05$ and $|\Gamma_{dns.off}| < 0.05$ eq. (8.5a) can be simplified further, resulting in [27, pg. 22]

$$\Delta G = \frac{1 - 2|\Gamma_{LNA.in}||\Gamma_{dns.off}|\cos(\arg(\Gamma_{LNA.in}) + \arg(\Gamma_{dns.off}))}{1 - 2|\Gamma_{LNA.in}||\Gamma_{dns.on}|\cos(\arg(\Gamma_{LNA.in}) + \arg(\Gamma_{dns.on}))} \quad (8.5b)$$

$\Gamma_{dns.on}$ and $\Gamma_{dns.off}$ are the on and off reflection coefficients of the DNS and $\Gamma_{LNA.in}$ is the input reflection coefficient of the LNA.

It is evident from eq. (8.5b) that the gain error is equal to 1 (0 dB) if $\Gamma_{LNA.in}$ is equal to zero or $\Gamma_{dns.on}$ is vectorially equal to $\Gamma_{dns.off}$. This means that *there will only be a gain error if there is a vectorial change in the impedance of the noise source between its on and off states, as well as a reflection at the input of the LNA*. The amount of gain error is therefore governed by the following:

1. The *vectorial* difference between $\Gamma_{dns.on}$ and $\Gamma_{dns.off}$. Since their magnitudes are in the same order of magnitude, their relative phase, which can differ substantially, is of great importance when evaluating their difference.
2. The relative phase between the LNA and the noise source, that is the argument of $\Gamma_{LNA.in}$.
3. The amount of reflection at the LNA input, that is the magnitude of $\Gamma_{LNA.in}$.

Since the vectorial difference mentioned in item 1 is of great importance, its worst-case magnitude is often given as a figure of merit in the technical specifications of noise sources. For both the Agilent N4000A and 346A low ENR noise sources $|\Gamma_{dns.on} - \Gamma_{dns.off}|$ is specified as being equal to 0.01 worst-case [9, pg. 4][11, pg. 4]. The actual amount varies with frequency and is usually considerably less though.

⁷ The actual change in LNA NF, when switching between the on and off impedances of the noise source, is dependent on the device specific noise parameters of the LNA. More precisely on the *noise resistance* and *optimum source impedance*.

The amount of gain error can be visualized by plotting eq. (8.5a) as a function of the input phase of the LNA, relative to the noise source. The result of such a simulation is shown in fig. 8.2. The simulated LNA has a 4 dB input return loss, while the low ENR noise source has the aforementioned worst-case impedance difference between its on and off states. The amplitude and phase position of the resulting gain error curve is unique to this particular noise source, since every noise source has its own set of magnitude and phase values for $\Gamma_{dns.on}$ and $\Gamma_{dns.off}$. The *maximum gain error* in the presented example amounts to ± 0.055 dB, occurring when $\arg(\Gamma_{LNA.in})$ is equal to 45° or 225° . Naturally, it is of interest to determine what amount of NF measurement uncertainty this maximum gain error will result in. Before doing so though, we will first examine a peculiar phenomenon which is at play when *tuning* an LNA for lowest NF during measurement, in the presence of gain error.

The measured Y-factor is directly proportional to the gain error in accordance with eq. (8.4). Assuming for simplicity that $T_{cold.in} = T_0$, the instrument uses this Y-factor in eq. (4.56b) on page 63 to calculate the desired NF. Since the NF is inversely proportional to the Y-factor, the minimum *indicated NF* will occur when the Y-factor is at its maximum. Furthermore, if tuning the LNA has a far greater impact on ΔG than on $T_{LNA.e}$, the Y-factor given by eq. (8.4) will in practice be governed by the former. Thus, *when tuning an LNA during measurement, this will inevitably result in a condition where the gain error and hence the Y-factor is maximized and the indicated NF is minimized. The tuning procedure will simply adjust the phase of the LNA input reflection coefficient $\Gamma_{LNA.in}$, to the one needed for maximum gain error for this particular noise source.* See fig. 8.2! The NF presented by the instrument to the operator could thus be totally misleading and in extreme cases even be negative! The *true NF* at this phase angle is higher, by an amount equal to the offset in NF created by the maximum gain error. At the same time *the true minimum NF and its associated phase angle are both unknown and could either be close to or far away from the faulty tuning phase just achieved.* On the other hand, if tuning the LNA has a non-negligible impact on $T_{LNA.e}$ in comparison to ΔG , the effect of gain error on tuning misalignment will be smaller. The indicated NF will then be a combination of the true NF and the gain error, differing less from the true minimum NF.

Having determined the error-maximizing property of the gain error, we now return to the example presented in fig. 8.2 to determine what amount of NF measurement uncertainty the 0.055 dB maximum gain error will result in. Thus, using the Y-factor from eq. (8.4) in eq. (4.56b) as mentioned previously, the resulting error in the indicated NF amounts to approximately -0.075 dB at a 45° phase angle. This means that the *true NF* at this phase angle is 0.075 dB higher than indicated by the instrument. Assuming more typical values for $\Gamma_{dns.on}$ and $\Gamma_{dns.off}$, the corresponding result might be reduced to the region of -0.020 dB. Even though the above given results assume a

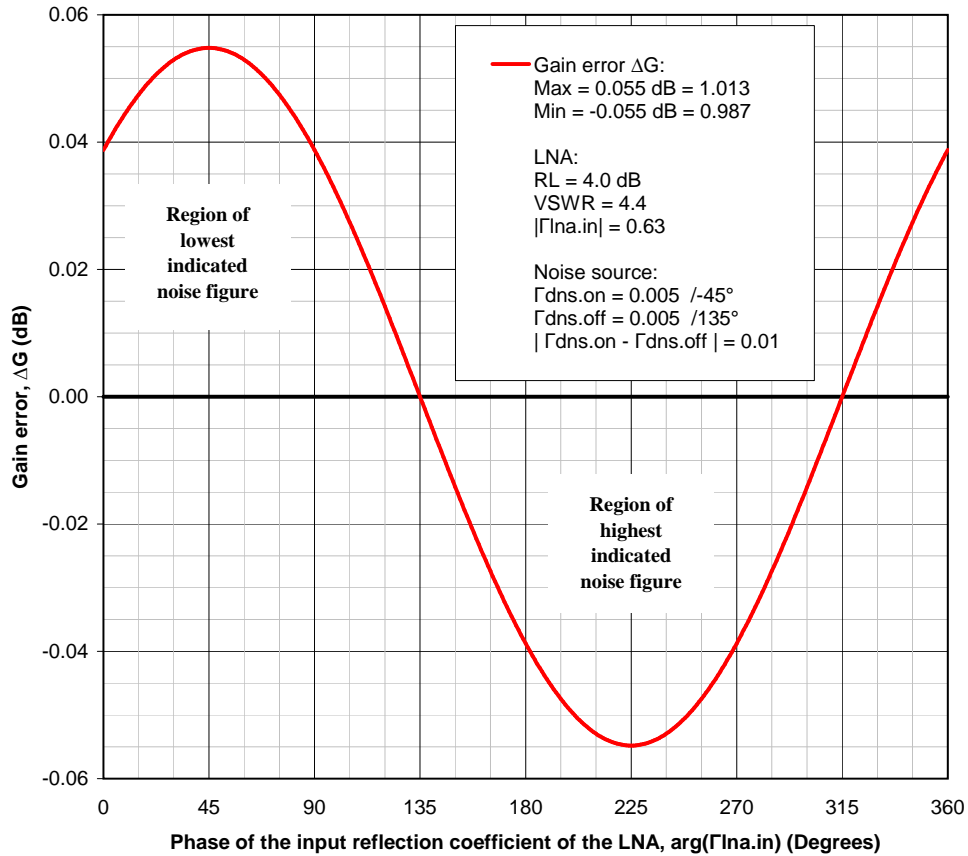


Figure 8.2 The gain error ΔG as a function of the phase of $\Gamma_{LNA.in}$ (relative to the noise source) according to eq. (8.5a). The simulated LNA has a 4 dB input return loss and a low ENR noise source with $|\Gamma_{dns.on} - \Gamma_{dns.off}| = 0.01$ (worst-case). The resulting gain error has a sine-shaped curve with a 360° period and a maximum deviation of approximately ± 0.055 dB, occurring at 45° and 225° for this specific noise source. Two points with a 180° phase shift will have the same gain error, but with opposite sign. The *indicated* NF will be lower than its true value when the gain error is positive and vice versa. It is evident from the above that a low loss phase line, inserted between the noise source and the LNA, can be used to determine the presence of gain error.

0.20 dB LNA NF, they are fairly independent of the actual NF of the device since $T_{LNA.e}$ is much smaller than either of $T_{hot.in}$ and $T_{cold.in}$ in eq. (8.4). Of course, what instead influences the gain error-induced NF uncertainty is the same as that which influences the gain error, that is items 1 to 3 in the list on page 134.

While an error in NF amounting to -0.075 dB and -0.020 dB might not seem like much, one has to relate this to EME LNAs having NFs ranging from a mere 0.13 dB to maybe no more than 0.40 dB. Furthermore, since EME systems at 1296 MHz have very low antenna temperatures, even small misalignments in NF could prove detrimental to the overall SNR performance of the system. Assuming for example a 40 K antenna temperature and a 0.20 dB LNA NF, a 0.075 dB misalignment in this NF would result in an SNR at the output of the LNA which is about 0.4 dB worse than expected. Fortunately, the corresponding value for the more realistic 0.020 dB NF degradation is only 0.1 dB.

Choosing a high ENR noise source which has an increased change in impedance between its on and off states, combined with an LNA with a higher degree of input reflection, will worsen gain error *significantly*. The degree to which an LNA is mistuned could easily reach levels where the resulting degradation of the expected output SNR reaches more than 1 dB. Since the actual NF of a non-impedance matched LNA could be quite different from what the instrument indicated during tuning, on-the-air performance could prove disappointing. This probably explains why some radio amateurs persist in re-tuning their LNAs when connecting them to the antenna, erroneously believing their problems are related to noise parameter effects from a differing antenna impedance, rather than to gain error effects during measurement.

Fortunately, NF measurement uncertainty due to gain error can be mitigated in several ways. As was mentioned previously in section 8.1.5, one should always choose a low ENR noise source if possible. These include an attenuator which reduces $|\Gamma_{dns.on} - \Gamma_{dns.off}|$ and hence the gain error. A lower degree of input reflection at the LNA will also improve matters. However, while such an approach is desirable for commercial products, EME operators are far more interested in high gain and the lowest possible NF, than in the conflicting interest of a better LNA input match. Furthermore, a significant additional improvement is to be had if an isolator and an attenuator are placed before the LNA during measurement, as was mentioned at the end of section 8.1.13.

While using an isolator and an attenuator in effect removes the gain error and thus make it possible to *tune* the LNA to its true minimum 50Ω NF, they also introduce measurement uncertainty even when compensated for. Fortunately, there is another measurement method which was proposed by Leif Åsbrink (SM5BSZ) [2] which permits measuring, though *not* tuning,

the **NF** of an **LNA** in the presence of gain error. The procedure takes two separate measurements: one with and one without a quarter wavelength cable in front of the **LNA**. Since the cable adds a 180° phase shift, the gain error will be the same in both cases *but with opposite sign*. See fig. 8.2! Correcting for the cable loss, one then takes the average of these two **NF** measurements. This will give a final **NF** value where the two gain errors have cancelled each other out. Of course, this assumes that the true **NF** of the **LNA** does not change too much with the 180° phase shift, due to noise parameter effects. That is, the **LNA** should already be reasonably well tuned to its minimum 50Ω **NF**, before this measurement method is used. Naturally, this can be achieved by using the isolator method as mentioned above.

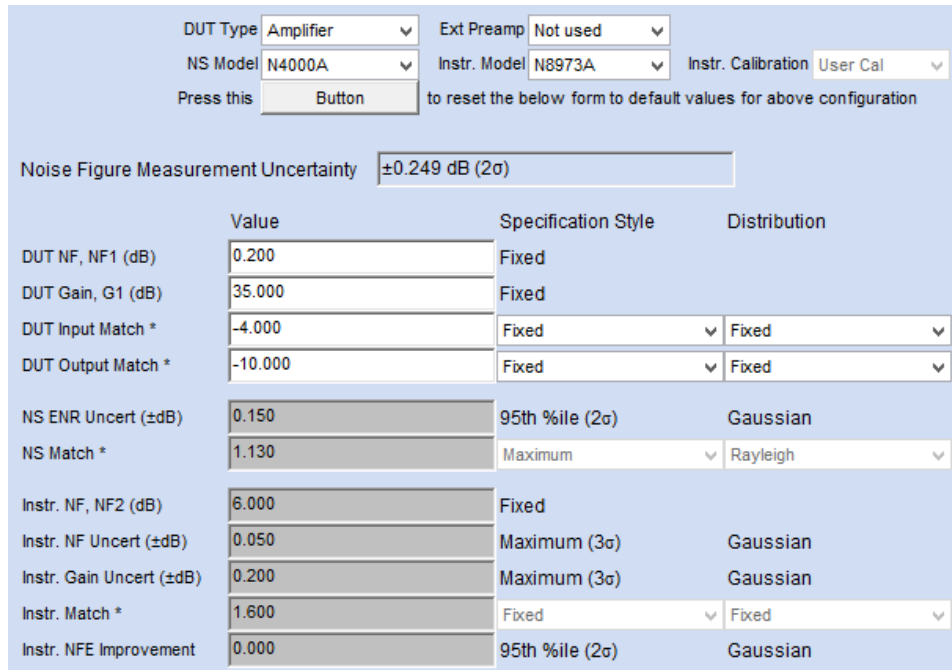
A number of very informative articles on gain error have been written by Rainer Bertelsmeier (DJ9BV) [27, 28, 29]. These are recommended reading for those wishing to acquire more detailed information on the subject.

8.2 Assessment of the combined uncertainty in LNA measurements

Having covered the individual sources of measurement uncertainty in section 8.1, it is of interest to determine the combined uncertainty of the final **NF** measurement. In doing this assessment it is assumed that reasonably avoidable uncertainties, such as the one caused by insufficient warm-up stabilization of the instrument, have been minimized. The remaining uncertainties used in the assessment, such as those related to mismatch and **ENR** calibration etc., are assumed uncorrelated. They can thus be combined in an **RSS** fashion through a propagation of uncertainty analysis involving eq. (4.62) on page 65. The lengthy details of this analysis are presented in an application note by Agilent Technologies [14, ch. 5, app. B] and will hence not be presented here.

Fortunately, the tedious labour of having to manually perform these error-prone uncertainty calculations has been abolished by an *NF uncertainty calculator*, readily available on the Internet [75].⁸ The necessary calculations can either be performed through the use of a Java applet, which runs directly in a web browser, or by downloading a spreadsheet which runs in LibreOffice Calc or Microsoft Excel. Both versions work equally well, though the spreadsheet provides the user with more detailed information whereas the Java applet will allow to plot various graphs.

⁸ The latest version of this calculator is capable of assuming Rayleigh distributed magnitudes for the reflection coefficients. Please refer to section 8.1.13 and the literature [10].



Press this to reset the below form to default values for above configuration

Noise Figure Measurement Uncertainty

	Value	Specification Style	Distribution
DUT NF, NF1 (dB)	0.200	Fixed	
DUT Gain, G1 (dB)	35.000	Fixed	
DUT Input Match *	-4.000	Fixed	Fixed
DUT Output Match *	-10.000	Fixed	Fixed
NS ENR Uncert (±dB)	0.150	95th %ile (2σ)	Gaussian
NS Match *	1.130	Maximum	Rayleigh
Instr. NF, NF2 (dB)	6.000	Fixed	
Instr. NF Uncert (±dB)	0.050	Maximum (3σ)	Gaussian
Instr. Gain Uncert (±dB)	0.200	Maximum (3σ)	Gaussian
Instr. Match *	1.600	Fixed	Fixed
Instr. NFE Improvement	0.000	95th %ile (2σ)	Gaussian

Figure 8.3 The NF uncertainty of a specific LNA, using the N4000A DNS and the N8973A NFM. The indicated uncertainty amounting to ± 0.249 dB has a coverage factor of 2, so the standard uncertainty is half of this.

To illustrate the combined NF uncertainties involved in NF measurements, a few simulations have been performed using the Java version of the NF uncertainty calculator. Figure 8.3 shows the combined NF uncertainty of an LNA having an indicated 0.20 dB NF, 35 dB gain, a 4 dB input return loss and a 10 dB output return loss. The chosen measurement equipment is an N4000A DNS and an N8973A NFM. The resulting NF uncertainty is ± 0.249 dB,⁹ which is problematic since this is greater than the NF of the LNA itself.

The subpar uncertainty presented in fig. 8.3 is mostly caused by the poor input match of the LNA, as well as by the ENR uncertainty of the DNS. Figure 8.4 shows a further simulation, where the combined NF uncertainty is given as a function of input match $\Gamma_{LNA.in}$. Unfortunately, not even a perfect 50Ω input impedance of the LNA will bring the NF uncertainty below ± 0.154 dB.⁹ This essentially equals the ENR uncertainty amounting to ± 0.15 dB,⁹ as specified in fig. 8.3.

While the effects of mismatch can be substantially mitigated by careful use of isolators and attenuators, as was mentioned in sections 8.1.13 and 8.1.14, the ENR uncertainty is in contrast set by the National Standards Institutes.

⁹ This is expanded by a coverage factor of 2, so the standard uncertainty is half of this.

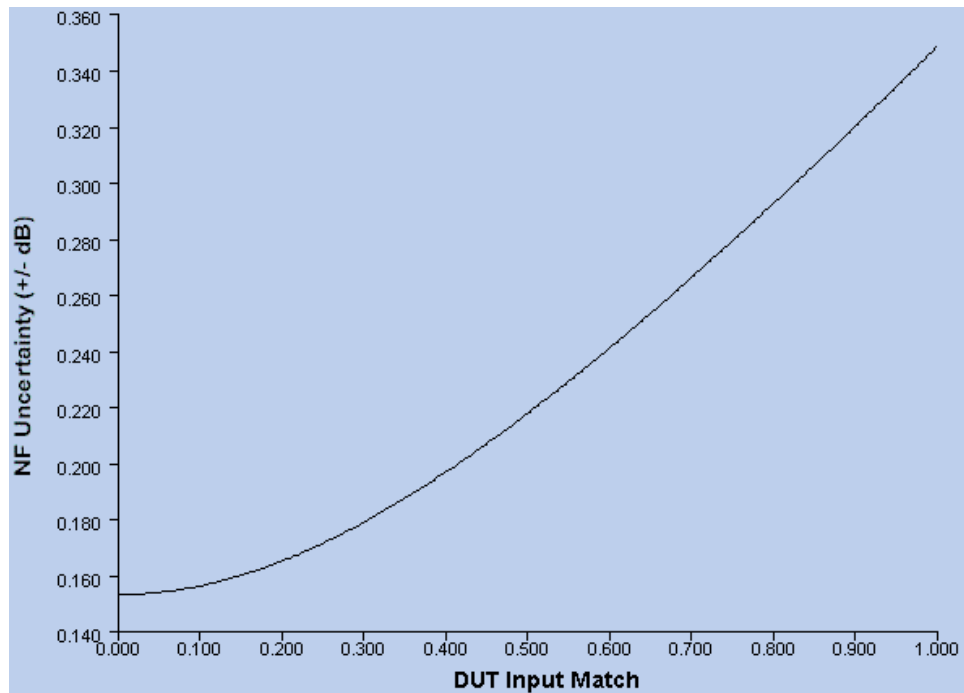


Figure 8.4 The NF uncertainty as a function of input match $\Gamma_{LNA.in}$. The simulated LNA has a 0.20 dB NF, a 35 dB gain and a 10 dB output return loss. The DNS is the N4000A and the instrument is the N8973A, with data according to fig. 8.3. The indicated uncertainty is expanded by a coverage factor equal to 2, so the standard uncertainty is half of this. Notice that the Y-axis does not start at zero!

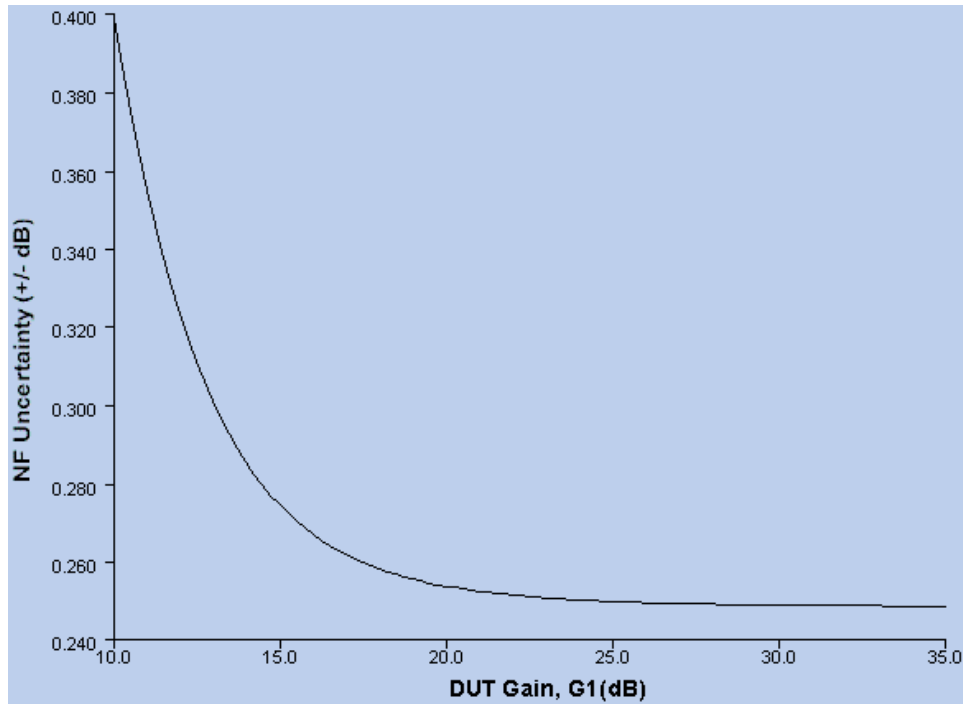


Figure 8.5 The **NF** uncertainty as a function of **LNA** gain. The simulated **LNA** has a 0.20 dB **NF**, a 4 dB input return loss and a 10 dB output return loss. The **DNS** is the N4000A and the instrument is the N8973A, with data according to fig. 8.3. The indicated uncertainty is expanded by a coverage factor equal to 2, so the standard uncertainty is half of this. Notice that the Y-axis does not start at zero!

Thus in practice, *the ENR uncertainty sets the lower bound for the combined measurement uncertainty*. The **ENR** uncertainty specified by Agilent Technologies might be rather conservative though, as was already mentioned on page 126 in section 8.1.6.

Another simulation is presented in fig. 8.5, which shows the combined **NF** uncertainty as a function of **LNA** gain. As can be seen in this figure, the uncertainty increases with a reduction in gain and vice versa. The reason for this being that certain uncertainties appearing *after* the **LNA**, such as the instrument **NF** uncertainty, get divided by the **LNA** gain. Fortunately, **EME LNAs** have high gain since this reduces the overall system noise temperature.

While *absolute* measurements are troubled by uncertainties, *relative* measurements are better off if using isolators, attenuators or a quarter wavelength cable as described in sections 8.1.13 and 8.1.14. According to investigations performed by Leif Åsbrink (SM5BSZ) and Mart Sakalov (SM0ERR) [6], such measurements can be compared to within 0.01 dB.

It is evident from the above that commercial **NF** instruments using **DNSs** are not well suited for absolute measurements of very low **NF** devices, such

as **EME LNAs**. The reason for this is simply that commercial users, for which these instruments are primarily intended, have measurement objectives which usually differ from those of **EME** operators. The respective objectives of these groups are

1. *Commercial users*

These want quick, easy and possibly automated measurements for the production line. The measured **LNAs** are well matched to **50 Ω** and are likely intended for terrestrial applications, where the antenna temperature is close to **290 K**. A very low **NF** is thus *not* critical to the total system noise temperature. As a result, the combined measurement uncertainty is relatively small.

2. *EME users*

These do not mind slow measurements since they are mostly interested in one-off measurements with a low uncertainty. The measured **LNAs** might possibly be very poorly matched to **50 Ω** since very low **NFs** are prioritized. The **LNAs** are intended for space applications, where the antenna temperature is maybe no more than **40 K**. A very low **NF** is thus critical to the total system noise temperature. As a result, the combined measurement uncertainty is relatively high.

From the above it becomes evident that alternative measurement methods, which would not prove practical in a commercial setting, could be attractive to **EME** operators. A few common factors which govern the measurement uncertainty of alternative systems will thus be analysed in section 8.3.

8.3 Reducing NF uncertainty through alternative measurement methods

Various sources of measurement uncertainty, such as those related to mismatch and **ENR** uncertainty, have been covered in the previous sections. What has not been covered however, is how $T_{hot.in}$, $T_{cold.in}$ and the bandwidth-integration time product $B\tau$ influences the measurement uncertainty and ultimately the choice of measurement method. This section will therefore serve to examine these matters more closely, by performing a propagation of uncertainty analysis of eq. (4.51a) on page 61. This equation is reproduced in eq. (8.6) below, where the subscript notation has been changed from ‘tp’ to ‘LNA’. The analysis at hand was inspired by Collier and Skinner [43, ch. 8.6] but it introduces a few alterations in regard to time integration.

$$T_{LNA.e} = \frac{T_{hot.in} - YT_{cold.in}}{Y - 1} \quad (8.6)$$

To arrive at the expression needed to perform a propagation of uncertainty analysis of eq. (8.6), one first has to do a Taylor series expansion of this equation. This entails performing a partial differentiation in regard to each of its input variables. Since the uncertainties of these variables are uncorrelated, the terms of this Taylor expansion can be summed up in an RSS fashion to arrive at the total uncertainty expression for $T_{LNA.e}$. Due to the second and higher order partial derivatives of the Taylor expansion being either zero or negligible, this result can be simplified to arrive at the needed propagation of uncertainty expression given as

$$u(T_{LNA.e}) = \left[\left(\frac{\partial T_{LNA.e}}{\partial T_{hot.in}} \cdot u(T_{hot.in}) \right)^2 + \left(\frac{\partial T_{LNA.e}}{\partial T_{cold.in}} \cdot u(T_{cold.in}) \right)^2 + \left(\frac{\partial T_{LNA.e}}{\partial Y} \cdot u(Y) \right)^2 \right]^{1/2} \quad (8.7)$$

Using eq. (8.6) the partial derivatives in eq. (8.7) are given by

$$\frac{\partial T_{LNA.e}}{\partial T_{hot.in}} = \frac{1}{Y-1} \quad (8.8a)$$

$$\frac{\partial T_{LNA.e}}{\partial T_{cold.in}} = -\frac{Y}{Y-1} \quad (8.8b)$$

$$\frac{\partial T_{LNA.e}}{\partial Y} = -\frac{T_{hot.in} - T_{cold.in}}{(Y-1)^2} \quad (8.8c)$$

$u(Y)$ in eq. (8.7) is the uncertainty of the Y-factor measurement, resulting from non-linearities and instabilities in the measurement equipment. Furthermore, $u(T_{hot.in})$ and $u(T_{cold.in})$ are the respective uncertainties of the hot and cold reference temperatures of the noise source, given by

$$u(T_{hot.in}) = \left(\Delta T_{hot.in}^2 + \left(\frac{T_{hot.in}}{\sqrt{B\tau}} \right)^2 \right)^{1/2} \quad (8.9a)$$

$$u(T_{cold.in}) = \left(\Delta T_{cold.in}^2 + \left(\frac{T_{cold.in}}{\sqrt{B\tau}} \right)^2 \right)^{1/2} \quad (8.9b)$$

where $\Delta T_{hot.in}$ and $\Delta T_{cold.in}$ are the specified uncertainties of $T_{hot.in}$ and $T_{cold.in}$ respectively. The former could be specified as the ENR uncertainty, while the latter could be specified as the uncertainty in determining the physical temperature of the noise source. The second terms, containing B

and τ , represent the uncertainties stemming from the random nature of noise. These uncertainties are approximated by using eq. (5.16b) on page 77, that is the radiometer equation.

Combining eqs. (8.7) to (8.9), the expression for the propagation of uncertainty analysis is finally given by

$$u(T_{LNA.e}) = \left[\left(\frac{1}{Y-1} \right)^2 \cdot \left(\Delta T_{hot.in}^2 + \frac{T_{hot.in}^2}{B\tau} \right) + \left(\frac{Y}{Y-1} \right)^2 \cdot \left(\Delta T_{cold.in}^2 + \frac{T_{cold.in}^2}{B\tau} \right) + \left(\frac{T_{hot.in} - T_{cold.in}}{(Y-1)^2} \right)^2 \cdot u^2(Y) \right]^{1/2} \quad (8.10)$$

As can be seen from eq. (8.10), the uncertainty of $T_{LNA.e}$ decreases if the

1. Y-factor Y increases
2. difference between $T_{hot.in}$ and $T_{cold.in}$ decreases
3. temperature uncertainty $\Delta T_{hot.in}$ decreases
4. temperature uncertainty $\Delta T_{cold.in}$ decreases
5. upper noise source temperature $T_{hot.in}$ decreases
6. lower noise source temperature $T_{cold.in}$ decreases
7. measurement bandwidth B increases
8. integration time τ increases

Two examples to visually illustrate some of the above are given in figs. 8.6 and 8.7. The former shows $u(T_{LNA.e})$ as a function of $T_{LNA.e}$,¹⁰ while the latter instead shows it as a function of $B\tau$. Each example provides simulation results for two different sets of input parameters, presented in table 8.2.

As can be seen in fig. 8.6, the position of the minimum value of $u(T_{LNA.e})$ will change depending on how the input parameters of eq. (8.10) are chosen. The reason for this is that some of the items listed above, such as items 1 and 2, are contradictory and have different amounts of impact depending on the input parameters.

Figure 8.6 furthermore shows that low noise devices will theoretically suffer from lower levels of measurement uncertainty if measured with a liquid nitrogen (LN₂) source, rather than with a low ENR DNS. This is quite intuitive since a 1.5% uncertainty at 77 K equals 1.2 K, which amounts to only 1.2/1400 = 0.09% at 1400 K. Achieving such a low degree of uncertainty

¹⁰ $T_{LNA.e}$ is embedded in the Y-factor according to eq. (4.50) on page 61.

Table 8.2 The input parameters used by the simulations presented in figs. 8.6 and 8.7. The ‘low ENR’ parameters are equivalent to those of a DNS having an ENR equal to 5.8 ± 0.08 dB. The ‘LN₂’ parameters are representative for a terminating resistor at either the temperature of liquid nitrogen or the ambient room temperature. In all cases the ambient temperature reference (295 K) has a fixed specified uncertainty equal to 0.5 K, while the other temperature references (1400 K and 77 K) have an uncertainty equal to 1.5%.

Parameter	Parameter values			
	Figure 8.6		Figure 8.7	
	Low ENR	LN ₂	Low ENR	LN ₂
$T_{hot.in}$ (K)	1400	295	1400	295
$\Delta T_{hot.in}$ (K)	21 ^a	0.5	21 ^a	0.5
$T_{cold.in}$ (K)	295	77	295	77
$\Delta T_{cold.in}$ (K)	0.5	1.2 ^b	0.5	1.2 ^b
$T_{LNA.e}$ (K)	10 to 10 ³		13.7 ^c	
$B\tau$	$2 \cdot 10^6$		100 to 10 ⁶	
$u(Y)$ (dB)	0.03		0.03	

^a 1.5% of 1400 K

^b 1.5% of 77 K

^c 0.20 dB NF

at 1400 K is not plausible with a DNS. Instead, the same 1.5% error, but now at 1400 K, amounts to 21 K which is equivalent to an ENR uncertainty of 0.08 dB which is more realistic. See section 8.1.6! Another intuitive way of looking at this is from the perspective of the measurement uncertainty of $T_{LNA.e}$. If $T_{LNA.e} = 14$ K is measured with an uncertainty of 10%, this is equal to 1.4 K. At 77 K this uncertainty is equal to $1.4/77 = 1.8\%$ while it is equal to only $1.4/1400 = 0.1\%$ at 1400 K. Generally speaking, higher reference temperatures thus lead to higher measurement uncertainties and vice versa; at least at reasonable device noise temperatures. One has to remember though that the results presented in fig. 8.6 omit other sources of uncertainty, associated with the LN₂ option, which could prove problematic. Mismatch related errors as well as unknown temperature gradients are probably among the most prominent of these. An example of a measurement using LN₂ will be presented in section 8.4.2.

The results presented in fig. 8.7, related to the bandwidth-integration time product, should come as no surprise either. It is intuitive that averaging several measurements will reduce the impact of random perturbations introduced by noise. It is furthermore quite understandable that these perturbations will be greater at higher temperatures, thus requiring more bandwidth or integration time. As can be seen in fig. 8.7, using for example a 1 MHz

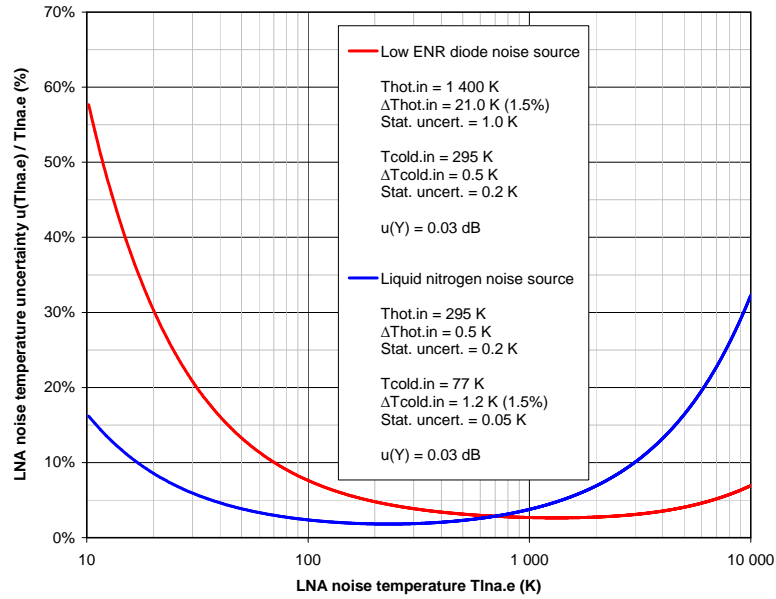


Figure 8.6 The measurement uncertainty of $T_{LNA,e}$ as a function of $T_{LNA,e}$, according to eq. (8.10). For low noise devices, an LN_2 source would theoretically provide lower levels of uncertainty than a low ENR DNS.

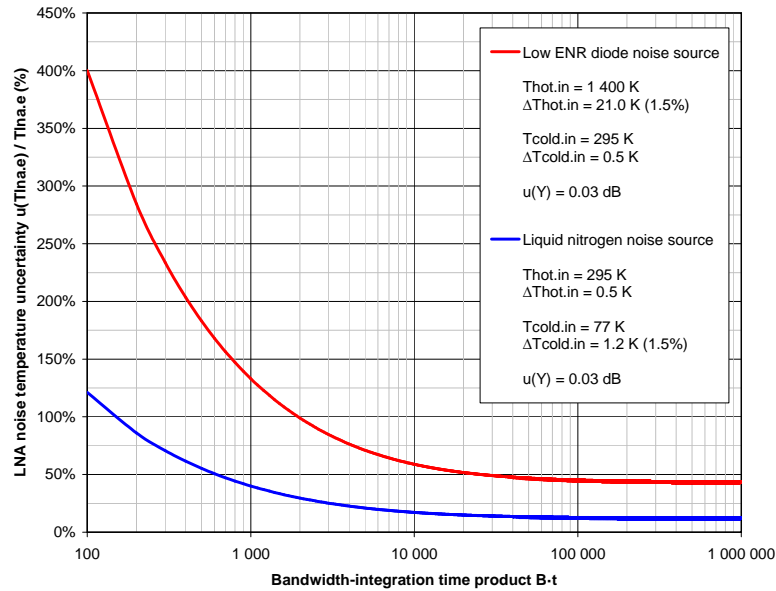


Figure 8.7 The measurement uncertainty of $T_{LNA,e}$ as a function of $B\tau$, according to eq. (8.10). It is evident that more bandwidth or integration time, as well as lower reference temperatures, will reduce the statistically determined part of the uncertainty.

measurement bandwidth B combined with a 1 s integration time τ , should be enough for both methods to virtually eliminate the uncertainty introduced by the random nature of noise. Though as was already mentioned in section 8.1.3, the device bandwidth amplitude must remain somewhat constant over the measurement bandwidth. As was furthermore mentioned on page 77 in section 5.6, system instability could be a limiting factor at longer integration times.

To recapitulate what has been said above, the choice of bandwidth, integration time and reference temperatures is important if a low level of measurement uncertainty is desired. This is especially true when measuring low noise devices, the measurement uncertainty of which benefits from lower reference temperatures. If permissible, a larger bandwidth–integration time product will also be of benefit. More generally though, the choice of measurement method depends on the properties of the DUT itself, the amount of effort one is prepared to put in to the measurement and not least how well one can manage various uncertainties. If longer integration times are tolerable and every conceivable measure can be taken to meticulously reduce various uncertainties, even low Y-factor measurements can prove very accurate. An example of this are measurements performed by Leif Åsbrink (SM5BSZ) using iced and boiling water [6]. Furthermore, if the reference temperatures can be lowered without a significant increase in associated uncertainties, $T_{LNA,e}$ can be measured with a very low level of uncertainty. Sergei Zhutyaev (RW3BP) has presented a very ambitious measurement set-up achieving exactly this [122]. Using a horn antenna to measure the sky temperature at 1296 MHz, Zhutyaev is able to achieve a cold reference temperature of only 14 K, while at the same time keeping uncertainties low. The hot reference temperature is achieved using a DNS connected through a directional coupler. The resulting *maximum* uncertainty is said to be only 2 K or 0.03 dB! Naturally though, methods like these would hardly prove practical in a commercial setting.

There are of course alternative measurement methods which mitigate sources of uncertainty besides those related to bandwidth, integration time or reference temperatures. Some of these try to overcome the uncertainty caused by the change in gain of the DUT, otherwise resulting in gain error as described in section 8.1.14. They accomplish this by measuring the actual degradation of the SNR of a signal being injected into the measurement path, for example by means of a directional coupler. Such methods come closer to the original definition of the NF, presented in eq. (4.6) on page 39, since they measure an actual SNR and do therefore not assume the gain of the DUT to be constant. For this assumption is readily made by methods which rely solely on the measurement of noise levels, as employed by NFMs. This can be seen in the equations presented in section 4.7.

If only relative measurements are of interest, such as when optimizing the NF of an LNA, simply maximizing the SNR at the output of the LNA will suffice. This can be done by measuring the SNR in real-time by means of a computer, running software such as SL [34] or Linrad [8] which both support sound cards and numerous SDRs. Another method, where one simply listens to a stable CW beacon in the speaker of the radio while tuning the LNA, can also be used. As soon as the signal gets stronger when tuning, the antenna is turned slightly away from the beacon until the signal is barely audible, after which the tuning process continues. This iterative process will result in an optimized SNR and hence lowest NF.

8.4 LNA noise temperature and gain measurements

This section will present a few gain and NF measurements of the G4DDK LNA which was introduced in section 7.3.1. One set of measurements were performed using an NFM and a DNS, while another set of measurements were performed using a computer controlled spectrum analyser and a terminating resistor. The latter is alternately subjected to the ambient temperature of its surroundings and the temperature of LN₂.

After having studied the below given measurements in more detail and being puzzled by some of the results, the author realized that the subject of low noise measurements and associated uncertainties was quite a bit more complicated than first anticipated. A *substantial* amount of time has therefore been spent, alas after the measurements were completed, on studying various sources of literature on these and related matters. The result of these studies prompted the author to put a great deal of effort into writing sections 4.2, 4.7, 5.6 and 8.1 to 8.3. With the benefit of hindsight, some of the procedures in this sections should therefore have been conducted in a different manner. However, realizing mistakes and not least gaining experience from them is as important a lesson as any other!

Unfortunately it was not feasible to do these measurements all over again. Firstly, the EME echo measurements in chapter 12 had already been completed. Secondly, the input transistor of the LNA was unfortunately destroyed due to a sequencing error, shortly thereafter. Retuning and remeasuring the repaired LNA would thus have entailed redoing all the echo measurements as well. The author considered this rather time consuming effort to be unjustifiable, especially after having made the assessment that the measurements, though not optimal, were at least satisfactory. Thus even though the NF and the accompanying measurement uncertainty of the LNA could likely have been lowered quite a bit, had the procedure been conducted in a more proper manner, the author chose to keep the measurements at hand.

8.4.1 Noise figure meter method

The NF of the LNA was tuned and measured using an NFM manufactured by Boonton and a home-made noise source having a 9 dB ENR. Both the instrument and the LNA were switched on and left for at least an hour to reach stable operating temperatures. Next, the values of the ENR calibration table were carefully entered into the NFM, which was then calibrated against the DNS. Finally, the LNA was connected to the measurement equipment.

Tuning for lowest indicated NF was accomplished by carefully adjusting the windings of the inductor, soldered to the gate of the first transistor at the input of the LNA, using an insulator. This inductor can be seen in the upper right corner of the LNA tin box in fig. 7.10 on page 109. After having tuned to what appeared to be the lowest possible NF value, the lid was put on the LNA box and the measurement results were recorded. The NF and gain were measured at $NF_{LNA} = 0.25$ dB and $G_{LNA} = 35.37$ dB respectively.

Both results are in the same order of magnitude as those reported by others owning this type of LNA and were therefore, at the time, considered plausible. A couple of mistakes were however made, which, when realized after the event, cast a shadow of a doubt over these results, at least in regard to the NF value. For one thing, the ambient temperature was not entered into the NFM. For another, the tuning was most likely subjected to gain error as described in section 8.1.14, so the true NF of the LNA is likely higher than that indicated by the instrument. The author bases this assertion on the fact that the noise source has a relatively high ENR value and is furthermore home-made. The vectorial difference between its on and off impedances could thus possibly be quite large. The input return loss of the LNA is also a contributing factor. The trustworthiness of the ENR calibration table can be questioned as well, due to the noise source being home-made and thus further down the calibration chain. As a consequence, the total uncertainty of this NF measurement is virtually impossible to estimate without investigating the noise source in more detail.

Fortunately, another set of measurements were performed using an *Agilent Technologies N8975A* NFM and an *N4000A* DNS. The ambient temperature and the ENR calibration table are automatically transferred from the DNS to the NFM, so human error is avoided in regards to this data. The NF was measured at $NF_{LNA} = 0.39$ dB and the gain amounted to $G_{LNA} = 36.20$ dB. Since the LNA was *not* being tuned while measured using this NFM, it is rather unlikely that the maximum amount of gain error was influencing the measurement. Nevertheless, the author should have measured the input return loss of the LNA and studied the calibration protocol of the DNS, to better be able to estimate this and other uncertainties. However, according to the LNA documentation the input return loss is about 4 dB for older models and about 7 dB for the most recent ones. Since the author has an older

Table 8.3 The LNA gain and NF measurement results at 1296 MHz. The equivalent input noise temperature is given in the rightmost column.

Noise figure meter	Gain G_{LNA} (dB)	Noise figure NF_{LNA} (dB)	Noise temp. $T_{LNA,e}$ (K)
Boonton (home-made DNS)	35.37	0.25	17.2
Agilent N8975A (N4000A)	36.20	0.39 ± 0.266^a	$27.2^{+20.0}_{-18.8}$

^a The reported expanded uncertainty is based on a standard uncertainty multiplied by a coverage factor of 2, providing a level of confidence of approximately 95% assuming a normal distribution.

model, a 4 dB input return loss is thus assumed. Calculations performed by the author consequently suggests that the influence of gain error on the NF should be below 0.07 dB. This assumes the maximum specified 0.01 dB impedance difference between the on and off states of the N4000A, as well as a 5.5 dB ENR at the measured frequency. Assuming instead a more realistic impedance difference between the on and off states, the influence of the gain error on the NF should instead be below 0.02 dB.

The results of the above given measurements are presented in table 8.3. Also presented is the uncertainty of the N8975A and N4000A measurement, as calculated by the Agilent Technologies NF uncertainty calculator [75]. The equivalent input noise temperature of the LNA, given by $T_{LNA,e}$ and calculated by means of eq. (4.18) on page 44, is also given for each of the two measurements.

As can be seen in table 8.3, the specified measurement uncertainty is in the same order of magnitude as the measurement itself, which is problematic. This uncertainty is mostly caused by a mismatch between the DNS and the LNA, but ENR uncertainty is also a contributing factor. See section 8.2 for more on these matters!

8.4.2 Liquid nitrogen method

The liquid nitrogen (LN_2) method, as employed by the author, uses a measurement set-up such as the one given in fig. 8.8 to determine the noise temperature and gain of the LNA. During the measurement the terminating resistor is alternately subjected to the ambient room temperature and the temperature of boiling nitrogen. Ideally, the effective output noise temperature of this resistor is equal to its corresponding physical temperature, as was described in section 4.1. The ambient temperature and the temperature of the LN_2 thus set the hot and cold reference temperatures for the Y-factor measurement.

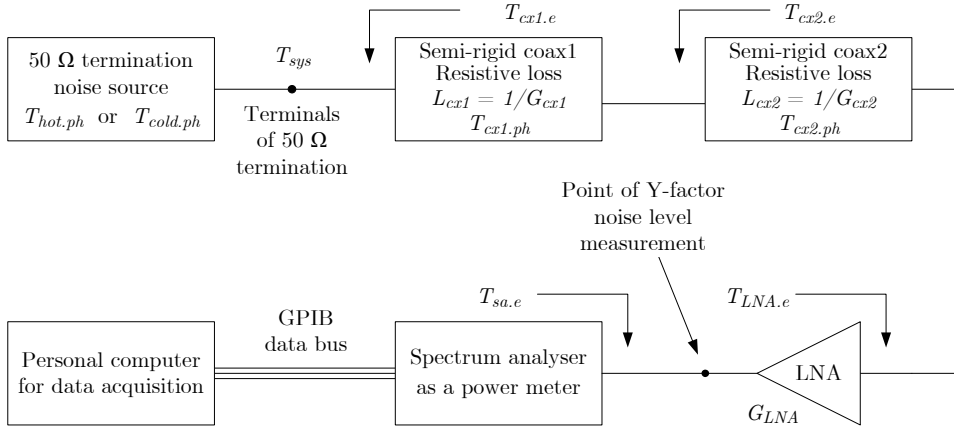


Figure 8.8 The LN_2 Y-factor measurement system used to determine the noise temperature and gain of the LNA. The $50\ \Omega$ terminating resistor is at either of two temperatures, $T_{hot,ph}$ or $T_{cold,ph}$. The semi-rigid coax in front of the LNA is divided into two logical parts having different temperatures. The spectrum analyser and the computer are used for power measurements and data acquisition. Losses are given by L , gains by G and temperatures by T .

The semi-rigid coax is subjected to a considerable temperature gradient during the cold phase of the measurement, and warmer parts of the coax add more noise to the system than cooler parts. It is therefore divided into two logical segments, where one part of its length is said to be at the cold temperature and the other part is said to be at the ambient room temperature. This method was chosen as a pragmatic alternative to a more rigorous approach [119, app. B], which integrates a temperature and loss profile along the length of the cable.

Using eq. (4.23) on page 49 and the fact that gain and loss are each others inverses, the total system noise temperature T_{sys} in fig. 8.8 can be written as

$$T_{sys} = T_{cx1,e} + T_{cx2,e} L_{cx1} + T_{LNA,e} L_{cx1} L_{cx2} + T_{sa,e} \frac{L_{cx1} L_{cx2}}{G_{LNA}} \quad (8.11)$$

By using eq. (4.21b) on page 48 in eq. (8.11), the effective input noise temperatures of the pieces of semi-rigid coax can be expressed in terms of their respective physical temperatures. By furthermore rearranging the resulting equation, the equivalent input noise temperature of the LNA is finally given by

$$T_{LNA,e} = \frac{T_{sys}}{L_{cx1} L_{cx2}} - T_{cx1,ph} \frac{1 - \frac{1}{L_{cx1}}}{L_{cx2}} - T_{cx2,ph} \left(1 - \frac{1}{L_{cx2}} \right) - \frac{T_{sa,e}}{G_{LNA}} \quad (8.12)$$

Naturally, the unknowns in this equation need also be determined. For T_{sys} this is done by means of a Y-factor measurement and by using eq. (4.51a)

on page 61, which is reproduced below.

$$T_{sys} = \frac{T_{hot.ph} - Y T_{cold.ph}}{Y - 1} \quad (8.13)$$

In this equation Y is the Y-factor as a function of frequency, as measured by the spectrum analyser. Furthermore, determining $T_{hot.ph}$ is done through direct measurement while $T_{cold.ph}$ is estimated from the boiling point of the LN₂. Analogous, the gain of the LNA can also be calculated using data from the Y-factor measurement. This is done using eq. (4.49) on page 61 and by compensating the result for the loss introduced by the coax. The latter can either be measured or estimated from technical specifications.

The equipment and the LNA were switched on for at least an hour prior to taking measurements, so as to reach stable operating temperatures. Once the measurements commenced $T_{hot.ph}$ was measured at 296 K using a precision thermometer. $T_{cold.ph}$ was approximated to 80 K, which is slightly higher than the true boiling point of nitrogen at 77.4 K. The reason for this assumption is due to the semi-rigid coax being at room temperature, thus heating the terminating resistor submerged in nitrogen. This can be seen in fig. 8.9. The attenuation $L_{cx} = L_{cx1} + L_{cx2}$ was measured at 0.17 dB using a network analyser.¹¹ 30% of this loss is attributed to L_{cx1} at the temperature of $T_{cold.ph}$, while the remaining 70% is attributed to L_{cx2} at $T_{hot.ph}$. This relationship is an estimate based on ocular inspections by the author. As can be seen in fig. 8.9a, only the terminating resistor and a part of the SMA junction were submerged in LN₂, while the whole coax was virtually surrounded by air at the ambient room temperature. Since the system was calibrated prior to the measurement, $T_{sa.e}$ was set to zero in eq. (8.12).

Unfortunately the author had no prior practical experience of LN₂ measurements, and had only a limited time to acquaint himself with the measurement system and the software used for data acquisition. With the benefit of hindsight, some aspects of this measurement should therefore have been conducted in a different manner. For instance, after having analysed the Y-factor data afterwards, the author realized that even more averaging time would have been beneficial. However, since measurements were taken in 50 kHz increments in a 50 MHz bandwidth, the author compensated by smoothing the data in a ± 8 MHz window in the frequency plane, centred around 1296 MHz. Since the data showed signs of periodicity in the frequency plane, power reflections and possibly also gain error were present during the measurement. Without having analysed this further, the author intuitively believes that the smoothing mentioned above probably mitigates the impact of these effects on the measurement result. Nonetheless, the author should have measured

¹¹This insertion loss is assumed to be purely resistive and includes not only the loss of the semi-rigid coax, but also that of the female-to-female adapter which can be seen in fig. 8.9.

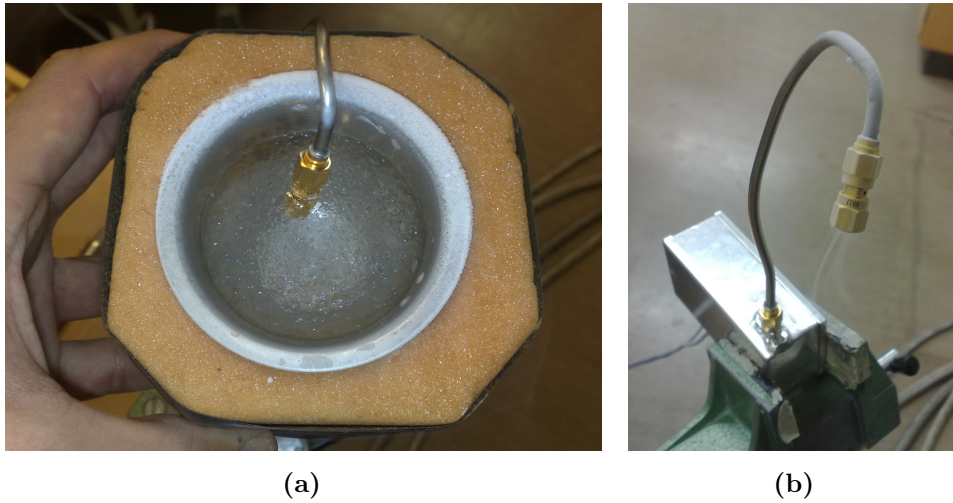


Figure 8.9 Two pictures taken during the LN_2 measurement. To the left (a) the $50\ \Omega$ terminating resistor is submerged in LN_2 . To the right (b) the LNA box is fixed in a vice, with a recently cooled terminating resistor connected to its input via the semi-rigid coax.

the vectorial change in impedance of the coax and terminating resistor-combination while cycling through the temperature extremes, to better assess mismatch effects. Another source of uncertainty is the 30/70 relationship chosen to approximate the temperature gradient. A few heat sinks along the semi-rigid coax, and a table fan for air circulation, would likely have led to better temperature control. Yet another source of uncertainty is the measurement of the insertion loss L_{cx} , and the assumption that it is purely resistive. The boiling point of the LN_2 is a further source of uncertainty. It could have been affected by oxygen and other impurities in the liquid or by the barometric pressure.

With the above being said, the noise temperature of the LNA was found to be $T_{LNA,e} = 28.6\ \text{K}$ equal to $NF_{LNA} = 0.41\ \text{dB}$ in terms of NF. This is a reasonable result and only slightly higher than the result obtained by the second NFM measurement presented in table 8.3, which is encouraging. Changing the 30/70 relationship to 50/50 instead, the resulting NF increases by only 0.02 dB or 1.7 K in noise temperature terms. The reason for this small change probably lies in L_{cx} being relatively low.

The measurement uncertainty should be in the region of what was derived in section 8.3. According to fig. 8.6 on page 146 this would approximately mean a 6% uncertainty at $T_{LNA,e} = 28.6\ \text{K}$, equalling 1.7 K or 0.02 dB in NF terms. The actual uncertainty is likely higher though, due to the reasons given above. However, it should still be lower than the uncertainty of the NFM measurement, also seen in fig. 8.6.

8.4.3 Comments on the LNA measurement results

If the true NF of the LNA really is in the region of 0.40 dB (28.0 K) as suggested above, this is higher than one would expect from this type of LNA. The reason for this probably lies in the afore mentioned mistuning of the LNA in the presence of gain error. Properly retuning the LNA would likely lower the NF to the region of 0.25 dB (17.2 K), which would increase the output SNR by as much as 0.7 dB.¹²

A *substantial* improvement of the NF would be achieved by modifying the LNA in a manner suggested by Sergei Zhutyaev (RW3BP) [123]. Implementing these changes, Zhutyaev has managed to lower the LNA NF to the region of a mere 0.13 dB (8.8 K), measured using his highly accurate horn antenna measurement system [122]. This would imply as much as a 1.3 dB increase in the output SNR, compared to a 0.40 dB NF.¹²

A redesign of the LNA, which incorporates some of Zhutyaev's more feasible suggestions, was presented by its designer Sam Jewell (G4DDK) [72]. These modifications are said to improve the NF to the vicinity of 0.20 dB (13.7 K), which would increase the output SNR by as much as 0.9 dB compared to a 0.40 dB NF.¹² Newer models of the G4DDK LNA are built according to this redesign. Please refer also to appendix A for general graphs relating to the above.

The measured gain at 36.20 dB is reasonable since the LNA employs a dual-stage amplifier design. It is furthermore in line with the results of others using this type of LNA. Even though it might seem high at first sight, this amount of gain is necessary in an EME communication system, since it reduces the impact of noise from stages following the LNA. This noise would otherwise come to increase relative to the low antenna and LNA temperatures in the receiver front-end. See also sections 4.4 and 8.5!

8.5 Receiver subsystem noise temperature estimation

Having finished the LNA measurements, it is possible to estimate the noise temperature $T_{rx.e}$ of the receiver subsystem following the antenna. This subsystem was first introduced in section 7.3, as a part of the complete EME system, but an equivalent system is described mathematically in section 4.6. Please refer to figs. 4.9 and 7.1 on pages 56 and 94 for a schematical representation of the parts composing this subsystem.

¹² Assuming a 40 K antenna temperature and 0.1 dB resistive loss at 290 K in front of the LNA. Noise contributions from stages following the LNA are not considered.

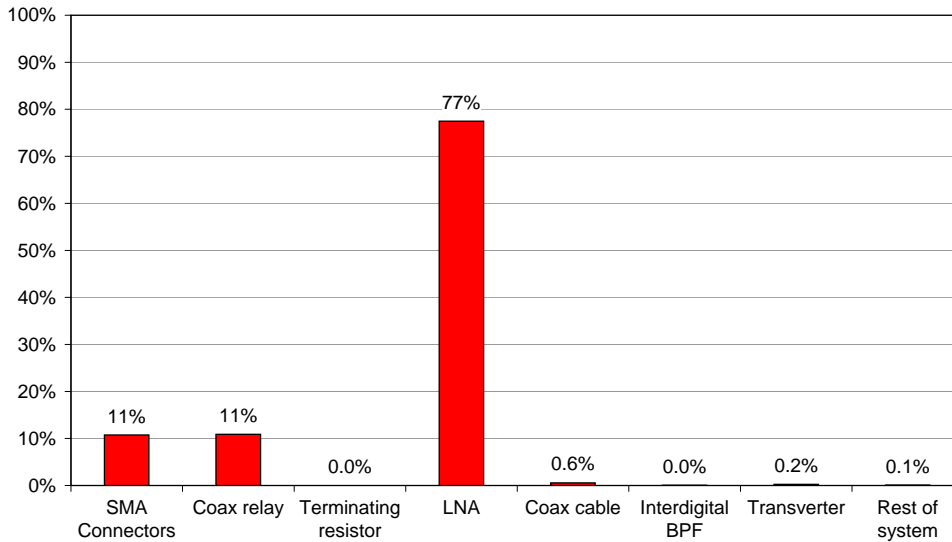


Figure 8.10 The receiver subsystem noise temperature distribution. Front-end noise predominates, indicating that the LNA gain is sufficient.

Calculating $T_{rx.e}$ is done using eqs. (4.40) and (4.41) on page 57, the parameters of which are presented in table 8.4. Performing this calculation yields $T_{rx.e} = 38.1$ K, corresponding to $NF_{rx} = 0.54$ dB when expressed in terms of NF. These results are included at the bottom of table 8.4 as well.

Having performed these calculations, it is of interest to see how the various system components contribute to $T_{rx.e}$. This gives a good indication of where efforts to improve the system performance are best put. Such an analysis is therefore presented in fig. 8.10, where all the component temperatures in table 8.4 have been referenced to the antenna terminals according to eq. (4.41) on page 57.

As can be seen from fig. 8.10, front-end noise predominates and most of the receiver subsystem noise temperature can be attributed to the LNA. However, resistive losses from the coaxial protection relay and SMA connectors, placed before the LNA input, play an important role as well. An effort should be made on reducing these losses. Components placed after the LNA output on the other hand, have a marginal impact on noise performance. This is not surprising, as was explained in section 4.4, since the gain of the LNA is relatively high.

Table 8.4 The parameters used to calculate the receiver subsystem noise temperature $T_{rx,e}$ and its accompanying NF NF_{rx} . The results of these two are presented at the bottom of the table. The noise temperature of each component is referenced to its respective input.

Parameter	Value	Comment
<i>SMA connectors</i>		
L_{SMA}	0.06 dB	Estimated from the resistive loss of individual SMA connectors, measured by Leif Åsbrink (SM5BSZ) [5].
$T_{SMA,ph}$	294 K	Measured ambient temperature.
<i>Coax protection relay</i>		
L_{rl}	0.06 dB	Estimated from the resistive loss of an equivalent relay, measured by Leif Åsbrink (SM5BSZ) [5].
$T_{rl,ph}$	294 K	Measured ambient temperature.
<i>Terminating resistor</i>		
T_{tr}	294 K	Measured ambient temperature.
I_{rl}	90 dB	Minimum value from the technical specification.
<i>Low noise amplifier</i>		
G_{LNA}	36.20 dB	Measured using an NFM.
NF_{LNA}	0.41 dB	Measured using LN ₂ .
<i>Coax cable</i>		
L_{cx}	6.0 dB	Estimated from 10 metres of RG58.
$T_{cx,ph}$	294 K	Measured ambient temperature.
<i>Interdigital BPF</i>		
L_{bp}	0.20 dB	Specified on the filter.
$T_{bp,ph}$	294 K	Measured ambient temperature.
<i>Transverter</i>		
G_{trv}	20 dB	Typical value from the technical specification.
NF_{trv}	1.2 dB	Typical value from the technical specification.
<i>Rest of the system</i>		
NF_{rest}	10 dB	Estimated worst-case value.
<i>Receiver subsystem noise temperature and NF results</i>		
$T_{rx,e}$	38.1 K	Referenced to the antenna terminals.
NF_{rx}	0.54 dB	Referenced to the antenna terminals.

8.6 G/T_{sys} figure of merit measurement

The G over T figure of merit can be determined by means of a Y-factor measurement using a celestial radio source, as was described in section 6.1. According to eq. (6.7) on page 82, two unknowns need to be determined in order to calculate G/T_{sys} : The source flux density S at 1296 MHz and the Y-factor Y . Determining these will be discussed first, before doing the final G/T_{sys} calculation.

8.6.1 Obtaining the solar radio flux

Naturally, the source flux density is dependent on which celestial radio source is chosen for the measurement. Even though there are a number of commonly used sources to choose from [94, Anx. 1], these are generally too weak to be of any use when measuring amateur EME stations at 1296 MHz, rendering Y-factors well below 1 dB. Fortunately, our own sun is a strong radio source, alas with a flux density which varies both short- and long-term. It depends on solar radio bursts and has a high degree of correlation with the sunspot cycle. The flux density therefore needs to be known as close in time as possible to the actual measurement. For more on this time aspect, please refer to the literature [105, ch. 6].

There are a number of observatories around the world which measure the so called ‘10.7 cm solar radio flux’ at 2800 MHz, and post their results to the Internet on a daily basis, referring to it as the *solar flux index (SFI)* or simply $F_{10.7}$. Other frequencies are measured as well, but unfortunately none in the amateur radio bands. However, using inter- and extrapolation¹³ the solar flux can be estimated at amateur frequencies as well, including at 1296 MHz. The ‘NOAA Space Weather Prediction Center’ in the USA collects and publishes historic and current solar flux data, from all measurement sites around the world,¹⁴ on their FTP server [113]. Longer time series can be found at ‘Space Weather Canada’ [101] as well as at the ‘Ionospheric Prediction Service of the Australian Bureau of Meteorology’ [68]. The latter furthermore publishes interpolated data at, among others, 1300 MHz which is probably close enough to 1296 MHz.

An alternative to visiting the above given websites is to use Dough McArthur’s (VK3UM) [82] EME Calc software [83], presented in section 7.5.3. This piece of software has the ability to retrieve solar flux data from the Learmonth observatory in Australia, which it then interpolates to various amateur radio

¹³The solar flux has a non-linear dependency with frequency. Linear inter- and extrapolation methods should thus be avoided.

¹⁴The observatories are: Learmonth, Australia; San Vito, Italy; Sagamore Hill, USA; Palehua, Hawaii; Penticton, Canada.

frequencies. Another source of interpolated data is presented by Owen Duffy (VK2OMD), in the form of a ‘web page calculator’ which uses spline interpolation [48]. This calculator has the advantage of letting the user choose from several observatories for its data retrieval, which implies more freedom in choosing the time of day of the solar flux measurement. It also has the ability to process measurements which are up to 45 days old, which is the maximum length of time provided by NOAA.

Yet another alternative is presented in a paper [105] published by Dr. Tapping at the ‘Dominion Radio Astrophysical Observatory’ in Canada. It proposes a method by which the 10.7 cm solar flux can be converted to other frequencies, with an uncertainty ‘to within a dB or so’ [105, ch. 5]. For the 23 cm solar flux, this conversion is given by

$$S = 0.72 \cdot (F_{10.7} - 64) + 47 \quad (8.14)$$

where both $F_{10.7}$ and S are given in SFUs. Even though this method has not been thoroughly evaluated by the author of this thesis, it is probably safe to assume that interpolation yields a lower level of uncertainty. Nevertheless, the paper is recommended reading for those wishing to know more about the Sun, its radio flux, the measurement thereof as well as its variation with time and frequency.

It is worth noting that since the solar radio flux is given in solar flux units (SFUs), it needs to be converted to Janskies (covered in section 4.5.2) before being used in eq. (6.7) on page 82 to calculate G/T_{sys} . Furthermore, *the solar flux measurements are corrected for tropospheric absorption before being published, that is their values represent what would be measured above the atmosphere* [105, ch. 4.5]. While atmospheric loss is negligible at 1296 MHz, it needs to be accounted for at certain other frequencies. Please refer to the references given in section 3.5.6 for more on atmospheric loss.

Even though local regions of circularly polarized emissions can be observed on the Sun, especially during its active periods, these cancel when averaged over the entire solar disc. When using wide beam antennas where $HPBW > 3^\circ$, the Sun can thus be assumed to be an unpolarized source [105, ch. 4.2, 7.3]. This implies a dish diameter of less than about 5.4 metres, which is a criterion satisfied by the author’s antenna. No corrections for polarization need therefore be applied to eq. (6.7) on page 82, since this equation assumes an unpolarized source. See also the comment at the end of section 4.5.4!

8.6.2 Measuring the Y-factor and calculating G/T_{sys}

The Y-factor was measured at AF in SSB mode, using the audio output from the accessory socket at the rear of the Icom transceiver. An advantage of using this output, instead of the external speaker or headphone output,

is that its level is constant, regardless of the adjustment of the volume control knob on the radio. This eliminates the need for level readjustment at every measurement occasion, or the risk of disrupting the measurement by inadvertently turning the knob. Bypassing the volume control circuit furthermore eliminates possible non-linearities, which it might otherwise introduce. This output also has a higher impedance than its alternatives.

A further source of non-linearity which needs to be avoided, is that of the [automatic gain control \(AGC\)](#) circuit in the transceiver. This circuit was therefore disabled which unfortunately required modifying the hardware of the Icom transceiver. Naturally, this depends on the transceiver model. The reason for having to do this lies in the statistical nature of noise itself, which sooner or later will reach amplitudes where the [AGC](#) is triggered, thus leading to non-linearities.

Apart from the [AGC](#), one must also try to make sure that the signal levels between the stages in the system as a whole are such, that front-end noise predominates and non-linearity through compression is avoided. Naturally, these matters are system specific since they depend on the dynamic range, gain, loss and noise contribution of each component within the system. [EME](#) operators are thus tasked with examining this for their own specific system.

The audio from the transceiver was fed to the audio and data interface, whose audio part contains an isolating audio transformer (repeating coil) as well as a potentiometer for level adjustment. The isolating transformer eliminates ground loops which might otherwise add hum and other types of noise to the measurement. The output from the interface was finally fed to the computer sound card. Please refer to [section 7.4.3](#) and [appendix C](#) for more information on the audio and data interface.

Having connected everything, the [AF](#) level was adjusted so as to *a)* avoid compression in the sound card during the hot sun measurement and *b)* increase the noise floor above that of the sound card, during the cold sky measurement. This adjustment was done using the potentiometer on the interface, as well as using the volume control slider in the audio control panel of the operating system, while alternately aiming the antenna towards and away from the Sun.

The hot and cold noise levels were measured and recorded using a script written by the author for [SL](#), presented in [section 7.5.1](#). A sufficient amount of time averaging was applied in software to get stable readings for each measurement. These results were then used to calculate the Y-factor. A number of measurements were performed round about noon, during a two day period, with similar results. Outlier measurements due to possible solar

radio bursts, which would have increased the Y-factor, could thus be ruled out.¹⁵

During the first measurement, a calibrated high-quality decade attenuator was inserted between the LNA and the transverter. More precisely, for practical reasons, at the input of the interdigital BPF. Please refer to figs. 4.9 and 7.1 on pages 56 and 94 respectively. The purpose of this attenuator was to check for signs of compression within the system which would have decreased the measured Y-factor. This check was performed by first setting the attenuator to 0 dB during the cold measurement. Then a hot measurement was performed, as soon as the Sun entered the antenna boresight. The difference between the hot and cold measurements (in decibels) was calculated next. Assuming that compression was not at play, this difference equals the true Y-factor. With the antenna still pointed straight at the Sun, the decade attenuator was increased to the same number of decibels as the just calculated Y-factor. *If the system is operating linearly, such a procedure should approximately bring the measured noise level down to what was measured during the cold measurement*, since the Y-factor is then cancelled by the attenuator. This was the case since only a slight discrepancy was noted.

However, had compression been observed, the resulting noise level would have been higher than the one from the cold measurement. In this case the attenuation should be increased even further, until the resulting noise level *does* equal the cold measurement level. The true Y-factor is then given by the attenuation of the attenuator. Depending on the LNA gain and Y-factor this procedure might however require mathematical compensation, since inserting an attenuator affects the system noise temperature in itself.¹⁶ The effect of the attenuator should be small though, as long as the LNA gain is high. For the particular system described in this report, the error introduced by the attenuator is theoretically calculated as being less than approximately 0.05 dB worst-case, assuming a constant 12 dB Y-factor and an LNA gain equal to 36.2 dB. Assuming the same Y-factor, but decreasing the gain by 6 dB, the error is still below 0.2 dB worst-case. Decreasing the Y-factor increases the error only slightly. However, since no compression could be observed during the Y-factor measurements presented in this section, these were performed without the use of a decade attenuator.

The solar radio flux, the accompanying Y-factor and the resulting G/T_{sys} figure of merit, calculated using eq. (6.7) on page 82, are presented in table 8.5. The results are in line with what can be expected for a dish this size and are thus considered reasonable. Figure 8.11 furthermore shows the 4 metre

¹⁵The ‘Radio Burst Event Reports’ at the ‘NOAA Space Weather Prediction Center’ FTP server [113] might give an indication if a burst is suspected.

¹⁶The noise contribution from the attenuator is added to the numerator of eq. (6.1c) on page 80, thus changing the Y-factor.

Table 8.5 The solar flux at 1296 MHz, Y-factor and resulting G/T_{sys} figure of merit, determined by sun to cold sky Y-factor measurement.

Solar radio flux S (10^{-22} W m $^{-2}$ Hz $^{-1}$)	Y-factor Y (dB)	G/T_{sys} (dBiK $^{-1}$)	Date
68	12.0	11.6	20 Oct 2010 ^a

^a At 11:00 (24h UTC): Az = 181°, El = 22° and $\delta_s = -10.4^\circ$.

dish pointed straight at the Sun during one of the Y-factor and drift-scan measurements, performed at noon time. A screenshot of **SL**, running the ‘Y-factor measurement’ script during one of these measurements, is shown in fig. 8.12. User control and status information is provided via on-screen buttons, which can be seen to the left. Pushing some of these buttons (or their accompanying keyboard function keys) fetches measurement data or lets the user change parameter values via a dialogue window. The source code for this script can be found in appendix D.1.

Possible sources of uncertainty during these measurements are system linearity and stability, as well as depointing loss due to the azimuth and elevation system of the antenna. No source size correction is required, because of the relatively small size of the antenna. See also sections 3.5.3 and 6.3!

A final note on antenna polarization is appropriate at this point. *Since the Sun can be considered an unpolarized source (see section 8.6.1), the G/T_{sys} result obtained above reveals nothing about the accompanying polarization property of the antenna.* The actual G/T_{sys} at the intended circular polarization is likely lower than the value obtained above. When needed, this discrepancy should be estimated and either compensated for or treated as an uncertainty in calculations involving G/T_{sys} . Please also refer to section 3.5.5 for more on polarization loss.

8.7 Antenna gain measurements

At the end of section 6.2 two methods were presented by which to obtain the antenna gain by means of a drift-scan measurement using an astronomical radio source. One method is through measuring the antenna HPBW, while the other is through measuring and integrating the (normalized) antenna power pattern. This section will show these two methods being applied in practice, using the Sun.

The measurement set-up is the same as in section 8.6.2. Precautions presented in that section, regarding system linearity, thus apply here as well. The same holds true for the possible source of measurement uncertainty, which were



Figure 8.11 The 4 metre dish pointed straight at the Sun during a Y-factor and drift-scan measurement. The antenna was not moved between the hot and cold measurements. Notice how the shadow of the feed horn is in the middle of the reflector. At the time of this photo, the measured noise level was at its maximum.

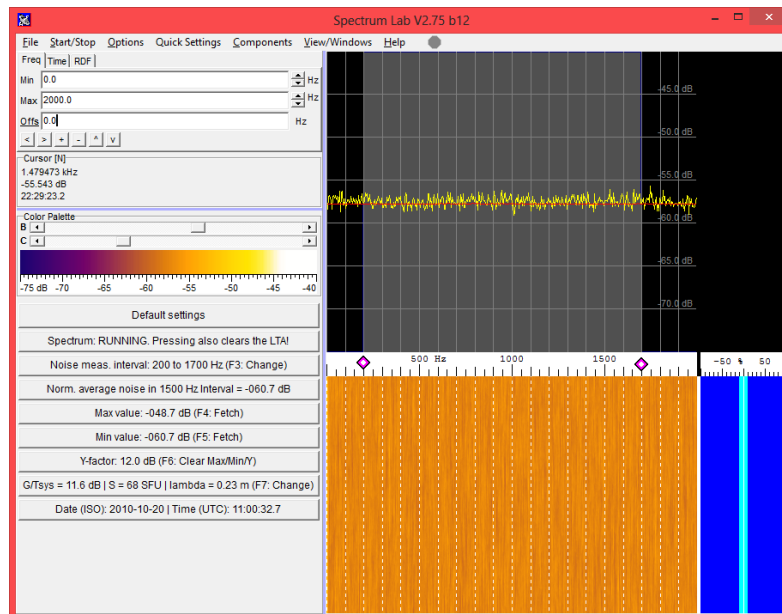


Figure 8.12 SL running the Y-factor measurement script. The buttons to the left shows the hot and cold measurements (on a relative scale), the Y-factor as well as the resulting G/T_{sys} . The solar flux S and the wavelength λ need to be entered by the user for the G over T calculation to be correct.

presented there as well. In regards to this the long-term system stability can be of particular interest, since it can take more than an hour to complete a drift-scan measurement.

8.7.1 Half-power beam width method

The measurements were performed according to the first method described at the end of section 6.2. As in the case of the Y-factor measurements presented in section 8.6.2, SL was once again used to record the noise levels on a relative noise scale. Time averaging was also applied, in order to get smoother results. Measurements of the antenna power pattern were taken every 30 seconds and saved to a text file, together with the time of each measurement. This file was then imported into a spreadsheet software for further analysis, as detailed below.

First, the ‘time x-axis’ of the measurement series was converted to degrees, using the fact that the Earth rotates 360° in about 24 hours with respect to the Sun. A time interval Δt , measured during a drift-scan, can thus be converted to an equivalent angle. If this time interval is given relative to the time when the Sun passes the boresight of the antenna, the angle offset from the boresight is given by

$$\xi(\text{deg}) = \frac{\Delta t \cdot 360^\circ}{24 \cdot 60} \cdot \cos \delta_s = \frac{\Delta t}{4} \cdot \cos \delta_s \quad (8.15)$$

where Δt is given in minutes, ξ in degrees and the cosine term compensates for the declination δ_s of the Sun. The latter can be obtained from the ‘NOAA Earth System Research Laboratory’ website [112]. If only the HPBW is of interest, eq. (8.15) can be written as

$$HPBW_{meas}(\text{deg}) = \frac{HPBW_{meas}(\text{minutes})}{4} \cdot \cos \delta_s \quad (8.16)$$

which converts an HPBW measured in minutes to degrees.

Next, the measured antenna power pattern P_{meas} was normalized. This was accomplished by applying the following equation, which only considers the ξ angle component since rotational symmetry is assumed:

$$P(\xi) = \frac{P_{meas}(\xi) - \min(P_{meas}(\xi))}{\max(P_{meas}(\xi)) - \min(P_{meas}(\xi))} \quad (8.17)$$

Finally, the data was plotted and some apparent outlier measurement points were altered. The resulting graph, containing about an hours worth of measurements, is shown in fig. 8.13.

As can be seen, the antenna pattern (red line) appears to have a symmetrical Gaussian bell-shape, which is to be expected. Its slightly wobbly nature can

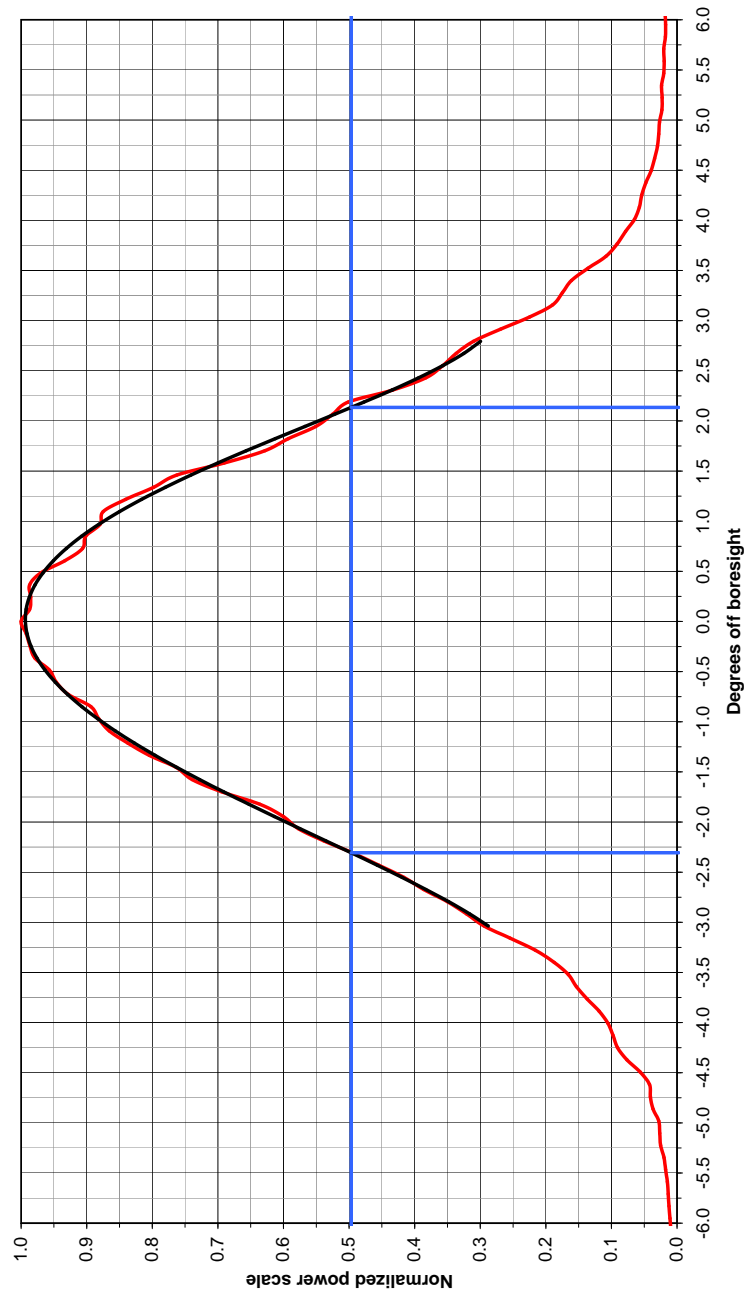


Figure 8.13 The normalized antenna power pattern, resulting from a drift-scan measurement using the Sun, is shown in red. The horizontal blue line indicates the -3 dB level, while the two vertical blue lines indicate the boundaries of the measured $HPBW$. These boundaries are set by the black curve, which is a 6th order polynomial fit to the power pattern. As is seen in the graph $HPBW_{meas} = 4.4^\circ$. Notice the approximate Gaussian bell shape of the power pattern. No side lobes could be detected, even beyond the 6° boundary of this graph.

likely be attributed to system instabilities and variations in the solar flux. As can be determined from the vertical blue lines, the measured half-power beam width $HPBW_{meas} = 4.4^\circ$ which is reasonable for a dish this size. From the graphs in section 6.3 it is furthermore evident that no source size correction is required, so that $HPBW \approx HPBW_{meas}$. Since no side lobes could be detected another plot was made, but this time with a relative dB scale on the y-axis and further out to the right on the x-axis. The result is shown in fig. 8.14.

No distinct side lobes can be detected in this graph either, though the vertical green line marks what appears to be a ‘null’ at approximately 10.8° . Using formulas provided by Solovey and Mittra [100], $HPBW_{meas}$ yields an illumination taper of about 23 dB. The same result is obtained using a method presented by Milligan [85, ch. 4-17], which furthermore estimates the level of the first side lobe to no less than about 39 dB below the main lobe! This would explain why no side lobes were detected by the receiving system. At first sight the illumination taper and the side lobe level seem relatively low, though as was mentioned in section 7.1.1 the dish was extended to be purposefully under-illuminated so as to lower the antenna temperature and increase the **G over T**. In contrast, a transmitting antenna optimized for maximum gain has an illumination taper of about 10 dB. This results in more spillover and thus a higher antenna temperature as well as a lower **G over T**, making such an antenna less suitable for reception of weak signals. Please refer also to section 5.4.

However, the **HPBW** measurement was performed along a plane which does *not* include the diagonal of the feed horn and thus neither the aluminium support struts. See fig. 8.11! A pattern measured along this diagonal would likely have had a wider **HPBW** and more prominent side lobes, due to scattering and diffraction. For this reason the beam efficiency is estimated at $\eta_{beam} = 0.75$. Furthermore, since the power pattern resembles a Gaussian bell-shape, a pattern factor $k_p = 1.13$ is chosen. See also section 6.2!

Using eqs. (6.15) and (6.16) on page 84 and inserting the values for **HPBW** (in radians), η_{beam} , k_p , λ and A_{ph} while furthermore assuming that the radiation efficiency $\eta_{rad} \approx 1$, the gain and aperture efficiency is calculated at $G = 31.4$ dBi and $\eta_{ap} = 46\%$ respectively. A second drift-scan measurement was also performed, yielding $HPBW_{meas} = 4.2^\circ$, $G = 31.9$ dBi and $\eta_{ap} = 52\%$. These aperture efficiencies are reasonable, though maybe a bit on the high side considering the under-illumination of the dish purporting a 23 dB illumination taper. All values are summarized in table 8.6 together with the results of section 8.7.2.

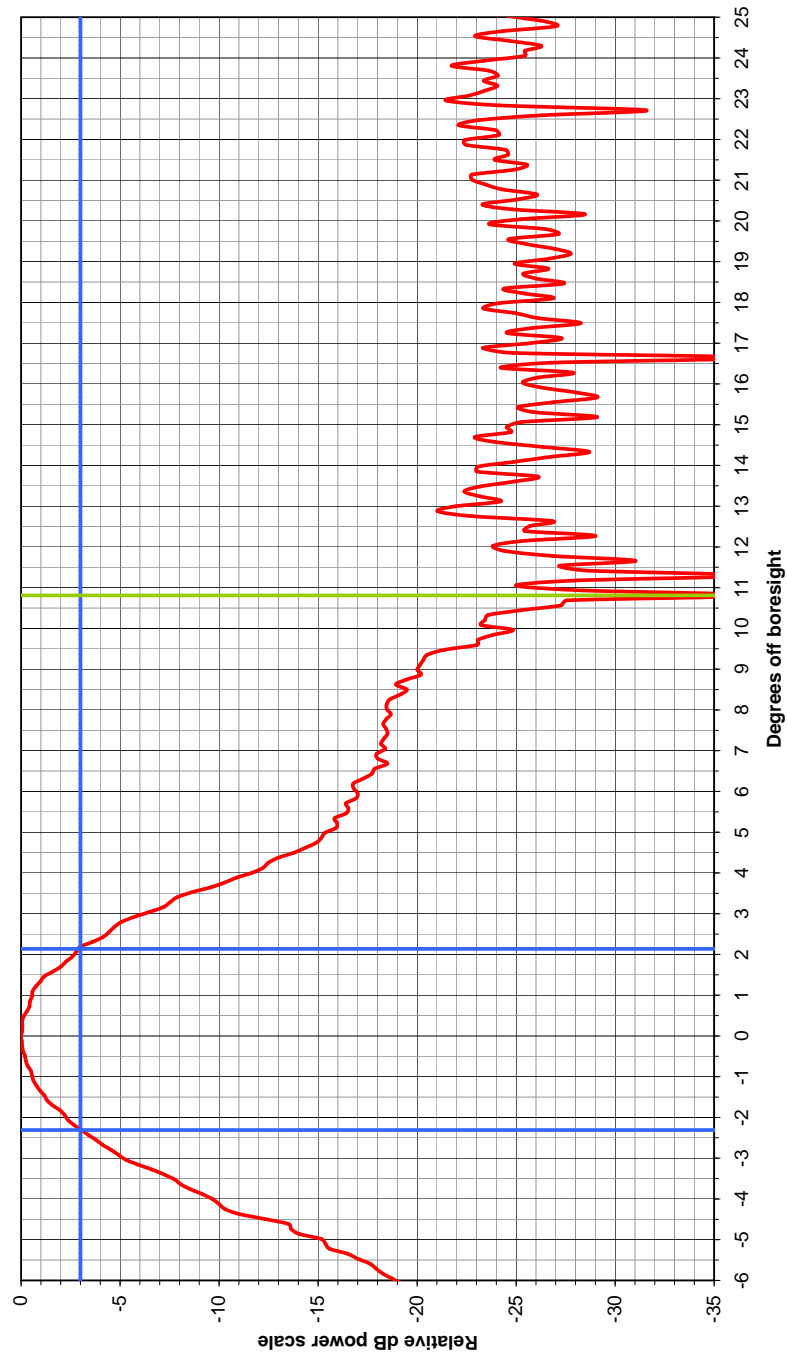


Figure 8.14 The normalized antenna power pattern, resulting from a drift-scan measurement using the Sun, is shown in red. A relative dB scale is used to emphasize small values. As in fig. 8.13 the horizontal blue line indicates the -3 dB level, while the two vertical blue lines indicate the boundaries of the measured HPBW. Even though no apparent side lobes can be seen, the vertical green line marks what appears to be a ‘null’ at approximately 10.8° .

Table 8.6 The measured HPBW, gain and aperture efficiency of the antenna for two different measurement series. For each series the gain was calculated according to two methods: The ‘HPBW method’ of section 8.7.1 and the ‘integration method’ of section 8.7.2. Overall, the integration method yielded lower results.

Series and method	Meas. HPBW $HPBW_{meas}$ (°)	Gain G (dBi)	Aperture eff. η_{ap} (%)
#1 ^a HPBW	4.4	31.4	46
#1 ^a Integration		31.1	43
#2 ^b HPBW	4.2	31.9	52
#2 ^b Integration		31.2	44

^a Measurement date: 16 August 2010. Solar radio flux: $S = 68$ SFU.

^b Measurement date: 15 August 2010. Solar radio flux: $S = 69$ SFU.

8.7.2 Main lobe integration method

The manner in which to obtain the antenna gain through integration was described at the end of section 6.2. In case of the author’s system, the method entails numerically integrating the normalized antenna power pattern in fig. 8.13, according to eq. (3.7b) on page 25. This equation assumes rotational symmetry. No measurements, in addition to those performed in section 8.7.1, are therefore necessary. However, instead of integrating from 0 to π to acquire Ω_A , the integration is performed from 0 to 0.188 (10.8°) to obtain Ω_M . The upper integration boundary of 10.8° is chosen as ‘the end’ of the main lobe, since it coincides with a ‘null’ according to the green vertical line of fig. 8.14.

Using eqs. (6.17) and (6.18) on page 84 and inserting the values for Ω_M , η_{beam} , λ and A_{ph} while furthermore assuming that the radiation efficiency $\eta_{rad} \approx 1$, the gain and aperture efficiency is calculated at $G = 31.1$ dBi and $\eta_{ap} = 43\%$ respectively. The second measurement series yielded $G = 31.2$ dBi and $\eta_{ap} = 44\%$. These aperture efficiencies are reasonable considering the under-illumination of the dish, purporting a 23 dB illumination taper. All values are summarized in table 8.6 together with the results of the HPBW method in section 8.7.1.

8.7.3 Comments on the antenna gain measurement results

As can be seen in table 8.6 the antenna gain results are in good agreement with each other, since they only differ by a maximum of 0.8 dB between the two methods. Within the HPBW and integration methods the differences are only 0.5 dB and 0.1 dB respectively. Overall, the integration method yielded lower results than the HPBW method. The author is of the opinion

that these lower results likely are closer to the true value, than those of the HPBW method. The reasons for this opinion are twofold:

1. The integration method calculates Ω_M through a numerical integration of actual measured data. From this, only η_{beam} and η_{rad} need to be estimated in order to calculate the antenna gain. See eq. (6.17)! The HPBW method on the other hand relies on an *approximation* using the HPBW to calculate Ω_M , according to eq. (6.14). Thus apart from only having to estimate η_{beam} and η_{rad} , this method also relies on having to estimate the pattern factor k_p when calculating the antenna gain. See eq. (6.15)! The uncertainty of the HPBW method is thus likely higher than for the integration method.
2. The feed horn in section 7.1.3 is designed for a dish with an $f/D \approx 0.36$, whereas the actual dish in section 7.1.1 has an $f/D = 0.30$. Thus as was already mentioned above, the dish is purposefully under-illuminated with an illumination taper calculated at 23 dB. Computer simulations [117] performed by Paul Wade (W1GHZ) [116] furthermore suggest that the real world aperture efficiency for a dish with this horn should be about 53% at most, provided that the dish has an $f/D \approx 0.36$ and a diameter equal to $20\lambda = 4.6$ metres. Since the actual dish f/D is lower and the diameter is smaller, the aperture efficiency should be lower as well. The aperture efficiencies obtained from the integration method thus seem more plausible than the even higher ones calculated from the HPBW method.

In support of the above an antenna gain $G = 31.1$ dBi will be used for the calculations that follow. There are however various sources of uncertainty associated with this value: Overall system linearity and stability, errors in the azimuth and elevation system, interference and solar flux variations to name a few. It is estimated that this uncertainty amounts to about 1.5 dB worst-case.

As with the G/T_{sys} determination in section 8.6.2 *the gain result obtained above reveals nothing about the accompanying polarization property of the antenna, since the Sun can be considered an unpolarized source* (see section 8.6.1). The co-polar gain or the axial ratio at various angles offset from boresight thus remain unknown. However, the actual gain at the intended circular polarization is likely lower than the value obtained above. When needed, this discrepancy should be estimated and either compensated for or treated as an uncertainty in calculations involving the antenna gain. Please also refer to section 3.5.5 for more on polarization loss.

8.8 Total system noise temperature estimation

Having determined G/T_{sys} as well as the antenna gain G , the total system noise temperature at the antenna terminals can be calculated as

$$T_{sys} = \frac{G}{G/T_{sys}} \quad (8.18)$$

Using this equation and inserting $G = 31.1$ dBi and $G/T_{sys} = 11.6$ dBiK⁻¹ (converted to linear terms) from sections 8.7.2 and 8.6.2, the total system noise temperature $T_{sys} = 89.9$ K. Unfortunately this is a relatively high system noise temperature, which instead should be in the vicinity of 70 K according to the ARRL Handbook [18, Table 30.8]. However, this discrepancy *could* be explained by the uncertainties of G and G/T_{sys} . To analyse the possibility of this theory further, an assessment of the antenna temperature will be performed in section 8.10.

8.9 Minimum detectable signal requirement

Using $T_{sys} = 89.9$ K from section 8.8 as well as $SNR_{out.min} = 3$ dB and $B = 100$ Hz from the task definition and criteria for success in section 1.1, it is possible to calculate the required MDS of the system by means of eq. (5.14a) on page 75. This yields $MDS = 2.5 \cdot 10^{-19}$ W = -156 dBm. Furthermore, using the definition from section 5.5, the receiver noise floor amounts to approximately -179 dBmHz⁻¹.

8.10 Antenna temperature estimation

The noise temperature of the antenna is given by solving eq. (4.39) on page 56 for T_{ant} as

$$T_{ant} = T_{sys} - T_{rx.e} \quad (8.19)$$

Inserting $T_{sys} = 89.9$ K and $T_{rx.e} = 38.1$ K from sections 8.8 and 8.5 into this equation yields $T_{ant} = 51.8$ K, which is a relatively high value.

The noise temperature of the lossless antenna, that is that part of T_{ant} which is solely determined by the noise from the surroundings of the antenna, is given by solving eq. (4.47a) on page 59 for T_a . By furthermore inserting eq. (4.46), the result is given as

$$T_a = L_{ant}T_{ant} - (L_{ant} - 1)T_{ant.ph} - L_{ant}\frac{T_{tx}}{I_{tx}} \quad (8.20)$$

To calculate T_a a number of assumptions have to be made regarding the unknowns of eq. (8.20):

1. The combined resistive (dissipative) loss of the antenna is assumed to be $L_{ant} = 0.04$ dB, corresponding to $\eta_{rad} = 99.1\%$, which includes the loss of the chassis N-connector of the feed horn Rx-port. While this loss can be neglected when determining the antenna *gain*, as was done in section 8.7, its impact on the antenna *temperature* is non-negligible.
2. The physical temperature of the antenna was estimated at $T_{ant.ph} = 290$ K at the time of the measurements. This estimate includes heating due to direct sun light.
3. The PA and coax cable were not connected to the Tx-port of the feed horn during the measurement, due to unrelated PA problems. However, the noise from the PA and coax is solely of resistive origin, since the transistor bias is turned off during reception. An equivalent amount of noise is thus generated by a terminating resistor, which was therefore connected to the Tx-port during the measurements so that $T_{tx} = T_{ant.ph} = 290$ K.¹⁷
4. The port-to-port isolation of the horn, *when installed in the dish*, could be measured using for example a network analyser. However, not having this kind of measurement equipment at hand at the antenna location, the author instead had to estimate its magnitude. Using information from an article by Jeffrey Pawlan (WA6KBL) and Rastislav Galuščák (OM6AA) [91], I_{tx} was estimated at 18 dB.

To the author the 18 dB isolation presented in assumption 4 constitutes a surprisingly low value. Not least since the *inherent* port-to-port isolation of this type of horn, that is when the horn is *not* installed in a dish, is said to be in the region of 25 dB. However, one has to remember that a wave reflected in the dish has its sense of polarization reversed. Anything re-entering the horn after reflection will therefore arrive at the opposite port from where it emerged, consequently reducing the port-to-port isolation. This effect is highly dependent on the focal length f , diameter D and edge illumination taper of the dish as well as on the axial position of the horn [91]. At the same time these parameters also govern the antenna temperature by changing the amount of illumination spillover and edge diffraction which, together with possible wire-mesh surface leakage, form the backward facing lobes.

Inserting the above values into eq. (8.20), the temperature of the lossless antenna is calculated at $T_a = 44.9$ K. Even though the ARRL Handbook

¹⁷The author furthermore assumes that the polarization property of the feed horn is designed with a 50Ω match at the Tx-port in mind. As a consequence, the port should not be left open since doing so would influence the field pattern inside the horn. Naturally, the same should be true for the Rx-port as was described in section 7.3.2.

suggests that this value should be in the vicinity of 33 K [18, Table 30.8], it is still plausible. This can be seen by performing a rough estimate of what T_a should approximately be. This is done by assuming that the main lobe and say half of the side lobes only see the sky, while the remaining half of the side lobes (including the back lobe) only see the ground at 290 K. The sky temperature can be estimated at about 10 K from the graph in fig. 8.15 or using similar graphs in the literature [95, ch. 3][79, fig. 17-4]. Using the above, as well as $\eta_{beam} = 0.75$ from section 8.7.1, T_a is estimated at

$$\begin{aligned}
 T_a &\approx \overbrace{0.75 \cdot 10 \text{ K}}^{\text{Main lobe contribution}} + \overbrace{(1 - 0.75)(1/2 \cdot 10 \text{ K} + 1/2 \cdot 290 \text{ K})}^{\text{Side and back lobes contribution}} \\
 &\quad \text{From the sky} \qquad \qquad \qquad \text{From the sky} \qquad \text{From the ground} \\
 &= 7.5 \text{ K} + 37.5 \text{ K} = 45 \text{ K}
 \end{aligned}$$

Note that about 80% of T_a originates from the side and back lobes, even though they only constitute 25% of the total beam area. The reason for this lies in the fact that the ground noise temperature is much higher than the temperature of the sky, which is the only temperature seen by the main lobe. *Side and back lobe noise contributions can thus have a significant impact on the overall EME system performance.* At low elevations however, the main lobe will contribute more to the antenna temperature; especially if it has a wide HPBW.

The elevated values of T_{sys} , T_{ant} and T_a could be explained by the author's antenna being unfavourably surrounded by tall trees and a few buildings. Another reason, as was speculated in section 8.8, could be an error associated in the measurements of G and G/T_{sys} . Assuming, for instance, that the combined error of $G/(G/T_{sys})$ amounts to 0.6 dB, correcting for this would instead yield $T_{sys} = 78.3 \text{ K}$, $T_{ant} = 40.2 \text{ K}$ and $T_a = 33.2 \text{ K}$ which is more in alignment with the ARRL Handbook [18, Table 30.8]. All of these values, including the measurement results above, are presented in table 8.7. Also shown are the estimated contributions to T_{ant} which have their origin in the resistive losses of the antenna, as well as in the noise at the Tx-port of the feed horn. See eqs. (4.44), (4.45) and (4.47a) on pages 58 and 59!

In regard to the above, the question arises as to what could cause an error amounting to say 0.6 dB. A number of sources of uncertainty for G/T_{sys} and G are mentioned in sections 8.6 and 8.7 respectively. One of these is the azimuth and elevation system of the antenna. From fig. 8.14 we see that if the antenna boresight is off by a mere 1° when pointing at the Sun, the hot antenna temperature $T_{ant.hot}$ will be about 0.6 dB below its possible maximum value. From eq. (6.1a) on page 79 we see that this error will essentially translate directly to the Y-factor since $T_{ant.hot} \gg T_{rx.e}$. From eq. (6.7) on page 82 we furthermore see that this, in its turn, will translate directly to G/T_{sys} since $Y \gg 1$. Finally, from eqs. (8.18) to (8.20) we see that

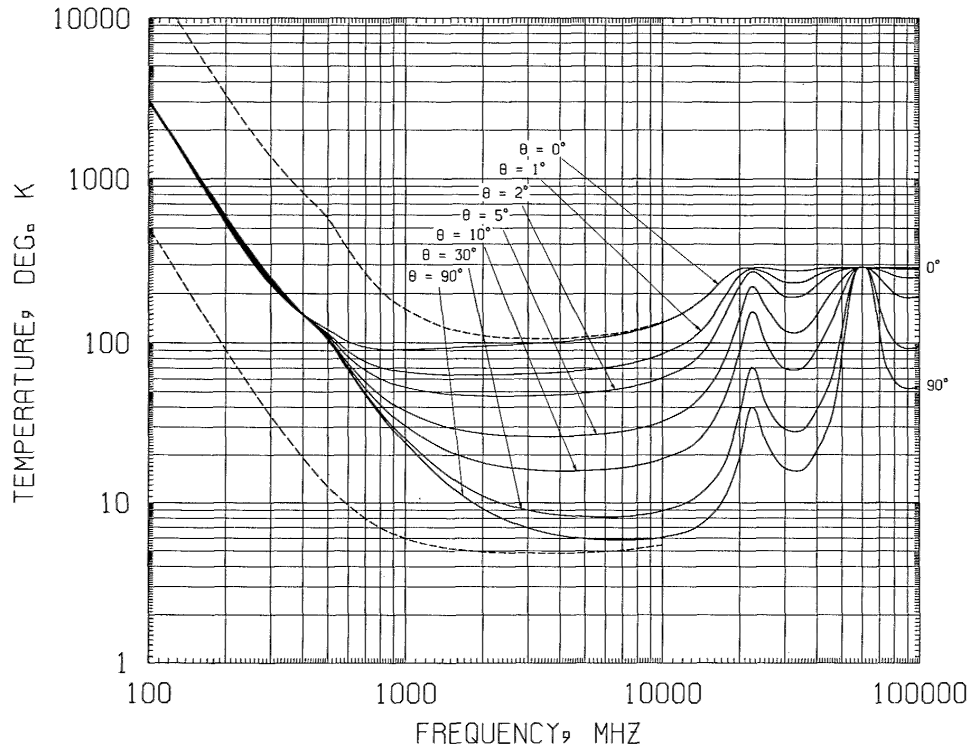


Figure 8.15 'Noise temperature of an idealized antenna (lossless, no earth-directed side lobes) at the earth's surface as a function of frequency for a number of beam elevation angles. The solid curves are for the geometric-mean galactic temperature, sun noise 10 times the quiet level, the sun in a unity-gain side lobe, a cool temperature-zone troposphere, 3 K cosmic blackbody radiation, and zero ground noise. The upper dashed curve is for maximum galactic noise (center of galaxy, narrow-beam antenna), sun noise 100 times the quiet level, zero elevation angle, and other factors the same as for the solid curves. The lower dashed curve is for minimum galactic noise, zero sun noise, and a 90° elevation angle. The slight bump in the curves at about 500 MHz is due to the sun noise characteristic. The curves for low elevation angles lie below those for high angles at frequencies below 400 MHz because of the reduction of galactic noise by atmospheric absorption. The maxima at 22.2 GHz and 60 GHz are due to water-vapor and oxygen absorption resonances.' (From [31, fig. 11])

Table 8.7 The results of the indirect measurements of the system noise temperature T_{sys} , the antenna temperature T_{ant} and the lossless antenna temperature T_a . Also shown are values where an assumed -0.6 dB correction has been applied to $G/(G/T_{sys})$ when calculating T_{sys} . Also shown are the contributions to T_{ant} originating in the physical temperature of the antenna and the noise temperature at the Tx-port.

Noise temperature	Measurement result (K)	With correction (K)
T_{sys}	89.9	78.3
T_{ant}	51.8	40.2
T_a	44.9	33.2
$T_{ant.e}^*$ ^a		2.7
T_{tx}^* ^b		4.6

^a Noise contribution from the physical temperature of the antenna. See eq. (4.44)!

^b Noise contribution from the Tx-port of the feed horn. See eq. (4.45)!

this will increase T_{sys} , T_{ant} and T_a by a mutual amount of kelvins (assuming L_{ant} is negligible in eq. (8.20)). From table B.1 in appendix B we furthermore notice that the resolution of the azimuth and elevation system is only 1° in each direction. Since there exist additional sources of uncertainty as well, such as rotator calibration error, a 0.6 or even 1.2 dB error in $G/(G/T_{sys})$ can likely be considered conservative.

Another error could be that $T_{rx.e}$, as it was determined in section 8.5, is too low at 38.1 K. If this is the case both T_{ant} and T_a are too high, according to eqs. (8.19) and (8.20). However, if the assumed 0.6 dB error in $G/(G/T_{sys})$ were to be solely attributed to $T_{rx.e}$, the error of the latter would amount to approximately $(89.9 - 78.3)/38.1 \approx 30\%$. The author considers such a large error in $T_{rx.e}$ to be improbable in light of the results of sections 8.4.2 and 8.5. Nevertheless, *if* an error (at least to some extent) lies in $T_{rx.e}$, it is not solely attributable to the uncertainties of the LNA NF. Likely more so, it is traceable to the estimate of the losses accompanying the SMA connectors and the protection relay in front of the LNA. Please refer to section 8.5.

There are other possible explanations for the relatively high values obtained for T_{sys} , T_{ant} and T_a , which are unrelated to measurement uncertainty. One such example is the possibility of an erroneous assumption in section 8.7.1 regarding the beam efficiency of the antenna. For instance, lowering η_{beam} from 0.75 to 0.65 would lower the calculated antenna gain by about 0.6 dB, lower the aperture efficiency by about 6 percentage points and reduce T_a from 44.9 K to 32.8 K. Man-made noise could be another culprit, even though no apparent sources could be observed during the measurements. Yet another explanation could be that the meshed wire netting, used to extend

the diameter of the antenna from 2.7 to 4 metres, is ‘leaking’ ground noise to the feed horn. See fig. 8.11 on page 162! However, considering that the mesh size (length) is only about 2% of the wavelength, that the central part of the dish is solid and that the dish is under-illuminated, this leakage should be very small.

A better and more preferable way of determining the antenna temperature, than presented here, would be to inject a known amount of noise into the signal path. This can be achieved by using a directional coupler, inserted between the Rx-port and the LNA protection relay. Such a set-up would allow for a Y-factor measurement, from which the antenna temperature could ultimately be determined.

8.11 Antenna temperature increase due to lunar noise

In case the SNR of an EME echo is to be estimated, the temperature contribution from the Moon to T_a needs to be accounted for, provided that it is non-negligible. The latter implies that the dish HPBW is narrow enough, as compared to the angular diameter of the Moon which is about 0.5° . Naturally, the increase in T_a will also increase T_{sys} . This, in its turn, will lower the value of G/T_{sys} and thus ultimately worsen the SNR results of the equations in section 5.2.

The increase in antenna temperature due to the Moon can be approximated using eq. (6.9) on page 83. In this case $T_{b.avg}$ is equal to the average disc noise temperature of the Moon, that is $T_{b.avg} = T_{moon} \approx 210$ K [18, ch. 30.10] [95, ch. 6].¹⁸ Furthermore, Ω_s is equal to the source solid angle of the Moon which can be approximated by use of eq. (6.11) on page 83, in which $\theta_s = 0.5^\circ$ is the angular diameter of the Moon. As before, Ω_A is the source solid angle of the antenna. It can either be estimated from eq. (6.12) on page 83 or by numerically integrating the normalized antenna power pattern according to eq. (3.7) on page 25. Both methods were used in sections 8.7.1 and 8.7.2 to calculate the antenna gain.

Using Ω_A from the calculations in section 8.7.2, the increase in antenna temperature due to the Moon is estimated at $\Delta T_a = 1.3$ K. This results in G/T_{sys} , and thus the accompanying SNR, decreasing by a mere 0.06 dB.

On a different note, an interesting result is found if the size of the antenna is increased so that $\Omega_A \lesssim \Omega_s$, that is if the antenna HPBW becomes about the same size or smaller than the angular diameter of the Moon. In this case

¹⁸In contrast to the Sun the lunar disc has a uniform temperature distribution which ‘is almost independent of frequency above 1 GHz’ [95, ch. 6].

T_a approaches T_{moon} and a low LNA NF therefore becomes less important. However, this increase in T_a and thus T_{sys} is accompanied by a significantly larger increase in the antenna gain G . This provides a considerable net increase in the resulting G/T_{sys} , thus improving the overall SNR performance of the system. Unfortunately this situation is beyond the reach of most EME operators at 1296 MHz, since it entails an antenna diameter of more than 30 metres. This corresponds to an antenna gain of more than 50 dBi.

Chapter 9

Transmitting system measurements and estimations

Having characterized the Rx subsystem in chapter 8, the same will now be done for the Tx part of the system. First, the procedure and results of the *power amplifier measurements* will be presented and commented on. This will also include an estimate of the feed line losses. After this, an estimation of the *transmitted power at the LNA input* will be presented. In connection with this the minimally required isolation of the LNA protection relay, when transmitting at the maximum legal power level, will also be determined.

Knowledge attained in this chapter will be used in chapter 10 to calculate the EME link budget, as well as in chapter 11 to estimate the SNR of the EME echoes.

9.1 Power amplifier measurements

The output powers of drive PA 1 and 2, presented in sections 7.2.1 and 7.2.2 respectively, were adjusted to match the required input powers of the subsequent stages. Ultimately, this implied maximizing the output power of the main PA, presented in section 7.2.3, while still retaining linear operation throughout the Tx chain, thus avoiding signal distortion and ‘splatter’ due to PA compression. The latter was guaranteed through signal inspection using a spectrum analyser connected to the coupled port of a directional coupler, in its turn connected between the output of the main PA and the feed line (antenna) coax. Since adjusting the signal levels in the Tx chain is

a system specific matter, EME operators are tasked with examining this for their own specific system. Hence it will not be dealt with here any further.

From an EME communication perspective the output power of the main PA is of great interest since it partly determines the attainable SNR at the receiving station. This can be seen from the equations in sections 5.1 and 5.2. The output power was therefore measured by replacing the aforementioned spectrum analyser with suitable attenuators and an ‘HP 478A Thermistor Mount’, connected to an ‘HP 432A Power Meter’. Both instruments, as well as the directional coupler, had been calibrated prior to the measurement. Great care was taken to ensure safe measurement power levels, so as not to damage the expensive thermistor mount which is rated at only 30 mW maximum average power.

Having applied a continuous wave (CW) signal from the transmitter, the output power from the main PA was measured at approximately 370 W, with negligible reflected power from the antenna. Unfortunately, this is a lot less than the anticipated 600 W which eight XRF286S LDMOS transistors should be able to produce. Furthermore, since the main PA is supplied with 28 VDC at 50 A during Tx, the DC power efficiency is only 26% which is far too low.

Having ruled out measurement and operator error, other possible reasons for these discouraging results were contemplated upon. Some of these, such as too little RF input power or erroneously connected 90° hybrid couplers, were investigated but could swiftly be ruled out. Other possible candidates however, needing further investigation, are the following:

1. The PTFE cables connecting the PA modules to the hybrid couplers could
 - a. be too thin and thus very lossy.
 - b. have slightly different electrical lengths which alter the relative phase of the combining signals in an unfortunate manner. This would result in power being lost in the terminations of the hybrid couplers.
 2. Placing the output combiner board (containing the three high power hybrid couplers) below the equivalent input board, as can be seen in fig. 7.9 on page 107, might have been an unwise design decision. This could influence the balance of the output couplers and thus result in power being lost in the terminations.
 3. The output power from the individual transistors could differ, even though they seem to consume the same amount of DC power. This would result in power being lost in the terminations of the hybrid couplers.
-

Apart from the above, experimental inquiries by Dominique Fässler (HB9BBD) [55], regarding the same type of dual transistor PA modules as used by the author,¹ suggest that:

4. There are problems with the impedance match of the transistors, which results in them running hot.
5. The hybrid couplers are not entirely balanced, resulting in power being lost in the terminations.

Even though the author has not personally investigated items 4 and 5, if correct they could help to explain the poor performance of the PA. For according to Fässler, it is possible to increase the output power of each dual transistor module to about 250 W through modification [55]. In case of the author's main PA this would push its final output power close to 1 kW, which is even well beyond the 600 W claimed by its designer. Naturally, the modifications proposed by Fässler need to be seriously considered.

Unfortunately, item 1a has already been verified by the author since the PTFE cables increase in temperature after a period of operation. This can be remedied by exchanging these for a lower loss alternative, preferably of semi-rigid type.

As for the remaining items, item 1b would be solved if care for the electrical length is taken when solving item 1a. Furthermore, item 2 is easily investigated by increasing the distance between the two hybrid coupler boards. The author does not expect this to result in a noticeable difference however. Item 3, if valid, would likely be solved by trying to remedy items 4 and 5 since impedance mismatch is a likely reason for unequal power being output from the transistors.

Apart from the above, there is an estimated 1.2 dB combined loss in the feed line connecting the main PA to the feed horn. This loss was estimated using coax cable datasheet information, as well as assuming a 0.06 dB loss per connector pair. Taking the combined loss into consideration, the power P_t at the terminals of the Tx-port of the antenna is only about 280 W. Arranging to house the PA closer to the antenna and using lower loss coax cable would thus be desirable.

Regardless of the above and though not optimal, calculations show that $P_t = 280 \text{ W} = 24.5 \text{ dBW}$ at the antenna should be enough to hear ones own EME echoes. The time-consuming but necessary undertaking of modifying the main PA will therefore be temporarily postponed until more time is available.

¹ Version 7.2, dated 6/09.

9.2 Transmitted power at the LNA input

Using the in-dish port-to-port isolation of the feed horn ($I_{tx} = 18$ dB) from section 8.10, the power at the Rx-port is approximately 36 dBm or 4.4 W during Tx, when $P_t = 280$ W. Furthermore, using the technical specifications for the port-to-port isolation of the LNA protection relay ($I_{rl} = 90$ dB), the power at the LNA input is approximately -54 dBm or 4.4 nW which is well within acceptable limits. The total isolation at 108 dB, between the Tx-port and the LNA input, is thus more than adequate to protect the LNA from damage during Tx when $P_t = 280$ W.

Even at the Swedish legal limit of $P_t = 1$ kW, the power at the LNA input would only be about -48 dBm or 16 nW. Assuming an upper limit of -30 dBm or 1 μ W at the LNA input, the LNA protection relay would require at least 72 dB of isolation for the LNA not to be damaged during Tx when $P_t = 1$ kW.

Chapter 10

EME signal path link budget estimation

Having measured the antenna gain G in section 8.7 as well as the output power P_t in section 9.1, it is finally possible to calculate the *link budget* of an EME echo. The necessary theory for doing so was presented in section 3.4 in which eq. (3.25), dealing with a monostatic radar, is of interest. In particular, eq. (3.25c) on page 30 will be used in the calculations that follow. Every part of this equation will have its own section in this chapter: *Transmission*, *transmission loss* and *reception*. The final result will be presented in the *link budget summary*.

Some of the results of this chapter will be used in chapter 11 to estimate the SNR of EME echoes.

10.1 Transmission

The transmission part of eq. (3.25c) consists of the transmitter EIRP, which is calculated according to eq. (3.10) on page 26. Using the antenna output power $P_t = 280 \text{ W} = 24.5 \text{ dBW}$ from section 9.1 and the antenna gain $G = 31.1 \text{ dBi}$ from section 8.7.2, the EIRP in dB is thus given by $EIRP = 24.5 \text{ dBW} + 31.1 \text{ dBi} = 55.6 \text{ dBW} \approx 360 \text{ kW}$.

10.2 Transmission loss

The second term of eq. (3.25c) is given by G_{obj}/L_{fsl}^2 . In keeping with the nomenclature of this report, where losses are greater than one (or positive in terms of dB), this term is the inverse of the transmission loss given by eq. (3.26) on page 31.

The gain G_{obj} is determined by the RCS σ of the Moon by means of eq. (3.23) on page 30. According to Evans [51] $\sigma = (0.065 \pm 0.008) \cdot A_{moon}$ for $\lambda = 23$ cm, where $A_{moon} = 9.49 \cdot 10^{12} \text{ m}^2$ is the *physical* cross section (projected area) of the Moon. Inserting these values into eq. (3.23) yields $G_{obj} = 141.7 \pm 0.6$ dBi. It might seem odd to the reader that the Moon is portrayed as having a gain. Though as was explained in section 3.4, the RCS is a purely hypothetical concept which assumes isotropical scattering of the signal. In reality however, the scattering is *not* isotropical. This discrepancy is compensated for by the hypothetical gain G_{obj} .

The free-space loss L_{fsl} is given by eq. (3.16) on page 27, in which the distance r to the Moon needs to be determined. Since the results of this section will be used to evaluate the SNR measurements of chapter 12, the actual lunar distance at the time of those measurements needs to be used here to calculate L_{fsl} . Using the MoonSked software, presented in section 7.5.2, the distance was determined to be $r = 364\,288$ km. Inserting the required values into eq. (3.16) yields $L_{fsl} = 206.0$ dB.

Using the above values for G_{obj} and L_{fsl} , the transmission loss in dB is equal to $L_{tl.m} = 2 \cdot L_{fsl} - G_{obj} = 2 \cdot 206.0 \text{ dB} - 141.7 \text{ dBi} = 270.3 \text{ dB}$. This is a considerable loss, but fully in line with what can be expected.

10.3 Reception

The reception part of eq. (3.25c) simply consists of the antenna gain $G = 31.1$ dBi from section 8.7.2.

10.4 Link budget summary

Having determined the three terms of eq. (3.25c) in sections 10.1 to 10.3, the received power at the antenna terminals is given by $P_r = 55.6 \text{ dBW} - 270.3 \text{ dB} + 31.1 \text{ dBi} \approx -183.6 \text{ dBW} = -153.6 \text{ dBm}$.

Chapter 11

Lunar echo SNR estimation

Having determined various system parameters in the previous chapters, it is finally possible to estimate the SNR of EME echoes, which is part of the task definition and criteria for success as stipulated in section 1.1. The necessary theory for doing so was presented in section 5.2 in which eq. (5.6) on page 70, dealing with a monostatic radar, is of particular interest. The SNR calculations are followed by a SNR uncertainty assessment.

The results of this chapter will be compared to those of chapter 12, dealing with the lunar echo SNR measurements. As was the case in chapter 10, certain parameters will thus have the same values as those which existed during the empirical measurements.

11.1 SNR calculations

From the left and right expressions of eq. (5.6a) on page 70, we see that the SNR estimate can be calculated by either of two methods:

1. By using the received signal power $P_r = -183.6$ dBW from section 10.4 and the system noise temperature $T_{sys} = 89.9$ K from section 8.8. Both are referenced to the terminals of the receiving antenna.
2. By using $EIRP = 55.6$ dBW, $G_{obj} = 141.7$ dBi and $L_{fsl} = 206.0$ dB from sections 10.1 and 10.2 as well as $G/T_{sys} = 11.6$ dBK⁻¹ from table 8.5 on page 161. (G_{obj} and L_{fsl} can furthermore be substituted by the transmission loss $L_{tl.m} = 270.3$ dB according to section 10.2.)

Naturally, both methods will yield the exact same results. Which one to choose is a matter of preference and which parameters have been determined beforehand. This sections will employ method 2, using dB values by means of eq. (5.6b). The bandwidth in which the SNR is to be determined is chosen at $B = 100$ Hz = 20 dBHz, which is the same as the measurement bandwidth

chosen in chapter 12. The calculated SNR estimate of the lunar echoes is thus equal to $SNR_{moon.c} = 55.6 \text{ dBW} + 141.7 \text{ dBi} - 2 \cdot 206.0 \text{ dB} + 11.6 \text{ dBK}^{-1} - 10 \cdot \log(1.381 \cdot 10^{-23}) \text{ dBJ K}^{-1} - 20 \text{ dBHz} \approx 5.4 \text{ dB}$. This is in line with the results of others using similar equipment and is thus considered plausible.

11.2 SNR uncertainty assessment

This section will not present a detailed, in-depth analysis of all the various sources which contribute to the combined uncertainty of $SNR_{moon.c}$. Rather, a rough worst-case uncertainty estimate, involving those sources which matter most, will be given. In eq. (5.6a) on page 70 this entails the uncertainties of $EIRP$, G_{obj} and G/T_{sys} which, in their turn, are composed of various sources of uncertainty as well. The uncertainty of L_{fsl} is given by the uncertainty of the distance to the Moon, as can be seen from eq. (3.16) on page 27. It is therefore neglected since this distance is very well known at all times. In the following, the use of the word ‘uncertainty’ assumes a worst-case uncertainty implying a coverage factor of 3.

The $EIRP$ is made up of the output power P_t and the antenna gain G according to eq. (3.10) on page 26. The uncertainty of these are estimated at 15% and 41% (corresponding to about 1.5 dB) respectively. Adding these in an RSS fashion, the uncertainty of the $EIRP$ is thus given by $U(EIRP) = \sqrt{15^2 + 41^2} \% \approx 44\%$.

The uncertainty of the gain G_{obj} of the radar object is entirely given by the uncertainty of the RCS σ , according to eq. (3.23) on page 30. From Evans [51] we thus get $U(G_{obj}) = 0.008/0.065 \% \approx 12\%$.¹

According to eq. (6.7) on page 82 the uncertainty of G/T_{sys} is given by the uncertainty of the Y-factor Y and the solar flux density S . These are estimated at 12% (corresponding to about 0.5 dB) and 4% (corresponding to about 3 SFUs) respectively, resulting in $U(G/T_{sys}) = \sqrt{12^2 + 4^2} \% \approx 13\%$.

Assuming that these three uncertainties are uncorrelated, they can be combined in an RSS fashion. This yields an SNR uncertainty amounting to $U(SNR_{moon.c}) = \sqrt{44^2 + 12^2 + 13^2} \% \approx 47\%$, corresponding to about +1.7 dB and -2.8 dB. Assuming instead a coverage factor of 2 the result is 2/3 of this, that is $U(SNR_{moon.c}) \approx 31\%$ corresponding to about +1.2 dB and -1.6 dB.

¹ This assumes that the uncertainty of σ , provided by Evans, is of ‘worst-case’ type.

Chapter 12

Lunar echo SNR measurements

Chapter 11 lead to an estimate of the SNR of EME echoes, calculated using previously measured and sometimes estimated system parameters. This chapter will present empirical SNR measurements of actual EME echoes, the results of which will be compared to those of chapter 11. The *echo-data acquisition process* will be presented first, followed by the *SNR measurement method and results*. Both methods make extensive use of the internal scripting functionality of SL, presented in section 7.5.1.

12.1 Echo-data acquisition process

Measuring a stable SNR of EME echoes would have been trivial, had their amplitudes been more or less constant. Unfortunately however, the signal amplitude fluctuates both rapidly and extensively due to libration fading which will be covered briefly in chapter 13. Suffice it to say here, the reason for this phenomenon lies in the fact that signal components, being reflected from different parts of the lunar surface, arrive at the receiving antenna with phase relationships which are random relative to each other. As a result, these components sometimes add and sometimes cancel as the Earth and Moon move relative to each other.

Establishing a reliable SNR result thus entails averaging several individual SNR measurements. However, for a monostatic EME radar system the maximum duration of each echo is only about 2.5 seconds, since this is the time it takes for the transmitted signal to return to Earth. Furthermore, switching the system from Rx-mode to Tx-mode and back to Rx-mode again requires a bit of time as well. This leaves barely two seconds of measurement

time for every echo, which is not enough for a stable SNR measurement. It is therefore necessary to average several consecutive echoes in some manner.

The author chose to solve this problem by automating the whole Rx–Tx–Rx sequence and record every echo as a separate audio file, using a computer running SL. Interfacing to the outside world was accomplished by means of RS-232 serial port communication, for PTT and CW control, as well as via the sound card for recording audio from the radio in 2 500 Hz SSB bandwidth. All signals were relayed via the audio and data interface, designed and built by the author. Please refer to section 7.4.3 and appendix C for more information on this interface. See also fig. 7.1 on page 94 for details regarding the signal paths.

The complete echo-data acquisition sequence used during the experiments is as follows:

1. Initiate PTT by setting the serial port request to send (RTS) control line to logic high.
2. Wait 0.5 seconds for the sequencer to switch the system to Tx-mode.
3. Initiate CW by setting the serial port data terminal ready (DTR) control line to logic high.
4. Transmit for 3 seconds.
5. Terminate CW by setting the serial port DTR control line to logic low.
6. Wait 0.1 seconds for CW to end.
7. Terminate PTT by setting the serial port RTS control line to logic low.
8. Wait 0.4 seconds for the sequencer to switch the system to Rx-mode.
9. Start the frequency spectrum and record the received EME echo as an audio wave-file.
10. Record for 1.7 seconds.
11. Stop the recording and the frequency spectrum.
12. Restart at step 1 unless the user has stopped the automation, in which case idle mode is entered.

As can be seen from this list, every measurement cycle takes 5.7 seconds to complete resulting in 1.7 seconds of echo-data.¹ Since the system transmits for 3 seconds, the Tx/Rx-duty cycle is about 53%.

To accomplish the above the author wrote a script, using SL's internal scripting language. Figure 12.1 shows a screenshot of SL running this 'EME echo-data acquisition' script, whose source code can be found in appendix D.2. User control and status information is provided via on-screen buttons, which

¹ In reality it takes about 3% longer due to delays in SL.

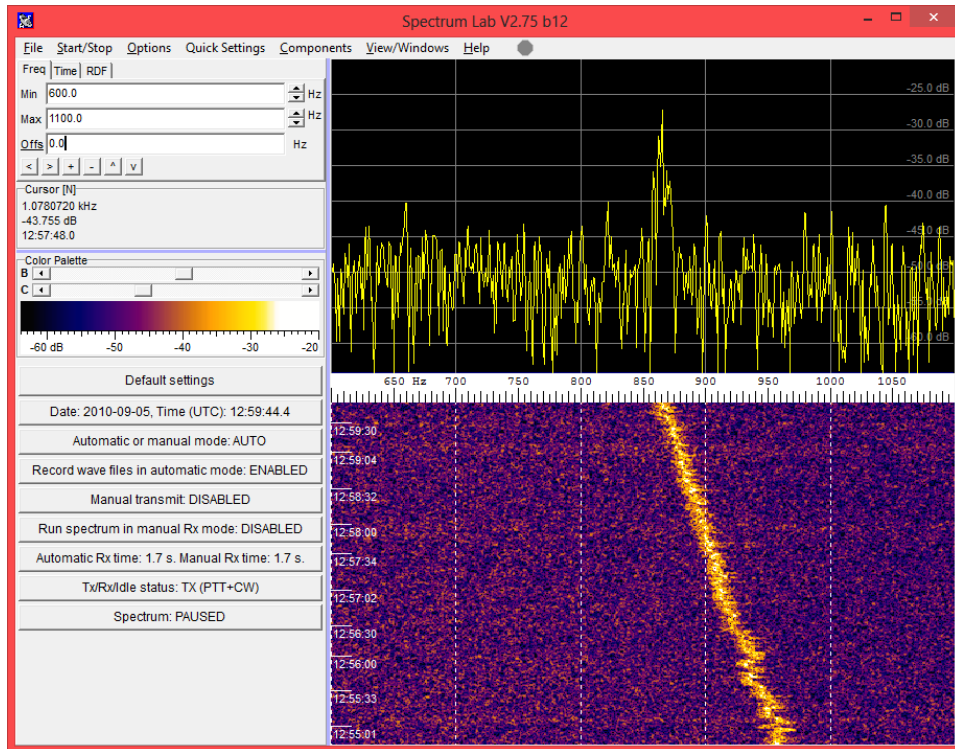


Figure 12.1 SL running the automatic EME echo-data acquisition script, with wave file recording enabled. One of the buttons to the left shows the current state as ‘TX (PTT+CW)’, corresponding to step 4 of the sequence described on page 185. Evident from the ‘waterfall’ part of the spectrum is a continuous frequency shift of the signal due to the Doppler effect and system instability. Notice also the width of the signal, resulting from lunar libration.

can be seen to the left. Pushing some of these buttons toggles their indicated state or lets the user change parameter values via a dialogue window. A continuous frequency shift of the signal can be seen in the lower ‘waterfall’ part of the spectrum. This is caused by the Doppler shift and frequency instability of the system.² One can also see that the signal is about 15 to 20 Hz wide due to libration-induced Doppler spread which will be explained in chapter 13.

Several measurement series were recorded during the course of a day, totalling 913 echoes or about 26 minutes worth of EME echo data, which took the system nearly one and a half hours to collect. Unfortunately, when the author studied these recordings in more detail after the fact, it was discovered that they sporadically (and to a varying degree) suffer from what appears to be

² The frequency instability was subsequently traced to a fault in the local oscillator of the transverter, alas after the measurements were completed. Even so, the author is not of the opinion that this fault influenced the quality of the SNR measurements.

man-made interference, which manifests itself as broadband noise. This can be seen as diffuse horizontal lines in the ‘waterfall’ part of the screenshot in fig. 12.1. The origin of this interference is still unknown and future investigations need to be conducted. Nevertheless, thanks to numerous recordings and mostly only short bursts of interference, the author succeeded in analysing several minutes of data which appeared to be interference-free. The results of this detailed analysis is presented in section 12.2 and chapter 13.

12.2 SNR measurement method and results

Having recorded a substantial amount of [EME](#) echoes as described in section 12.1, the author wrote another [SL](#) script to analyse some of this data. The main goal set out for this script was to measure the [SNR](#), obtained from the [SNNR](#) using eq. (5.7b) on page 71, and continuously present it to the user. Another goal was to try and measure the Doppler spread of the signal, a matter which will be discussed in chapter 13. Since the amplitude of an echo varies substantially due to libration fading, yet another goal was to apply time averaging in order to obtain more stable readings. However, achieving all of the above proved at bit challenging due to the Doppler shift and the aforementioned frequency instability of the system. The problem of taking a long-term average of a signal moving in frequency thus had to be solved first.

The author succeeded in solving this problem by using [SL](#)’s [FFT](#) filter function. As with most functions in [SL](#), the filter is programmable via the internal scripting language. A feature of the filter is that its output signal can be shifted (translated) in frequency by a desired amount. [SL](#) also has the ability to find the frequency of a signal peak within a specified bandwidth. Combining these two features and setting the filter to band-pass type, the author implemented a dynamic frequency shift of the signal to a constant frequency location. Thus as the input signal to the filter is moving in frequency, the filter continuously follows the peak of this signal while at the same time keeping the peak of the output signal stationary. Even though the execution speed of [SL](#)’s script interpreter is only 50 ms this works surprisingly well, at least as long as the shift in input frequency is not too drastic. For most of the time the output signal peak is within about 1.5 Hz of its designated frequency, provided that it is subjected to a sufficient amount of time-averaging and that the [FFT](#) resolutions of the signal and filter are sufficient.³ Nevertheless, the results are positive as can be seen in fig. 12.2 which shows a screenshot of [SL](#) running the ‘[EME](#) echo-data analysis’ script.

³ If the [FFT](#) resolutions are too low the discrete steps of the frequency shift will be too coarse.

Table 12.1 Two measurement results of the average SNR of the EME echoes. The PA was cooler during the second measurement series than during the first one. Also shown is the estimated average SNR from section 11.1, including the associated uncertainties from section 11.2.

SNR	Result (dB)	Date
$SNR_{moon.m}$ #1	4.8	05 Sep 2010 ^a
$SNR_{moon.m}$ #2	6.2	05 Sep 2010 ^b
$SNR_{moon.c}$	$5.4^{+1.2}_{-1.6}$	20 Oct 2010 ^c

^a 08:39 to 08:52 (24h UTC): Az = 188° to 193°, El = 50° to 51°.

^b 09:03 to 09:09 (24h UTC): Az = 197° to 199°, El = 50° (unchanged).

^c The date of the G/T_{sys} measurement. See table 8.5 on page 161!

The source code for this script is found in appendix D.3. The FFT settings used during most of the SNR measurements are shown in fig. 12.3.

One of the buttons to the left in fig. 12.2 shows the echo SNR at various levels of averaging. The single measurement value (yellow curve in channel 1) is 2.0 dB, the 50 FFTs average (yellow curve in channel 2) is 7.3 dB and the long-term average (red curve in channel 2) is 6.8 dB. Furthermore, having temporarily decreased the FFT window time, the peak SNR measured during the entire series was about 19 dB, albeit only during a split second. These values provide a good example of the drastic variations in the SNR, which one can experience from EME echoes. This is even more evident in fig. 12.4 which shows the measured SNR at various levels of averaging, as a function of time. These curves were produced from single SNR measurements which were exported to a text file during the SL analysis.

Taking the total average of the entire measurement series yields $SNR_{moon.m} \approx 4.8$ dB, represented by the blue line in fig. 12.4. Comparing the estimate from section 11.1 to this result we see that it is only 0.6 dB higher at $SNR_{moon.c} = 5.4$ dB, given by the red line. This is within the estimated expanded uncertainty $U(SNR_{moon.c}) = +1.2/-1.6$ dB from section 11.2, shown as dashed red lines. The criteria for success, as stipulated in section 1.1, have thus been met. A summary of the results are given in table 12.1.

As can be seen from the black curve in fig. 12.4, the SNR decreases as time goes by. This is likely a result of the PA output power decreasing, as the temperatures of the LDMOS transistors increase during operation. This increase is significant even though the Tx/Rx-duty cycle is only 53%, since the main PA DC efficiency is only 26%.⁴ On average, this results in

⁴ The unfortunate reasons for this low efficiency were contemplated upon in section 9.1.

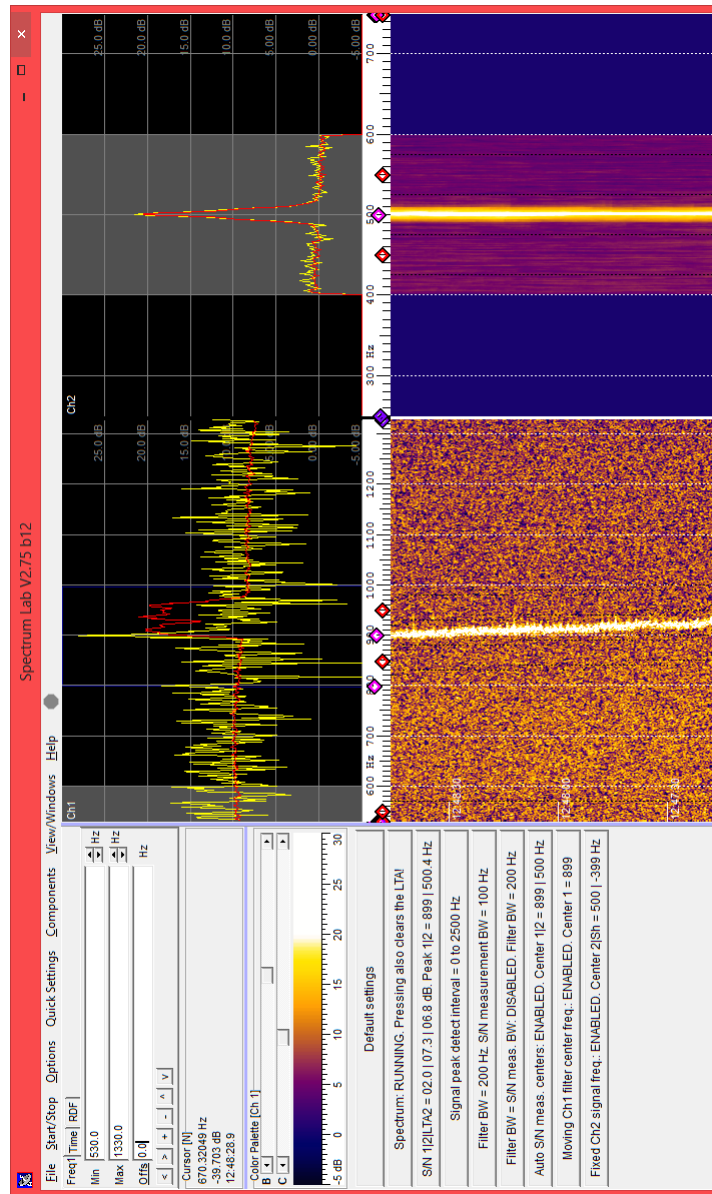


Figure 12.2 SL running the EME echo-data analysis script, reading recorded wave files. Even though the input signal (yellow curve in channel 1) is subjected to a continuous frequency shift, the frequency of the output signal (yellow curve in channel 2) is virtually constant at 500 Hz (chosen arbitrarily). The filter ‘listening’ bandwidth is set to 200 Hz while the SNR measurement bandwidth is set to 100 Hz. SNR results are shown in button number three from the top. The Doppler spread of the output signal at about 20 Hz is more evident here than in fig. 12.1. Most parameter can be changed by pushing the buttons and a few also by dragging some of the ‘diamond markers’ in the frequency scale.

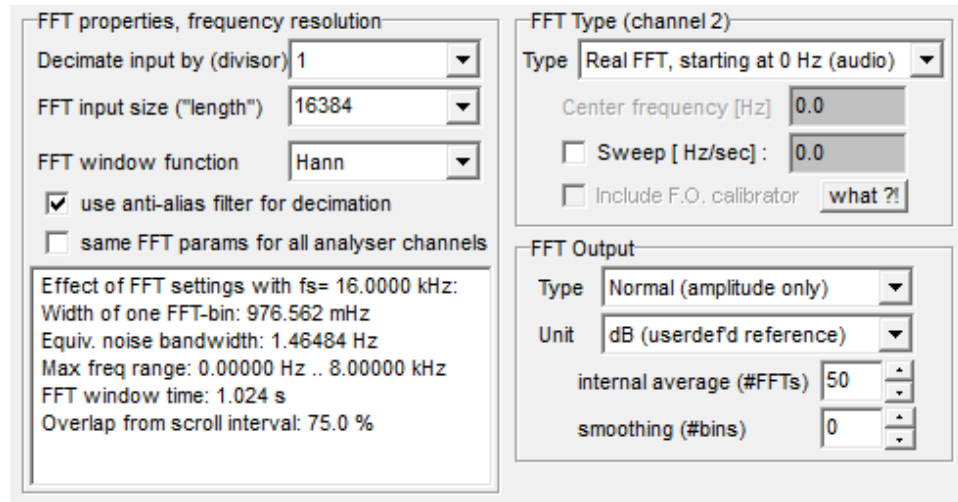


Figure 12.3 The [SL FFT](#) settings used during the [SNR](#) measurements.

about 500 W of continuous power being dissipated in the heat spreader! Additionally, thermal resistances play a role as well.

The overall temperature of the heat spreaders were already elevated when the measurements presented in this section commenced. The reason for this was that several long-lasting measurement sequences had just been conducted, in close succession. The author therefore chose to conduct another measurement sequence, after having let the system cool down for several minutes. This resulted in the average [SNR](#) increasing from 4.8 dB to 6.2 dB, that is by 1.4 dB. Please refer to table [12.1](#). As in the previous measurement however, the sloping decrease in the [SNR](#) could still be observed.

A way of mitigating this phenomenon is to increase the cooling capacity of the heat spreader. This can be achieved by increasing its size, increasing the airflow through the cooling flanges or even by using water cooling. First and foremost though, in regard to what was said in item [4](#) on page [178](#), improving the impedance match of the transistors would lower their operating temperatures. The findings in this section thus constitute another reason for implementing the [PA](#) modifications contemplated upon in section [9.1](#).

In hindsight, the author should have measured the output power at regular intervals, to compensate for its drift in the [SNR](#) calculations. An optimal solution would have been to continuously measure the output power using a power detector connected to the computer. These measurements could then have been saved to a text file (or even polled by [SL](#)) during the echo-data acquisition process, for further analysis.

Of course, instability in the output power is not the only parameter influencing the measurement uncertainty. Instabilities related to the overall gain, linearity

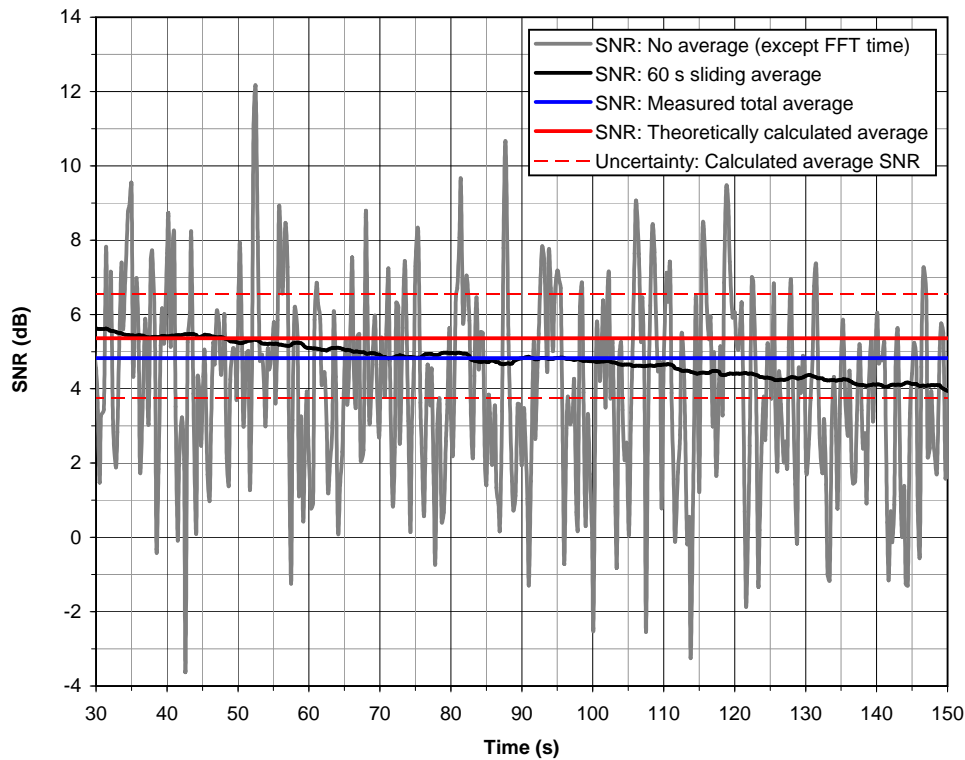


Figure 12.4 The measured SNR of the EME echoes as a function of time, for different levels of averaging: No averaging except for the FFT window time (grey curve), 60 seconds sliding average (black curve) and total average at $SNR_{moon.m} = 4.8$ dB (blue line). Also shown is the estimated SNR at $SNR_{moon.c} = 5.4$ dB (red line) and its associated uncertainty boundaries (dashed red lines) having a coverage factor of 2. The unaveraged grey curve shows the rapid and significant fluctuations in the SNR, resulting from libration fading. From the 60 seconds sliding average (black curve) the SNR can be observed decreasing as time goes by.

and bandwidth of the receiver subsystem contribute as well. Man-made noise and antenna depointing loss are further factors, as are the effects related to ionospheric propagation and lunar reflection.

Another factor which needs to be considered is the difference in antenna direction, and thus in antenna temperature, at the time of the G/T_{sys} and $SNR_{moon.m}$ measurements. This can be important when comparing $SNR_{moon.c}$ to $SNR_{moon.m}$, since the former is calculated using G/T_{sys} . Even though the azimuth directions are close between the G/T_{sys} and $SNR_{moon.m}$ measurements, their elevation angles differ by almost 30° . However, from the results of the antenna characterization in section 8.7 as well as from the topography of the surroundings of the antenna, the author assesses that the change in antenna temperature is of secondary importance in this particular case.

The topic of antenna polarization, in regard to the G/T_{sys} and G measurement results, was discussed at the end of sections 8.6.2 and 8.7.3. It was concluded that the polarization accompanying these results is unknown and that the actual values of G/T_{sys} and G are likely lower at the intended circular polarization of the antenna. The suggestion was that calculations involving these quantities therefore be corrected for this fact. However, the author does not see any need to apply such corrections to $SNR_{moon.c}$ when comparing it to $SNR_{moon.m}$, since the same antenna has been used during both the G/T_{sys} and $SNR_{moon.m}$ measurements. Furthermore, in a monostatic radar system the same antenna is used during both transmission and reception. Thus, simply put, the author assumes that the antenna is matched to its own polarization and that no correction therefore needs to be applied. Naturally, there are still polarization losses incurred by the EME-propagation path, though these are rightfully part of the SNR results.

Chapter 13

Lunar echo Doppler spread measurements

During the 1960s scientists in the United States were probing the Moon using high-powered (megawatt) *radars*, emitting microsecond pulses at various wavelengths such as 23 cm. The purpose of their investigations was to analyse the properties of the lunar surface for the ensuing lunar landings. Properties such as the average surface slope, depth of the surface layer, surface density, surface roughness, particle sizes, electrical conductivity and dielectric constant were thus of interest. These parameters were indirectly determined by measuring and analysing the *radar* echo power as a function of wavelength, wave polarization and range, with the latter in regard to the curvature of the Moon.

In this chapter the author's *EME* echoes will be analysed and compared to the ones obtained during the experiments of the 1960s. In order to achieve this, some *historical results* will be presented and discussed first. This will be followed by a presentation of the author's *doppler spread measurement method and results*. Since this chapter does not solve any problems related to the *task definition and criteria for success* presented in section 1.1, the matters contained herein will only be dealt with in a brief manner. For those seeking more information, please refer to the literature [51, 108][18, ch. 30.9].

13.1 Historical results

When transmitting a *radar* pulse towards the Moon the point closest to the *radar* antenna, that is the *subradar point*, will be hit first. Due to the curvature of the Moon, the remainder of the pulse will have to travel an extra distance before being scattered. For that part of the pulse which hits the lunar limb, this distance will be equal to twice the lunar radius ($2 \cdot 1738$ km),

equivalent to a delay of about 11.6 ms. A short radar pulse striking the Moon will thus be stretched out in time by this amount. This phenomenon is shown schematically in fig. 13.1.

In a paper titled ‘Study of radio echoes from the Moon at 23 centimeters wavelength’ [51], Evans and Hagfors presented plots showing the relative power of lunar echoes as a function of the time delay and wavelength. The results of these measurements, for the polarized¹ echo component, are reproduced in fig. 13.2. As can be seen in this figure, the received echo power at 23 cm wavelength decreases sharply with the distance from the subradar point. This means that the Moon appears relatively smooth at this and longer wavelengths, showing *specular* reflection properties. Reflections do still occur towards the limb however, and at shorter wavelengths this phenomenon becomes even more apparent, that is the reflection becomes more *diffuse*. As a result, radar reflections from the Moon are often referred to as ‘quasi-specular’.

Another and perhaps more interesting way of presenting the information in fig. 13.2, is given in fig. 13.3. This figure shows the ‘cumulative fraction of total echo power received from inside specified fractions of the lunar radius’ [108, fig. 2]. In the 23 cm band we see that 50% of the total power is received from within only 19% of the lunar disc radius. Furthermore, from within half of the lunar radius about 85% of the total power has already been received. Thus when illuminating the Moon at 23 cm wavelength, there is a bright spot at the centre of the disc and a considerable darkening towards the limb. See also the green and blue lines in fig. 13.1!

However, not all of the returned echo power is contained within the polarized¹ component, though at 23 cm wavelength most of it fortunately is. This can be seen in fig. 13.4 which shows the relative power of the polarized and depolarized components as a function of delay. Most of the energy reflected in the centre region of the lunar disc retains its polarization, though this decreases significantly towards the limb. However, so does the power which is received from these regions. This means that depolarization due to lunar reflection is of minor importance at 23 cm wavelength.

13.2 Doppler spread measurement method and results

Section 13.1 briefly recapitulated some of the results of lunar echo measurements performed by scientists in the 1960s. This section will present the results of similar measurements performed by the author. Unfortunately

¹ In this context ‘polarized’ refers to the *intended* polarization after reflection, whereas ‘depolarized’ refers to the *unintended* polarization after reflection.

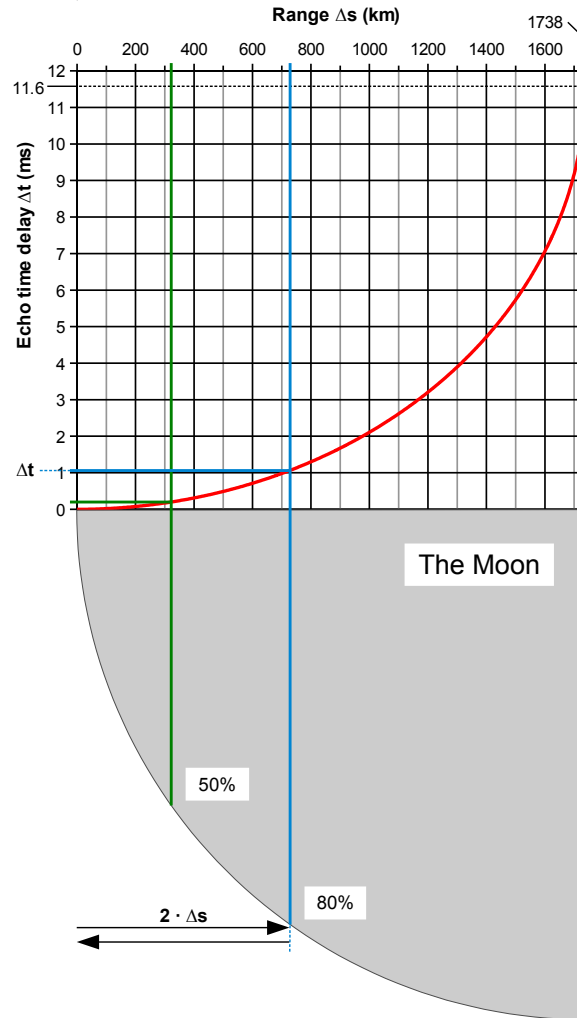


Figure 13.1 The delay of a radar pulse as a function the geometric depth of the Moon. The radar pulse hits the lunar surface orthogonally from the left. The green line shows the radius from within which half of the total echo power is received at 23 cm. Analogous, the blue line shows the radius for 80%. (This figure was inspired by [59, fig. 4].)

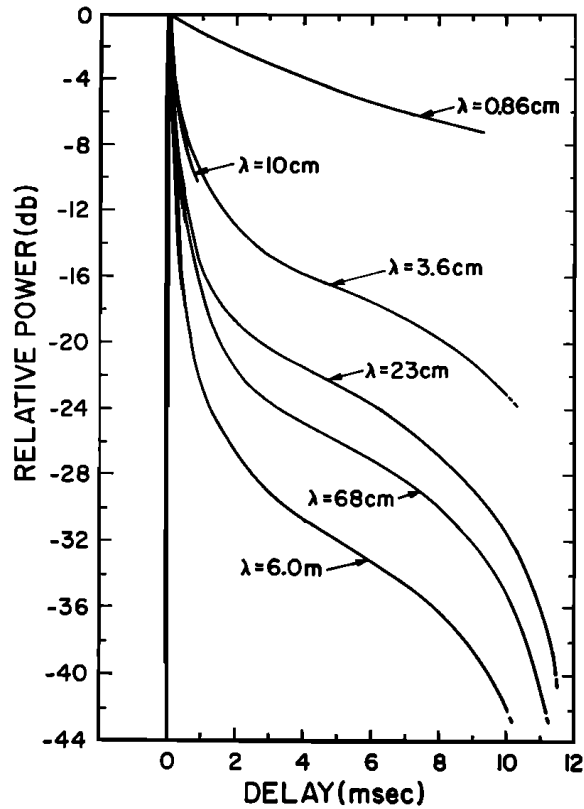


Figure 13.2 The relative EME echo power at different wavelengths as a function of delay. Most of the received power is reflected from the centre region of the lunar disc, though this decreases at shorter wavelengths. 10 μs pulse lengths were used for the 23 cm measurements. (From [51, fig. 11]. Copyright © 1966 the American Geophysical Union.)

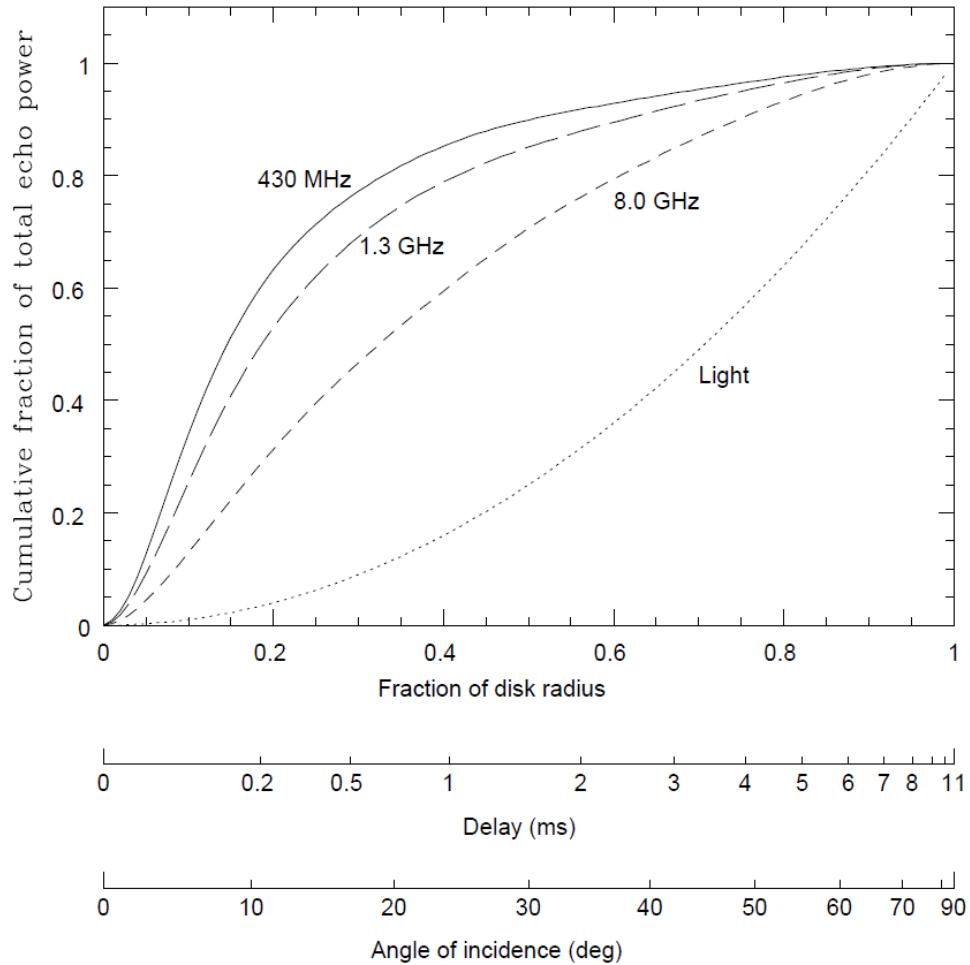


Figure 13.3 The 'cumulative fraction of total echo power received from inside specified fractions of the lunar radius'. At 1296 MHz most of the power is received from within 19% of the disc radius. (From [108, fig. 2]. Plot courtesy of Joe Taylor (K1JT) [106].)

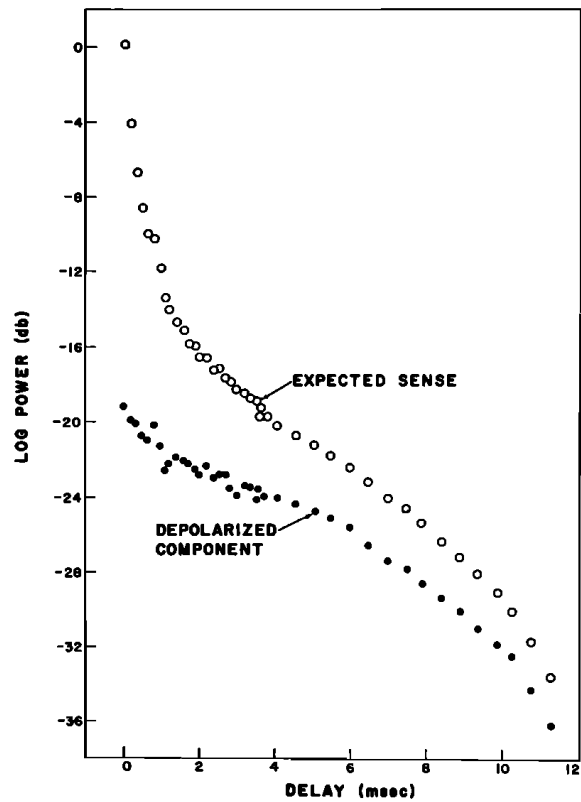


Figure 13.4 The relative EME echo power of the polarized and depolarized components at 23 cm wavelength, as a function of delay. A greater amount of depolarization will be observed at shorter wavelengths, where lunar reflection is more diffuse. (From [51, fig. 7]. Copyright © 1966 the American Geophysical Union.)

however, the author's EME system is incapable of producing radar pulses of microsecond duration. Furthermore, even if this were possible, the energy contained within each pulse would be very low considering the relatively low output power of the system. Making these pulses visible at the receiver end would thus require a considerable amount of time integration, which in its turn would require a more stable system.

There is however a solution to this problem: Instead of studying the echoes in the time-domain they can be studied in the frequency-domain. In order to understand why and how this solves the problem, the concept of *lunar libration* needs to be introduced first. In short, lunar libration is the oscillatory motion of the Moon as it is perceived by an observer on Earth. Over the lunar cycle, this motion enables the observer to see slightly more than half of the Moon's hemisphere. There are three types of librations which are of importance in EME communication, namely *a)* libration in longitude, *b)* libration in latitude and *c)* diurnal libration. These will be described briefly below, with the help of fig. 13.5.

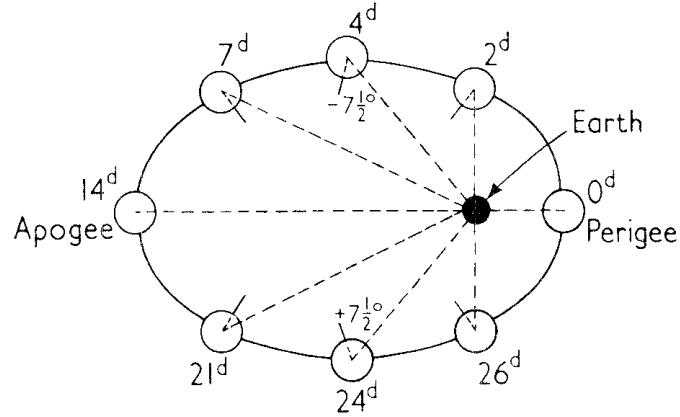
The libration in longitude is caused by the fact that the Moon has an elliptical orbit. According to Kepler's law, this prevents it from having a constant speed in its orbit around the Earth. However, the Moon still spins about its own axis at a constant rate which is synchronized to its orbital period. As seen by an observer on Earth, this will result in the Moon having an east-west 'rocking' motion over a lunar cycle. See fig. 13.5a!

The libration in latitude is a result of the lunar orbit being inclined to the ecliptic plane of the Earth. Over a lunar cycle this causes the Moon to have a perceived north-south 'nodding' motion. See fig. 13.5b for a simplified explanation!

Finally, the diurnal libration is a result of the Earth's rotation, causing an observer to see the Moon from different angles on a daily basis. See fig. 13.5c!

Combining these three libration components results in an apparent 'wobbly' motion of the Moon over the lunar cycle, as seen by an observer on Earth. During this period, the left and right sides of the lunar disc are alternately approaching and receding. This motion, though relatively slow, will inevitably cause a differential Doppler shift of reflected EME echoes. That is, the signal will be 'spread out' in the frequency-domain. The basic mechanism of this so called *Doppler spread*, which is both time and location specific, is shown schematically in fig. 13.6. Note that the Doppler spread is not to be confused with the *Doppler shift* of the whole signal as such, which also occurs.

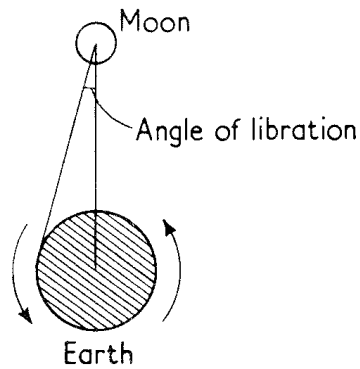
Having established the concept of Doppler spread, it is possible to understand why the analysis of the relative echo power can be transferred from the time-domain to the frequency-domain. Each frequency component within the reflected signal originates at a certain distance from the apparent rotational



(a) Libration in longitude



(b) Libration in latitude



(c) Diurnal libration

Figure 13.5 The three causes of lunar libration: (a) 'Libration in longitude is caused by the elliptical orbit of the moon, which prevents the moon from presenting exactly the same face to the earth', (b) 'libration in latitude caused by the tilt of the lunar spin axis with respect to the plane of its orbit' and (c) 'diurnal libration caused by the motion of a terrestrial observer'. (From [50, fig. 4]. Copyright © 1995, IET.)

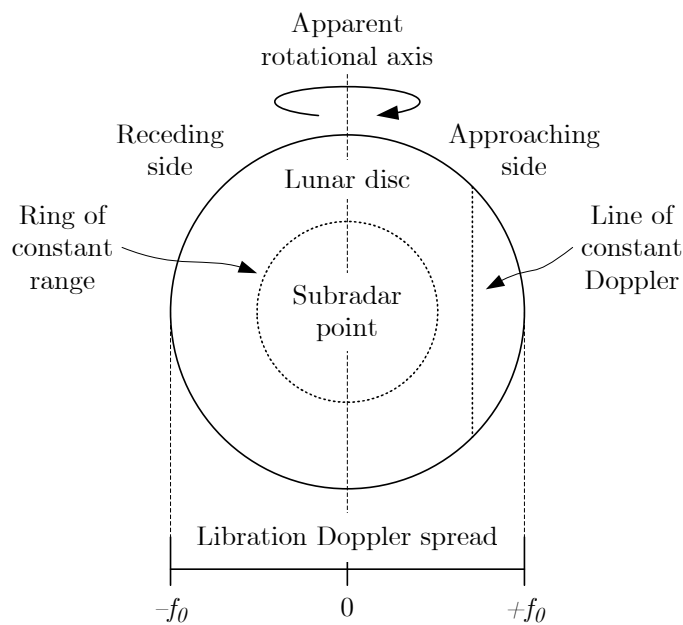


Figure 13.6 The basic mechanism of libration-induced Doppler spread of EME echoes. As observed from Earth, the left and right sides of the Moon alternately approach and recede over the lunar cycle. This causes a differential Doppler spread of the signal, amounting to a maximum of $\pm f_0$ Hz at the lunar limb. Regions of constant Doppler spread are given by straight lines parallel to the apparent rotational axis, whereas regions of constant range are given by circles about the subradar point.

axis of the lunar disc, as is shown in fig. 13.6. This means that the amplitude of each component is a measure of the reflected power at each of these distances. Thus instead of plotting the relative echo power as a function of delay, as was done in fig. 13.2, it can instead be plotted as a function of the Doppler spread frequency.

Using SL, running the same script as in section 12.2 (found in appendix D.3) but with a longer integration time, frequency spectrum measurements were performed involving the author's echoes. The Doppler spread plots in fig. 13.7 were then produced by simply taking screenshots of SL's frequency spectrum. Manually added to these plots is the predicted maximum Doppler spread f_0 at the time of the measurement. This amounts to about 8.5 Hz, which can be seen is in good agreement with the measured results. The predicted limb-to-limb Doppler spread or the 'echo width' is thus $2 \cdot f_0 = 17$ Hz. The prediction was calculated using MoonSked, presented in section 7.5.2, but alternative software applications are available as well [84, 107]. From fig. 13.7 it is furthermore evident that most of the received power originates from the centre region of the lunar disc. This is in good agreement with the historical results presented in fig. 13.2.

Using MoonSked it is also possible to predict the echo width as a function of time. Figure 13.8 shows a plot of this data, for the day during which the measurements in fig. 13.7 were performed. Even though predictions like these are frequency, location and time specific, they still illustrate the time scales and the magnitudes involved in EME Doppler spread at 1296 MHz.

On a final note, a few words on the topic of *libration fading* will be presented, since this phenomenon is just another way of looking at Doppler spread. Libration fading is a multipath fading phenomenon caused by the signal components reflected off the Moon. Since these components are Doppler shifted, the relative phase between them change over time. When they arrive at the receiving antenna they either add constructively or destructively. The resulting fades, which are Rayleigh distributed, occur at a time scale (the coherence time) which is inversely related to the Doppler spread. Needless to say, libration fading adds a considerable amount of difficulty to any communication effort.

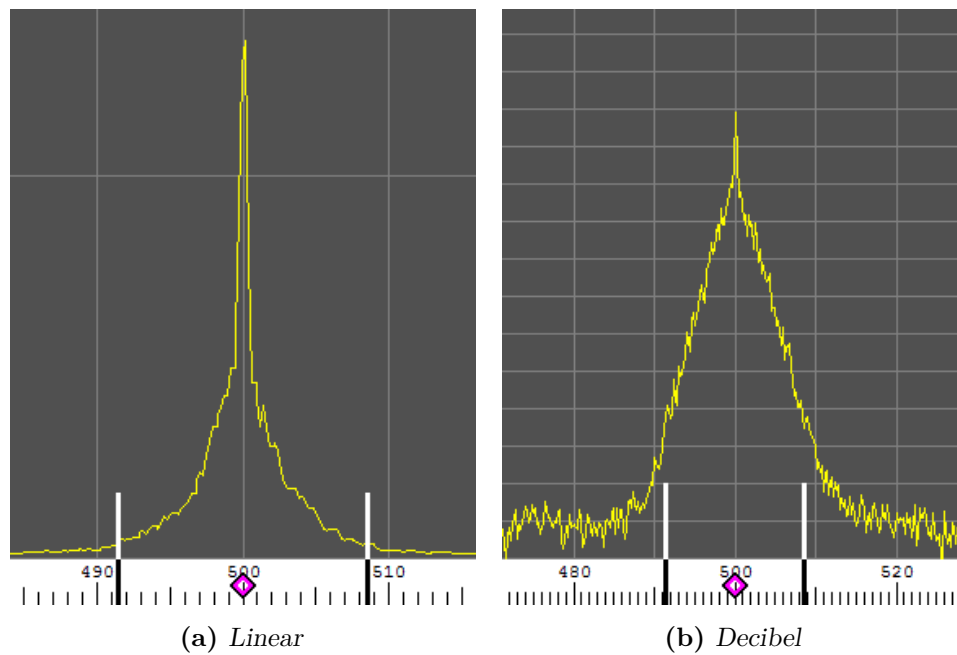


Figure 13.7 Two Doppler spread measurements of the author’s EME echoes, performed using SL. Measurement (a) uses a linear scale for the y-axis, whereas measurement (b) uses a dB scale (2 dB/division) in order to emphasize weak echo components. Zero Doppler is at the 500 Hz-mark and the vertical lines indicate the predicted maximum Doppler spread at about $\pm f_0 = \pm 8.5$ Hz, which coincides well with the measured results. It is clearly evident that most of the reflected energy originates from the centre region of the lunar disc. Note that the measurements are not normalized and that the frequency scales differ. The measurements were performed 05 September 2010, between 11:45 and 12:25 (24h UTC).

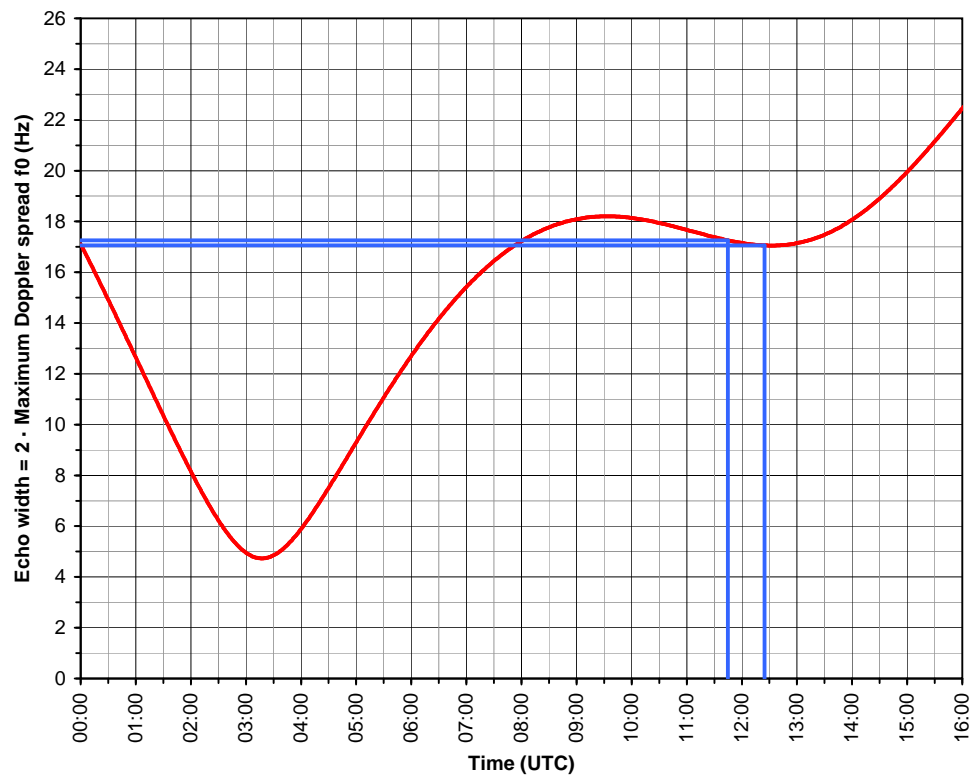


Figure 13.8 The predicted EME echo width as a function of time, according to data exported from MoonSked. The blue lines indicate the interval during which the measurements in fig. 13.7 were performed, predicting $2 \cdot f_0$ at slightly above 17 Hz. The simulation date is 05 September 2010.

Part IV

THE END

Chapter 14

Conclusion

The goal of designing, building and characterizing an [EME](#) communication system in the 1296 MHz amateur radio band has been reached. The expected [SNR](#) in a 100 Hz bandwidth was theoretically estimated at $5.4_{-1.6}^{+1.2}$ dB, with an uncertainty coverage factor of 2. Correspondingly, the empirically measured [SNR](#) yielded long-term averaged values amounting to 4.8 dB and 6.2 dB, measured about ten minutes apart. Both measurement results are thus within the uncertainty boundaries of the estimate. Furthermore, they are also greater than the 3 dB limit initially set by the author. As such, the tasks specified in section 1.1 have been accomplished and the criteria for success have thus been met. Additionally, though not part of the [task definition and criteria for success](#), the measured Doppler spread of the lunar echoes were in good agreement with theoretical results.

Some of the most critical receiver subsystem parameters are the [LNA NF](#), the combined resistive loss of the components in front of the [LNA](#) and the antenna noise temperature. Unfortunately, using the applied methods, these parameters are also the most difficult to measure with a low degree of uncertainty. They are also hard to improve upon, at least beyond a certain point. Together, they essentially determine the total system noise temperature and in combination with the antenna gain they form the all-encompassing [G over T](#) figure of merit of a receiver subsystem. In this project, the [G over T](#) was measured at approximately 11.6 dBiK^{-1} .

Naturally, there are transmitter side parameters which are important as well. The output power of the [PA](#) as well as the antenna gain being two prominent examples. Accounting for feed line loss, they form the all-encompassing [EIRP](#) figure of merit which was measured at 55.6 dBW, equalling about 360 kW.

The success of this project shows that it is possible to estimate the [SNR](#) of lunar echoes by employing a model based on the [radar](#) equation and thermal

noise theory, using measured and estimated system parameters as input data. It furthermore shows that it is possible, using amateur equipment, to perform long-term averaged SNR measurements of lunar echoes, which are in good agreement with estimated results. Finally, it also demonstrates that it is possible to achieve a good agreement between theory and practice, in regard to the Doppler spread of lunar echoes. However, since there are many system parameters, further experiments should be conducted in order to assess the repeatability of the measurements performed in this project.

Chapter 15

Recommendations and future studies

During the course of this project a number of system deficiencies have been revealed, some of which are more pressing to attend to than others. In regards to this, several recommendations will now be presented which, if implemented, would increase the overall system performance.

1. *Lowering the LNA NF* (receiver subsystem improvement)

In section 8.4.2 the LNA NF was measured at approximately $NF_{LNA} = 0.41$ dB equal to $T_{LNA.e} = 28.6$ K in noise temperature terms. It is highly desirable to lower these values by

- a. Implementing the redesign suggested by Sam Jewell (G4DDK) [72] and properly retuning the device. This should make it possible to lower the NF to the region of 0.20 dB or 13.7 K, which would increase the resulting SNR by almost a dB. More information on this is presented in section 8.4.3.
- b. Choosing an altogether different type of LNA. Leif Åsbrink (SM5-BSZ) has presented an interesting experimental ‘proof of concept’ LNA which is based on the G4DDK design [3]. This LNA is claimed to exhibit an NF comparable to the one achieved by Sergei Zhutyaev’s (RW3BP) modified G4DDK design [123], that is in the region of 0.15 dB or about 10 K. Such a low NF would increase the resulting SNR by more than a dB.
- c. Cooling down the LNA using for example a Peltier element cooler. Moisture due to condensing water could prove problematic however. Section 8.1.8 presents more information on the relationship between the NF and the physical temperature of the LNA.

2. *Reducing the resistive loss in front of the LNA* (receiver subsystem improvement)

Since resistive loss in front of the LNA is highly detrimental to receiver performance, reducing it is of great interest. Even though this task can be difficult beyond a certain point, Sergei Zhutyaev (RW3BP) has demonstrated what is possible when this is taken to the extreme [121]. It should be possible to increase the resulting SNR by up to a dB or so, which makes this improvement comparable to the one presented in recommendation 1. More information on this matter can be found in sections 4.4 and 8.5 and appendix A.

3. *Increasing the G over T by reducing the antenna temperature* (receiver subsystem improvement)

The antenna temperature is another important factor since it adds directly to the total system noise temperature, thus influencing the G over T and the SNR in an inverse manner. The author has already extended the diameter of the dish in order to reduce ground noise. There are however further improvements which can be made, such as

- a. Removing the feed horn choke ring added by the previous owner, to see if this improves the G over T.
- b. Choosing a different feed horn in order to get a cleaner radiation pattern and better polarization properties. There are several horns to consider in the literature [52, 56, 80, 111].
- c. Choosing a different feed horn in order to increase the port-to-port isolation, so as to reduce noise from the Tx-port emerging at the Rx-port during reception. In regards to this, there is an interesting paper on the topic of a ‘triangular-shaped stepped septum polarizer for satellite communication’ [76]. The results of this paper suggests that triangular-shaped septum polarizer steps will improve not only the port-to-port isolation, but also the axial ratio and return loss of the horn, as compared to when using a conventionally shaped septum polarizer. It would be interesting to see if these improvements can be translated from the 8–8.4 GHz range presented in the paper, to the 1296 MHz amateur radio band. Naturally, an increased port-to-port isolation would also be beneficial during transmission, since it lowers the risk of damaging the LNA.
- d. Switching the Tx-port of the feed horn to an open circuit during reception, using a high-power relay. Doing so, the noise temperature T_{tx} at the Tx-port would no longer be in the region of 290 K, but rather in the vicinity of the antenna temperature T_a , which in the author’s system is approximately 45 K. Using the

estimated in-dish port-to-port isolation $I_{tx} = 18$ dB of the feed horn (from section 8.10), the noise temperature contribution at the Rx-port would be reduced from $T_{tx}^* = 4.6$ K to about 0.7 K which is a considerable improvement. It is unclear however, how the above procedure would affect the polarization properties of the feed horn.¹ More information about these matters can be found in sections 4.6 and 8.10.

- e. Reducing the number of feed horn support struts from four to three. This would reduce scattering and diffraction, thus reducing side lobe levels. Using struts made out of a dielectric material instead of metal might also be beneficial.
 - f. Choosing an offset dish instead of a prime focus dish. This would reduce aperture blockage and thus scattering. It would also limit the amount of spillover noise being picked up from the ground.
4. *Improving the azimuth and elevation control system* (antenna subsystem improvement)

From appendix B we see that the resolution of the Az/EI rotators is only 1° each. Since the antenna HPBW is only 4.4° and the angular extension of the Moon is only 0.5°, this can result in a considerable loss of potential antenna gain during both transmission and reception, which directly influences the SNR. The following improvements should thus be made:

- a. Choosing an Az/EI control system which is more robust, has a better resolution and a higher degree of accuracy. This would increase the likelihood of the antenna boresight pointing straight at the target at all times.
 - b. Exchanging the horizontal aluminium pipe in fig. 7.4 on page 99 for one made out of iron, in order to make the mechanical construction more robust.
5. *Increasing the output power at the antenna* (transmitter subsystem improvement)

The output power at the antenna is a parameter which adds directly to the SNR. It is therefore desirable to increase the output power as close to the legal limit as possible. In the author's system, this can be done by

- a. Redesigning the main PA (and PA 2) after having evaluated the suggested PA improvements presented in section 9.1. This should increase the output power of the main PA from approximately 370 W to almost 1 kW, which is the legal limit in Sweden.

¹ See also footnote 17 on page 170.

- b. Reducing the 1.2 dB feed line loss of the current system by placing the main PA closer to the antenna.

By combining recommendations 5a and 5b it should be possible to increase the output power P_t at the antenna from 280 W to maybe 900 W, which would increase the echo SNR by about 5 dB. Unfortunately however, this would not improve the capability of hearing other EME stations.

In relation to the above, note that an increase in P_t would also increase the amount of power emerging at the Rx-port of the feed horn. One would therefore need to make sure that the coaxial protection relay is capable of handling such an increase.

- 6. *Reducing man-made interference levels* (environmental improvement)

Man-made interference, which manifested itself as a sporadic and broadband increase in the noise floor, was unfortunately observed when analysing the lunar echo SNR measurements of chapter 12. Since interference has a negative impact on the SNR, its origin needs to be identified and addressed.

- 7. *Increasing the frequency stability of the system* (transmitter and receiver subsystem improvement)

A considerable frequency instability of the system was noticed during the echo-data acquisition process, presented in section 12.1. As was noted in section 12.2 this made analysing the echo data more difficult. The transceiver and transverter should thus be upgraded to incorporate stable local oscillators based on for example oven-controlled crystal oscillators (OCXOs). Preferably, these OCXOs should in their turn be locked to a 10 MHz reference source, such as a GPS or Rubidium standard (an ‘atomic clock’) or even a combination of both. Naturally, this would also benefit the stability of the transmitted signal.

- 8. *Increasing the dynamic range of the system* (receiver subsystem improvement)

During the experiments the author noticed that the system was sometimes close to saturation. Primarily, this can likely be attributed to the computer sound card, but the transceiver and transverter should not be ruled out. It would thus be desirable to increase the dynamic range of the system. One step in doing this would be to use more modern equipment, such as an SDR supported by SL.

- 9. *Reducing the polarization mismatch loss* (experimental transmitter and receiver subsystem improvement)

The polarization mismatch loss, presented in section 3.5.5, can be reduced by implementing dual transmitter and receiver chains with

adaptive receiver polarization. An experimental system redesign which accomplishes this can be realized by exchanging the current feed horn for one without a septum polarizer, but which has vertical and horizontal exciter probes instead. Since these probes have a natural 90° phase difference, circular polarization can be achieved during transmission by providing an equal amount of 90° -phased power to each port. This can be achieved by omitting the final 90° hybrid coupler in the main PA, and using two feed lines of equal lengths to connect the PA to each port of the feed horn. Two high-power relays can furthermore be used for Tx/Rx-switching, so that the receiver chain will consist of two separate receiver systems, that is one for each port. Adaptive receiver polarization can finally be achieved by using phase-coherent receivers and combining the signals using computer software such as Linrad [8].

Some of the recommendations provided above would, if implemented, open up the possibility for new and interesting experiments. Increasing the frequency stability, according to recommendation 7, would for example enable the measurement of the Doppler shift, resulting from the relative motion between the Earth and the Moon. It would also be possible to perform chirp radar experiments using SL as well as enable the use of weak signal digital communication modes such as WSJT/JT65 (which employs MFSK modulation) by Joe Taylor (K1JT) [107] and EMEpsk (which employs PSK modulation) by Klaus von der Heide (DJ5HG) [62]. Both communication modes are specifically developed for EME communication at SNRs where the signal is inaudible to the human ear. Implementing recommendation 7 would furthermore allow for radio astronomical experiments, especially if the LNA is re-tuned to the 21 cm hydrogen line. Since SL can be locked to GPS and stream data over the Internet, it should also be possible to synchronize signals from two EME stations, thus enabling interferometry experiments or diversity reception of EME signals. Yet another interesting experiment would be to measure the amplitude distribution of the lunar echoes, to see if these are Rayleigh distributed as one would expect. Furthermore, in addition to studying the polarized component of the lunar echoes it would also be interesting to study the depolarized component, to see if results similar to those of fig. 13.4 on page 198 are obtained. One way of controlling the receiver polarization would in this case be to implement recommendation 9.

The recommendations given above are aimed at the EME system as such. However, there have also been a few shortcomings in regard to the measurements performed throughout this project. Improving the accuracy of these measurements would not only be beneficial to the system characterization and the concluding SNR estimate, but it would also settle a number of questions and uncertainties along the way. In some cases, the preferable solution would be to use alternative measurement methods altogether. A

few additional recommendations, in regard to the above, are therefore given below.

10. *Reducing the LNA NF measurement uncertainty* (measurement related improvement)

The LNA NF measurements presented in this project suffer from undesirable uncertainties. This is especially true for the NFM measurements presented in section 8.4.1. While it is true that the overall uncertainty of such measurements can be mitigated by following the recommendations given in section 8.1, this only works to a certain degree as was shown in section 8.2. However, as was explained in section 8.3 the uncertainty can also be reduced through alternative measurement methods. The author therefore recommends that the following be considered:

- a. Using attenuators and an isolator to *tune* the LNA and the ‘quarter wavelength cable–method’ to *measure* the LNA, when using an NFM. More information about this can be found in sections 8.1.13 and 8.1.14.
 - b. Replicating the ‘horn method’ used by Sergei Zhutyaev (RW3BP) [122], which is claimed to have a worst-case uncertainty of only 0.03 dB. Section 8.3 provides a bit more information about this.
11. *Using an alternative method for measuring the system noise temperature and the antenna gain* (measurement related improvement)

Using a directional coupler which is placed between the feed horn and the coaxial protection relay, a known amount of noise can be introduced into the system by connecting a DNS to its coupled port. Using the DNS, as well as equations from section 6.1, the system noise temperature T_{sys} can be determined by performing a Y-factor measurement. Once T_{sys} is known another Y-factor measurement, this time performed using a celestial radio source such as the Sun, will determine the antenna gain G . This procedure would eliminate the need for estimating the main beam efficiency η_{beam} in order to calculate the antenna gain, as was done in section 8.7.

References

For those wanting to get a deeper understanding of the various topics, the references below are intended to serve as a basis for further study.

During the course of writing this thesis ‘Agilent Technologies’ was renamed ‘Keysight Technologies’. Should any of the URLs related to the Agilent Technologies application notes stop working, it is likely that newer versions of these documents can be found at the [Keysight Technologies website](http://www.keysight.com/) (<http://www.keysight.com/>).

- [1] L. Åsbrink (SM5BSZ). SM5BSZ webpage. URL <http://www.sm5bsz.com/>. (Cited on page 127)
- [2] L. Åsbrink (SM5BSZ). Comparing different kinds of NF measurements, May 30 2013. URL <http://www.sm5bsz.com/lir/nf/eme2012.htm>. (Cited on page 137)
- [3] L. Åsbrink (SM5BSZ). An experimental LNA for 1296 MHz, May 2 2013. URL <http://www.sm5bsz.com/lir/loss/1296/lna/explna.htm>. (Cited on page 211)
- [4] L. Åsbrink (SM5BSZ). Section on LNAs, June 2013. URL <http://www.sm5bsz.com/index.htm#LNA>. (Cited on page 120)
- [5] L. Åsbrink (SM5BSZ). Losses in relays, cables, adapters and connectors, June 27 2013. URL <http://www.sm5bsz.com/lir/loss/loss.htm>. (Cited on pages 129 and 156)
- [6] L. Åsbrink (SM5BSZ). Precision measurements of noise figures, Jan 3 2013. URL <http://www.sm5bsz.com/lir/nfprec/nfprec.htm>. (Cited on pages 126, 141, and 147)
- [7] L. Åsbrink (SM5BSZ). Noise temperature and physical temperature of LNAs, June 4 2013. URL <http://www.sm5bsz.com/lir/loss/1296/orebro/phystemp.htm>. (Cited on page 127)
- [8] L. Åsbrink (SM5BSZ). Linrad – Linux radio, Mar 9 2014. URL <http://www.sm5bsz.com/linuxdsp/linrad.htm>. (Cited on pages 148 and 215)

-
- [9] Agilent Technologies. Operating and service guide for the SNS series N4000A, N4001A and N4002A smart noise sources, March 2001. URL <http://cp.literature.agilent.com/litweb/pdf/N4000-90001.pdf>. (Cited on pages 125, 126, and 134)
- [10] Agilent Technologies. Revisiting mismatch uncertainty with the Rayleigh distribution, October 6 2011. URL <http://cp.literature.agilent.com/litweb/pdf/5990-9185EN.pdf>. (Cited on pages 120, 132, and 138)
- [11] Agilent Technologies. Operating and service manual for the Agilent 346A/B/C noise source, June 2013. URL <http://cp.literature.agilent.com/litweb/pdf/00346-90148.pdf>. (Cited on pages 125, 126, and 134)
- [12] Agilent Technologies AN1408–20. High-accuracy noise figure measurements using the PNA-X series network analyzer, July 8 2010. URL <http://cp.literature.agilent.com/litweb/pdf/5990-5800EN.pdf>. (Cited on pages 47, 59, 120, and 133)
- [13] Agilent Technologies AN57–1. Fundamentals of RF and microwave noise figure measurement, September 14 2006. URL <http://cp.literature.agilent.com/litweb/pdf/5952-8255E.pdf>. (Cited on pages 35, 36, 39, 41, 59, 120, 124, 129, and 133)
- [14] Agilent Technologies AN57–2. Noise figure measurement accuracy - The Y-factor method, March 19 2004. URL <http://cp.literature.agilent.com/litweb/pdf/5952-3706E.pdf>. (Cited on pages 62, 120, 122, 123, 124, 128, 129, 130, 133, and 138)
- [15] Agilent Technologies AN57–3. 10 hints for making successful noise figure measurements, November 21 2000. URL <http://cp.literature.agilent.com/litweb/pdf/5980-0288E.pdf>. (Cited on pages 120, 122, 123, 124, 127, 128, 129, 130, and 133)
- [16] Alfa Radio Ltd. RAS Az/El rotator specifications. URL http://alfaradio.ca/docs/AlfaSpid_RAK_RAS_REAL-Specification.pdf. (Cited on page 239)
- [17] American Radio Relay League. *ARRL Handbook for Radio Communications 2007*. American Radio Relay League, 84th edition, 2007. ISBN 978-0-87259-976-5. (Cited on page 115)
- [18] American Radio Relay League. *ARRL Handbook for Radio Communications 2011*. American Radio Relay League, 88th edition, 2011. ISBN 978-0-87259-096-0. (Cited on pages 75, 169, 171, 174, and 193)
-

-
- [19] American Radio Relay League. [ARRL test procedures manual](#), May 2011. URL <http://www.arrl.org/files/file/Technology/ProcedureManual2011withpagebreaks.pdf>. (Cited on page 75)
- [20] AMSAT-DL. Erde–Venus–Erde-Experiment der AMSAT-DL erfolgreich, March 2009. URL <http://www.amsat-dl.org/index.php/pressemedien-othermenu-87/press-releases-othermenu-144/168-erde-venus-erde-experiment-der-amsat-dl-erfolgreich>. (Cited on page 18)
- [21] D. Anderson (GM4JJJ). GM4JJJ webpage. URL <http://www.gm4jjj.co.uk/>. (Cited on pages 98 and 118)
- [22] D. Anderson (GM4JJJ). MoonSked moonbounce scheduling software. URL <http://www.gm4jjj.co.uk/MoonSked/moonsked.htm>. (Cited on pages 98 and 118)
- [23] J. Baars. The measurement of large antennas with cosmic radio sources. In *IEEE Transactions on Antennas and Propagation*, volume 21, pages 461–474, July 1973. doi: 10.1109/TAP.1973.1140521. (Cited on pages 85 and 88)
- [24] J. Baars. *The Paraboloidal Reflector Antenna in Radio Astronomy and Communication*. Springer, 2007. ISBN 978-0-387-69734-5. (Cited on page 85)
- [25] Z. Bay. Reflection of microwaves from the Moon. In *Hungarica Acta Physica*, volume 1, pages 1–22. Springer-Verlag, 1947. doi: 10.1007/BF03161123. (Cited on page 11)
- [26] A. O. Benz. 4.1.1.6 radio emission of the quiet Sun. In *Landolt–Börnstein – Group VI Astronomy and Astrophysics*, volume 4B: Solar System. The Landolt–Börnstein Database. Springer-Verlag Berlin Heidelberg, 2009. ISBN 978-3-540-88054-7. doi: 10.1007/978-3-540-88055-4_5. (Cited on page 86)
- [27] R. Bertelsmeier (DJ9BV). Low noise [GaAs-FET](#) preamps for [EME](#): Construction and measurement problems. In *DUBUS Magazine*, number 4, pages 8–25, 1988. (Cited on pages 120, 134, and 138)
- [28] R. Bertelsmeier (DJ9BV). How to use a noise figure meter. In *DUBUS Magazine*, number 4, pages 11–30, 1990. (Cited on pages 120, 134, and 138)
- [29] R. Bertelsmeier (DJ9BV). *DUBUS Technik V*. Number V. DUBUS Magazine, 1998. (Cited on pages 120 and 138)
-

-
- [30] P. Blair (G3LTF). How good were the EME systems of the 1960s and 70s? (extended cover CD version). In *EME 2012 Conference Papers (15th International EME Conference, Cambridge, England)*. Radio Society of Great Britain and The UK Microwave Group, August 2012. ISBN 9781-9050-8683-2. (Cited on page 17)
- [31] L. V. Blake. A guide to basic pulse-radar maximum-range calculation, part 1. Report 6930, Naval Research Laboratory, Washington D.C., December 1969. URL <http://www.dtic.mil/docs/citations/AD0701321>. (Cited on page 172)
- [32] L. Brown. *Technical and military imperatives: A radar history of World War II*. Taylor & Francis, 1999. ISBN 978-1-4200-5066-0. (Cited on page 11)
- [33] W. Büscher (DL4YHF). DL4YHF webpage. URL <http://www.qsl.net/dl4yhf/>. (Cited on page 117)
- [34] W. Büscher (DL4YHF). Spectrum Lab audio spectrum analyzer software. URL <http://www.qsl.net/dl4yhf/spectral1.html>. (Cited on pages 117, 148, and 243)
- [35] A. J. Butrica. *To See the Unseen: A History of Planetary Radar Astronomy*. NASA SP. U.S. National Aeronautics and Space Administration, NASA History Office, 1996. ISBN 978-0-16-048578-7. URL <http://history.nasa.gov/SP-4218/contents.htm>. (Cited on page 10)
- [36] A. J. Butrica. *Beyond the Ionosphere: Fifty Years of Satellite Communication*. NASA SP. U.S. National Aeronautics and Space Administration, NASA History Office, 1997. ISBN 978-0-16-049054-5. URL <http://history.nasa.gov/SP-4217/contents.htm>. (Cited on pages 10 and 15)
- [37] CadSoft Inc. Company webpage. URL <http://www.cadsoftusa.com/>. (Cited on page 118)
- [38] CadSoft Inc. Eagle PCB design software. URL <http://www.cadsoftusa.com/eagle-pcb-design-software/>. (Cited on page 118)
- [39] Camp Evans InfoAge WWII museum and national historic landmark. Organization webpage. URL <http://www.campevans.org/>. (Cited on pages 10 and 12)
- [40] D. B. Campbell. Measurement in radio astronomy. In *Single-Dish Radio Astronomy: Techniques and Applications*, volume 278, pages
-

- 81–90, December 2002. ISBN 1-58381-120-6. URL <http://labs.adsabs.harvard.edu/ui/abs/2002ASPC..278...81C>. Astrophysics Data System. (Cited on pages 51, 54, and 78)
- [41] W. van Capellen. Efficiency and sensitivity definitions for reflector antennas in radio astronomy, November 2007. URL <http://www.astron.nl/other/workshop/MCCT/TuesdayCappellen.pdf>. (Cited on pages 24 and 33)
- [42] M. H. Chen and G. N. Tsandoulas. A wide-band square-waveguide array polarizer. In *IEEE Transactions on Antennas and Propagation*, volume 21, pages 389–391, May 1973. doi: 10.1109/TAP.1973.1140486. (Cited on page 100)
- [43] R. J. Collier and A. D. Skinner. *Microwave Measurements*. The Institution of Engineering and Technology, third edition, 2007. ISBN 978-0-86341-735-1. (Cited on pages 35, 47, 120, 132, and 142)
- [44] F. R. Connor. *Noise*. Edward Arnold, 1973. ISBN 0-7131-3306-6. (Cited on pages 36, 37, and 59)
- [45] J. H. DeWitt Jr. (W4ERI) and E. K. Stodola (W3IYF). Detection of radio signals reflected from the Moon. In *Proceedings of the I.R.E.*, volume 37, pages 229–242, March 1949. doi: 10.1109/JRPROC.1949.231276. (Cited on page 12)
- [46] A. Dubovtsev (R7AB). R7AB webpage. URL <http://www.73.ru/>. (Cited on pages 18 and 19)
- [47] DUBUS Magazine. URL <http://www.dubus.org/>. (Cited on page 8)
- [48] O. Duffy (VK2OMD formerly VK1OD). Quiet Sun radio flux interpolations. URL <http://owenduffy.net/calc/qsrf/index.htm>. (Cited on page 158)
- [49] F. Eliot. *Moon Bounce ELINT – The monitoring of Soviet radars by way of the lunar surface*. The U.S. Central Intelligence Agency, CIA, 1967. URL https://www.cia.gov/library/center-for-the-study-of-intelligence/kent-csi/vol11no2/html/v11i2a05p_0001.htm. (Cited on page 14)
- [50] J. V. Evans (N3HBX). Radio communication via the Moon. In *Proceedings of the 1995 International Conference on 100 Years of Radio*, pages 207–212. IET, September 1995. ISBN 0-85296-649-0. doi: 10.1049/cp:19950814. (Cited on page 200)
- [51] J. V. Evans (N3HBX) and T. Hagfors. Study of radio echoes from the Moon at 23 centimeters wavelength. In *Journal of Geophysical*
-

- Research*, volume 71, pages 4871–4889, October 1966. doi: 10.1029/JZ071i020p04871. (Cited on pages 181, 183, 193, 194, 196, and 198)
- [52] M. J. Franco (N2UO). A high-performance dual-mode feed horn for parabolic reflectors with a steppedseptum polarizer in a circular waveguide. In *IEEE Antennas and Propagation Magazine*, volume 53, pages 142–146, June 2011. doi: 10.1109/MAP.2011.6028434. (Cited on pages 100 and 212)
- [53] H. T. Friis. Noise figures of radio receivers. In *Proceedings of the I.R.E.*, volume 32, pages 419–422, July 1944. doi: 10.1109/JRPROC.1944.232049. (Cited on pages 38, 40, 41, and 46)
- [54] H. T. Friis. A note on a simple transmission formula. In *Proceedings of the I.R.E.*, volume 34, pages 254–256, May 1946. doi: 10.1109/JRPROC.1946.234568. (Cited on pages 23, 26, 27, and 28)
- [55] D. Fässler (HB9BBD). How to increase 23 cm power to 250 W with 2 x XRF286. *EME 2010 Conference Presentation (14th International EME Conference, Dallas, Texas)*. North Texas Microwave Society, August 2010. URL http://www.ntms.org/eme/presentations/w5lua/HB9BBD_Howtoincrease23cmPowerto250WR1.pdf. (Cited on page 178)
- [56] R. Galuščák (OM6AA) and P. Hazdra. Prime-focus circular waveguide feed with septum polarization transformer. In *DUBUS Magazine*, number 1, pages 8–32, 2007. (Cited on pages 100 and 212)
- [57] R. Galuščák (OM6AA), P. Hazdra, and M. Mazánek. Parabolic antenna noise characteristic with dual-mode feed. In *DUBUS Magazine*, number 3, pages 8–14, 2011. (Cited on page 72)
- [58] G. Gervais (F2CT). *EME communications: History and evolutions*. In *EME 2014 Conference Papers (16th International EME Conference, Pleumeur-Bodou, France)*, pages 163–166. Observation Radio Pleumeur-Bodou, August 2014. ISBN 978-2-919009-57-2. (Cited on page 17)
- [59] V. Grassmann (DF5AI). Der Mond als passiver Reflektor – Physikalische Grundlagen von *EME-Funkverbindungen*, Juli 2002. URL <http://www.df5ai.net/ArticlesDL/EMEPysics.pdf>. (Cited on page 195)
- [60] D. D. Grieg, S. Metzger, and R. Waer. Considerations of moon-relay communication. In *Proceedings of the I.R.E.*, volume 36, pages 652–663, May 1948. doi: 10.1109/JRPROC.1948.226208. (Cited on pages 12 and 15)
-

-
- [61] D. A. Guidice and J. P. Castelli. The use of extraterrestrial radio sources in the measurement of antenna parameters. In *IEEE Transactions on Aerospace and Electronic Systems*, volume AES-7, pages 226–234, March 1971. doi: 10.1109/TAES.1971.310353. (Cited on pages 85 and 88)
- [62] K. von der Heide (DJ5HG). EMEpsk weak-signal radio communication software. URL <http://www.dj5hg.de/digitalmodes/digitalmodes.html>. (Cited on page 215)
- [63] Icom Inc. Company webpage. URL <http://www.icom.co.jp/world/>. (Cited on page 112)
- [64] ID-Elektronik GmbH. Company webpage. URL <http://www.id-elektronik.de/>. (Cited on page 110)
- [65] IEEE Aerospace and Electronic Systems Society. IEEE standard radar definitions. *IEEE Std 686-2008 (Revision of IEEE Std 686-1997)*, 2008. doi: 10.1109/IEEESTD.2008.4530766. (Cited on pages 23, 29, and 73)
- [66] IEEE Antennas and Propagation Society. IEEE standard definitions of terms for antennas. *IEEE Std 145-1993*, 1993. doi: 10.1109/IEEESTD.1993.119664. (Cited on pages 23, 24, 25, 26, 27, 29, 33, 59, and 83)
- [67] IEEE Antennas and Propagation Society. IEEE standard definitions of terms for radio wave propagation. *IEEE Std 211-1997*, 1998. doi: 10.1109/IEEESTD.1998.87897. (Cited on pages 23, 26, 27, 29, and 98)
- [68] Ionospheric Prediction Service of the Australian Bureau of Meteorology. Daily solar radio flux archive. URL <http://www.ips.gov.au/pipermail/ips-iflux-dailyvalues/>. (Cited on page 157)
- [69] IRE Standards Committee. IRE standards on electron tubes: Definitions of terms, 1957 (57 IRE 7. s2). In *Proceedings of the I.R.E.*, volume 45, pages 983–1010, July 1957. doi: 10.1109/JRPROC.1957.278510. (Cited on pages 39, 41, and 43)
- [70] IRE Standards Committee. IRE standards on electron tubes: Definitions of terms, 1962 (62 IRE 7. s2). In *Proceedings of the I.R.E.*, volume 51, pages 434–435, March 1963. doi: 10.1109/PROC.1963.1845. (Cited on page 43)
- [71] K. G. Jansky. Electrical disturbances apparently of extraterrestrial origin. In *Proceedings of the I.R.E.*, volume 21, pages 1387–1398, Oct 1933. doi: 10.1109/JRPROC.1933.227458. (Cited on page 11)
- [72] S. Jewell (G4DDK). G4DDK webpage. URL <http://www.g4ddk.com/>. (Cited on pages 108, 109, 127, 154, and 211)
-

-
- [73] J. B. Johnson. Thermal agitation of electricity in conductors. In *Physical Review*, volume 32, pages 97–109, July 1928. (Cited on pages 35 and 36)
- [74] H. P. Kauffman (W2OQU). A DX record: To the Moon and back. In *QST*, pages 65–68, May 1946. (Cited on page 12)
- [75] Keysight Technologies. Noise figure uncertainty calculator. URL <http://sa.support.keysight.com/nfcalc/>. (Cited on pages 125, 126, 138, and 150)
- [76] J. H. Kim, S. S. Yoon, E. Y. Jung, J. W. Lee, T. K. Lee, and W. K. Lee. Triangular-shaped stepped septum polarizer for satellite communication. In *Proceedings of the 2011 IEEE International Symposium on Antennas and Propagation (APSURSI)*, pages 854–857. IEEE, July 2011. ISBN 978-1-4244-9562-7. doi: 10.1109/APS.2011.5996409. (Cited on page 212)
- [77] J. Klitzing (W6PQL). W6PQL webpage. URL <http://www.w6pql.com/>. (Cited on pages 104 and 106)
- [78] J. D. Kraus (W8JK). *Radio Astronomy*. McGraw–Hill, first edition, 1966. ISBN 07-035392-1. (Cited on pages 50, 51, 54, 77, and 78)
- [79] J. D. Kraus (W8JK). *Antennas*. McGraw–Hill, second edition, 1988. ISBN 0-07-100482-3. (Cited on pages 24, 25, 26, 28, 30, 33, 83, and 171)
- [80] I. Larsson (SM6FHZ) and H. Illipe (SM6PGP). Presentation on a novel 5 step septum feed suite. URL <http://www.2ingandlin.se/Presentations.html>. (Cited on pages 100 and 212)
- [81] G. Maral and M. Bousquet. *Satellite Communications Systems*. John Wiley & Sons Ltd., fourth edition, 2003. ISBN 0-471-49654-5. (Cited on pages 26, 27, and 34)
- [82] D. McArthur (VK3UM). VK3UM webpage. URL <http://www.vk3um.com/>. (Cited on pages 118 and 157)
- [83] D. McArthur (VK3UM). VK3UM EME Calculator software. URL <http://www.vk3um.com/eme%20calculator.html>. (Cited on pages 118 and 157)
- [84] D. McArthur (VK3UM). VK3UM libration calculator software. URL <http://www.vk3um.com/libration%20calculator.html>. (Cited on page 202)
- [85] T. A. Milligan. *Modern Antenna Design*. John Wiley & Sons Ltd., second edition, 2005. ISBN 0-471-45776-0. (Cited on pages 29, 33, 73, and 165)
-

-
- [86] J. Mofenson. Radar echoes from the Moon. In *Electronics*, volume 19, pages 92–98, April 1946. (Cited on page 12)
- [87] R. J. Mohr. Mohr on receiver noise – characterization, insights & surprises (revision 2), 2010. URL http://www.ieee.li/pdf/viewgraphs_mohr_noise.pdf. (Cited on page 38)
- [88] H. Nyquist. Thermal agitation of electric charge in conductors. In *Physical Review*, volume 32, pages 110–113, July 1928. doi: 10.1103/PhysRev.32.110. (Cited on pages 35 and 36)
- [89] OK2KKW Club Station. The first amateur lunar tests and contacts – 1st part: 1953–1965. URL <http://www.ok2kkw.com/eme1960/eme1960eng.htm>. (Cited on page 17)
- [90] OK2KKW Club Station. The first amateur lunar tests and contacts – 2nd part: 1966–1976. URL <http://www.ok2kkw.com/eme1960/eme1965eng.htm>. (Cited on page 17)
- [91] J. Pawlan (WA6KBL) and R. Galuščák (OM6AA). Simulation and measurement of the effects of reflections from a prime focus dish back into a circularly polarized feed. In *DUBUS Magazine*, number 4, pages 67–77, 2010. (Cited on pages 58, 72, and 170)
- [92] D. M. Pozar. *Microwave and RF Design of Wireless Systems*. John Wiley & Sons Ltd., first edition, 2001. ISBN 0-471-32282-2. (Cited on pages 41, 47, 48, 73, and 75)
- [93] Radiocommunication sector of the ITU. Recommendations on radiowave propagation. URL <http://www.itu.int/rec/R-REC-P/en>. (Cited on pages 27 and 34)
- [94] Radiocommunication sector of the ITU. Recommendation ITU-R S.733: Determination of the G/T ratio for earth stations operating in the fixed-satellite service, January 2000. URL <http://www.itu.int/rec/R-REC-S.733/en>. (Cited on pages 82 and 157)
- [95] Radiocommunication sector of the ITU. Recommendation ITU-R P.372: Radio noise, September 2013. URL <http://www.itu.int/rec/R-REC-P.372/en>. (Cited on pages 171 and 174)
- [96] Z. Samek (OK1DFC). OK1DFC webpage. URL <http://www.ok1dfc.com/>. (Cited on page 100)
- [97] Z. Samek (OK1DFC). OK1DFC square septum polarized feed horn. URL <http://www.ok1dfc.com/EME/emeweb.htm#Septum>. (Cited on page 100)
-

-
- [98] J. S. Seybold. *Introduction to RF Propagation*. John Wiley & Sons Ltd., first edition, 2005. ISBN 0-471-65596-1. (Cited on page 34)
- [99] M. I. Skolnik. *Introduction to radar systems*. McGraw-Hill, second intl. edition, 1980. ISBN 0-07-066572-9. (Cited on page 29)
- [100] A. Solovey and R. Mittra. Extended source size correction factor in antenna gain measurements. In *Proceedings of the 38th European Microwave Conference*, pages 983–986, October 2008. ISBN 978-2-87487-006-4. doi: 10.1109/EUMC.2008.4751620. (Cited on pages 85 and 165)
- [101] Space Weather Canada. Solar radio flux measurements archive. URL <http://www.spaceweather.gc.ca/solarflux/sx-5-eng.php>. (Cited on page 157)
- [102] SPID Elektronik. Company webpage. URL <http://spid.net.pl/en/>. (Cited on pages 98 and 239)
- [103] D. Stockton (GM4ZNX) and I. White (GM3SEK). Noise figure measurement – A reality check (extended cover CD version). In *EME 2012 Conference Papers (15th International EME Conference, Cambridge, England)*. Radio Society of Great Britain and The UK Microwave Group, August 2012. ISBN 9781-9050-8683-2. (Cited on pages 120, 126, and 128)
- [104] W. Stutzman and H. Ko. On the measurement of antenna beamwidth using extraterrestrial radio sources. In *IEEE Transactions on Antennas and Propagation*, volume 22, pages 493–495, May 1974. doi: 10.1109/TAP.1974.1140793. (Cited on page 86)
- [105] K. Tapping. *Antenna Calibration Using the 10.7cm Solar Flux*. Dominion Radio Astrophysical Observatory, Herzberg Institute of Astrophysics, Canadian National Research Council, 2001. (Cited on pages 157 and 158)
- [106] J. Taylor (K1JT). K1JT webpage. URL <http://physics.princeton.edu/pulsar/k1jt/>. (Cited on page 197)
- [107] J. Taylor (K1JT). WSJT weak-signal radio communication software. URL <http://physics.princeton.edu/pulsar/k1jt/wsjt.html>. (Cited on pages 18, 202, and 215)
- [108] J. Taylor (K1JT). Frequency-dependent characteristics of the EME path. EME 2010 Conference Presentation (14th International EME Conference, Dallas, Texas). North Texas Microwave Society, August 2010. URL http://www.physics.princeton.edu/pulsar/K1JT/EME2010_K1JT.pdf. (Cited on pages 193, 194, and 197)
-

-
- [109] E. P. Tilton (W1HDQ). Lunar DX on 144 Mc! W4AO and W3GKP bounce 2-meter signals off the Moon. In *QST*, March 1953. (Cited on pages 16 and 17)
- [110] J. H. Trexler. Lunar radio echoes. In *Proceedings of the I.R.E.*, volume 46, pages 286–292, Jan 1958. doi: 10.1109/JRPROC.1958.286789. (Cited on pages 9, 12, and 15)
- [111] R. H. Turrin (W2IMU). Dual mode small-aperture antennas. In *IEEE Transactions on Antennas and Propagation*, volume 15, pages 307–308, March 1967. doi: 10.1109/TAP.1967.1138883. (Cited on pages 72 and 212)
- [112] U.S. NOAA Earth System Research Laboratory. NOAA solar calculator. URL <http://www.esrl.noaa.gov/gmd/grad/solcalc/>. (Cited on page 163)
- [113] U.S. NOAA Space Weather Prediction Center. Lists of solar-geophysical data and solar radio flux data. URL <ftp://ftp.swpc.noaa.gov/pub/lists/radio/>. (Cited on pages 157 and 160)
- [114] U.S. National Astronomy and Ionosphere Center. NAIC webpage. URL <http://www.naic.edu/>. (Cited on page 17)
- [115] U.S. Naval Research Laboratory. NRL webpage. URL <http://www.nrl.navy.mil/>. (Cited on pages 9, 13, and 15)
- [116] P. Wade (W1GHZ). W1GHZ webpage. URL <http://www.w1ghz.org/>. (Cited on page 168)
- [117] P. Wade (W1GHZ). Enhancing the OK1DFC square septum feed with a choke ring or chaparral-style horn and a comparison of some septum polarizers, 2007. URL http://www.w1ghz.org/antbook/conf/Enhanced_Septum_Feed_MUD07.pdf. (Cited on page 168)
- [118] P. Wade (W1GHZ). Septum feeds – Tolerances and sensitivity (extended cover CD version). In *EME 2012 Conference Papers (15th International EME Conference, Cambridge, England)*. Radio Society of Great Britain and The UK Microwave Group, August 2012. ISBN 9781-9050-8683-2. (Cited on page 102)
- [119] J. S. Ward. *Observations of Carbon Monoxide in the Starburst Galaxy M82 with a 690 GHz Wide Spectral Bandwidth Receiver*. PhD thesis, California Institute of Technology, 2002. (Cited on page 151)
- [120] R. Wilson. Fatilary calculus. In *Transactions of the Student Union of Chalmers University of Technology*, volume 1, 1956. (Cited on page 120)
-

-
- [121] S. Zhutyaev (RW3BP). 1296 MHz small [EME](#) station with good capability (part 5): Antenna switching, June 4 2010. URL <http://www.vhfdx.ru/apparatura/1296-mhz-small-eme-station-with-good-capability-part-5>.
(Cited on page 212)
- [122] S. Zhutyaev (RW3BP). 1296 MHz small [EME](#) station with good capability (part 3): Accurate [NF](#) measurements on 1296 MHz, April 24 2010. URL http://www.vhfdx.ru/apparatura/accurate_noise_figure_measurements_1296_mhz. (Cited on pages 147, 154, and 216)
- [123] S. Zhutyaev (RW3BP). 1296 MHz small [EME](#) station with good capability (part 4): [LNA](#) optimization, April 15 2010. URL http://www.vhfdx.ru/apparatura/rw3bp_1296mhz_lna_optimization. (Cited on pages 108, 154, and 211)
-

Appendix A

SNR degradation due to resistive loss

Using equations from sections 4.2.1, 4.3 and 4.4 it is possible to calculate the degradation of the SNR caused by a receiver system. Figures A.2 to A.5 shows this degradation as a function of resistive loss in front of the LNA of such a system, for various antenna temperatures. Please refer to fig. A.1 for the circuit used to derive these graphs.

Using these graphs, it is easy to assess the impact resistive loss in front of the LNA will have on the final SNR of the system. It is also possible to see what NF a system *with* loss in front of the LNA would need to have, in order to achieve the same SNR degradation as a system *without* loss. Notice that the SNR degradation due to loss in front of the LNA is more severe the lower the antenna temperature is.

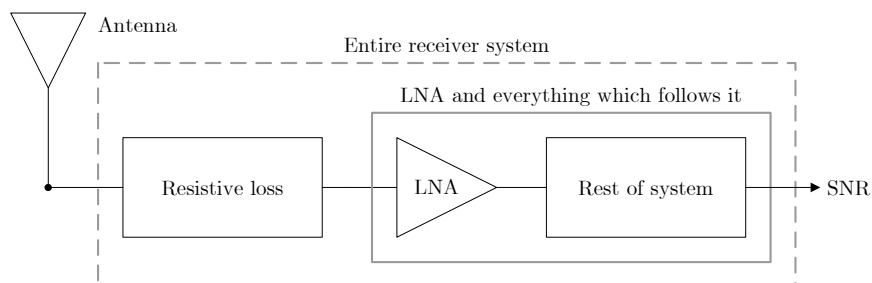


Figure A.1 The circuit used to derive the SNR degradation graphs in figs. A.2 to A.5.

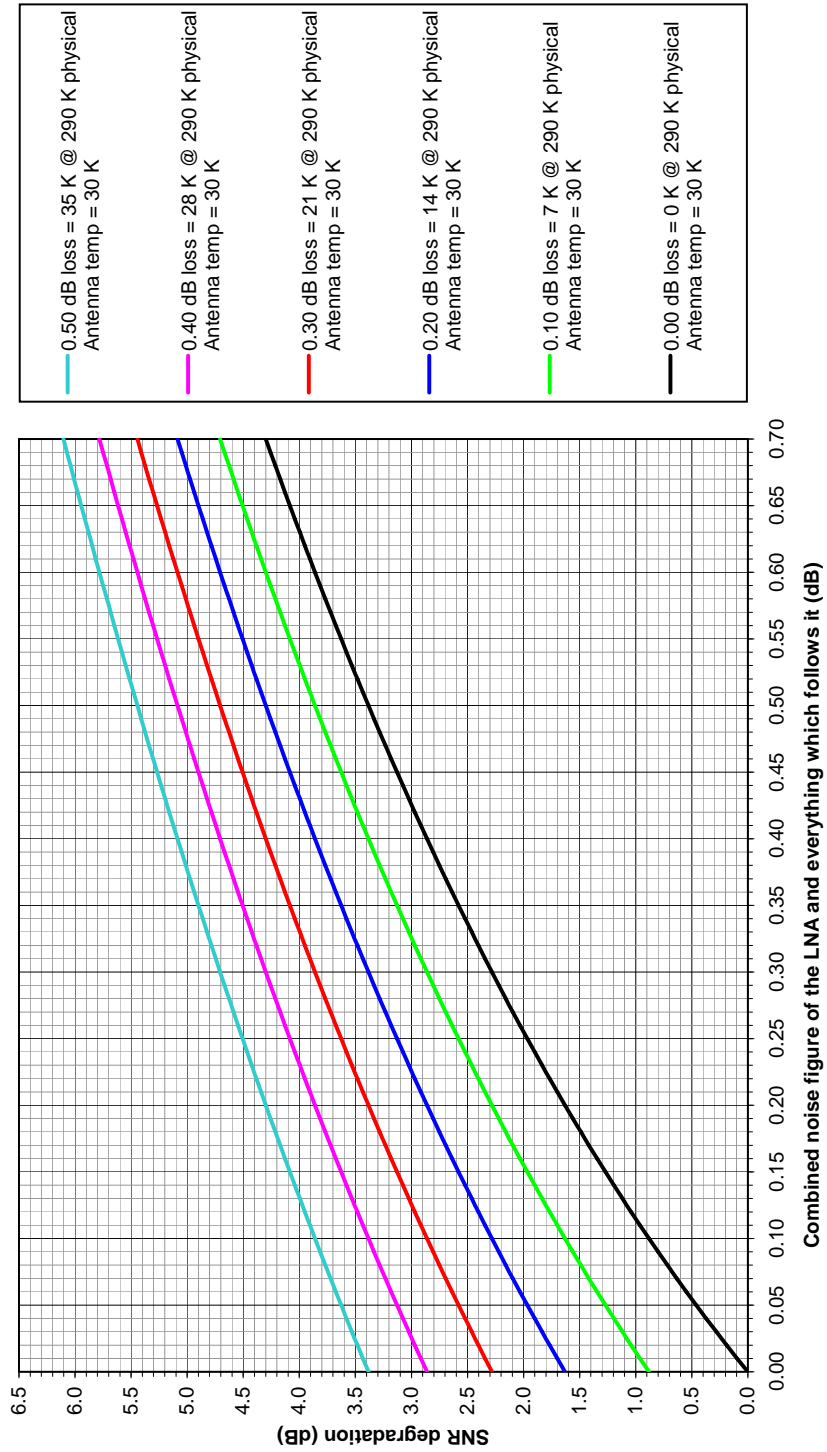


Figure A.2 The SNR degradation caused by the entire receiver system as a function of *a*) the combined NF of the LNA and everything which follows it and *b*) the resistive loss in front of the LNA. The antenna temperature is 30 K.

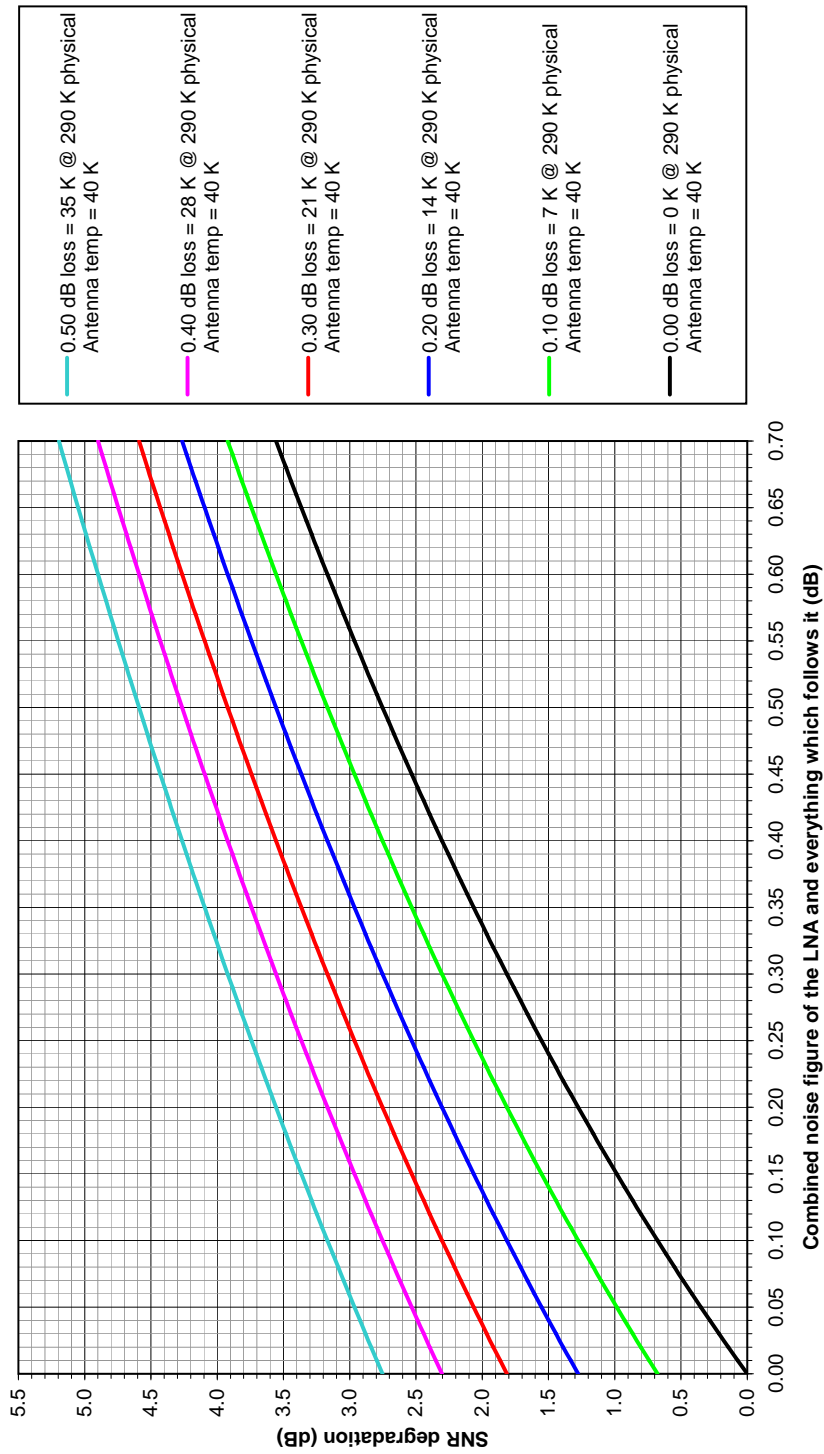


Figure A.3 The SNR degradation caused by the entire receiver system as a function of *a*) the combined NF of the LNA and everything which follows it and *b*) the resistive loss in front of the LNA. The antenna temperature is 40 K.

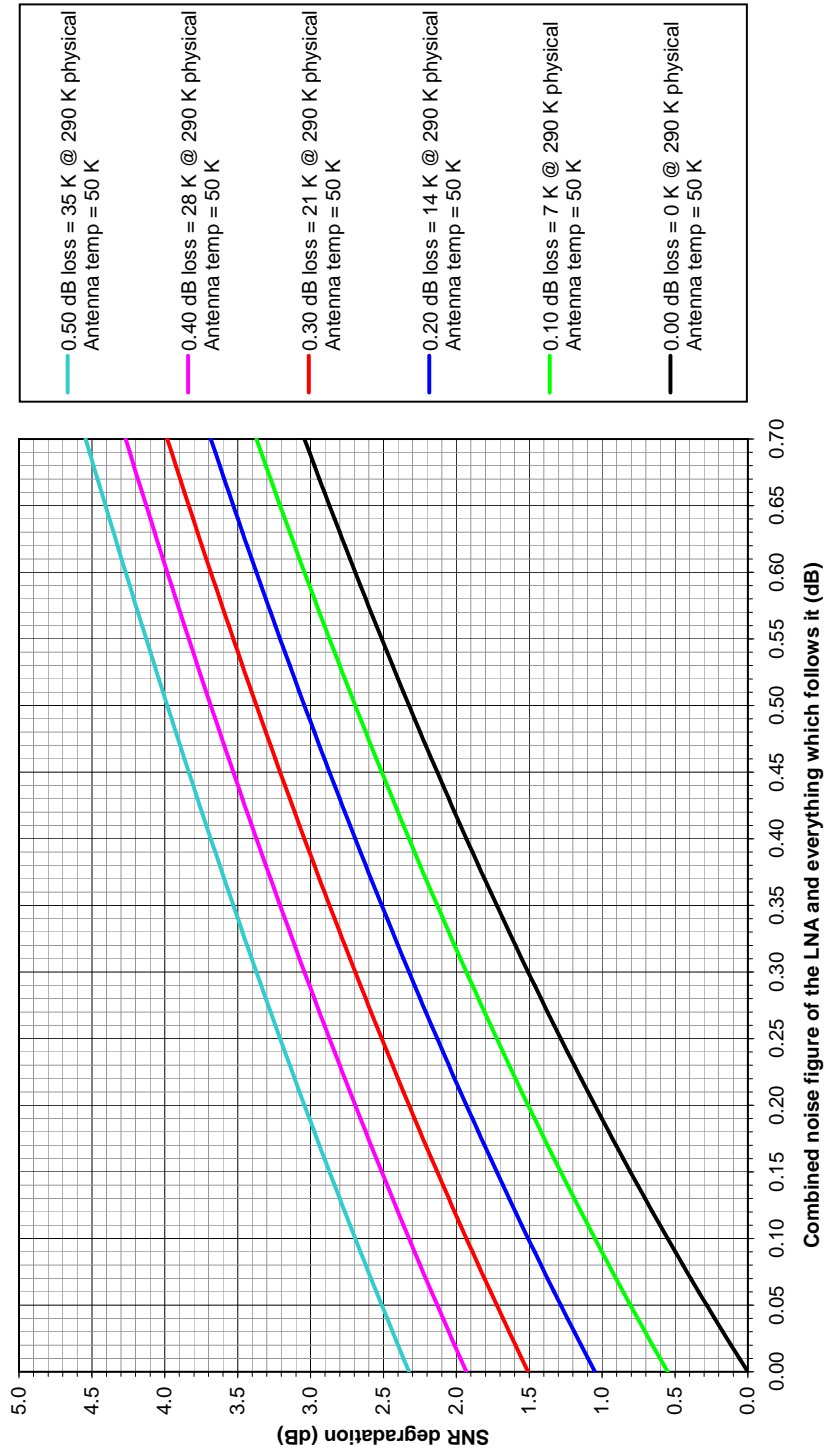


Figure A.4 The SNR degradation caused by the entire receiver system as a function of *a*) the combined NF of the LNA and everything which follows it and *b*) the resistive loss in front of the LNA. The antenna temperature is 50 K.

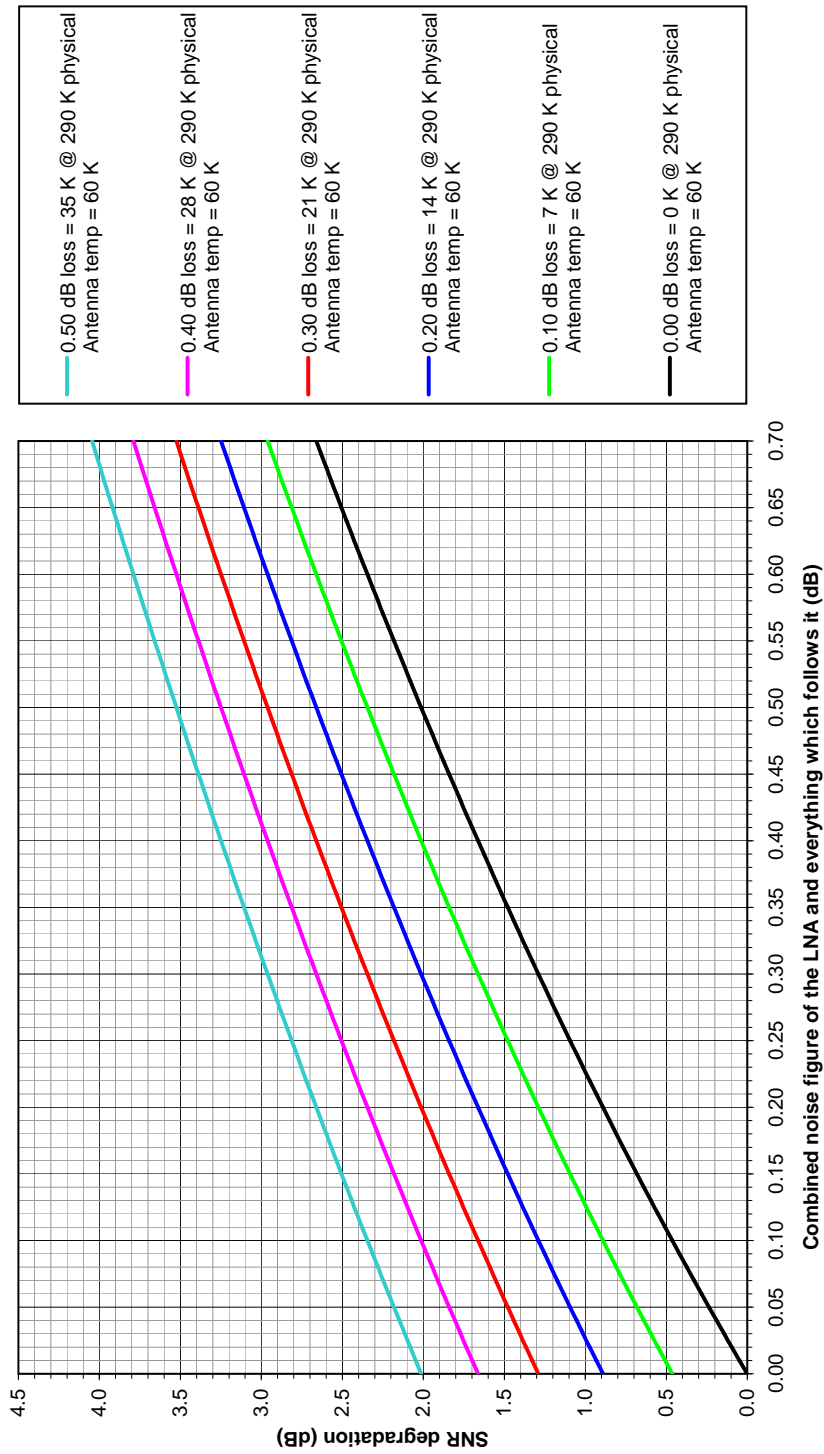


Figure A.5 The SNR degradation caused by the entire receiver system as a function of *a*) the combined NF of the LNA and everything which follows it and *b*) the resistive loss in front of the LNA. The antenna temperature is 60 K.

Appendix B

RAS rotator specifications

The technical specifications for the RAS rotator and the accompanying control box, presented in section [7.1.2](#), are given in tables [B.1](#) and [B.2](#).

Table B.1 The RAS rotator specifications, compiled from information from the manufacturer [102], one of the resellers [16, pg. 2] and documentation delivered with the product.

RAS Az/El rotator	Supply voltage	
	12 V (min)	24 V (max)
Az/El turning torque (Nm)	158	366
Az/El brake torque (Nm)	> 1582	> 1582
Brake construction	DWG	DWG
Az rotation range (°)	360±180	360±180
Az rotation speed (360°) (s)	120	60
El rotation range (°)	180±20	180±20
El rotation speed (180°) (s)	60	30
Resolution (°)	1	1
Vertical load (kg)	250	250
Weight (kg)	14	14
Mast size (bottom) (mm)	66	66
Mast size (elevation) (mm)	50	50

Table B.2 The RAS rotator control box specifications, compiled from information from the manufacturer [102], one of the resellers [16, pg. 3] and documentation delivered with the product.

RAS Az/El rotator control box	
Operating voltage (V)	13.8 to 24 (AC or DC)
Computer interface	RS232 600 baud 8N1
Protocol emulation	SPID, Yaesu
Limit settings	4 (2 Az and 2 El)
User settable calibration	Az and El (any degree)
Resolution (°)	1, 0.5, 0.25
Az rotation range (°)	180 (ACW) to 540 (CW)
El rotation range (°)	-20 to 200
Connections to rotator	Az 4 wires (sensor and motor) El 4 wires (sensor and motor)

Appendix C

Audio and data interface circuit description

The audio and data interface was presented in section 7.4.3. It was designed and built by the author and the circuit diagram was made using Eagle PCB, presented in section 7.5.4. The result is shown in fig. C.1 and consists of mainly three parts: A power supply, a digital communication interface and an audio interface. These will now be described in more detail.

The power supply is implemented using a 7805 linear voltage regulator IC, which supplies the digital circuitry with the needed 5 volts. The input voltage to this regulator is supplied by the transceiver at 13.8 V. A red LED is used to indicate when the power supply is active. Due to an increase in temperature, it is necessary to equip the 7805 with a heatsink.

At the centre of the digital circuitry are two MAX232 line driver/receiver ICs, which convert between serial port (RS-232) and TTL voltage levels. The RS-232 I/O-pins of the MAX232 ICs are connected to a 9-pin D-SUB connector which interfaces directly with the serial port of the computer. The TTL I/O-pins are connected to two 74LS07 hex buffer/driver ICs with high-voltage (30 V max) open-collector outputs. Some of these buffers are connected to the PTT, CW and CI-V ports which interface with the transceiver and sequencer. Since the open-collector outputs are capable of sinking 30 mA each, additional buffers are used to drive the indicator LEDs for the PTT (yellow), CW (yellow) and CI-V (green) activity. A changeover switch lets the user choose if the CW output port is to be controlled by the computer or by an external Morse key. Another changeover switch lets the user redirect the computer PTT signal to either the transceiver accessory socket or to an external connector. Since this switch has a stable off position in the centre, it is also possible to disable the computer PTT entirely. Finally, unused IC-pins are either grounded or left open in accordance with proper

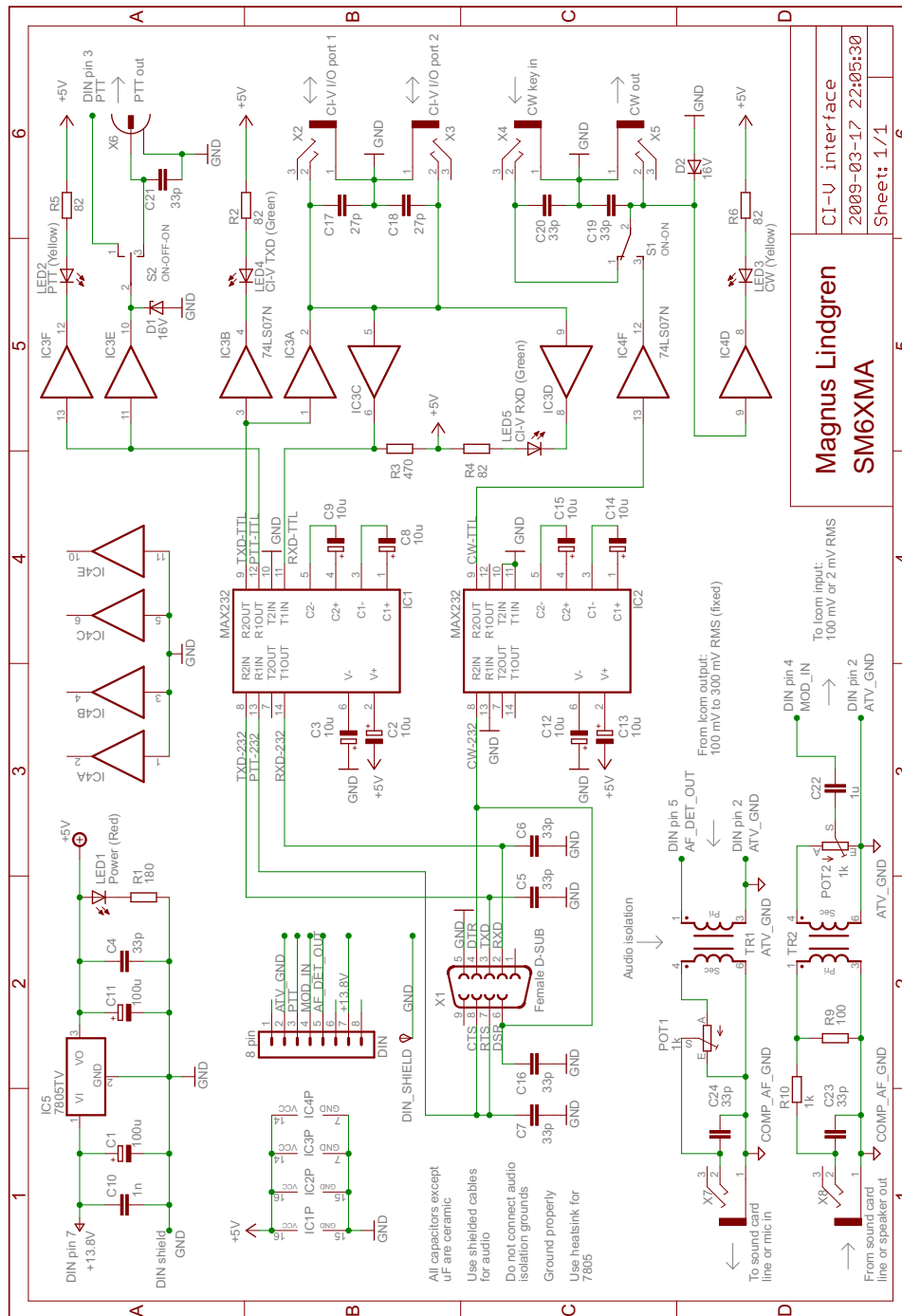


Figure C.1 The circuit diagram of the audio and data interface. Looking from the right, the power supply is shown in the upper left corner whereas the audio part is shown in the lower left corner. The rest of the circuit is dedicated to the digital PTT, CW and CI-V signals. LEDs are used for indicating power supply status and digital signal activity. The audio and signal grounds are all isolated from each other, in order to avoid ground loops and thus reduce interference.

practice. Since the **PTT** and **CW** ports are ‘active low’, these are not in need of pull-up resistors. For the **CI-V** port, pull-up is handled via the data bus. Two 16 V Zener diodes are used as elementary surge protectors, in case of inductive loads at the **PTT** and **CW** outputs.

The audio part is entirely passive, essentially consisting of two isolating audio transformers (repeating coils) and two potentiometers for audio level adjustment. The bandwidth of the repeating coils is about 3.5 kHz which is wider than the 2.5 kHz **SSB** bandwidth of the transceiver. The audio transformers ensure that the audio grounds of the computer (**COMP_AF_GND**) and the transceiver (**ATV_GND**) are isolated from each other. Great care was also taken during the construction to isolate each of these from the signal ground (**GND**). **COMP_AF_GND** and **GND** as well as **ATV_GND** and **GND** are thus only connected to each other in the computer and the transceiver respectively. All of this avoids ground loops which otherwise could result in interference, such as mains hum.

Since only one interface needed to be built, the author chose to solder the entire circuit onto a single Veroboard, instead of designing and etching a single **PCB**. The assembled board was then placed inside an aluminium box, with **I/O**-ports, switches, volume control knobs and **LEDs** accessible from the outside. See fig. 7.13 on page 114! For more information about the interface, please also refer to section 7.4.3.

A final note on ‘**RS-232** serial ports’ versus ‘**USB** ports’ is appropriate at this point. The **D-SUB** connector and **MAX232 ICs** can be replaced by a **USB** connector and an ‘**USB** to **UART** bridge’ circuit using **TTL** levels. It is also possible to replace the audio connection to the computer with a **USB** sound card. In this case, adding an internal **USB** hub circuit would eliminate the need for an additional **USB** connector.

Appendix D

Spectrum Lab scripts

The scripts in this appendix have been tested using [SL](#) version 2.75 b12. While this version of [SL](#) can ‘load’ and ‘save’ conditional actions scripts, the same is unfortunately not true for the code in the macro buttons and the frequency markers. Using these entails creating and editing a `.usr` file in the `configurations` folder of the [SL](#) installation path.¹

The user is advised to acquire a basic understanding of [SL](#) before using these scripts, so that functions such as [FFT](#) averaging, setting the sample rate etc. are not foreign. Even though [SL](#) can be a bit daunting at first, it has a very extensive user manual and an active user community willing to answer questions [34].

When running these scripts on a computer with a regular sound card as input, be sure to check that the dynamic range is adequate. Noise added to the signal can otherwise reach levels where saturation of the analogue-to-digital converter is the result. Note that [SL](#) also has the ability to make use of various [SDRs](#), which likely is a better alternative than using a regular sound card.

Please refer to section 7.5.1 for a brief introduction on how [SL](#) is used in the project presented in this thesis.

D.1 Y-factor measurement

The script presented below assists the operator in performing a Y-factor measurement. In case of a *solar* Y-factor measurement, the solar radio flux and measurement wavelength can be entered by the user after which the [G over T](#) is calculated. Please refer to fig. 8.12 on page 162 for a screenshot of [SL](#) running this script.

¹ It is however possible to load or save whole `.usr` files.

D.1.1 Conditional actions

```

1 if( initialising ) then ScanLo=0:ScanHi=2500:Max=0:Min=0:Y=0:S
  =1:lambda=0.23:GTsys=0:k=1.381e-23 // Initialise vars
2 if( initialising ) then filter[0].fft.options=1000000:filter
  [0].fft.type=3 // Set filter type to BPF
3 if( always ) then filter[0].fft.fc=ScanLo+(ScanHi-ScanLo)/2 //
  Set the filter centre frequency
4 if( always ) then filter[0].fft.bw=ScanHi-ScanLo // Set the
  filter BW
5 if( always ) then Average_noise=avrg_n(ScanLo,ScanHi) //
  Measure the noise level in the selected BW
6 if( always ) then Y=Max-Min // Calculate the Y-factor in dB
7 if( always ) then GTsys=10*log(8*pi*k*((10^(Y/10))-1)/((S*1E
  -22)*lambda^2)) // Calculate the G over Tsys in dB

```

D.1.2 Macro buttons

```

1 [MACRO_BUTTONS]
2 Exprs0="$Spectrum: "+(sp.pause?"PAUSED":"RUNNING")+". Pressing
  also clears the LTA!"
3 Commands0=sp.pause=!sp.pause:spa.clear_avrg
4 Options0=2
5 Hotkey0=0
6 Exprs1="$Noise meas. interval: "+str("###0 to ",ScanLo)+str
  ("###0 Hz",ScanHi)+" (F3: Change)"
7 Commands1=edit(ScanLo,"Lower Noise Measurement Frequency","
  Enter the lower noise measurement frequency!"):edit(ScanHi,"
  Upper Noise Measurement Frequency","Enter the upper noise
  measurement frequency!")
8 Options1=2
9 Hotkey1=114
10 Exprs2="$Norm. average noise in "+str("###0 Hz",ScanHi-ScanLo)
  +" Interval = "+str("000.0 ",Average_noise)+spa.ampl_unit
11 Commands2=
12 Options2=2
13 Hotkey2=0
14 Exprs3="$Max value: "+str("#000.0 ",Max)+spa.ampl_unit+" (F4:
  Fetch)"
15 Commands3=Max=Average_noise
16 Options3=2
17 Hotkey3=115
18 Exprs4="$Min value: "+str("#000.0 ",Min)+spa.ampl_unit+" (F5:
  Fetch)"
19 Commands4=Min=Average_noise
20 Options4=2
21 Hotkey4=116
22 Exprs5="$Y-factor: "+str("#00.0 ",Y)+spa.ampl_unit+" (F6: Clear
  Max/Min/Y)"
23 Commands5=Max=0:Min=0:Y=0
24 Options5=2
25 Hotkey5=117

```

```
26 Exprs6="$G/Tsys = "+str("#00.0 dB",GTsys)+" | S = "+str("#00.#
    SFU",S)+" | lambda = "+str("#0.### m",lambda)+" (F7: Change)"
27 Commands6=edit(S,"Solar Radio Flux","Enter the solar radio flux
    in SFUs!"):edit(lambda,"Wavelength","Enter the wavelength in
    metres!")
28 Options6=2
29 Hotkey6=118
30 Exprs7="$Date (ISO): "+str("YYYY-MM-DD",now)+" | Time (UTC): "+
    str("hh:mm:ss.s",now)
31 Commands7=
32 Options7=2
33 Hotkey7=0
```

D.1.3 Frequency markers

```
1 [FREQ_MARKERS]
2 Hidden=0
3 ShowInScreenshot=1
4 Name0=Noise measurement interval (lower)
5 Type0=s
6 Color0=16711808
7 FreqIncludesVF00=0
8 SetProc0=ScanLo=x
9 GetFunc0=ScanLo
10 InfoStr0=Noise measurement interval (lower)
11 Name1=Noise measurement interval (upper)
12 Type1=s
13 Color1=16711808
14 FreqIncludesVF01=0
15 SetProc1=ScanHi=x
16 GetFunc1=ScanHi
17 InfoStr1=Noise measurement interval (upper)
```

D.2 EME echo-data acquisition

The script presented below automates the **Rx-Tx-Rx** sequence as well as the process of recording every echo to a separate **.wav** file. These files are saved in the **SL** installation folder, with a timestamped filename beginning with ‘**EME-**’. It is also possible to initiate manual operation, though recordings are then disabled. Please refer to fig. 12.1 on page 186 for a screenshot of **SL** running this script.

This script uses the **RTS** and **DTR** control lines of the RS-232 serial port to control the **PTT** and **CW** functionalities of the system. This behaviour, as well as choosing the correct serial port, needs to be configured in the ‘**TRX Control**’ tab of the **SL** configuration window.

D.2.1 Conditional actions

```

1 if( never ) then ---- Initialising state machine flags ----
2 if( initialising ) then Flag1=0:Flag2=0:Flag3=0:Flag4=0:
   RecordedFlag=1:IdleFlag=1 // Set various flags
3 if( initialising ) then ManualMode=1:ManualTransmit=0 // Manual
   mode "ON" but Manual Tx "OFF" by default
4 if( initialising ) then WaveLog=0 // Wave file logging "OFF"
   by default
5 if( initialising ) then RunSpectrumInManualMode=0 // Spectrum "
   OFF" by default in manual mode
6 if( never ) then ---- Initialising timing parameters ----
7 if( initialising ) then PTTtoCWtime=0.5
8 if( initialising ) then CWtime=3.0
9 if( initialising ) then CWtoPTTtime=0.1
10 if( initialising ) then PTTtoOFFtime=0.4
11 if( initialising ) then RXtime=1.7
12 if( initialising ) then ManualRXtime = RXtime
13 if( never ) then ---- Initialising COM-port state ----
14 if( initialising ) then ptt_port.dtr=1 // Needed for things to
   work. Make sure this doesn't initiate Tx!
15 if( initialising ) then ptt_port.dtr=0 // No CW at start-up
16 if( initialising ) then ptt_port.rts=0 // No PTT at start-up
17 if( initialising ) then sp.pause=1 // Pause the spectrum at
   start-up
18 if( never ) then ---- Automatic mode ----
19 if( (!ManualMode) && (!Flag1) && (!Flag2) ) then IdleFlag=0 :
   Flag1=1 : ptt_port.rts=1 : timer1.start(PTTtoCWtime) //
   Automatic mode: Set flags, switch on PTT, wait <PTTtoCWtime>
   seconds for sequencer to switch system into Tx sequence
20 if( timer1.expired(1) ) then ptt_port.dtr=1 : timer2.start(
   CWtime) // Start CW and transmit for <CWtime> seconds
21 if( timer2.expired(1) ) then ptt_port.dtr=0 : timer3.start(
   CWtoPTTtime) // Stop CW, wait <CWtoPTTtime> seconds before
   switching off PTT
22 if( timer3.expired(1) ) then ptt_port.rts=0 : timer4.start(
   PTTtoOFFtime) // Switch off PTT, wait <PTTtoOFFtime> seconds
   for sequencer to switch system into "ready for Rx"
23 if( timer4.expired(1) ) then RecordedFlag=0 : timer5.start(
   RXtime) : sp.pause=0 // Wave RecordedFlag FALSE, start <
   RXtime> seconds Rx sequence, start the spectrum
24 if( (Flag1) && (WaveLog) && (!RecordedFlag) ) then wave.record
   ("EME-"+str("YYYYMMDD_hhmmss.s",now)+".wav") : RecordedFlag=1
   // Rx sequence started, start saving wave file, set wave
   RecordedFlag to TRUE
25 if( never ) then ---- Manual mode ----
26 if( (ManualMode) && (ManualTransmit) && (!Flag1) && (!Flag2) )
   then IdleFlag=0 : Flag2=1 : Flag3=1 : ptt_port.rts=1 : timer6
   .start(PTTtoCWtime) // Manual mode: Set flags, switch on PTT,
   wait <PTTtoCWtime> seconds for sequencer to switch system
   into Tx sequence
27 if( timer6.expired(1) ) then ptt_port.dtr=1 // Start CW and
   transmit

```

```

28 if( (ManualMode) && (!ManualTransmit) && (!Flag1) && (Flag2) &&
    (Flag3) ) then Flag3=0 : ptt_port.dtr=0 : timer7.start(
    CWtoPTTtime) // Stop CW, wait <CWtoPTTtime> seconds before
    switching off PTT
29 if( timer7.expired(1) ) then ptt_port.rts=0 : timer8.start(
    PTTtoOFFtime) // Switch off PTT, wait <PTTtoOFFtime> seconds
    for sequencer to switch system into "ready for Rx"
30 if( timer8.expired(1) ) then Flag4=1 // Set flag when system is
    "ready for Rx"
31 if( (Flag4) && (RunSpectrumInManualMode) ) then Flag4=0 :
    timer5.start(ManualRXtime) : sp.pause=0 // Manual Tx sequence
    just ended, start <RXtime> seconds Rx sequence, start the
    spectrum
32 if( (Flag4) && (!RunSpectrumInManualMode) ) then Flag4=0 :
    timer5.start(ManualRXtime) // Manual Tx sequence just ended,
    start <RXtime> seconds Rx sequence
33 if( never ) then ---- Automatic / Manual common ending ----
34 if( timer5.expired(1) ) then wave.stop : sp.pause=1 : Flag1=0 :
    Flag2=0 : IdleFlag=1 // Rx sequence just ended, if ever
    started -> stop recording wave-file, pause the spectrum,
    reset flags, enter idle mode

```

D.2.2 Macro buttons

```

1 [MACRO_BUTTONS]
2 Exprs0="$Date: "+str("YYYY-MM-DD",now)+" , Time (UTC): "+str("hh
    :mm:ss.s",now)
3 Commands0=
4 Options0=2
5 Hotkey0=0
6 Exprs1="$Automatic or manual mode: "+(ManualMode?"MANUAL":"AUTO
    ")
7 Commands1=ManualMode=!ManualMode
8 Options1=2
9 Hotkey1=0
10 Exprs2="$Record wave files in automatic mode: "+(WaveLog?"
    ENABLED":"DISABLED")
11 Commands2=WaveLog=!WaveLog
12 Options2=2
13 Hotkey2=0
14 Exprs3="$Manual transmit: "+(((ManualTransmit)&&(ManualMode))?"
    ENABLED":"DISABLED")
15 Commands3=ManualTransmit=!ManualTransmit
16 Options3=2
17 Hotkey3=0
18 Exprs4="$Run spectrum in manual Rx mode: "+(
    RunSpectrumInManualMode?"ENABLED":"DISABLED")
19 Commands4=RunSpectrumInManualMode=!RunSpectrumInManualMode
20 Options4=2
21 Hotkey4=0
22 Exprs5="$Automatic Rx time: "+str("#0.#",RXtime)+" s. Manual Rx
    time: "+str("#0.#",ManualRXtime)+" s."

```

```

23 Commands5=edit(RXtime,"Automatic Rx Time","Enter the automatic
    Rx time!"):edit(ManualRXtime,"Manual Rx Time","Enter the
    automatic Rx time!")
24 Options5=2
25 Hotkey5=0
26 Exprs6="$Tx/Rx/Idle status: "+(IdleFlag?"IDLE":(((timer5.value
    <>0)|(timer5.expired))?"RX":((ptt_port.dtr)"TX (PTT+CW)": "TX
    (PTT)"))))
27 Commands6=
28 Options6=2
29 Hotkey6=0
30 Exprs7="$Spectrum: "+(sp.pause?"PAUSED":"RUNNING")
31 Commands7=sp.pause=!sp.pause
32 Options7=2
33 Hotkey7=0

```

D.3 EME echo-data analysis

The script presented below lets the user analyse pre-recorded [EME](#) echoes, to determine parameters such as the [SNR](#) and the Doppler spread of the signal. A few things need to be kept in mind though, when using this script. The ‘filter bandwidth’ needs to be wider than the ‘[SNR](#) measurement bandwidth’, for the [SNR](#) indication of the output signal in channel 2 (and its long-term average) to be correctly calculated. Furthermore, for the dynamic frequency shift to work as intended, the change in frequency of the input signal in channel 1 must not be too drastic. In this aspect, it helps if the [FFT](#) averaging of channel 1 is kept to a minimum. On the other hand, to get a smoother indication of the [SNR](#) of channel 2, [FFT](#) averaging needs to be applied. The ‘same [FFT](#) params for all analyser channels’ checkbox, in the ‘[FFT](#)’ tab of the [SL](#) configuration window, must thus not be checked. See [fig. 12.3](#) on page 190! Please also refer to [fig. 12.2](#) on page 189 for a screenshot of [SL](#) running this script.

D.3.1 Conditional actions

```

1 if( never ) then MovingCh1FilterFlag = 1: Continuously sets the
    channel 1 filter center to the peak of the signal
2 if( never ) then BWFlag = 1: Sets the (shifted) filter BW equal
    to the SNR measurement BW (else to a specified value)
3 if( never ) then AutoSNFlag = 1: Continuously sets the SNR
    measurement center to the peak of the signal
4 if( never ) then FixedCh2SignalFlag = 1: Continuously keeps the
    shifted output signal frequency at a constant location/value
5 if( never ) then MarginFactor: Safety factor used to guarantee
    a correct noise measurement BW when calculating the SNR
6 if( never ) then CWwidth: The maximum anticipated width of the
    received CW signal (used for SNR noise calculations)

```

```

7 if( never ) then SNBW: The SNR measurement BW
8 if( never ) then SignalPeakFrequency: The frequency of the
  input signal
9 if( never ) then SNC: Center frequencies of the SNR measurments
  in channel 1
10 if( never ) then Ch2SignalPeakFrequency: The frequency of the
  shifted output signal
11 if( never ) then Ch2SNC: Center frequencies of the SNR
  measurments in channel 2
12 if( never ) then ScanLo: The lower frequency limit in which to
  look for a signal peak
13 if( never ) then ScanHi: The upper frequency limit in which to
  look for a signal peak
14 if( initialising ) then sp.pause=0 // Run the spectrum at
  startup
15 if( initialising ) then MovingCh1FilterFlag=1:BWFlag=0:
  AutoSNFlag=1:FixedCh2SignalFlag=1 // Initialise flags
16 if( initialising ) then Button3Flag=0:Button4Flag=0:Button5Flag
  =0:Button6Flag=0:Button7Flag=0 // Initialise button flags (
  for conditional actions with buttons)
17 if( initialising ) then MarginFactor=1.5:CWWidth=50:SNBW=100:
  SignalPeakFrequency=800:SNC=SignalPeakFrequency:
  Ch2SignalPeakFrequency=SignalPeakFrequency-300:Ch2SNC=
  Ch2SignalPeakFrequency:ScanLo=0:ScanHi=2500 // Initialise
  vars
18 if( initialising ) then filter[0].fft.options=1000000:filter
  [0].fft.type=3:filter[0].fft.bw=MarginFactor*SNBW+CWWidth //
  Set filter to shift down, set filter to be a BPF and set BW
19 if( always ) then SignalPeakFrequency=peak_f(ScanLo,ScanHi) //
  Get the input signal center frequency from the peak in the
  range ScanLo to ScanHi
20 if( MovingCh1FilterFlag ) then filter[0].fft.fc=
  SignalPeakFrequency // Set the input center frequency of the
  filter equal to the center frequency of the input signal
21 if( BWFlag ) then filter[0].fft.bw=SNBW // Set the filter BW
  equal to the SNR measurement BW (this will give false S/N
  indication)
22 if( FixedCh2SignalFlag ) then filter[0].fft.fs=
  Ch2SignalPeakFrequency-SignalPeakFrequency // If the new
  center frequency of the signal shall be constant -> calculate
  the new frequency shift from the center frequency
23 if( else ) then Ch2SignalPeakFrequency=filter[0].fft.fs+
  SignalPeakFrequency // If not -> calculate the new center
  frequency of the signal from the frequency shift
24 if( AutoSNFlag ) then SNC=SignalPeakFrequency : Ch2SNC=
  Ch2SignalPeakFrequency // Set the center of the SNR
  measurement in channel 1 & 2 at the peak of the signal
25 if( always ) then PeakSNFreq=peak_f(SignalPeakFrequency-(SNBW
  /2),SignalPeakFrequency+(SNBW/2)) // Check the actual
  frequency of the signal plus noise peak
26 if( always ) then PeakDiff=PeakSNFreq-SignalPeakFrequency //
  Difference between actual and intended output center
  frequency

```

```

27 if( always ) then PeakSNamp=peak_a(SignalPeakFrequency-(SNBW/2)
    ,SignalPeakFrequency+(SNBW/2)) // Amplitude of the signal
    plus noise peak
28 if( always ) then AverageSN=avrg_n(SNC-(SNBW/2),SNC+(SNBW/2))
    // Total signal plus noise power in the SNR measurement BW
29 if( always ) then AverageSNLin=10^(AverageSN/10) // Total
    signal plus noise power in linear terms
30 if( always ) then AverageN11=avrg_n(SNC-(CWWidth/2)-(SNBW/2),
    SNC-(CWWidth/2)) // Left half of the noise power
31 if( always ) then AverageN12=avrg_n(SNC+(CWWidth/2),SNC+(
    CWWidth/2)+(SNBW/2)) // Right half of the noise power
32 if( always ) then AverageN1Lin=((10^(AverageN11/10))+(10^(
    AverageN12/10)))/2 // Total noise power in linear terms
33 if( always ) then StoN1=10*log((AverageSNLin/AverageN1Lin)-1)
    // Calculate the SNR
34 if( never ) then ---- Channel 2 calculations ----
35 if( always ) then Ch2PeakSNFreq=peak_f(#2,
    Ch2SignalPeakFrequency-(SNBW/2),Ch2SignalPeakFrequency+(SNBW
    /2)) // Check the actual frequency of the signal plus noise
    peak
36 if( always ) then Ch2PeakDiff=Ch2PeakSNFreq-
    Ch2SignalPeakFrequency // Difference between actual and
    intended output center frequency
37 if( always ) then Ch2PeakSNamp=peak_a(#2,Ch2SignalPeakFrequency
    -(SNBW/2),Ch2SignalPeakFrequency+(SNBW/2)) // Amplitude of
    the signal plus noise peak
38 if( always ) then Ch2AverageSN=avrg_n(#2,Ch2SNC-(SNBW/2),Ch2SNC
    +(SNBW/2)) // Total signal plus noise power in the SNR
    measurement BW
39 if( always ) then Ch2AverageSNLin=10^(Ch2AverageSN/10) // Total
    signal plus noise power in linear terms
40 if( always ) then Ch2AverageN11=avrg_n(#2,Ch2SNC-(CWWidth/2)-(
    SNBW/2),Ch2SNC-(CWWidth/2)) // Left half of the noise power
41 if( always ) then Ch2AverageN12=avrg_n(#2,Ch2SNC+(CWWidth/2),
    Ch2SNC+(CWWidth/2)+(SNBW/2)) // Right half of the noise power
42 if( always ) then Ch2AverageN1Lin=((10^(Ch2AverageN11/10))
    +(10^(Ch2AverageN12/10)))/2 // Total noise power in linear
    terms
43 if( always ) then Ch2StoN1=10*log((Ch2AverageSNLin/
    Ch2AverageN1Lin)-1) // Calculate the SNR
44 if( never ) then ---- Long-Term Average (LTA) 2 calculations
    ----
45 if( always ) then LTA2PeakSNFreq=peak_f(#LTA2,
    Ch2SignalPeakFrequency-(SNBW/2),Ch2SignalPeakFrequency+(SNBW
    /2)) // Check the actual frequency of the signal plus noise
    peak
46 if( always ) then LTA2PeakDiff=LTA2PeakSNFreq-
    Ch2SignalPeakFrequency // Difference between actual and
    intended output center frequency
47 if( always ) then LTA2PeakSNamp=peak_a(#LTA2,
    Ch2SignalPeakFrequency-(SNBW/2),Ch2SignalPeakFrequency+(SNBW
    /2)) // Amplitude of the signal plus noise peak

```



```

48 if( always ) then LTA2AverageSN=avrg_n(#LTA2,Ch2SNC-(SNBW/2),
    Ch2SNC+(SNBW/2)) // Total signal plus noise power in the SNR
    measurement BW
49 if( always ) then LTA2AverageSNLin=10^(LTA2AverageSN/10) //
    Total signal plus noise power in linear terms
50 if( always ) then LTA2AverageN11=avrg_n(#LTA2,Ch2SNC-(CWidth
    /2)-(SNBW/2),Ch2SNC-(CWidth/2)) // Left half of the noise
    power
51 if( always ) then LTA2AverageN12=avrg_n(#LTA2,Ch2SNC+(CWidth
    /2),Ch2SNC+(CWidth/2)+(SNBW/2)) // Right half of the noise
    power
52 if( always ) then LTA2AverageN1Lin=((10^(LTA2AverageN11/10))
    +(10^(LTA2AverageN12/10)))/2 // Total noise power in linear
    terms
53 if( always ) then LTA2StoN1=10*log((LTA2AverageSNLin/
    LTA2AverageN1Lin)-1) // Calculate the SNR
54 if( never ) then ---- Conditional Button Actions ----
55 if( Button3Flag && (!BWFlag) ) then tmpbw=MarginFactor*SNBW+
    CWidth : edit(tmpbw,"Filter Bandwidth","Enter a filter
    bandwidth!") : filter[0].fft.bw=tmpbw
56 if( !else ) then tmpsnbw=(filter[0].fft.bw-CWidth)/
    MarginFactor : edit(tmpsnbw,"S/N Bandwidth","Enter a S/N
    measurement bandwidth!") : SNBW=tmpsnbw : Button3Flag=0 //
    Continue from the previous row
57 if( Button4Flag && (!BWFlag) ) then tmpbw=MarginFactor*SNBW+
    CWidth : edit(tmpbw,"Filter Bandwidth","Enter a filter
    bandwidth!") : filter[0].fft.bw=tmpbw : Button4Flag=0
58 if( Button5Flag && (!AutoSNFlag) ) then edit(SNC,"Channel 1 S/N
    Center Frequency","Enter a S/N measurement center frequency
    for channel 1!") : edit(Ch2SNC,"Channel 2 S/N Center
    Frequency","Enter a S/N measurement center frequency for
    channel 2!") : Button5Flag=0
59 if( Button6Flag && (!MovingCh1FilterFlag) ) then
    SignalPeakFrequency=filter[0].fft.fc : edit(
    SignalPeakFrequency,"Filter Center Frequency","Enter a filter
    center frequency!") : filter[0].fft.fc=SignalPeakFrequency :
    Button6Flag=0
60 if( Button7Flag && FixedCh2SignalFlag ) then edit(
    Ch2SignalPeakFrequency,"Signal Center Frequency","Enter a new
    signal center frequency") : Button7Flag=0
61 if( Button7Flag && (!FixedCh2SignalFlag) ) then tmps=filter[0].
    fft.fs : edit(tmps,"Filter Frequency Shift","Enter a filter
    frequency shift!") : filter[0].fft.fs=tmps : Button7Flag=0

```

D.3.2 Macro buttons

```

1 [MACRO_BUTTONS]
2 Exprs0="$Spectrum: "+(sp.pause?"PAUSED":"RUNNING")+". Pressing
    also clears the LTA!"
3 Commands0=sp.pause=!sp.pause:spa.clear_avrg
4 Options0=2
5 Hotkey0=0

```

```

6 Exprs1="$S/N 1|2|LTA2 = "+str("#00.0",StoN1)+" | "+str("#00.0",
  Ch2StoN1)+" | "+str("#00.0 dB",LTA2StoN1)+". Peak 1|2 = "+str
  ("###0.",PeakSNFreq)+" | "+str("###0.0 Hz",Ch2PeakSNFreq)
7 Commands1=edit(CWWidth,"Estimated CW Width","Enter the
  estimated width of the signal!")
8 Options1=2
9 Hotkey1=0
10 Exprs2="$Signal peak detect interval = "+str("###0 to ",ScanLo)
  +str("###0 Hz",ScanHi)
11 Commands2=edit(ScanLo,"Lower Peak Detect Frequency","Enter the
  lower peak detect frequency!"):edit(ScanHi,"Upper Peak Detect
  Frequency","Enter the upper peak detect frequency!")
12 Options2=2
13 Hotkey2=0
14 Exprs3="$Filter BW = "+str("###0. Hz",filter[0].fft.bw)+". S/N
  measurement BW = "+str("###0.# Hz",SNBW)
15 Commands3=Button3Flag=1
16 Options3=2
17 Hotkey3=0
18 Exprs4="$Filter BW = S/N meas. BW: "+(BWFlag?"ENABLED":"
  DISABLED")+". Filter BW = "+str("###0.# Hz",filter[0].fft.bw)
19 Commands4=BWFlag=!BWFlag : Button4Flag=1
20 Options4=2
21 Hotkey4=0
22 Exprs5="$Auto S/N meas. centers: "+(AutoSNFlag?"ENABLED":"
  DISABLED")+". Center 1|2 = "+str("###0.",SNC)+" | "+str
  ("###0. Hz",Ch2SNC)
23 Commands5=AutoSNFlag=!AutoSNFlag : Button5Flag=1
24 Options5=2
25 Hotkey5=0
26 Exprs6="$Moving Ch1 filter center freq.: "+(MovingCh1FilterFlag
  ?"ENABLED":"DISABLED")+". Center 1 = "+str("###0.",filter[0].
  fft.fc)
27 Commands6=MovingCh1FilterFlag=!MovingCh1FilterFlag :
  Button6Flag=1
28 Options6=2
29 Hotkey6=0
30 Exprs7="$Fixed Ch2 signal freq.: "+(FixedCh2SignalFlag?"ENABLED
  ":"DISABLED")+". Center 2|Sh = "+str("###0",
  Ch2SignalPeakFrequency)+" | "+str("###0. Hz",filter[0].fft.fs
  )
31 Commands7=FixedCh2SignalFlag=!FixedCh2SignalFlag : Button7Flag
  =1
32 Options7=2
33 Hotkey7=0

```

D.3.3 Frequency markers

```

1 [FREQ_MARKERS]
2 Hidden=0
3 ShowInScreenshot=1
4 Name0=Filter bandwidth slider

```

```
5 Type0=s
6 Color0=16711935
7 FreqIncludesVF00=0
8 SetProc0=filter[0].fft.bw=2*(filter[0].fft.fc-x)
9 GetFunc0=filter[0].fft.fc-filter[0].fft.bw/2
10 InfoStr0=Bandwidth adjustment
11 Name1=Filter center frequency slider
12 Type1=s
13 Color1=16711935
14 FreqIncludesVF01=0
15 SetProc1=filter[0].fft.fc=x
16 GetFunc1=filter[0].fft.fc
17 InfoStr1=Filter center frequency
18 Name2=Center frequency of shifted signal
19 Type2=s
20 Color2=16711935
21 FreqIncludesVF02=0
22 SetProc2=Ch2SignalPeakFrequency=x:filter[0].fft.fs=x-peak_f(
    ScanLo,ScanHi)
23 GetFunc2=Ch2SignalPeakFrequency
24 InfoStr2=Center frequency of shifted signal
25 Name3=Peak detect interval marker (lower)
26 Type3=s
27 Color3=16711808
28 FreqIncludesVF03=0
29 SetProc3=ScanLo=x
30 GetFunc3=ScanLo
31 InfoStr3=Peak detect interval marker (lower)
32 Name4=Peak detect interval marker (upper)
33 Type4=s
34 Color4=16711808
35 FreqIncludesVF04=0
36 SetProc4=ScanHi=x
37 GetFunc4=ScanHi
38 InfoStr4=Peak detect interval marker (upper)
39 Name5=S/N bandwidth marker (lower)
40 Type5=s
41 Color5=255
42 FreqIncludesVF05=0
43 GetFunc5=SNC-SNBW/2
44 InfoStr5=S/N bandwidth marker (lower)
45 Name6=S/N bandwidth marker (upper)
46 Type6=s
47 Color6=255
48 FreqIncludesVF06=0
49 GetFunc6=SNC+SNBW/2
50 InfoStr6=S/N bandwidth marker (upper)
51 Name7=S/N bandwidth marker StoN1 (lower lower)
52 Type7=w
53 Color7=0
54 FreqIncludesVF07=0
55 GetFunc7=SNC-(CWwidth/2)-(SNBW/2)
56 InfoStr7=S/N bandwidth marker StoN1 (lower lower)
57 Name8=S/N bandwidth marker StoN1 (upper lower)
```

```
58 Type8=w
59 Color8=0
60 FreqIncludesVF08=0
61 GetFunc8=SNC-(CWwidth/2)
62 InfoStr8=S/N bandwidth marker StoN1 (upper lower)
63 Name9=S/N bandwidth marker StoN1 (lower upper)
64 Type9=w
65 Color9=0
66 FreqIncludesVF09=0
67 GetFunc9=SNC+(CWwidth/2)
68 InfoStr9=S/N bandwidth marker StoN1 (lower upper)
69 Name10=S/N bandwidth marker StoN1 (upper upper)
70 Type10=w
71 Color10=0
72 FreqIncludesVF010=0
73 GetFunc10=SNC+(CWwidth/2)+(SNBW/2)
74 InfoStr10=S/N bandwidth marker StoN1 (upper upper)
75 Name11=S/N bandwidth marker Ch2StoN1 (lower lower)
76 Type11=w
77 Color11=0
78 FreqIncludesVF011=0
79 GetFunc11=Ch2SNC-(CWwidth/2)-(SNBW/2)
80 InfoStr11=S/N bandwidth marker Ch2StoN1 (lower lower)
81 Name12=S/N bandwidth marker Ch2StoN1 (upper lower)
82 Type12=w
83 Color12=0
84 FreqIncludesVF012=0
85 GetFunc12=Ch2SNC-(CWwidth/2)
86 InfoStr12=S/N bandwidth marker Ch2StoN1 (upper lower)
87 Name13=S/N bandwidth marker Ch2StoN1 (lower upper)
88 Type13=w
89 Color13=0
90 FreqIncludesVF013=0
91 GetFunc13=Ch2SNC+(CWwidth/2)
92 InfoStr13=S/N bandwidth marker Ch2StoN1 (lower upper)
93 Name14=S/N bandwidth marker Ch2StoN1 (upper upper)
94 Type14=w
95 Color14=0
96 FreqIncludesVF014=0
97 GetFunc14=Ch2SNC+(CWwidth/2)+(SNBW/2)
98 InfoStr14=S/N bandwidth marker Ch2StoN1 (upper upper)
99 Name15=S/N bandwidth marker Ch. 2 (lower)
100 Type15=s
101 Color15=255
102 FreqIncludesVF015=0
103 GetFunc15=Ch2SNC-SNBW/2
104 InfoStr15=S/N bandwidth marker Ch. 2 (lower)
105 Name16=S/N bandwidth marker Ch. 2 (upper)
106 Type16=s
107 Color16=255
108 FreqIncludesVF016=0
109 GetFunc16=Ch2SNC+SNBW/2
110 InfoStr16=S/N bandwidth marker Ch. 2 (upper)
```

